UNIVERSITY OF
BIRMINGHAM

Synthesis and Characterisation of Novel Metal Pyrophosphates

by

Annabelle R. Baker

A thesis submitted to
the University of Birmingham
for the degree of
Doctor of Philosophy

School of Chemistry
College of Engineering and Physical Sciences
University of Birmingham
September 2014

Abstract

This thesis describes the synthesis, properties and structural characterisation of Mg^{2+}, Mn^{2+} and Ti^{4+} pyrophosphates and Li and V substituted analogues.

Two polymorphs of $MgH_2P_2O_7$, hereby designated α and β, were isolated by a novel acid melt synthetic route. Both polymorphs crystallised in monoclinic space groups, with α-$MgH_2P_2O_7$ isostructural with $NiH_2P_2O_7$ and β-$MgH_2P_2O_7$ isostructural with $CaH_2P_2O_7$. Rietveld refinements of NPD data gave excellent fits to both structural models. Addition of lithium carbonate during synthesis resulted in a new phase, $MgLi_{0.8}H_{1.2}P_2O_7$. Flame photometry and VT-XRD confirm the presence of Li, and Rietveld refinement of NPD data suggests two similar possible structural models.

$MnH_2P_2O_7$, a structural polymorph of β-$MgH_2P_2O_7$ was also synthesised via a similar route. Magnetic analysis revealed $MnH_2P_2O_7$ to be paramagnetic, with a small underlying antiferromagnetic component. Incorporation of Li was again achieved via the addition of lithium carbonate during synthesis. Rietveld refinement of NPD data suggests a similar structure to that of $MnH_2P_2O_7$ and a composition of $MLi_{0.5}H_{1.5}P_2O_7$.

A metastable polymorph of TiP_2O_7 has been successfully synthesised at low temperature and appears to adopt a structure similar to the ideal cubic structure. Incorporation of vanadium during synthesis was successful and resulted in an expansion of the unit cell. Both phases undergo a phase transition above 275°C to the ideal cubic structure. SAED and NPD data show V-doped TiP_2O_7 is not cubic. Addition of vanadium results in an unusual uniform spherical morphology unseen in parent phase, with different vanadium sources resulting in variation in the uniformity of shape and size of the synthesized particles.

To my parents

Acknowledgements

First and foremost, I would like to thank my supervisor, Dr Adrian Wright, for his support, help and advice, and generally putting up with me for the last 4 years.

I would like to thank Dr Jackie Deans for all her technical assistance, training and always being ready to go above and beyond when I've asked for help! I will miss our chats. I would also like to thank Dr Louise Male for all the XRD training and assistance, and Terry Green for the assistance in collected ESR data. Externally I would like to thank Dr Ron Smith at ISIS for his help in the collection of NPD data and Scott King for collecting solid state NMR data.

I would like to thank the Wright group past and present for all their assistance in and out of the lab, especially Yasmin for all the help when I first started.

I would also like to thank the members of floor 5 past and present for making my PhD such an enjoyable time, especially Evin, Cathryn, Little Ben, Maz, Julie, Tom C, Laura, Phil, Jose, Trang and Rosie. I would especially like to thank James for keeping me entertained whilst writing this thesis and for all the chats over tea and biscuits; and Big Ben for always being ready to chat and keeping us all entertained with his upbeat personality.

I would also like to thank Alaric for all his love, help and support over the last 2 ½ years, it's been wonderful.

And lastly I would like to thank my family, in particular my dad, for all their love and support.

Abbreviations

AMP/ADP/ATP	Adenosine Mono/Di/Tri-phosphate
BVS	Bond Valence Sum
CPC	Calcium Phosphate Cements
ESR	Electron Spin Resonance
FCFW	Field Cooled/Field Warmed
GII	Global Instability Index
GSAS	General Structure Analysis System
HA	Hydroxyapatite
ICSD	Inorganic Crystal Structure Database
JCPDS	Joint Committee on Powder Diffraction Studies
LTS-TiP_2O_7	Low Temperature Synthesised Titanium Pyrophosphate
MAS	Magic Angle Spinning
MRI	Materials Research Instruments
MPMS	Magnetic Properties Measurement System
NMR	Nuclear Magnetic Resonance
NPD	Neutron Powder Diffraction
PXRD	Powder X-ray Diffraction
PSD	Position Sensitive Detector
SAED	Selected Area Electron Diffraction
SEM	Scanning Electron Microscopy
SQUID	Superconducting Quantum Interference Device
TEM	Transmission Electron Microscopy
TGA-MS	Thermogravimetric Analysis-Mass Spectrometry
XRD	X-ray Diffraction
XRF	X-ray Fluorescence
VT-XRD	Variable Temperature X-ray Diffraction
ZFCFW	Zero-Field Cooled/Field Warmed

Table of Contents

Chapter 1: Introduction

1.1 General Background of Phosphate Chemistry 1

1.1.1 Condensed Phosphates 2

1.2 Calcium Phosphates as Biomaterials 4

1.3 Acidic Pyrophosphates 6

1.3.1 Nickel/Cobalt Acid Pyrophosphates 6

1.3.2 Iron Acid Pyrophosphate 8

1.3.3 Magnesium and Manganese Pyrophosphates 11

1.4 Condensed Phosphates as Lithium Conductors 12

1.5 Titanium Pyrophosphate and the AX_2O_7 Series 13

1.5.1 Tin Pyrophosphate 14

1.5.2 Zirconium Pyrophosphate and Negative Thermal Expansion Materials 15

1.6 Project Aims 17

References 18

Chapter 2: Experimental Techniques

2.1 Introduction 22

2.2 Synthesis 22

2.3 Modification of Condensed Phosphates 23

2.3.1 Ion Exchange of $MgH_2P_2O_7$ 23

2.4 Characterisation Techniques 23

2.4.1 Diffraction 23

2.4.1.1 Crystallography 23

2.4.1.2 Bragg's Law 26

2.4.2 X-ray Diffraction 27

2.4.2.1 Generation of X-rays 28

2.4.2.2 Powder Diffraction 29

2.4.2.3 Monochromation 32

2.4.2.4 X-ray Detectors 32

2.4.2.5 Laboratory Diffractometers 32

2.4.3 Neutron Diffraction 33

2.4.4 Rietveld Analysis 35
2.4.5 Thermogravimetric Analysis-Mass Spectrometry 37
2.4.6 Electron Microscopy 39
2.4.6.1 Scanning Electron Microscopy 39
2.4.6.2 Transmission Electron Microscopy 40
2.4.7 X-ray Fluorescence 41
2.4.8 Solid State Nuclear Magnetic Resonance Spectroscopy 41
2.4.9 Magnetic Analysis 43
2.4.10 Electron Spin Resonance 47
2.4.11 Flame Emission Photometry 48
References 49

Chapter 3: Synthesis and Characterisation of $MgH_2P_2O_7$ and Li-Doped $MgH_2P_2O_7$

3.1 Introduction 51
3.2 Experimental 52
3.2.1 Synthesis of α-$MgH_2P_2O_7$ 52
3.2.2 Synthesis of β-$MgH_2P_2O_7$ 52
3.2.3 Synthesis of Li-Doped $MgH_2P_2O_7$ 52
3.2.4 Collection of Diffraction Data 53
3.3 Results and Discussion 53
3.3.1 α-$MgH_2P_2O_7$ 53
3.3.1.1 Crystal Structure of α-$MgH_2P_2O_7$ 53
3.3.1.2 ^{31}P MAS-NMR 60
3.3.1.3 Thermal Behaviour of α-$MgH_2P_2O_7$ 61
3.3.2 β-$MgH_2P_2O_7$ 63
3.3.2.1 Crystal Structure of β-$MgH_2P_2O_7$ 65
3.3.2.2 ^{31}P MAS-NMR 69
2.4.2.3 Thermal Behaviour of β-$MgH_2P_2O_7$ 70
3.3.3 Polymorphism in $MgH_2P_2O_7$ 71
3.3.4 Li-Doped MgH2P2O7 72
3.3.4.1 Thermal Behaviour in Li-Doped $MgH_2P_2O_7$ 75
3.3.4.2 Crystal Structure of Li-Doped $MgH_2P_2O_7$ 77

3.3.5 Crystal Morphology 91
3.4 Conclusion 93
References 94

Chapter 4: Synthesis and Characterisation of $MnH_2P_2O_7$ and Li-Doped $MnH_2P_2O_7$

4.1 Introduction 96
4.2 Experimental 97
4.2.1 Synthesis of $MnH_2P_2O_7$ 97
4.2.2 Synthesis of Li-doped $MnH_2P_2O_7$ 97
4.2.3 Collection of Diffraction Data 97
4.3 Results and Discussion 98
4.3.1 $MnH_2P_2O_7$ 98
4.3.1.1 Crystal Structure of $MnH_2P_2O_7$ 100
4.3.1.2 Thermal Behaviour of $MnH_2P_2O_7$ 103
4.3.1.3 Magnetic Analysis of $MnH_2P_2O_7$ 104
4.3.1.4 Polymorphism 105
4.3.2 Li-Doped $MnH_2P_2O_7$ 106
4.3.2.1 Thermal Behaviour of Li-Doped $MnH_2P_2O_7$ 107
4.3.2.2 Crystal Structure of Li-Doped $MnH_2P_2O_7$ 109
4.3.2.3 Magnetic Analysis of Li-Doped $MnH_2P_2O_7$ 113
4.4 Conclusion 114
References 115

Chapter 5: Low Temperature Synthesis of TiP_2O_7 and V-Doped TiP_2O_7

5.1 Introduction 117
5.2 Experimental 118
5.2.1 Low Temperature Synthesis of TiP_2O_7 118
5.2.2 Synthesis of V-Doped TiP_2O_7 118
5.2.3 Collection of Diffraction Data 118
5.3 Results and Discussion 119
5.3.1 TiP_2O_7 119
5.3.1.1 Thermal Stability of LTS-TiP_2O_7 123

5.3.2 V-Doped TiP_2O_7 134
5.3.2.1 Thermal Stability of V-Doped TiP_2O_7 139
5.3.2.2 Crystal Structure of V-Doped TiP_2O_7 148
5.3.3 Crystal Morphology 157
5.3.3.1 LTS-TiP_2O_7 Crystal Morphology 157
5.3.3.2 V-Doped TiP_2O_7 Crystal Morphology 159
5.3.3.3 Vanadium's Effect on Crystal Morphology 168
5.4 Conclusion 172
References 173

Chapter 6: Conclusions and Further Work

6.1 Research Summary 176
6.2 Further Work 178

Appendices

A1 The Bond Valence Sum Model and the Global Instability Index 181
A2 Lithium Flame Photometry Data 183
A3 Rietveld Refinement Details of Heat Treated TiP_2O_7 and V-Doped TiP_2O_7 184
A4 EDS Spectra of V-Doped TiP_2O_7 and Heat Treated V-Doped TiP_2O_7 186
A5 Refined VT-XRD Lattice Parameters of LTS-TiP_2O_7 and V-Doped TiP_2O_7 188
A6 Selected Area Electron Diffraction Patterns and d-spacing Calculations 196

Chapter 1

Introduction

This thesis describes the detailed study into metal pyrophosphate materials, focussing on the synthesis, structure and thermal behaviour. Phosphates are incredibly versatile materials, and can be used for a variety of roles, such as inorganic pigments,[1] catalysts,[2, 3] biomaterials,[4] proton conductors,[5] lasing materials[6] and host materials for nuclear waste.[7, 8] Biologically, phosphates are fundamental to life. They are found in DNA and RNA, as adenosine phosphates (AMP, ADP and ATP) which are used in energy storage in biological systems and also in fertilizers.

The objective of this first chapter is to introduce the general background of phosphate chemistry, with specific emphasis on the areas relevant to this research.

1.1 General Background of Phosphate Chemistry

The term 'phosphate' is used to define the oxyanions of phosphorus (V). Phosphates, in general, are salts of monophosphoric acid H_3PO_4 and its various other condensed and polymeric forms.[9] Phosphates are often compared to solid silicates, mainly due to the similarity in the tetrahedral arrangement of their anionic units (PO_4^- and SiO_4^-). It is largely recognised that the bonds in the tetrahedra are equivalent.

Phosphate materials can be broken down into three main categories: monophosphates, condensed phosphates, and oxyphosphates.[10] Monophosphates are salts derived from H_3PO_4 and are the simplest phosphates, with an isolated PO_4^{3-} tetrahedron as the anionic unit, and an O/P ratio of 4:1. They are the widest family of phosphates; all natural phosphates are monophosphates.[9, 10] Substituted phosphates can also be included in the phosphate family, where one or more of the oxygens in the PO_4 tetrahedron has been substituted, for example PO_3H (phosphonate), PO_3S (thiophosphate) and PO_3F (fluorophosphates).[9, 10]

Oxyphosphates, sometimes known as "basic phosphates", contain separate oxygen atoms within the structure that are not associated with the anionic unit, which in all reported cases has been PO_4^{3-}. In general, they can be defined as having an apparent O/P ratio greater than 4:1. Other anions can also be seen to be included in the structure, for example fluoroapatite, where F^- is incorporated into the structure as a second anion.

1.1.1 Condensed Phosphates

Condensed phosphates (also known as oligophosphates) are phosphates that have a P-O-P bond within the anionic unit and are built from corner sharing PO_4 tetrahedra.[9, 10] The P-O-P bonds are formed in various different processes, the simplest of which is via a condensation reaction, where water is eliminated, shown in figure 1.1. This P-O-P bond is susceptible to hydrolysis in acidic conditions and when heated, and so are considered less stable than monophosphates.

Figure 1.1 - Formation of the phosphorus – oxygen bond found in condensed phosphates

The O/P ratio in condensed phosphates is less than 4:1, as a direct consequence of the loss of oxygen during their formation.[9, 10]

There are 3 different geometries observed in the condensed phosphates: polyphosphates, cyclic phosphates and ultraphosphates.[9-11] Polyphosphates are formed when a condensation reaction occurs, forming linear chains of phosphate tetrahedra, which share one or two of their oxygen atoms. The anionic unit in this geometry corresponds to the general formula $[P_nO_{(3n+1)}]^{(n+2)-}$, where n is the number of phosphate tetrahedral.[9-11]

Diphosphates, also known as pyrophosphates, are the simplest polyphosphate, where n = 2. These along with the triphosphates and the infinite chain materials are the most studied of the polyphosphates[10] and were first discovered by Berzelius.[12] Discrete polyphosphates where n > 4 are rare.[10] Pyrophosphates can take the general formulae of $A^{IV}P_2O_7$, $A_2^{I}P_2O_7$, $A^{I}A^{III}P_2O_7$, $A_2^{I}A^{II}P_2O_7$ and $A_4^{I}P_2O_7$. Acidic anions are also known within these categories, such as $H_2P_2O_7^{2-}$ characterised by strong hydrogen bonding between the anions. This leads to ribbons, planes and infinite chains.

Cyclic phosphates (or cyclophosphates) have a ring anionic unit, and have the general formula $[P_nO_{3n}]^{n-}$, where $n \leq 3$. In this geometry each phosphate tetrahedron shares 2 oxygen atoms with its neighbour, giving an O/P ratio of 3:1.[10]

Ultraphosphates, in contrast to polyphosphates and cyclic phosphates, are branched: meaning the anionic unit contains phosphate tetrahedra that share 3 of their oxygen atoms, which can form various different geometries such as three dimensional networks, infinite ribbons and layers,[6] or finite groups.[10] Ultraphosphates undergo hydrolysis rapidly due to the triply linked tetrahedra and so are somewhat unstable. The general anionic formula for ultraphosphates is $[P_{(n+2)}O_{(3n+5)}]^{n-}$.[10]

1.2 Calcium Phosphates as Biomaterials

Calcium phosphates have been thoroughly researched for use in hard tissue replacement. This is due to their similarity in composition to the inorganic component of bone and teeth,[13] a poorly crystalline hydroxyapatite (HA),[14] $Ca_{10}(PO_4)_6(OH)_2$, shown in figure 1.2.

HA is a common component in synthetic bone grafts.[15] Calcium phosphate cements (CPCs) are a development in hard tissue replacement, overcoming some of the issues related to using ceramics, such as poor fit and slow osseointegration of the implant.[16] Brushite, $CaHPO_4.2H_2O$, a precursor to HA, is commonly used in CPCs due to its metastability under physiological conditions.[16] This means it can be resorbed by the body much faster than cements containing HA, which resorbs at a much slower rate.[15] Combinations of brushite and other phosphates have shown promising results. Grover *et al.*[17] investigated a brushite containing cement with added pyrophosphate anion, which was found to retard crystallisation of HA, which is thought to prevent the degradation of the cement in vivo.

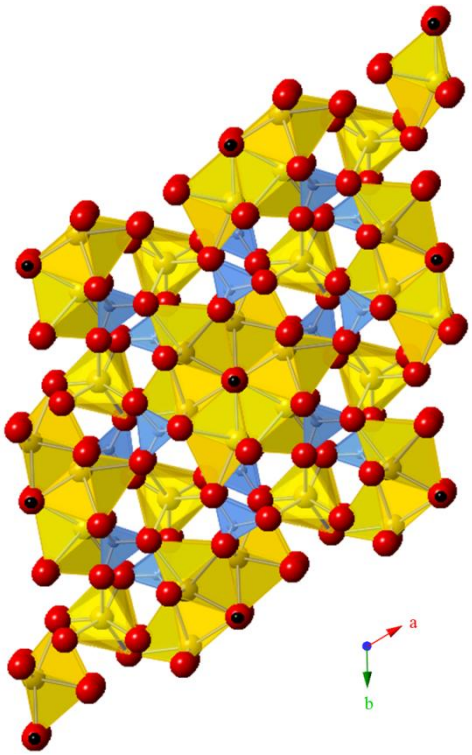

Figure 1.2 - Structure of hydroxyapatite[14] (HA) in the *ab* plane, where the CaO_6 octahedra are yellow, the PO_4 tetrahedra are blue and protons are black spheres

The addition of other anions has also been shown to be beneficial in CPC's. Addition of Zn^{2+} and Mg^{2+} has led to greater porosity of the cement, which has previously been reported to enhance cell adhesion and proliferation,[18] which we would expect to help the cements to support new bone growth.

Magnesium phosphates could also be used in biomaterial applications; Mg^{2+} has also been shown to inhibit HA crystallisation[17] and is used by the phosphatase[19] enzymes to hydrolyse phosphate bonds, which occurs during resorption of the implant.

1.3 Acidic Pyrophosphates

Acidic anions are commonly found in smaller polyphosphates, such as pyrophosphate and triphosphates, but are very rare in long chain polyphosphates and cyclophosphates.[11] A common synthetic route is via an acid melt.

1.3.1 Nickel/Cobalt Acid Pyrophosphates

$NiH_2P_2O_7$ and $CoH_2P_2O_7$ are two acidic pyrophosphates, with interesting magnetic behaviour.[20] Synthesis requires the addition of the metal acetate to concentrated monophosphoric acid. The solution is then heated for 4 days at 220°C, resulting in purple crystals (Co) and green crystals (Ni).[20]

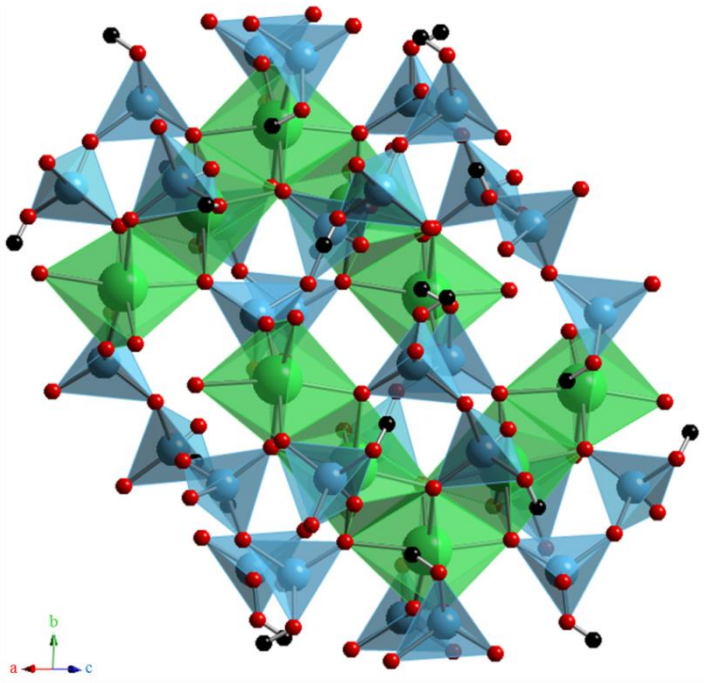

Figure 1.3 - Structure of $NiH_2P_2O_7$ [20], where NiO_6 octahedra are green, PO_4 tetrahedra are blue, and protons are black spheres

The compounds are isostructural; both crystallising into a monoclinic cell, with space group $P2_1/c$. The structure, shown in figure 1.3, is channelled, containing

zigzag edge-sharing MO_6, running along the *c* axis. The MO_6 octahedra chains stack along the *a* axis, and are interconnected by corner sharing phosphate tetrahedra, forming a 3-dimensional structure. Protons are located as hydroxyl groups on the phosphate tetrahedra, facing into the [001] channel. Thermal analysis of the two compounds has found that at approximately 400°C a further condensation reaction occurs, resulting in the cyclic tetraphosphates, $Ni_2P_4O_{12}$ and $Co_2P_4O_{12}$.[20, 21] Due to the metal-metal distances, the structure can be considered as one dimensional in terms of magnetic behaviour. Both materials show field-induced metamagnetic behaviour from an antiferromagnetic (anti-aligned spins) state to a ferromagnetic (aligned spins). The observed behaviour can be understood if we assume there is a strong ferromagnetic intra-chain interaction and a weak antiferromagnetic inter-chain interaction, which if exposed to a high magnetic field may switch the orientation of the magnetic moments to an overall ferromagnetic (FM) ordering.[20]

Addition of lithium nitrate to the reaction vessel results in $LiM_2H_3(P_2O_7)_2$ for both M = Ni & Co.[22] Interestingly, the addition of Li results in an increase in symmetry from $P2_1/c$ to $C2/c$. Topologically, $LiM_2H_3(P_2O_7)_2$ (structure shown in figure 1.4) is identical to $MH_2P_2O_7$ despite the differences in crystal symmetry, with M1, M2 and Li all occupying special sites. Lithium resides on a two-fold axis, tetrahedrally co-ordinated. MO_6 octahedra form edge-sharing zig-zag chains along the *a*-axis; these chains are interconnected via P_2O_7 units, forming a 3-dimensional network.[22] $LiM_2H_3(P_2O_7)_2$ can also be considered quasi-1D magnets; both show FM interactions in the MO_6 chains, however the magnetic ground state for each is different. $LiNi_2H_3(P_2O_7)_2$ is ferromagnetic, whereas $LiCo_2H_3(P_2O_7)_2$ is antiferromagnetic.[22]

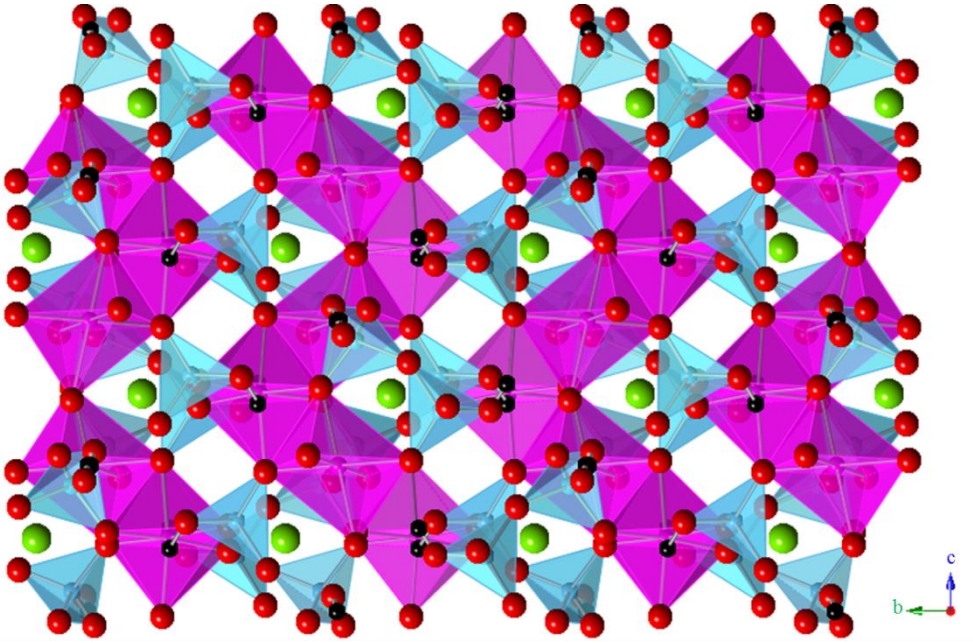

Figure 1.4 - Structure of $LiCo_2H_3(P_2O_7)_2$[22] as viewed in the *bc* plane, where CoO_6 octahedra are pink, PO_4 tetrahedra are blue, lithium atoms are green & protons black

1.3.2 Iron Acid Pyrophosphate

An analogous compound, $FeH_2P_2O_7$,[23] has been synthesised in a similar fashion; iron oxide is heated along with monophosphoric acid at 200°C for 48 hours, resulting in a white precipitate. $FeH_2P_2O_7$, shown in figure 1.5, is isostructural with the nickel and cobalt dihydrogen-pyrophosphate. Protons were not located during the structural refinement, but the authors have surmised that, like the Ni/Co structure, the protons are located as hydroxyl groups, due to the free apexes of the phosphate tetrahedra facing into the [001] tunnels.[23]

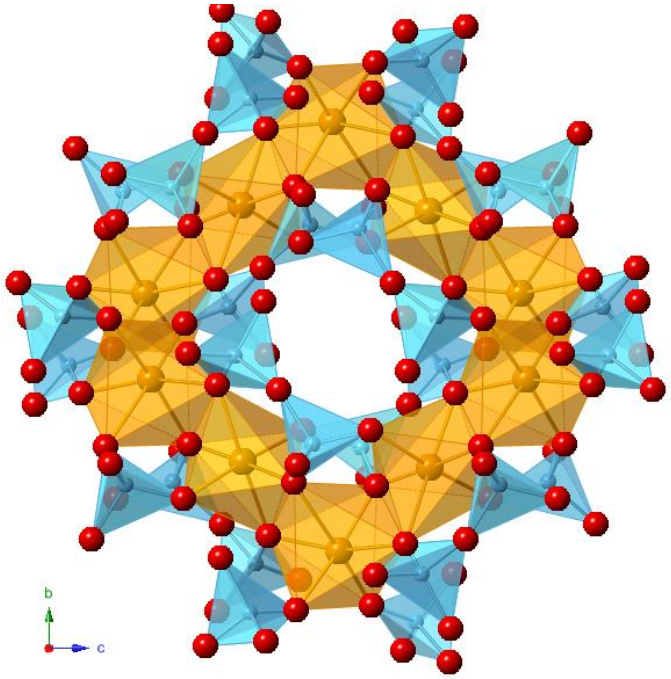

Figure 1.5 - Structure of $FeH_2P_2O_7$[23], where the FeO_6 octahedra are orange and PO_4 tetrahedra are blue

Thermal analysis of the iron compound confirms the presence of protons, with a water loss of 0.9 moles, giving an amorphous product. The loss of 0.9 moles of water suggests the initial phase possesses a partial oxidation of iron to 3+, giving $FeH_{2-\delta}P_2O_7$. This is confirmed as $FeH_{1.8}P_2O_7$ by Mössbauer spectroscopy. The magnetic properties of the Fe compound are also similar to that of the cobalt and nickel pyrophosphates; the compound is paramagnetic, ferromagnetic coupling is observed along the FeO_6 chains, whilst antiferromagnetic coupling is observed between the chains. Below the Néel temperature (11 K) short range ferromagnetic coupling is observed.[23]

Addition of lithium carbonate into the iron/phosphate reaction mixture resulted in the synthesis of $LiFe_2H_3(P_2O_7)_2$.[23] The structure, shown in figure 1.6, is orthorhombic, crystallising into the space group *Pbnb*. It is interesting to note that

despite the fact that $FeH_2P_2O_7$ is isostructural with $Ni/CoH_2P_2O_7$, the addition of Li does not result in an isostructural material, but instead a higher symmetry structure.

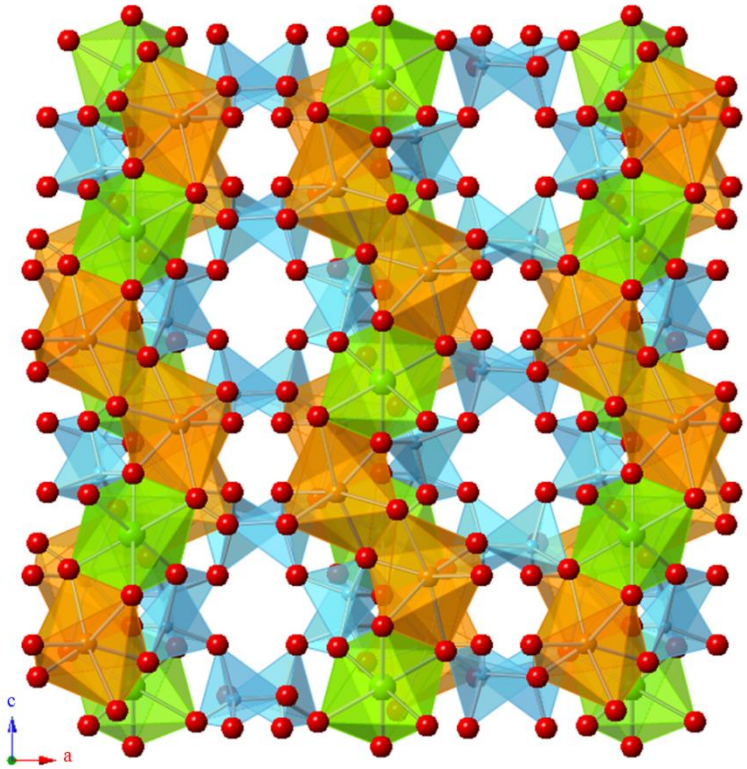

Figure 1.6 - Structure of $LiFe_2H_3(P_2O_7)_2$[23] in the *ac* plane, where FeO_6 octahedra are orange, LiO_6 octahedra are green and PO_4 tetrahedra are blue. Protons were not located.

The structure consists of zig-zag chains of edge-sharing MO_6 octahedra running along the *c* axis, stacking along the *b* axis, with one LiO_6 unit replacing every 3rd FeO_6 unit. These layers are interconnected by layers of P_2O_7 groups. Protons could not be located, but the author surmises the protons are located on Li-O5-P1 and Fe-O4-P2 due to low calculated valences.[23] The lithium in the chain disrupts the ferromagnetic ordering in the MO_6 chains seen in $FeH_2P_2O_7$, whilst the antiferromagnetic ordering remains, occurring below the Néel temperature (7.5 K). Due to the presence of protons/lithium ions, both $FeH_2P_2O_7$ and $LiFe_2H_3(P_2O_7)_2$ were

tested for ionic conductivity, but found no evidence of any ionic conduction in either sample.[23]

1.3.3 Magnesium and Manganese Acid Pyrophosphates

Melts are not the only synthetic route to acidic phosphates; another synthetic route is through the thermal dehydration of hydrogen phosphates. Hinsch *et al*.[24] investigated the dehydration of various $M^{2+}(H_2PO_4)_2.2H_2O$ phases including Mg^{2+} and Mn^{2+}. The hydrogen phosphates were initially synthesised using the metal carbonate/oxide, heated in excess dilute H_3PO_4 over 30 hours. The $M(H_2PO_4)_2.2H_2O$ were then heated in situ, using a variable temperature X-ray diffractometer. The first dehydration step involved the loss of the 2 moles of water to form the anhydrous $M(H_2PO_4)_2$; for both Mg and Mn this step occurs at 90°C. The second step is the formation of acidic pyrophosphate $MH_2P_2O_7$ via a condensation reaction. For Mn this happens at 210°C, which is a much lower temperature than the Mg acid pyrophosphate, which forms at 250°C. The next step involves the formation of the cyclic phosphate after another condensation to form $M_2P_4O_{12}$, where M = Mg[25] or Mn,[26] once again $Mg_2P_4O_{12}$ forms at a higher temperature than the Mn cyclic tetraphosphate (400°C compared to 320°C). Further heating of the Mg phosphate leads to a glassy substance at approximately 1100°C, unlike the Mn tetraphosphate which undergoes an additional transformation to forms another phase, identified as $Mn_3(P_3O_9)_2$, the cyclic triphosphate.[24] This phase forms at 720°C, and exists until 1000°C when it turns glassy like the Mg tetraphosphate.[24] The crystal structures of both the magnesium and manganese (II) acid pyrophosphates were not reported by the authors.

1.4 Condensed Phosphates as Lithium Conductors

Lithium phosphates are receiving increased interest for applications in battery materials, due to high thermal stability with the presence of the strong P-O bond,[27] which improves the safety of the device. $LiFePO_4$[28] is a commercially used cathode material, which adopts the olivine structure.[28] Whilst $LiFePO_4$ shows a high capacity, comparable to that of Li_xCoO_2, and is cheap and non-toxic, synthesis and optimisation can be problematic and complicated.[29] This has prompted further research into new materials.

Transition metal phosphates have great potential as cathode materials due to their variable oxidation states.[30, 31] The lithium arrangement in $Li_2MnP_2O_7$[31] shows potential for lithium conductivity; $Li_2MnP_2O_7$ adopts a tunnelled structure, with lithium residing in the tunnels, which could mean they are mobile and removable. However measurements performed on a sample showed no ionic conductivity. When the structure is doped with iron,[32] a better performance is observed for the extraction and insertion of lithium, with the best performance observed for $Li_2FeP_2O_7$.[32] Only one lithium ion was found to be removed; cyclic voltammetry shows the potential for a second oxidation and the removal of the second ion, so if a stable electrolyte was found the electronic conductivity could be enhanced.[32]

Another potential battery material is titanium pyrophosphate. Although it shows poor performance in the intercalation of lithium, it has potential as a negative electrode in aqueous lithium ion batteries. Palacín *et al.*[33] synthesised two polymorphs of TiP_2O_7; a low temperature polymorph, LT-TiP_2O_7, which adopts a cubic structure ($Pa\bar{3}$) with a = 7.9118(1) Å and a high temperature polymorph, HT-

TiP_2O_7, which adopts a cubic $3a \times 3a \times 3a$ superstructure ($Pa\bar{3}$). The flexible framework of these TiP_2O_7 polymorphs allow for the reversible intercalation of lithium ions in a solid solution. The structural study shows LT-TiP_2O_7 has a lower density compared to HT-TiP_2O_7, and so is able to host larger cations than HT-TiP_2O_7 like Na^+. It is the presence of the flexible P_2O_7 unit that allows the intercalation of cations; the pyrophosphate network in HT-TiP_2O_7 is more rigid compared to LT-TiP_2O_7 and slightly more dense, preventing the intercalation of cations larger than Li^+. TiP_2O_7 belongs to a series of compounds with the formula of $A^{IV}X_2O_7$. This series has attracted much attention over the years due to the interesting structures the series adopt, their thermal behaviour and potential applications.

1.5 Titanium Pyrophosphate and the AX_2O_7 Series

The structure of titanium pyrophosphate was first reported by Levi and Peyronel,[34] along with a series of other isostructural pyrophosphates, as cubic, with a small lattice parameter of 7.80(1) Å[34]. The structure can be related to the rock salt structure, with face-centred arrangement of TiO_6 octahedra with corner-sharing pyrophosphate groups,[8, 35-38] shown in figure 1.7. Subsequent studies have shown that for TiP_2O_7 and many other members of the series, the structure is more complex than first thought. TiP_2O_7 has been reported to adopt a cubic $3a \times 3a \times 3a$ super-structure at room temperature,[39] reverting to the subcell at higher temperatures,[39] supported by solid state NMR[40, 41] and selected area electron diffraction.[42] The pyrophosphate group in subcell structure (where a = 7.80 Å) contains a P-O-P bond angle of 180°, which is very strained. By adopting the cubic superstructure the strain on some of the pyrophosphate units is relieved. TiP_2O_7 has many potential

applications, including ionic conduction (proton[42, 43]/lithium[33]/sodium[33]) and catalysis.[3, 44]

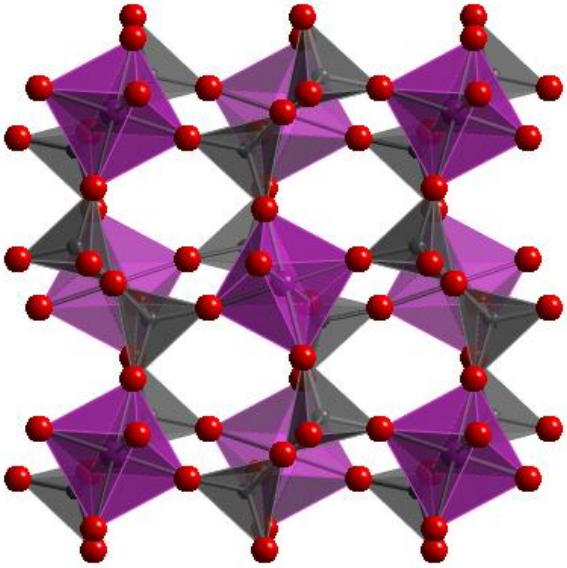

Figure 1.7 - Sub-cell structure of AX_2O_7[37] where the AO_6 octahedra are purple and the XO_4 tetrahedra are grey

1.5.1 Tin Pyrophosphate

SnP_2O_7 is another member of the series which has attracted interest as a proton conducting material.[5, 45, 46] Initially thought to adopt the cubic subcell structure,[47] it was later shown to also adopt a cubic $3a \times 3a \times 3a$ super-structure at room temperature.[48] Above 287°C the structure distorts to a triclinic subcell structure, with a rhombohedral distortion occurring above 557°C.[48] Irvine *et al*.[46] investigated the material as a potential intermediate temperature proton conductor by synthesising SnP_2O_7-H_3PO_4 composites. When tested for proton conductivity, the composites showed good proton conductivity, and were found to be stable (at 300°C in both wet and dry H_2 atmosphere), however, it was surmised that the conductivity

mainly arises from the residual acid, not the SnP_2O_7, which was found to be a relatively poor conductor.[46]

1.5.2 Zirconium Pyrophosphate and Negative Thermal Expansion Materials

The series is well known for its ability to host a wide range of cations; A^{IV} = Ce,[36] Ti,[39] Zr,[35] Si,[49] U,[8] Hf,[50] Ge,[51] Sn,[48] and X^{V} = P,[52] V[52] or As.[53] Perhaps the most widely studied member of this series is ZrP_2O_7, due to its interesting thermal expansion properties.[35] Below 293°C, the structure shows positive thermal expansion (PTE); above this temperature the structure expansion slows. When regarding the ZrV_2O_7 system, the structure shows isotropic negative thermal expansion (NTE) just over 100°C. NTE is also observed in ThP_2O_7,[37] UP_2O_7[8] and HfV_2O_7,[52] above room temperature.[52]

The $ZrV_{2-x}P_xO_7$ solid solution has been studied extensively; all compositions adopt the AX_2O_7 structure type, with superstructure peaks observable in the diffraction patterns of the end members of the solid solution, as well as compositions close to the end members, confirmed by ^{51}V and ^{31}P solid state NMR. At high temperature all adopt the ideal structure. The superstructure of ZrP_2O_7 was initially thought to be cubic but has since shown to be orthorhombic.[50, 54] Below a transition temperature, positive thermal expansion is observed when the 3 × 3 × 3 superstructures are adopted, approximately 100°C for members of the series with a high vanadium content. This phase transition is completely suppressed for the middle members of the series (between x = 1.2 and 1.8), leading to NTE and very low PTE. Modelling suggests the NTE arises from bending of P_2O_7/PVO_7 units away from the ideal angle of 180°, leading to a smaller cell volume.[35]

In the AX_2O_7 series, as the unit cell size increase, the tendency to undergo NTE becomes apparent.[55] In order to undergo NTE, the polyhedra must be able to distort and change shape in order to allow for the rocking motion of the octahedra and tetrahedra. When the polyhedra are larger, changing shape is much easier due to the increased distance between anions.[55] ThP_2O_7,[37, 55] UP_2O_7[8, 55] and CeP_2O_7[36] all display NTE, all with larger M^{4+} cations than ZrP_2O_7,[56] therefore, larger MO_6 octahedra. Interestingly, none of these pyrophosphates adopt a superstructure, and a triclinic distortion is observable in both UP_2O_7 and CeP_2O_7. ThP_2O_7 shows no sign of any ordering[37] and Rietveld analysis[57] of PXRD data show the ideal cubic structure, however, the high thermal parameter on the bridging oxygen in the pyrophosphate unit may indicate that this may not be the case. Neutron powder diffraction or synchrotron powder diffraction may show ordering or a structural distortion as seen in CeP_2O_7 and UP_2O_7.

At room temperature, both CeP_2O_7 and UP_2O_7 are pseudocubic.[8, 36] Initial PXRD of CeP_2O_7 showed slight shoulders on the peaks which suggested a lower symmetry than cubic. Synchrotron data confirmed a lower symmetry, leading to the discovery of the triclinic cell, space group $P1$. A similar process was used to investigate the structure of UP_2O_7, with low temperature synchrotron diffraction showing the peak splitting caused by the triclinic distortion, which was confirmed by ^{31}P NMR. The distortion is very slight for both pyrophosphates; hence they are pseudocubic. Both undergo NTE, CeP_2O_7 initially shows PTE from room temperature to approximately 115°C where a phase transition occurs to the ideal cubic sub-cell model, space group $Pa\bar{3}$.[36] NTE occurs above 445°C until decomposition occurs at 805°C.[36] The expansion profile for UP_2O_7 is very similar. The phase transition from

triclinic to cubic occurs at 155°C and the thermal expansion inverts from PTE to NTE at 330°C.[8]

1.6 Project Aims

The primary aim of this project was to investigate the synthesis, structure and properties of a number of metal pyrophosphates.

The initial aim was to focus on the synthesis and structural characterisation of $M^{II}H_2P_2O_7$, where M^{II}= Mg or Mn, the synthesis of which had been previously reported by Hinsch *et al*.[24], but no structural details were reported. Following on from this, the thermal behaviour was also of interest, as was the effect of substituting H^+ for Li^+ on the structure, thermal stability and magnetic properties (for M^{II} = Mn).

Following the previous success at synthesis of condensed phosphates via the acid flux method[58, 59] and the increased interest in the MP_2O_7 series, the low temperature synthesis of TiP_2O_7 was investigated, with particular focus on the structural characterisation and thermal stability. Another aim was to investigate the effect of the addition of vanadium (a similar sized cation to Ti) in the starting reaction mixture, following the increased attention on ZrP_2O_7 and the vanadium-doped solid solution, $ZrV_xP_{2-x}O_7$,[35, 52, 55] once again with particular focus on the structural characterisation and thermal stability and behaviour.

References

1. M. M. Rao, *Materials Research Bulletin*, 1991, **26**, 813-819.
2. M. A. Aramedia, V. Borau, C. Jimenez, J. M. Marinas, F. J. Romero and J. R. Ruiz, *Journal of Colloid and Interface Science*, 1998, **202**, 456-461.
3. I. C. Marcu, I. Sandulescu and J. M. M. Millet, *Applied Catalysis A-General*, 2002, **227**, 309-320.
4. T. Kasuga, *Acta Biomaterialia*, 2005, **1**, 55-64.
5. Y. Jin, Y. Shen and T. Hibino, *Journal of Materials Chemistry*, 2010, **20**, 6214-6217.
6. A. Mbarek, M. Graia, G. Chadeyron, D. Zambon, J. Bouazia and A. M. Fourati, *Journal of Solid State Chemistry*, 2009, **182**, 509-516.
7. C. E. Bamberger, R. G. Haire, G. M. Begum and H. E. Hellwege, *Journal of the Less Common Metals*, 1984, **102**, 179-186.
8. G. Wallez, P. E. Raison, N. Dacheux, N. Clavier, D. Bykov, L. Delevoye, K. Popa, D. Bregiroux, A. N. Fitch and R. J. M. Konings, *Inorganic Chemistry*, 2012, **51**, 4314-4322.
9. M. T. Averbuch-Pouchot and D. A, *Topics in Phosphate Chemistry*, World Scientific, 1996.
10. A.Durif, *Crystal Chemistry of Condensed Phosphates*, Plenum Press, 1995.
11. I. S. Kulaev, V. M. Vagabov and T. V. Kulakovskaya, *The Biochemistry of Inorganic Polyphosphates*, John Wiley & Sons, Ltd., 2006.
12. J. Berzelius, *Annalen der Physik*, 1816, **54**, 31-52.
13. M. R. Cave, D. Farrar and A. J. Wright, *Journal of Physics and Chemistry of Solids*, 2007, **68**, 431-437.
14. A. Bigi and G. Cojazzie, *Journal of Inorganic Biochemistry*, 1997, **68**, 45-51.
15. I. R. Gibson and W. Bonfield, *Journal of Biomedical Materials Research*, 2002, **59**, 697-708.
16. F. Theiss, D. Apelt, B. Brand and A. Kutter, *Biomaterials*, 2005, **26**, 4383-4394.
17. L. M. Grover, U. Gbureck, A. J. Wright, M. Tremayne and J. E. Barralet, *Biomaterials*, 2006, **27**, 2178-2185.

18. R. Murugan, A. Ramakrishna and P. R. K., *Materials Letters*, 2006, **60**, 2844-2847.
19. M. E. Maguire and J. A. Cowan, *Biometals*, 2002, **15**, 203-210.
20. T. Yang, J. Ju, G. Li, S. Yang, J. Sun, F. Liao, J. Lin, J. Saski and N. Toyota, *Inorganic Chemistry*, 2007, **46**, 2343-2344.
21. A. Olbertz, D. Satchel, I. Svoboda and H. Fuess, *Zeitschrift für Kristallographie - New Crystal Structures*, 1998, **213**, 241-242.
22. T. Yang, S. Yang, F. Liao and J. Lin, *Journal of Solid State Chemistry*, 2008, **181**, 1347-1353.
23. V. Pralong, R. Baies, V. Caignaert and B. Raveau, *Inorganic Chemistry*, 2009, **48**, 6835-6844.
24. T. R. Hinsch, W. Guse and H. Saalfeld, *Journal of Crystal Growth*, 1986, **79**, 205-209.
25. A. G. Nord and K. B. Lindberg, *Acta Chemica Scandinavica A*, 1975, **29**, 1-6.
26. R. Glaum, H. Thauern, A. Schmidt and M. Gerk, *Zeitschrift fur Anorganische und Allgemeine Chemie*, 2002, **628**, 2800-2808.
27. M. Kopec, C. V. Ramana, X. Zhang, A. Mauger, F. Gendron, J. F. Morhange, K. Zghib and C. M. Julien, *Electrochemica Acta*, 2009, **54**, 5500-5508.
28. A. K. Padhi, K. S. Nanjundaswamy and J. B. Goodenough, *Journal of The Electrochemical Society*, 1997, **144**, 1188-1194.
29. B. L. Ellis, K. T. Lee and L. F. Nazar, *Chemistry of Materials*, 2010, **22**, 691.
30. V. Aravindan, J. Gnanaraj, Y. S. Lee and S. Madhavi, *Journal of Materials Chemistry A*, 2013, **1**, 3518-3539.
31. L. Adam, A. Guesdon and B. Raveau, *Journal of Solid State Chemistry*, 2008, **181**, 3110-3115.
32. H. Zhou, S. Upreti, N. A. Chernova, G. Hautier, G. Ceder and M. S. Whittingham, *Chemistry of Materials*, 2011, **23**, 293-300.
33. P. Senguttuvan, G. Rousse, J. Oro-Sole, J. M. Tarascon and M. R. Palacin, *Journal of Materials Chemistry A*, 2013, **1**, 15284-15291.
34. G. R. Levi and G. Peyronel, *Zeitschrift fuer Kristallographie, Kristallgeometrie, Kristallphysik, Kristallchemie*, 1935, **92**, 190-209.

35. V. Korthius, N. Khosrovani, A. W. Sleight, N. Roberts, R. Dupree and J. W. W. Warren, *Chemistry of Materials*, 1995, **7**, 412-417.
36. K. M. White, P. L. Lee, P. J. Chupas, K. W. Chapman, E. A. Payzant, A. C. Jupe, W. A. Bassett, C.-S. Zha and A. P. Wilkinson, *Chemistry of Materials*, 2008, **20**, 3728-3734.
37. N. Clavier, G. Wallez, N. Dacheux, D. Bregiroux, M. Quarton and P. Beaunier, *Journal of Solid State Chemistry*, 2008, **181**, 3352-3356.
38. S. Carlson and A. M. K. Anderson, *Journal of Applied Crystallography*, 2001, **34**, 7-12.
39. S. T. Norberg, G. Svensson and J. Albertsson, *Acta Crystallographica Section C*, 2001, **C57**, 225-227.
40. J. Sanz, J. E. Iglesias, J. Soria, E. R. Losilla, M. A. G. Aranda and S. Bruque, *Chemistry of Materials*, 1997, **9**, 996-1003.
41. X. Helluy, C. Marichal and A. Sebald, *The Journal of Physical Chemistry B*, 2000, **104**, 2836-2845.
42. V. Nalini, M. H. Sorby, K. Amezawa, R. Haugsrud, H. Fjellvag and T. Norby, *Journal of American Ceramic Society*, 2011, **94**, 1514-1522.
43. M. Nagao, T. Kamiya, P. Heo, A. Tomita, T. Hibino and M. Sano, *Journal of The Electrochemical Society*, 2006, **153**, A1604-A1609.
44. S. Loridant, I. C. Marcu, G. Bergeret and J. M. M. Millet, *Physical Chemistry Chemical Physics*, 2003, **5**, 4384-4389.
45. H. Wang, J. Xiao, F. Zhang and G. Ma, *Solid State Ionics*, 2010, **46**, 1521-1524.
46. X. Xu, S. Tao, P. Wormald and J. T. S. Irvine, *Journal of Materials Chemistry*, 2010, **20**, 7827-7833.
47. C. H. Huang, O. Knop, D. A. Othen, F. W. D. Woodhams and R. A. Howie, *Canadian Journal of Chemistry*, 1975, **53**, 79-91.
48. R. K. B. Gover, N. D. Withers, S. Allen, R. L. Withers and J. S. O. Evans, *Journal of Solid State Chemistry*, 2002, **166**, 42-48.
49. E. Tillmanns, W. Gebert and W. H. Baur, *Journal of Solid State Chemistry*, 1973, **7**, 69-84.
50. G. W. Stinton, M. R. Hampson and J. S. O. Evans, *Inorganic Chemistry*, 2006, **45**, 4352-4358.

51. E. R. Losilla, A. Cabeza, S. Bruque, M. A. G. Aranda, J. Sanz, J. L. Iglesias and J. A. Alonso, *Journal of Solid State Chemistry*, 2001, **156**, 213-219.
52. A. W. Sleight, *Annual Review of Materials Science*, 1998, **28**, 29-43.
53. W. T. A. Harrison, T. E. Gier and G. D. Stucky, *European Journal of Solid State Inorganic Chemistry*, 1993, **30**, 761-771.
54. H. Birkedal, A. M. K. Andersen, A. Arakcheeva, G. Chapuis, P. Norby and P. Pattison, *Inorganic Chemistry*, 2006, **45**, 4346-4351.
55. A. W. Sleight, *Inorganic Chemistry*, 1998, **37**, 2854-2860.
56. R. D. Shannon and C. T. Prewitt, *Acta Crystallographica Section B*, 1969, **25**, 925-946.
57. H. M. Rietveld, *Journal of Applied Crystallography*, 1969, **2**, 65-71.
58. Y. Begum and A. J. Wright, *Journal of Materials Chemistry*, 2012, **22**, 21110-21116.
59. F. C. Coomer, N. J. Checker and A. J. Wright, *Inorganic Chemistry*, 2010, **49**, 934-942.

Chapter 2

Experimental Techniques

2.1 Introduction

This chapter introduces the main experimental techniques employed to synthesise and characterise the materials produced in this research. All samples were prepared using the acid melt technique. The resulting materials were then characterised using a variety of techniques described in this chapter including powder X-ray and neutron diffraction, Rietveld analysis, SEM, TEM, XRF, ESR, thermogravimetric analysis-mass spectrometry and solid state NMR.

2.2 Synthesis

All pyrophosphates synthesised in this research were produced using a phosphoric acid melt. An acid melt involves the addition of a metal source to orthophosphoric acid in a specific metal to phosphorus ratio in a reaction vessel. The reaction vessel is then placed in an oven or on a hot plate at a set temperature for a set length of time. The resulting paste is then washed with deionised water, and suction filtered. Specific synthetic conditions will be discussed in the relevant sections of Chapters 3-5.

2.3 Modification of Condensed Phosphates

2.3.1 Ion exchange of $MgH_2P_2O_7$

Ion exchange in the $MgH_2P_2O_7$ series was attempted as a route to the formation of $MgLi_2P_2O_7$ by replacing protons with Li. The host $MgH_2P_2O_7$ was stirred for 6 hours in solution of LiCl (using either water or ethanol as a solvent) with a H:Li molar ratio of 1:3. The resulting solid was then washed with either water or ethanol and recovered via vacuum filtration. More details on this will be provided in the relevant section of Chapter 3.

2.4 Characterisation Techniques

2.4.1 Diffraction

The term diffraction is used to describe the phenomenon which occurs when waves encounter a set of obstacles with a regular arrangement, leading to the mutual scattering of waves. Once scattered, the waves will travel in different directions; if the waves remain in phase they are said to constructively interfere, leading to diffraction. If the waves scatter out of phase they destructively interfere with one another, effectively cancelling each other out.

2.4.1.1 Crystallography

Crystalline materials are solids that possess long range order, having a regular and periodic arrangement of atoms/ions or molecules in space. Their periodic structure can most easily be described by a lattice. The unit cell is the smallest

repeating unit from which the entire crystal lattice can be reconstructed via translation only. The unit cell in 3 dimensions is a parallelepiped with 3 lengths (*a*, *b* and *c*) and 3 angles (α, β and γ), which are known as the lattice parameters. An example unit cell is shown in figure 2.1.

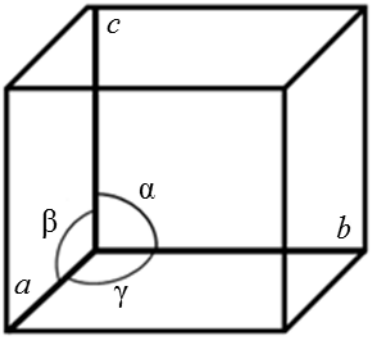

Figure 2.1 - Representation of a 3-d unit cell

Crystals can be classified into 7 crystal systems, which can then be subdivided into the 14 Bravais lattices when combining the crystal systems with the 4 lattice types (P, I, F and C) (table 2.1).

Table 2.1 - The seven crystal systems and the fourteen Bravais lattices

Crystal System	Unit Cell Dimensions		Bravais Lattices
Cubic	$a = b = c$	$\alpha = \beta = \gamma = 90°$	P, I, F
Tetragonal	$a = b \neq c$	$\alpha = \beta = \gamma = 90°$	P, I
Orthorhombic	$a \neq b \neq c$	$\alpha = \beta = \gamma = 90°$	P, I, F, C/B
Monoclinic	$a \neq b \neq c$	$\alpha = \gamma = 90° \beta \neq 90°$	P, C
Triclinic	$a \neq b \neq c$	$\alpha \neq \beta \neq \gamma \neq 90°$	P
Hexagonal	$a = b \neq c$	$\alpha = \beta = 90° \gamma = 120°$	P
Trigonal/Rhombohedral	$a = b = c$	$\alpha = \beta = 90° \gamma \neq 90°$	P(R)*

* Primitive in the rhombohedral system is often labelled as R

The Bravais lattices describe the symmetry of the lattice and the location of equivalent positions in the structure via lattice points within the cell, but cannot provide details on where the atoms reside in the unit cell. Atomic positions are given

as fractional coordinates, which are expressed as coordinates of *x, y* and *z*. These coordinates are plotted with respect to unit cell axes.

Combining these 14 lattice types with the 32 crystallographic point groups gives rise to the 230 three-dimensional crystallographic space groups, from which you can describe the full symmetry of a structure.

In order to understand diffraction from a crystal, the concept of crystallographic lattice planes has been established. Miller indices are used to describe crystallographic lattice planes within the crystal. These parallel planes are equally spaced and intersect at lattice points within the crystal. Each plane is defined by 3 Miller indices, *h*, *k* and *l*, which intercept *a*, *b* and *c,* respectively. If the plane runs parallel to a particular crystallographic axis, the equivalent Miller index is designated 0 as the axis will only be intersected at infinity. Example representations of some Miller indices are shown in figure 2.2.

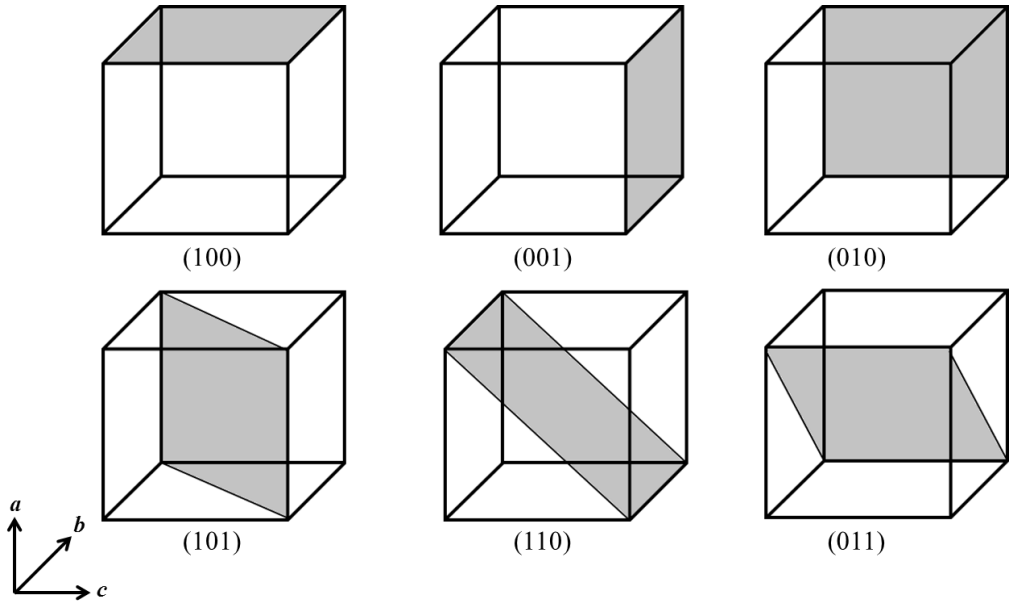

Figure 2.2 - Representations of some Miller indices

The perpendicular distances between these planes is known as the d-spacing, usually denoted as d_{hkl}. The relationship between d-spacing and the lattice parameter(s) for both cubic and monoclinic systems, such as those investigated in this work, are shown in equations 2.1 (cubic) and 2.2 (monoclinic).

$$\frac{1}{d^2} = \frac{h^2 + k^2 + l^2}{a^2} \tag{2.1}$$

$$\frac{1}{d^2} = \frac{1}{\sin^2\beta}\left(\frac{h^2}{a^2} + \frac{k^2\sin^2\beta}{b^2} + \frac{l^2}{c^2} - \frac{2hl\cos\beta}{ac}\right) \tag{2.2}$$

2.4.1.2 Bragg's Law

After the discovery that crystals could diffract X-rays,[1, 2] Bragg derived the equation[3] that describes the relationship of reflected X-rays or neutrons from lattice planes which is used universally to describe the basis of diffraction.

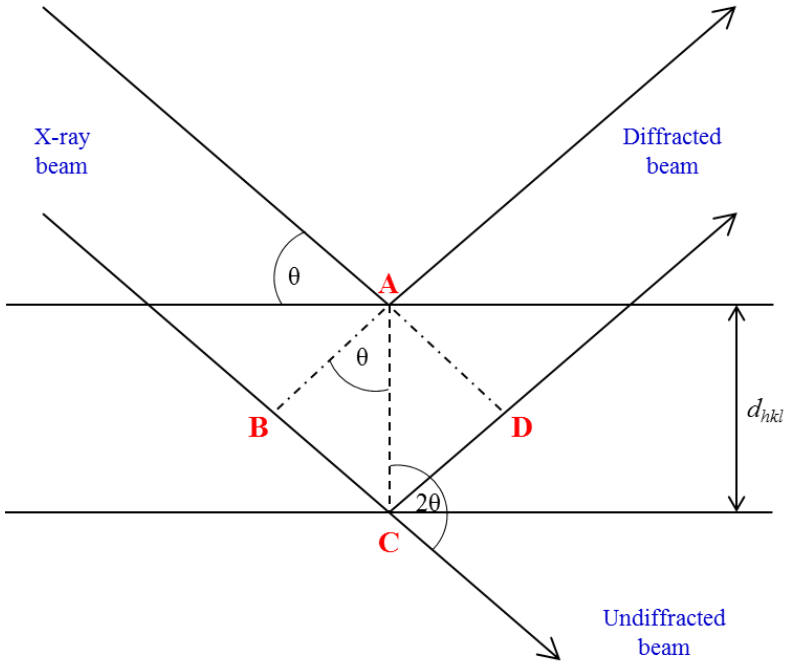

Figure 2.3 - Geometric representation of Bragg's law

Bragg's law treats X-rays/neutrons like light that is reflected by lattice planes. In contrast to light, X-rays can partially penetrate the surface of a crystalline solid. Figure 2.3 shows a geometric representation of Bragg's law, where two X-rays are reflected by lattice planes. The second reflected X-ray must travel a longer distance, pre (BC) and post reflection (CD), to the detector leading to a relative phase shift. Bragg's law gives this path difference in terms of the plane separation (d_{hkl}) and the incident angle of the radiation (θ):

$$BC + CD = 2d_{hkl}\sin\theta \tag{2.3}$$

If the extra distance is a multiple of the X-ray wavelength, constructive interference will occur as the two waves will remain in phase. This can allow for the modification of equation 2.3 to give the Bragg equation:

$$n\lambda = 2d_{hkl}\sin\theta \tag{2.4}$$

When *n* is a non-integer value, destructive interference occurs as the reflected beams will always be out of phase with respect to one another, leading to intensity maxima when Bragg's law is satisfied and no intensity when it is not.

2.4.2 X-Ray Diffraction

X-ray diffraction (XRD) is a powerful technique for the characterisation of crystalline materials. It allows for the identification of phases within the sample, and the assessment of the sample purity using a database of diffraction patterns, such as the JCPDS.[4] In this work, XRD was used both for initial characterisation and structural determination prior to proceeding to neutron diffraction for detailed structural analyses.

2.4.2.1 Generation of X-rays[5]

X-ray tubes are used an X-ray source for laboratory X-ray diffractometers. The most commonly used is a sealed tube, where electrons are emitted by a tungsten filament (cathode). The electrons are accelerated towards an anode, and X-rays are emitted at impact. The anode is made of high quality copper, but may be coated with another metal such as cobalt, molybdenum or chromium to produce a target other than copper. The X-ray spectrum produced from a conventional source is shown in figure 2.4. The spectrum consists of 3 characteristic wavelengths, known as $K\alpha_1$, $K\alpha_2$ and Kβ. These arise from the ejection of electrons from core atomic shells in the metal target. Transitions occur from L (2p) and M (3p) shells to the vacant K (1s) shell, giving Kα and Kβ. Kα is split due to spin multiplicity giving $K\alpha_1$ and $K\alpha_2$.

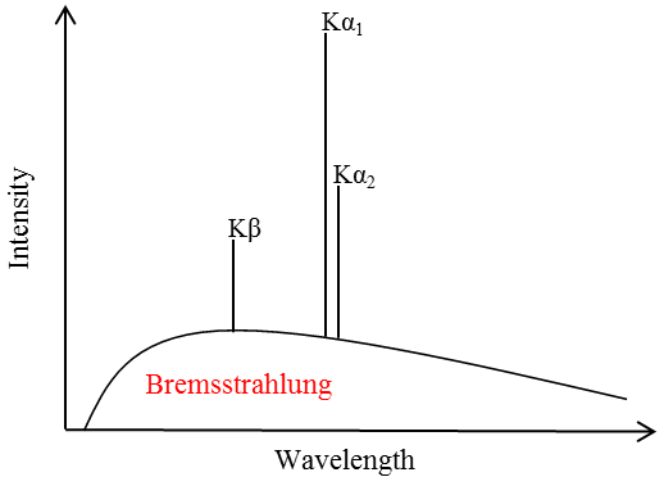

Figure 2.4 - X-ray emission spectrum

White radiation, or Bremsstrahlung, occurs when electrons are rapidly slowed down after collision with the target.

2.4.2.2 Powder Diffraction[5, 6]

Single crystal X-ray diffraction results in a diffraction pattern which consists of spots of intensity which can be assigned to specific (*hkl*) values. Polycrystalline samples contain crystallites, the orientations of which are completely random. This leads to a smearing of the diffraction spots forming rings of intensity. Each ring corresponds to a peak in the diffraction pattern.

Every crystalline material has a characteristic diffraction pattern, allowing for the phase identification in a sample. Figure 2.5 shows the components of a powder XRD pattern. The peak position is determined by the phase symmetry and unit cell parameters. The positions correspond to lattice plane separation distances as described by the Bragg Equation. Peak position can also be affected by the zero error of the diffractometer. Both instrument and sample effects contribute to the background of a XRD pattern. This can include the sample holder, detector noise, amorphous material and fluorescence of the sample.

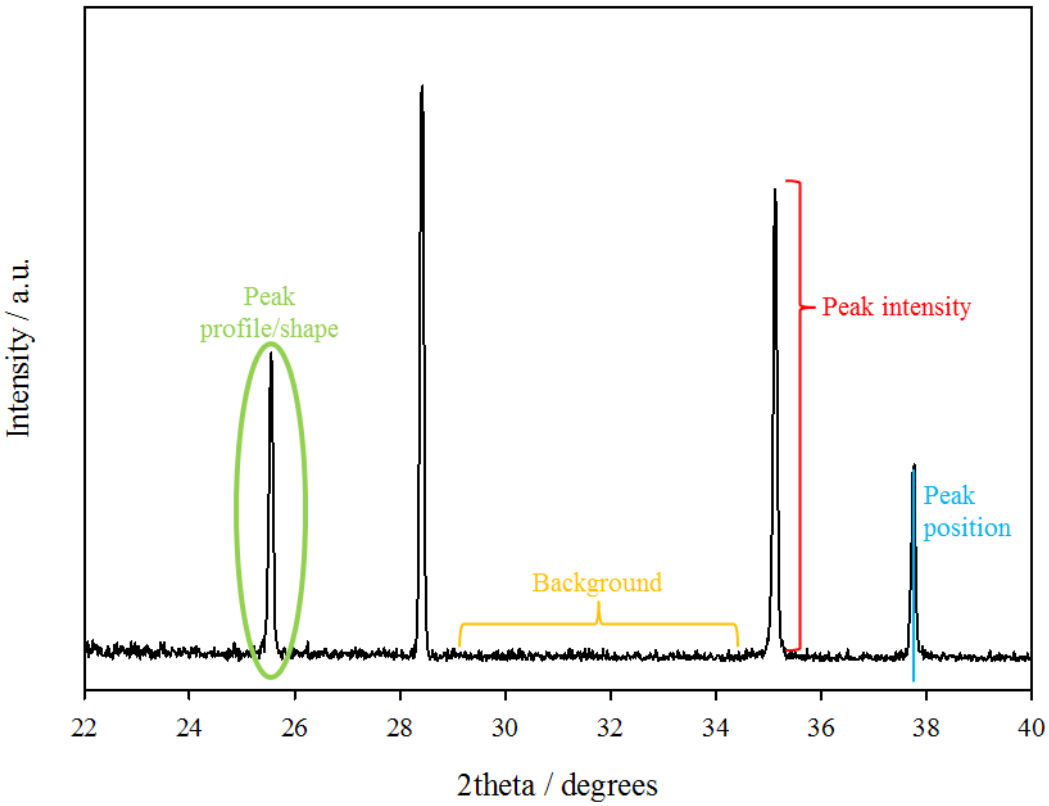

Figure 2.5 - Components of a typical powder XRD pattern

A number of factors contribute to peak shape; instrument effects include the source geometry, location and slits. Crystallite size, crystallinity and microstrains all can have a considerable effect on peak shape. Peak intensities are primarily determined by the atoms in the unit cell, the type, their position within the unit cell and their thermal motion. Other factors also contribute to peak intensity; these include the beam intensity, properties of the detector and crystallite orientation.

The measure of an atom's X-ray scattering power is known as the atomic scattering factor, *f*. X-rays interact with the electron density of the atom, and so atoms with a higher atomic number (therefore a higher number of electrons) will scatter more strongly than atoms with a low atomic number. For example iron will scatter X-rays more strongly than hydrogen. A consequence of this is that light atoms

are much more difficult to locate, as are atoms with similar atomic numbers, such as titanium/vanadium or oxygen/fluorine.

The total intensity of radiation scattered by all atoms in the unit cell can be defined by the structure factor, F_{hkl}, for each *hkl* plane. The structure factor can be calculated using the form factors and atomic coordinates for each atom, shown in equation 2.5.

$$F_{hkl} = \sum_{n=1}^{N} f_n \, exp[2\pi i(hx_n + ky_n + lz_n)] \tag{2.5}$$

The intensity of a particular *hkl* reflection is proportional to the square of the structure factor, and can be calculated using the equation 2.6:

$$I_{hkl} = K \times p_{hkl} \times L_\theta \times P_\theta \times A_\theta \times T_{hkl} \times E_{hkl} \times |F_{hkl}|^2 \tag{2.6}$$

Where:

- K is the scale factor
- p_{hkl} is the multiplicity factor – accounts for equivalent *hkl* planes
- L_θ is the Lorentz multiplier – defined by the geometry of diffraction
- P_θ is the polarisation factor – accounts for partial polarisation of the diffracted beam
- A_θ is the absorption multiplier – accounts for absorption of both the incident and diffracted beam
- T_{hkl} is the preferred orientation factor
- E_{hkl} is the extinction multiplier – usually very small in powder diffraction and so is usually neglected
- F_{hkl} is the structure factor

2.4.2.3 Monochromation[5]

In order to produce radiation of a single wavelength monochromation is required. In laboratory diffractometers, two types of monochromator are frequently used. Crystal monochromators are usually single crystals (typically germanium or silicon) set in a particular orientation so that the required wavelength is selected via Bragg's law. Göbel Mirrors are multilayer crystals produced in a parabolic shape. They are used to transform a divergent beam to a bright parallel beam.

2.4.2.4 X-ray Detectors[5]

The main 3 detector types used in laboratory X-ray diffractometers are scintillation, gas-proportional and solid state. Scintillation detectors detect X-rays via the generation of photons of light in response to scattered X-rays. The emitted light is converted into an electrical signal by photomultiplier tubes. Gas-proportional position sensitive detectors (PSD's) detect X-rays via the ionisation of gas molecules (typically CH_4 or CO_2 with Xe or Ar) which induces an electrical current. Solid state PSD's are manufactured from semiconductors, usually Si or Ge. Scattered X-rays produce electron holes; the photon induced electric current is measured allowing for the positions of the scattered to be calculated. The latter two types of detector were used in this work.

2.4.2.5 Laboratory Diffractometers

The main diffractometer used in this work was the Bruker AXS; D8 Advance diffractometer operating in transmission geometry, with a copper X-ray tube and a germanium crystal monochromator (Cu $K\alpha_1$, λ = 1.5406 Å) with a solid state Lynxeye

PSD, collecting from $5 \leq 2\theta \geq 90°$ using a step size of ~0.02°. Variable temperature XRD measurements were carried out on both a Bruker AXS; D8 Advance diffractometer fitted with a heating stage (either an Anton Paar HTK 1200 or a Materials Research Institute (MRI) heating stage) operating in reflection geometry and a Siemens D5000 diffractometer fitted with an Oxford cryostream operating in capillary transmission mode, with a Braun PSD. Both diffractometers operate with a copper X-ray tube and a germanium crystal monochromator giving solely Cu $K\alpha_1$ radiation.

2.4.3 Neutron Diffraction[7]

Neutrons will also undergo diffraction by crystalline materials in a similar fashion to X-rays providing the neutron's wavelength is a comparable magnitude to interatomic distances. However, unlike X-rays, neutrons are not scattered by the electron density of atoms, but the atomic nuclei themselves. This results in a complex pattern in neutron scattering power, which does not vary linearly with atomic number. This can allow for the location of light atoms, such as oxygen and hydrogen, and the differentiation of elements with similar atomic number, and even different isotopes of the same element.

Neutrons can undergo magnetic scattering from atoms with unpaired electrons (paramagnetic atoms) as they possess a spin, therefore a magnetic moment. The magnetic scattering allows for information about the magnetic unit cell and the magnetic ordering.

Neutrons are produced in two separate ways: spallation and nuclear reactor. Spallation involves the bombardment of high energy protons on a metal target which generates a pulsed neutron beam, commonly used in *time of flight* (TOF) experiments. TOF neutron diffraction experiments use neutrons with a range of different wavelengths. Detectors are set at fixed angles (θ) and known distances from the sample, with the intensity of diffracted neutrons recorded as a function of time of flight. The second method produces neutrons via the fission of a uranium target. These neutrons are very high energy, and so need to be slowed using heavy water to produce neutrons with wavelengths suitable for diffraction experiments. A monochromator can be used to select for a particular wavelength, and so these experiments are known as *constant wavelength* (CW) experiments, and diffraction is measured as a function of θ.

Neutron diffraction studies were carried out at ISIS at the Rutherford Appleton Laboratory in Oxfordshire on the Polaris instrument, a medium resolution diffractometer. Figure 2.6 shows the Polaris instrument, where the detector banks are differentiated by colour.

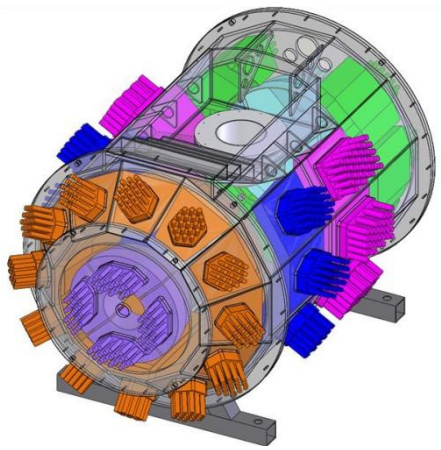

Figure 2.6 - Polaris instrument at ISIS[8]

2.4.4 Rietveld Analysis[9]

The Rietveld method was used in this research to obtain structural details from both x-ray and neutron powder diffraction data. When the Rietveld method is used correctly, it can provide accurate structural details for materials from which adequate single crystals cannot be prepared. The method uses much larger sample sizes than single crystal measurements and so the results are much more representative of the bulk material compared to a single crystal. The method was developed by Hugo Rietveld[10] and revolutionised the analysis of powder diffraction data. Previous to this most structural determinations relied on single crystal diffraction.

A structural model whose diffraction pattern resembles that of the sample of interest is required; this structural model would contain information about the unit cell symmetry, dimensions and atomic positions, as well as instrument parameters such as wavelength and peak shape. The basis of the Rietveld refinement is a least squares method, the aim of which is to minimise the residual, S_y, which represents the difference between the observed and the calculated intensities, which is shown in equation 2.7.

$$S_y = \sum_i w_i \left[y_i(obs) - y_i(calc)\right]^2 \tag{2.7}$$

where $y_i(obs)$ is the observed intensity at the i^{th} step, $y_i(calc)$ is the calculated intensity at the i^{th} step and w_i is the weighting of each data point, i, which is equal to $[y_i(obs)]^{-1}$ summed over all data points.

A diffraction pattern consists of a collection of reflection profiles, of which each have a peak height, position, shape and an integrated area which is proportional to the Bragg intensity, I_{hkl}. Many Bragg peaks can contribute to the intensity, y_i, at any chosen point, i, in the pattern. The calculated intensity, y_i, can be calculated from the model by summing the intensities of the neighbouring Bragg reflections and background intensity:

$$y_i(calc) = \left[s \sum_{hkl} L_{hkl} |F_{hkl}|^2 \phi(2\theta_i - 2\theta_{hkl}) T_{hkl} + A \right] + y_{bi} \tag{2.8}$$

where s is the scale factor, L_{hkl} is a term for the Lorentz, multiplicity and polarisation factors, F_{hkl} is the structure factor for the (hkl) reflection, ϕ is the reflection profile function, T_{hkl} is the preferred orientation function, A is the absorption factor and y_{bi} is the background intensity at the i^{th} step.

To reduce the difference and improve the fit between the observed and calculated data, calculated shifts are applied to the parameters in the structural model to improve the starting model, and then the entire process is repeated. The refinement is continued until S_y, is minimised as much as possible to achieve the best fit.

The quality of the Rietveld refinement can be visually assessed by the difference line, which ideally should be flat. There are also a number of statistical figures of merit which can be used to evaluate the fit. These include the R structure-factor, the R-profile, the R-weighted profile and the R-expected.

$$R_F = \frac{\sum_{hkl} |F_{hkl}(obs) - F_{hkl}(calc)|}{\sum_{hkl} F_{hkl}(obs)} \tag{2.9}$$

$$R_{\mathrm{p}} = \frac{\sum_{i=1}^{n} |y_i(obs) - y_i(calc)|}{\sum_{i=1}^{n} y_i(obs)} \tag{2.10}$$

$$R_{\mathrm{wp}} = \left[\frac{\sum_{i=1}^{n} w_i [y_i(obs) - y_i(obs)]^2}{\sum_{i=1}^{n} w_i [y_i(obs)]^2} \right]^{1/2} \tag{2.11}$$

$$R_{\mathrm{exp}} = \left[\frac{(N-P-C)}{\sum_{i=1}^{n} w_i [y_i(obs)]^2} \right]^{1/2} \tag{2.12}$$

where N is the number of observed data points in the diffraction pattern, P is the number of refined parameters and C is the number of constraints.

R_{wp} contains the S residual that needs to be minimised and so is usually reported, R_F can be used as an indicator to the reliability of the structural model as it is based upon the Bragg intensities which are calculated from the model. Combining R_{wp} and R_{exp} gives χ^2, the 'goodness of fit' value. In a perfect refinement χ^2 would equal 1, but realistically this is not achieved.

$$\chi^2 = \left[\frac{R_{wp}}{R_{exp}} \right]^2 \tag{2.13}$$

Various different software packages can be used to carry out Rietveld refinements; in this research the GSAS[11] suite of programs and the EXPGUI[12] were used for both X-ray and neutron powder diffraction data.

2.4.5 Thermogravimetric Analysis-Mass Spectrometry

Thermogravimetric analysis (TGA) is used to monitor the change in mass of a sample as it is subjected to changes in temperature. It can be used to investigate the

sample's thermal stability, composition, decomposition temperature and phase transitions.

The thermogravimetric analyser is a sensitive instrument which consists of a precise balance and a furnace. A small amount of sample (~40-60 mg) is weighed into an alumina crucible and placed in a furnace. The furnace contains a thermocouple which accurately measures the temperature whilst the balance monitors any changes in mass. The atmosphere can be changed depending on the sample.

In this research, all samples were heated under an O_2/N_2 atmosphere at a rate of 10K min^{-1} in a Netzsch STA 449 F1 Jupiter instrument. The instrument was coupled to Quadrupole Mass Spectrometer (QMS) system via a fused silica capillary. This allows for the qualitative analysis of any evolved gases. The evolved gases are transferred along the heated capillary into the electron impact ion source.

Heat flow and energy changes within the sample can also be detected via a Differential Thermal Analysis (DTA) unit within the TGA by measuring the temperature difference between the sample crucible and the reference crucible. This can allow changes not associated with mass change, such as phase changes or crystallisation, to be detected. This technique is also able to indicate whether the thermal event is exothermic or endothermic.

2.4.6 Electron Microscopy

Electron microscopes can be used to give high resolution images on a very small scale (100 μm – 1 nm). Due to the small De Broglie wavelength of electrons, significantly higher resolution images can be produced compared to an optical microscope. They can be used to investigate the particle morphology, surface topography, composition and crystal structure. In this research, two types of electron microscopy were used: scanning electron microscopy (SEM) and transmission electron microscopy (TEM).

2.4.6.1 Scanning Electron Microscopy[13]

SEM is an incredibly versatile technique for the investigation of a sample's microstructure. An electron beam is fired at the sample and interacts with the near surface region of the sample to form an image. This interaction generates many signals; the two most commonly used to produce images are secondary electrons and backscattered electrons. The electron beam can also cause the ejection of characteristic X-rays from the elements within the sample, which can be analysed to provide elemental composition. This technique is called energy dispersive X-ray spectroscopy (EDS) and the detector is fitted in the SEM, allowing for simultaneous analysis.

In this research, SEM was carried out using a Philips XL-30 microscope operating under vacuum with a 20.0 kV electron beam, fitted with an Oxford Instruments INCA EDS system. The samples were mounted onto an adhesive carbon

pad and coated with either gold or carbon to aid their conductivity and prevent charge build-up on the sample surface.

2.4.6.2 Transmission Electron Microscopy[14]

TEM involves the irradiation of a very thin sample using an electron beam with an accelerating voltage between 200-500 keV. The electrons that pass through the sample form a two dimensional image. TEM images the bulk of the sample, not just the surface like SEM and so crystal defects, grain boundaries and interfaces can be observed. Information about crystal structure can be obtained via selected area electron diffraction (SAED), which can be performed inside the TEM. Due to the charged nature of electrons, they interact more strongly with the electron cloud of atoms than X-rays and therefore the scattering is much more intense compared to X-ray diffraction. The pattern formed consists of diffraction spots of varying intensity which are observed in a reciprocal lattice, and d-spacings can be calculated from the distance between the diffracted spots. The calculated d-spacings can then be compared to known values, allowing the pattern to be indexed and *hkl*'s to be assigned to each spot.

In this research, TEM was carried out using a JEOL 2100 microscope operating under vacuum with a 200.0 keV electron beam. Samples were prepared by dispersing the powder in ethanol and drop casting onto a carbon-coated nickel grid.

2.47 X-ray Fluorescence

X-ray fluorescence spectroscopy is a technique for elemental analysis of materials. It was used in this research for both qualitative and quantitative analysis of materials. High energy X-rays bombard the sample which causes the removal of core electrons. Electrons from higher energy shells drop down to fill these holes which cause the emission of X-rays characteristic to the elements present in the sample. A spectrum is produced, the energy of the peaks is representative of the element and the intensity of the peaks is related to the elemental concentration.

In this research the Bruker S8 Tiger spectrometer was used, and samples were measured as both loose powder for initial qualitative measurements and later as fused beads for quantitative measurements. Fused beads give a more accurate elemental composition as they produce a homogeneous sample and minimise matrix effects such as particle size.

2.4.8 Solid State Nuclear Magnetic Resonance Spectroscopy[15]

Solid state NMR spectroscopy is a powerful technique for the structural characterisation of materials. Whereas PXRD investigates the long range order of a material, solid state NMR probes the atomic scale, allowing the analysis of both amorphous and crystalline materials.

NMR relies on the nucleus in question possessing a nuclear spin. When the nucleus is placed in a strong magnetic field, the energy levels between the spin states are split. This is known as the Zeeman effect. The magnetic moment of the nucleus or magnetisation vector, M, precesses about the principal axis of the applied field, B_0.

The sample is then irradiated with radiofrequency magnetic pulse, which causes the magnetisation vector to incline, away from the principal axis. This is shown below in figure 2.7.

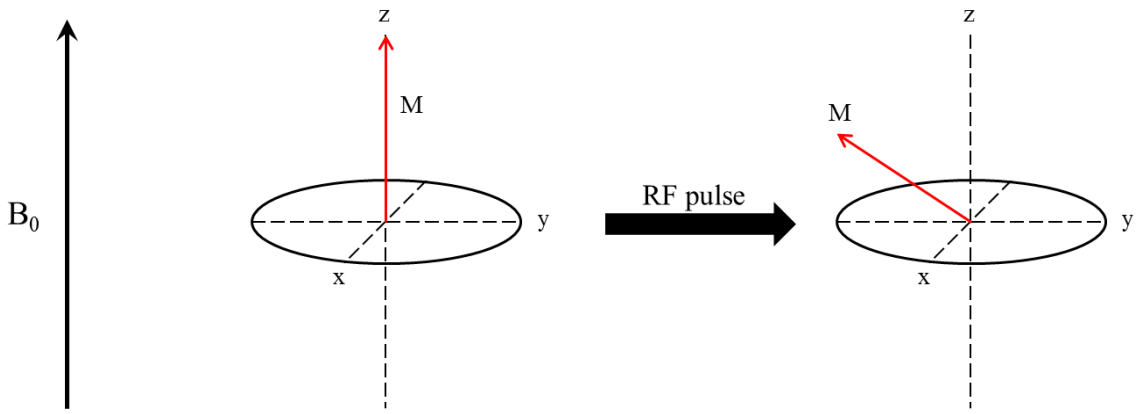

Figure 2.7 - Vector model of NMR Spectroscopy

Each nuclei magnetic moment precesses at characteristic frequency, known as the Larmor frequency. Once the pulse is turned off, the magnetisation vector relaxes back to the principal axis, producing a signal, known as the Free Induction Decay (FID). Frequency information is mathematically extracted from the FID via a Fourier Transformation, resulting in an NMR spectrum.

Broad peaks are often found in NMR spectra of solid samples due to a number of interactions including magnetic dipolar interactions and chemical shielding anisotropy. In solution NMR, the constant molecular motion cancels these interactions out. One way of reducing this peak broadening is to spin the sample rapidly (approximately 10 kHz) at an angle of 54.74°. This is known as magic angle spinning NMR spectroscopy (MAS NMR) and is shown in figure 2.8.

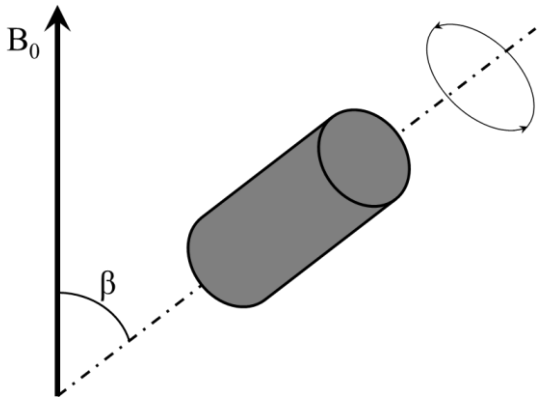

Figure 2.8- Magic Angle Spinning

NMR measurements were carried out and data interpreted by Scott King at the Department of Physics at the University of Warwick.

2.4.9 Magnetic Analysis[16, 17]

Magnetisation in materials occurs as a result of the magnetic field generated in atoms from the orbital and spin angular momenta of electrons.

The magnetisation of a sample, *M*, can be defined as the field generated when the sample is placed in the applied field, *H*. This can be related to magnetic susceptibility, χ, through the following equation:

$$\chi = \frac{M}{H} \tag{2.14}$$

Magnetic materials can be classified in terms of the arrangement of magnetic dipoles within the material. Diamagnetism occurs when atom possesses no unpaired electrons, leading to repulsion of the applied field and negative susceptibilities. Diamagnetism is present in all materials, but is usually very weak and so not normally observable, especially when other effects are also present. When an atom

possesses unpaired electrons, this gives rise to paramagnetism. The individual magnetic moments are randomly orientated in paramagnetic materials. When applying an external field to the sample the moments will attempt to align themselves with the field, and hence each other; however, this process may be hampered by thermal energy. The Curie law, shown below in equation 2.15, can be used to describe the temperature dependence on the magnetic susceptibility of paramagnetic materials:

$$\chi = \frac{C}{T}$$

where C is known as the Curie constant and T is the temperature in Kelvin.

It may be possible for the magnetic moments on the individual atoms to overcome the excess thermal energy and interact with each other to produce ordered magnetic moments. Ferromagnetism occurs when the spins align parallel to each other, whereas anti-ferromagnetism occurs when they align antiparallel to one another (as shown in figure 2.9). The temperatures at which such ordering occurs are known as the Curie temperature (T_C) and the Néel temperature (T_N), respectively.

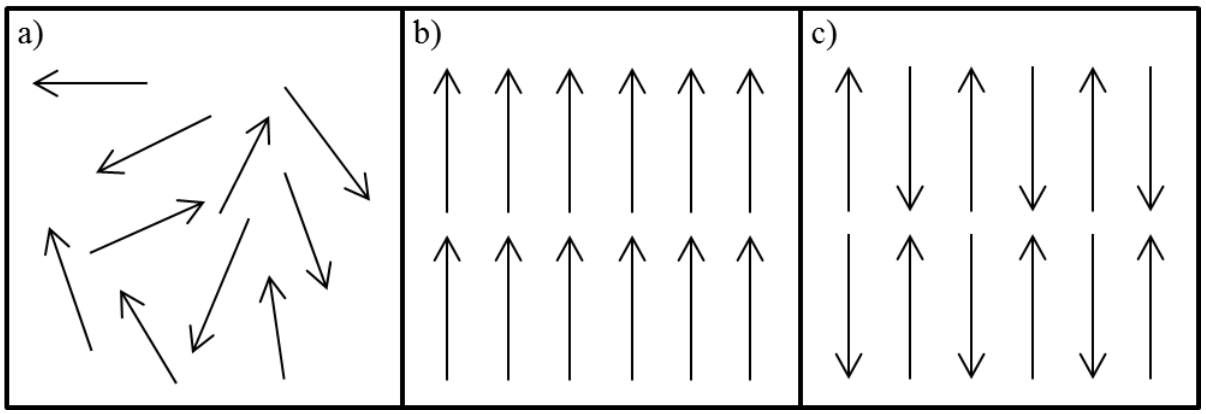

Figure 2.9 - Arrangements of unpaired electron spins; *a* is a paramagnetic arrangement, *b* is a ferromagnetic arrangement and *c* is an antiferromagnetic arrangement

The high temperature paramagnetic behaviour of ferro and antiferromagnets can be described by the Curie-Weiss law:

$$\chi = \frac{C}{T - \theta} \tag{2.16}$$

where θ is the Weiss constant, which can indicate whether the underlying interactions are ferromagnetic or antiferromagnetic in nature (see figure 2.10).

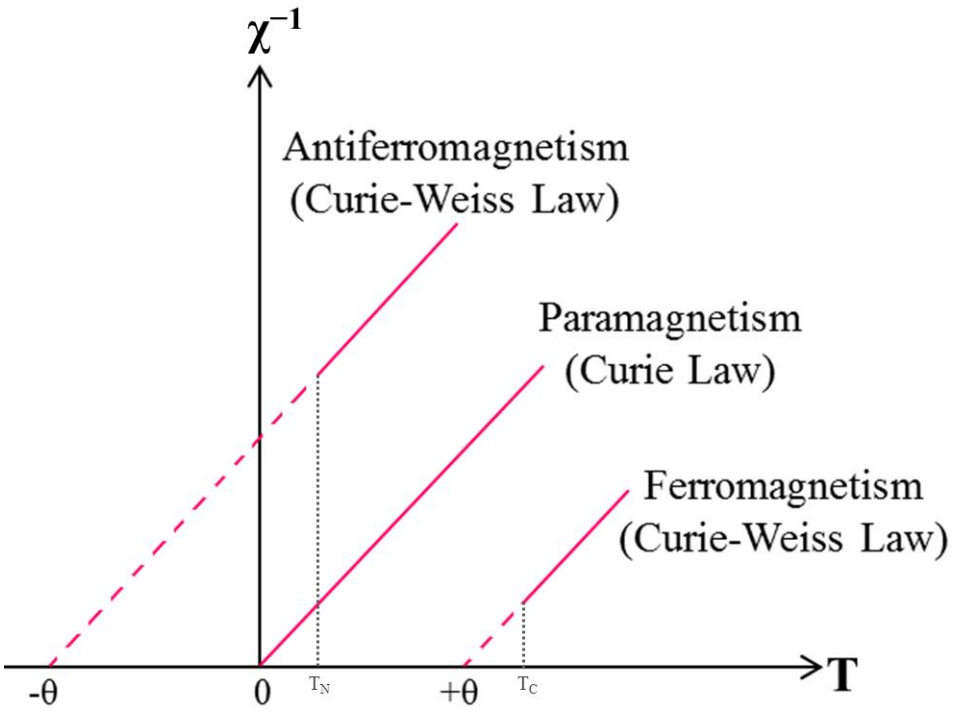

Figure 2.10 - Trends in magnetic behaviour of materials obeying the Curie and Curie-Weiss laws

The antiparallel alignment of moments does not always result in a net cancellation; canted antiferromagnetism arises when the moments are not entirely collinear and ferrimagnetism occurs when moments of different magnitudes interact. Both lead to a net overall ferromagnetic moment.

The effective magnetic moment, μ_{eff} is usually used to indicate the magnetic properties of a material. It can be related to molar susceptibility, χ_m, through the following equation:

$$\chi_m = \frac{N_A \mu_0 \mu_{eff}^2}{3kT} \qquad (2.17)$$

where N_A is Avogadro constant, μ_0 is the permeability of free space, k is the Boltzmann constant and T is temperature. The Curie constant should equal the gradient of a plot of χ_m vs. T^{-1}.

The magnetic moment of an atom from the unpaired electrons (spin only) can be calculated from the following equation:

$$\mu_S = \sqrt{n(n+2)}\ \mu_B \tag{2.18}$$

where n is the number of unpaired electrons and μ_B is the units of the Bohr magneton.

Magnetic susceptibility measurements were carried out using a Quantum Design Magnetic Properties Measurements System (MPMS). An accurately weighed sample was placed in a gelatine capsule, which was then placed in a plastic straw. Both field cooled/field warmed and zero-field cooled/field warmed measurements were performed from 5 to 300K with a field-strength of 500 Oe.

2.4.10 Electron Spin Resonance[18]

Electron spin resonance (ESR) or electron paramagnetic resonance spectroscopy is a technique used to investigate materials with unpaired electrons. The technique has a similar basis to NMR spectroscopy; however it is electron spins that are excited in this technique as opposed to nuclei spins in NMR spectroscopy. ESR can be used to identify the paramagnetic species in the sample.

A sample is placed in a magnetic field; the electron degeneracy is removed, and the electron spins can either align with the magnetic field (low energy) or against the field (high energy) known as the Zeeman Effect, as shown in figure 2.11.

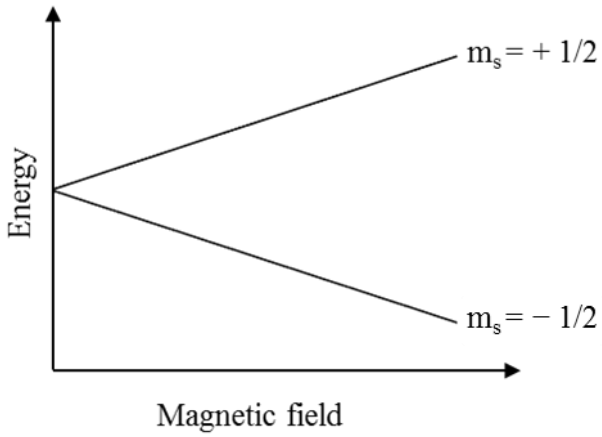

Figure 2.11 – The Zeeman Effect

The energy levels of the paramagnetic species can be affected by the surrounding atoms and by external magnetic fields, and transitions in these energy levels can be detected by monitoring the absorption from an alternating magnetic field. Comparing the observed transitions with calculations can allow the environment of the paramagnetic species to be deduced. In this thesis measurements were carried out on a Bruker ESP 300 spectrometer operating at X-band frequencies (~ 9.5 GHz) and initial analysis carried out by Dr Paul Anderson.

2.4.12 Flame Emission Photometry[19]

The basis of this technique is the classic flame test, where the emission of characteristic radiation is caused by the excitation of elements in the flame. The flame photometer instrument consists of a flame unit, in which solution based samples are aerosolised and sprayed into the flame. The light emitted from the

sample is focussed and passed through a filter specific to the element in question. A photodiode detector is used to convert the light detected into an electrical signal which is proportional to the intensity of the radiation. The signal is sent to a readout system after amplification. In this work measurements were carried out on a Corning 400 flame photometer, with samples dissolved in 0.1 M HNO_3.

References

1. M. v. Laue, *Physikalische Zeitschrift*, 1913, **14**, 1075-1079.
2. M. v. Laue, *Annalen der Physik*, 1913, **41**, 989-1002.
3. W. L. Bragg, *Proceedings of the Cambridge Philosophical Society*, 1913, **17**, 43-57.
4. JCPDS, *International Centre for Diffraction Data*, 1999, P.1., Swathmore, Pennsylvania, PA 19081, USA 11990
5. V. J. Pecharsky and P. Y. Zavalij, *Fundamentals of Powder Diffraction and Structural Charaterization of Materials*, 2nd edn., Springer, New York, 2009.
6. R. Tilley, *Crystals and Crystal Structures*, Wiley, Chichester, 2006.
7. E. H. Kisi and C. J. Howard, *Applications of Neutron Powder Diffraction*, Oxford University Press, New York, 2008.
8. *ISIS Polaris*, http://www.isis.stfc.ac.uk/instruments/polaris/polaris4643.html, Accessed June, 2014.
9. R. A. Young, *The Rietveld Method, IUCr Monographs on Crystallography*, Oxford University Press, New York, 1993.
10. H. M. Rietveld, *Journal of Applied Crystallography*, 1969, **2**, 65-71.
11. A. C. Larson and R. B. Von Dreele, Los Alamos National Laboratory, Los Alamos NM, Editon edn., 1994.
12. B. H. Toby, *Journal of Applied Crystallography,* 2001, **34**, 210-213.
13. J. I. Goldstein, D. E. Newbury, P. Echlin, D. C. Joy, A. D. R. Jr., C. E. Lyman, C. Fiori and E. Lifshin, *Scanning Electron Microscopy and X-ray Microanalysis*, 2nd. edn., Plenum Press, New York, 1992.

14. L. Reimer, *Transmission Electron Microscopy*, 4th edn., Springer, New York, 1997.
15. K. J. D. Mackenzie and M. E. Smith, *Multinuclear Solid-State NMR of Inorganic Materials*, Pergamon, Oxford, 2002.
16. L. E. Smart and E. A. Moore, *Solid State Chemistry: An Introduction*, Taylor & Francis Group, Boca Raton, 2005.
17. M. T. Weller, *Inorganic Materials Chemistry* Oxford University Press, New York, 1999.
18. P. Rieger, *Electron Spin Resonance: Analysis and Interpretation*, Royal Society of Chemistry, Cambridge, 2007.
19. E. Pungor and R. A. Chalmers, *Flame Photometry Theory*, D. Van Nostrand Company Limited, London, 1967.

Chapter 3

Synthesis and Characterisation of $MgH_2P_2O_7$ and Li-Doped $MgH_2P_2O_7$

3.1 Introduction

Calcium phosphates have been the focus of research into bone substitutes and hard tissue replacements due to their similarity in composition to the inorganic component of bone.[1, 2] Recently, focus has shifted to the use of magnesium and magnesium phosphates in hard tissue replacement. Not only is Mg^{2+} found in bone tissue,[3] it has also been seen to stimulate bone growth.[3] Addition of magnesium salts to brushite cements leads to inhibition of hydroxyapatite formation,[2, 4] thus limiting this obstacle to the resorption of the bone cement and the growth of new bone tissue. Addition of pyrophosphates ($P_2O_7^{4-}$) was also found to inhibit hydroxyapatite formation.[4, 5] Magnesium based phosphates also have potential for applications as ionic conductors; they are light-weight, non-toxic and earth abundant materials. Phosphate materials have been found to be thermally stable at high temperature due to the presence of the strong P–O bond, which improves the safety of a device.[6] This chapter details the investigation of $MgH_2P_2O_7$ and Li-doped $MgH_2P_2O_7$. This study focuses on the structural characterisation and thermal stability.

3.2 Experimental

3.2.1 Synthesis of α-$MgH_2P_2O_7$

α-$MgH_2P_2O_7$ was prepared via an acid melt. The optimised conditions were found to involve a solution of MgO and H_3PO_4 (85 wt. %), with a Mg:P ratio of 1:4. This was heated in a porcelain crucible at 180°C for 12 hours in an oven, and then allowed to cool to room temperature The resulting paste was then washed with deionised water to remove any excess H_3PO_4 and suction filtered, leaving a white powder.

3.2.2 Synthesis of β-$MgH_2P_2O_7$

β-$MgH_2P_2O_7$ was prepared via an acid melt. The reaction described in 3.2.1 but performed at higher temperatures (200-250°C) resulted in a mixture of β-$MgH_2P_2O_7$ and $Mg_2P_4O_{12}$. Seeding the reaction with a small amount of $CaH_2P_2O_7$ was found to produce single phase β-$MgH_2P_2O_7$. Therefore, a solution of MgO and H_3PO_4 (Mg:P ratio of 1:4) with the addition of 1 mg of $CaH_2P_2O_7$ was heated in a porcelain crucible at 200°C for 12 hours and then allowed to cool to room temperature. The resulting paste was then washed with deionised water to remove any excess H_3PO_4 and suction filtered, leaving a white powder.

3.2.3 Synthesis of Li-Doped $MgH_2P_2O_7$

Li-doped $MgH_2P_2O_7$ was prepared via an acid melt. The synthetic conditions were optimised to give the most crystalline product: a solution of MgO, Li_2CO_3 and H_3PO_4 with a Mg:Li:P ratio of 1:1:4, was heated in a porcelain crucible at 180°C for 48

hours and then allowed to cool to room temperature. The resulting paste was then washed with deionised water to remove any excess H_3PO_4 and suction filtered, leaving a white powder.

3.2.4 Collection of Diffraction Data

Powder diffraction data were collected on the Bruker AXS: D8 Advance diffractometer in transmission mode using a 2θ range of 5-90°. Neutron powder diffraction data of both the α & β polymorphs of $MgH_2P_2O_7$ and $Mg(Li, H)_2P_2O_7$ were recorded on the TOF powder diffractometer Polaris instrument at ISIS, Rutherford Appleton Laboratory. Variable temperature data were collected on the Bruker AXS: D8 Advance diffractometer, fitted with an MRI heating stage.

3.3 Results and Discussion

3.3.1 α-$MgH_2P_2O_7$

Synthesis of α-$MgH_2P_2O_7$ resulted in a single phase product. Hinsch *et al.*[7] had previously reported a synthetic route to a $MgH_2P_2O_7$ polymorph via the thermal dehydration of $Mg(H_2PO_4)_2{\cdot}2H_2O$, but had not reported a structure. A suitable structural model in the form of $NiH_2P_2O_7$[8] was found via a search of the ICSD,[9] and this polymorph was labelled α-$MgH_2P_2O_7$.

3.3.1.1 Crystal structure of α-$MgH_2P_2O_7$

The crystal structure of α-$MgH_2P_2O_7$ was determined via Rietveld refinement[10] of neutron powder diffraction data using $NiH_2P_2O_7$[8] as a structural

model. The GSAS suite of programs[11] and the EXPGUI[12] were used to perform the refinement. The refinement converged to a low R_{wp} 0.6%. The sample was not deuterated, but still gave an excellent fit despite the high background. The Rietveld refinement plot is shown in figure 3.1. An additional peak from the sample holder (vanadium can) was visible at 2.14 Å.

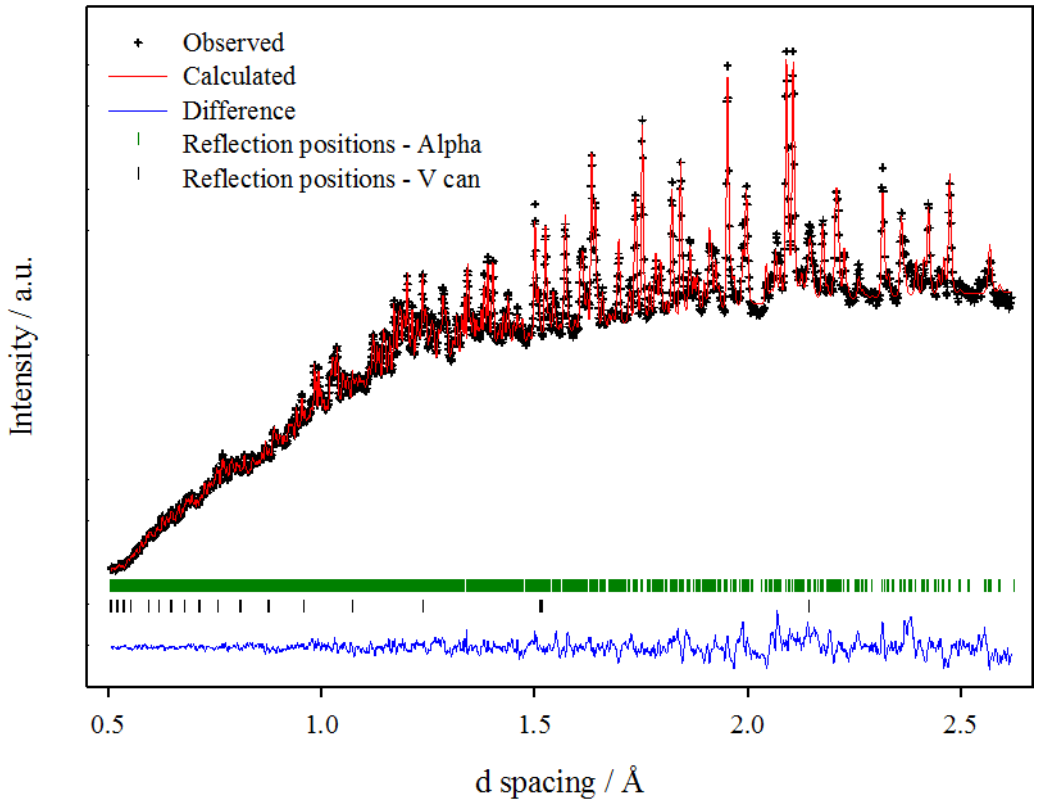

Figure 3.1 - Rietveld refinement plot of α-$MgH_2P_2O_7$

The refinement confirms that α-$MgH_2P_2O_7$ adopts the $NiH_2P_2O_7$[8] structure type, crystallising into a monoclinic cell, space group $P2_1/c$ with lattice parameters; a = 9.0500(4) Å, b = 12.7528(5) Å, c = 9.6407(4) Å and β = 106.142(2)°. Table 3.1 shows the refined structural parameters and bond angles and lengths are shown in table 3.2.

Table 3.1- Refined structural parameters of α-$MgH_2P_2O_7$ at room temperature

Atom	Site	Occupancy	x	y	z	U_{iso} / Å^2	BVS
Mg1	4*e*	1	0.256(1)	0.2546(7)	0.247(1)	0.0023(8)	2.081
Mg2	4*e*	1	0.248(1)	0.4113(4)	0.005(1)	0.0054(9)	2.175
P1	4*e*	1	0.494(1)	0.2785(7)	0.572(1)	0.0010(1)	5.004
P2	4*e*	1	0.471(1)	0.0492(8)	0.289(1)	0.0008(2)	4.928
P3	4*e*	1	0.022(1)	0.2023(7)	-0.058(1)	0.0013(1)	5.325
P4	4*e*	1	0.037(1)	0.4551(7)	0.223(1)	0.0004(1)	4.993
O1	4*e*	1	0.151(1)	0.3898(7)	0.176(1)	0.0008(1)	2.259
O2	4*e*	1	0.337(1)	0.1028(7)	0.319(1)	0.0009(1)	1.802
O3	4*e*	1	0.424(1)	0.3192(7)	0.411(1)	0.0015(1)	1.467
O4	4*e*	1	0.058(1)	0.1703(6)	0.080(1)	0.0010(1)	2.298
O5	4*e*	1	0.384(1)	0.2831(7)	0.114(1)	0.0007(1)	2.450
O6	4*e*	1	-0.0449(9)	0.3704(6)	0.3168(9)	0.0007(1)	2.019
O7	4*e*	1	0.390(1)	-0.0594(6)	0.2091(8)	0.015(1)	1.662
O8	4*e*	1	0.1093(9)	0.5379(6)	0.3238(8)	0.014(1)	2.296
O9	4*e*	1	0.123(1)	0.2210(7)	0.385(1)	0.0008(1)	1.500
O10	4*e*	1	0.101(1)	0.5175(7)	-0.100(1)	0.0008(1)	1.808
O11	4*e*	1	0.5157(9)	0.3913(6)	0.6616(9)	0.017(1)	2.226
O12	4*e*	1	0.387(1)	0.5199(7)	0.103(1)	0.015(2)	1.862
O13	4*e*	1	0.657(1)	0.2374(7)	0.6027(9)	0.015(1)	2.214
O14	4*e*	1	-0.146(1)	0.2774(7)	-0.080(1)	0.025(2)	2.033
H1	4*e*	1	0.036(3)	0.591(2)	0.337(2)	0.026(3)	0.670
H2	4*e*	1	0.547(2)	0.393(2)	0.340(2)	0.027(3)	0.767
H3	4*e*	1	0.200(2)	0.711(1)	0.033(2)	0.056(4)	0.878
H4	4*e*	1	0.645(2)	0.329(1)	0.138(2)	0.053(4)	1.354

Space group $P2_1/c$; a = 9.0500(4) Å, b = 12.7528(5) Å, c = 9.6407(4) Å and β = 106.142(2)°. Figure of merit: R_{wp} = 0.60%, R_p = 1.12%, χ^2 = 6.995

Table 3.2 - Selected bond distances (Å) and angles (°) for α-$MgH_2P_2O_7$

Mg1-O1	2.00(1)	**Mg2-O1**	2.10(2)
Mg1-O2	2.12(1)	**Mg2-O2**	2.17(2)
Mg1-O3	2.04(1)	**Mg2-O5**	2.14(1)
Mg1-O4	2.32(1)	**Mg2-O9**	2.18(1)
Mg1-O5	1.99(2)	**Mg2-O10**	1.97(1)
Mg1-O9	2.07(1)	**Mg2-O12**	1.93(1)
O1-Mg1-O2	172.2(7)	**O1-Mg2-O2**	167.3(4)
O1-Mg1-O3	95.8(5)	**O1-Mg2-O5**	79.8(5)
O1-Mg1-O4	87.5(5)	**O1-Mg2-O9**	92.6(5)
O1-Mg1-O5	85.8(5)	**O1-Mg2-O10**	96.7(6)
O1-Mg1-O9	95.3(6)	**O1-Mg2-O12**	94.0(6)
O2-Mg1-O3	90.0(5)	**O2-Mg2-O5**	92.8(5)
O2-Mg1-O4	86.3(5)	**O2-Mg2-O9**	75.8(5)
O2-Mg1-O5	99.5(6)	**O2-Mg2-O10**	89.4(6)
O2-Mg1-O9	79.2(5)	**O2-Mg2-O12**	97.1(5)
O3-Mg1-O4	173.9(6)	**O5-Mg2-O9**	79.2(3)
O3-Mg1-O5	91.9(5)	**O5-Mg2-O10**	172.7(6)
O3-Mg1-O9	91.9(5)	**O5-Mg2-O12**	95.8(6)
O4-Mg1-O5	96.5(5)	**O9-Mg2-O10**	94.6(6)
O4-Mg1-O9	82.7(4)	**O9-Mg2-O12**	171.0(7)
O5-Mg1-O9	178.5(7)	**O10-Mg2-O12**	90.7(3)
P1-O3	1.59(1)	**P2-O2**	1.53(1)
P1-O5	1.42(1)	**P2-O7**	1.62(2)
P1-O11	1.66(1)	**P2-O11**	1.51(1)
P1-O13	1.51(1)	**P2-O12**	1.51(1)
O3-P1-O5	110.1(8)	**O2-P2-O7**	101.0(7)
O3-P1-O11	100.6(7)	**O2-P2-O11**	111.3(8)
O3-P1-O13	114.1(8)	**O2-P2-O12**	119.0(9)
O5-P1-O11	108.6(8)	**O7-P2-O11**	107.7(8)
O5-P1-O13	118.3(8)	**O7-P2-O12**	107.0(9)
O11-P1-O13	103.2(7)	**O11-P2-O12**	109.9(7)
P3-O4	1.34(1)	**P4-O1**	1.49(1)
P3-O6	1.52(1)	**P4-O6**	1.739(1)
P3-O9	1.54(1)	**P4-O8**	1.46(1)
P3-O14	1.76(1)	**P4-O10**	1.51(2)
O4-P3-O6	122.3(8)	**O1-P4-O6**	105.2(7)
O4-P3-O9	123.2(8)	**O1-P4-O8**	112.6(7)
O4-P3-O14	104.0(8)	**O1-P4-O10**	112.0(9)
O6-P3-O9	105.6(7)	**O6-P4-O8**	107.1(8)
O6-P3-O14	94.2(6)	**O6-P4-O10**	99.5(7)
O9-P3-O14	100.8(7)	**O8-P4-O10**	118.6(8)
P1-O11-P2	144.0(7)	**P3-O6-P4**	129.8(7)
H1-O8	0.98(2)	**H3-O14**	0.77(2)
H2-O7	1.03(3)	**H4-O13**	0.93(2)
P4-O8-H1	113(1)	**P3-O14-H3**	135(2)
P2-O7-H2	117(1)	**P1-O13-H4**	101(1)

The structure, shown in figure 3.2, consists of zig-zag chains of edge-sharing MgO_6 octahedra which run along the *c* axis. These chains stack along *a*, and form a channelled structure. The PO_4 tetrahedra corner share with the MgO_6 octahedra, interconnecting the chains. Protons are located as hydroxyl groups on the phosphate tetrahedra facing into the channel. Protons are also able to form hydrogen bonds with their nearest oxygen neighbour (see figure 3.3); for H1 and H2 their nearest neighbour is an oxygen bridging the Mg octahedra and the phosphate tetrahedra. This leads to a long Mg1–O4 bond (2.32(1) Å), a short P3–O4 of 1.34(1) Å and a H1–O4 hydrogen bond of 1.67(2) Å. H2 - O3 forms a slightly longer hydrogen bond of 1.74(2) Å and a marginally longer than average P1–O3 bond of 1.59(1). H3 and H4 form hydrogen bonds with hydroxyl units. H3 forms a long hydrogen bond with O13 of 2.1(2) Å, and H4 forms a hydrogen bond of the same length with O7.

Bond Valence Sum[13] (BVS) calculations (see appendix 1) for Mg^{2+} give a valence of +2.081 and +2.175, with an average of +2.13, indicating that Mg is slightly over bonded. BVS values calculated for P^{5+} are +5.004, +4.928, +5.325 and +4.993, with an average of +5.06, which is close to the valence expected for P^{5+}. The calculated valences for O range from 1.467 to 2.45, but on average the BVS is 1.99, very close to the expected valence of O^{2-}. The Global Instability Index[14] (GII) can be used as a measure of the strain within a structure by comparing how much the BVS deviates from the ideal valence sum, as determined by taking the root mean square of the bond valence sum deviations. Generally a value of 0.1 to 0.2 valence units indicates a strained structure, and values above 0.2 suggest an unstable structure. The calculated value for α-$MgH_2P_2O_7$ of 0.059 v.u. shows the structure is not significantly strained.

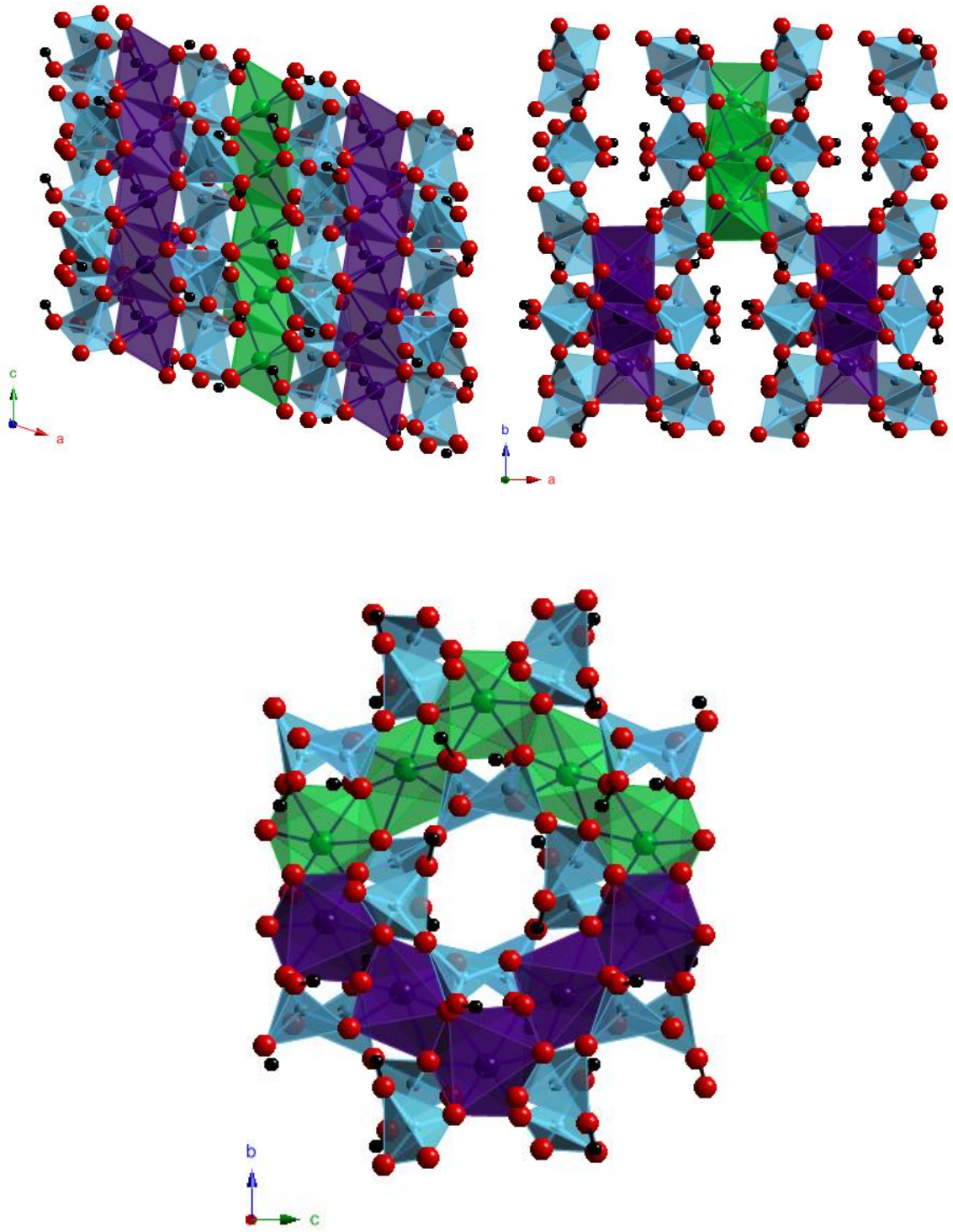

Figure 3.2 - Structure of α-$MgH_2P_2O_7$ as viewed in the *ac*, *ab* and *bc* planes. MgO_6 octahedra are purple and green to differentiate the chains; PO_4 tetrahedra are blue and protons are black.

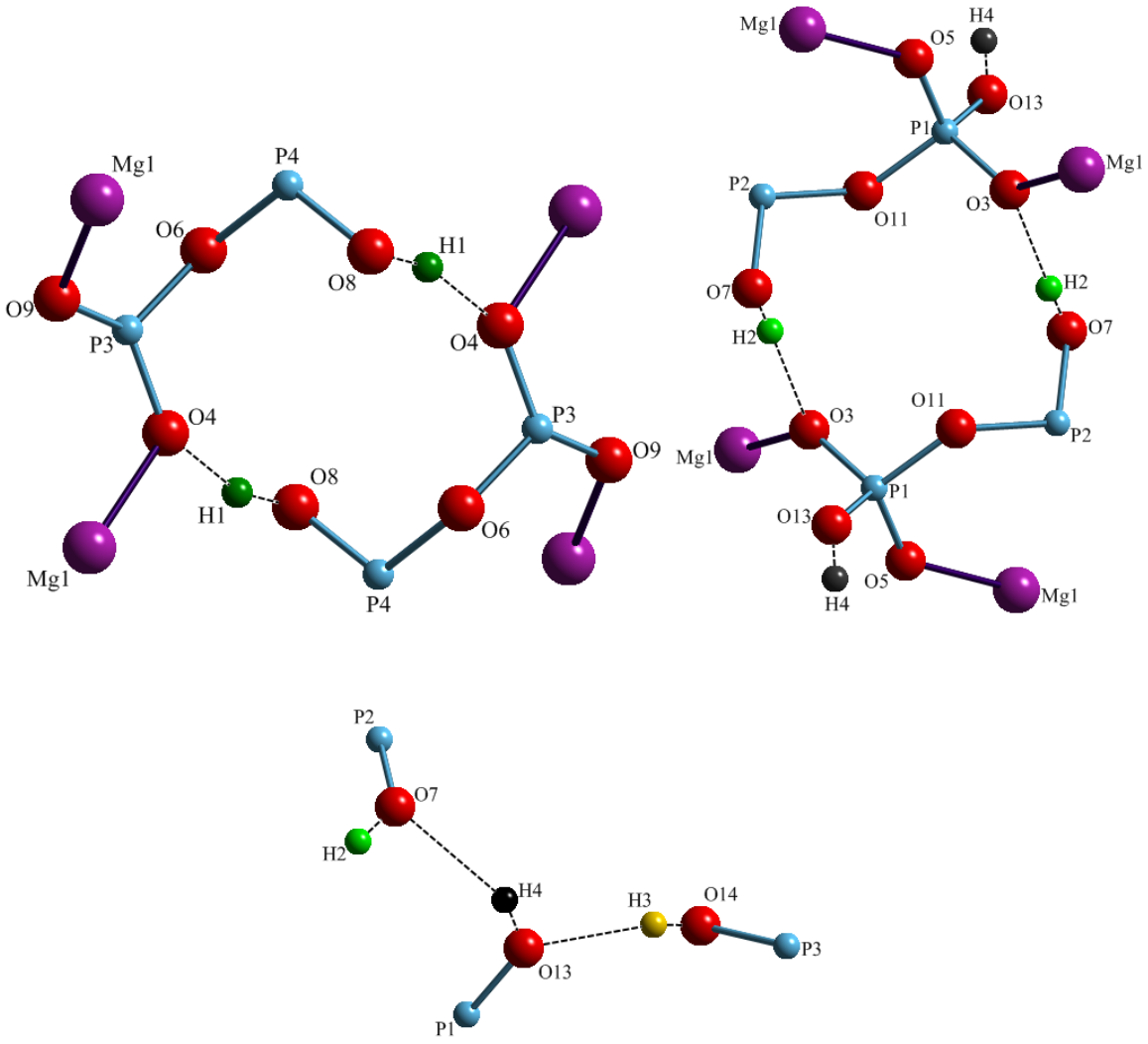

Figure 3.3 - Ball and stick models displaying the hydrogen bonding network within α-$MgH_2P_2O_7$

3.3.1.2 ^{31}P MAS-NMR

To confirm the presence of 4 crystallographically distinct P sites, MAS-NMR was used. The experimental data were compared to simulated data, using the structural model, which is shown in figure 3.4.

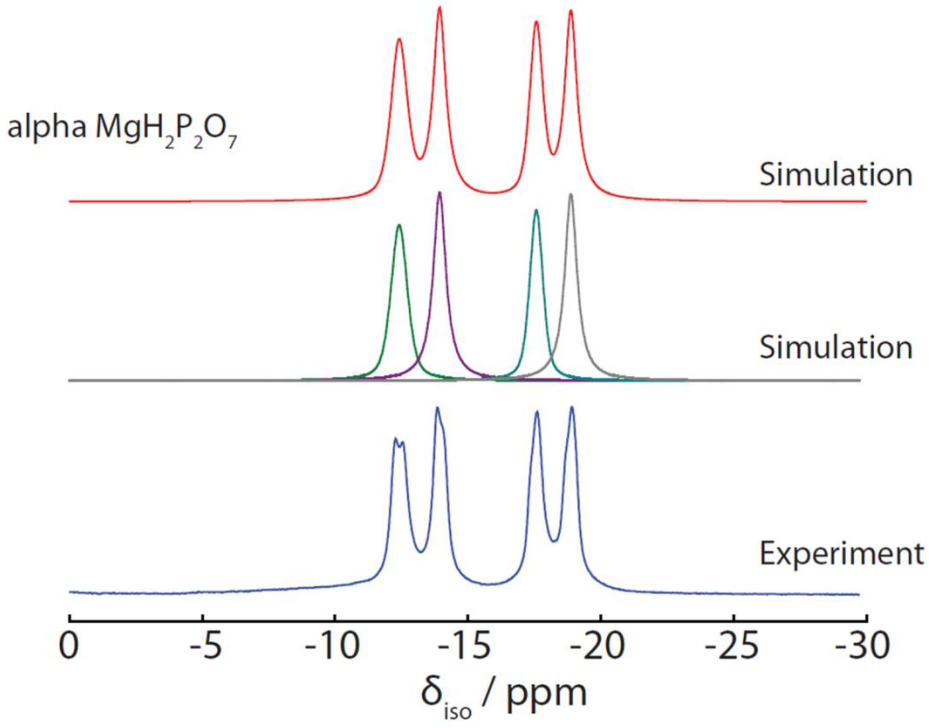

Figure 3.4 – ^{31}P Cross-polarisation spectra of α-$MgH_2P_2O_7$ at 9.4 T (10kHz MAS), showing the simulated deconvoluted spectrum for each individual P environment, and the overall simulated spectrum compared to the experimental data

The experimental data fit very well with the simulation, giving 4 distinct peaks indicating 4 separate P environments. Peak 1, -12.41 ppm, appears to be slightly split; this is most likely down to J-coupling (an indirect interaction between two nuclear spins) to its nearest P neighbour causing the peak to split. The two P environments closest in physical space are P3 and P4 so it is likely peaks 1 and 2 (-13.93 ppm) are due to P3 and P4.

3.3.1.3 Thermal Behaviour of α-$MgH_2P_2O_7$

Thermogravimetric analysis was used to investigate the thermal stability of α-$MgH_2P_2O_7$. A sample of α-$MgH_2P_2O_7$ was heated at 10K min^{-1} to 600°C. The plot is shown in figure 3.5.

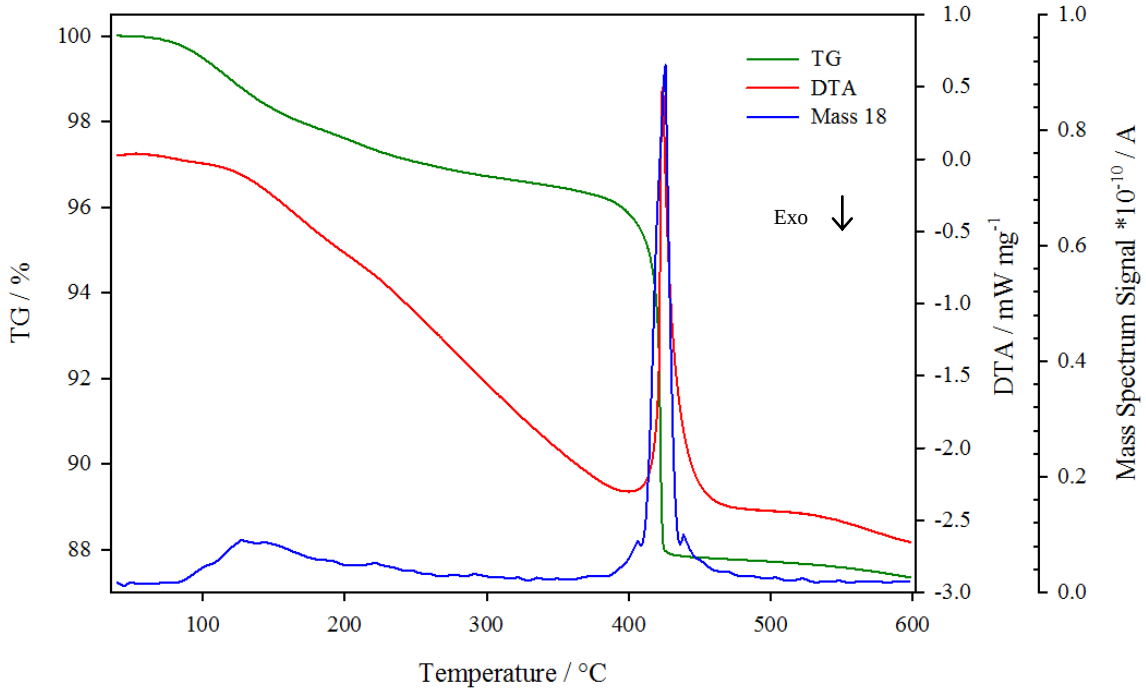

Figure 3.5 - TGA-MS plot of α-$MgH_2P_2O_7$

At approximately 120°C there is a small mass loss coinciding with a broad shallow peak in the mass spectrum for mass 18, consistent with the loss of surface water, followed by a small steady mass loss of 2% over a temperature range of 300°C, which is then followed by a large mass loss of ~9%, onset at around 400°C, coinciding with a sharp endothermic peak in the DTA and a large sharp peak in mass spectrum signal for mass 18. This is from the loss of water from the structure, due to a condensation reaction. This is consistent with the given stoichiometry, as 1 formula unit of water is evolved when two HP_2O_7 units combine to form magnesium

tetrametaphosphate, $Mg_2P_4O_{12}$,[15] a cyclic polyphosphate. This reaction is shown in equation 3.1.

$$2MgH_2P_2O_7 \rightarrow Mg_2P_4O_{12} + 2H_2O \quad (3.1)$$

The cause of the steady mass loss of around 2% prior to the condensation is not known. The reported TGA data of the isostructural $FeH_2P_2O_7$[16] also contains a small steady mass loss prior to a larger mass loss around 335°C where the structure breakdowns, leaving an amorphous product. This could indicate an amorphous component in the reaction precipitate, however the ^{31}P NMR provides no supporting evidence for this being a phosphorus based amorphous impurity phase.

To confirm this decomposition pathway, variable temperature XRD was used. A sample was heated in an MRI heating stage in an alumina sample holder, and diffraction patterns were taken at approximately 50°C intervals from 50 to 650°C. A stack plot is shown in figure 3.6. The structure remains stable and unchanged up until 272°C. At 324°C the condensation begins to occur and peaks belonging to $Mg_2P_4O_{12}$ become evident. Full conversion to $Mg_2P_4O_{12}$ has occurred by 375°C, which is earlier than seen in the TGA-MS measurement. This is mostly likely due to reaction kinetics; the condensation of α-$MgH_2P_2O_7$ is a slow reaction and so occurs at a lower temperature in the VT-XRD heating stage compared to the TGA. In the VT-XRD heating stage the sample is heated in 50°C steps and then held there for a length of time to equilibrate at the set temperature and obtain a diffraction pattern, which allows the condensation to complete. In the TGA the sample is heated linearly at 10°C min^{-1} to 600°C and so the condensation reaction occurs whilst the TGA is still heating, leading to condensation at a higher temperature.

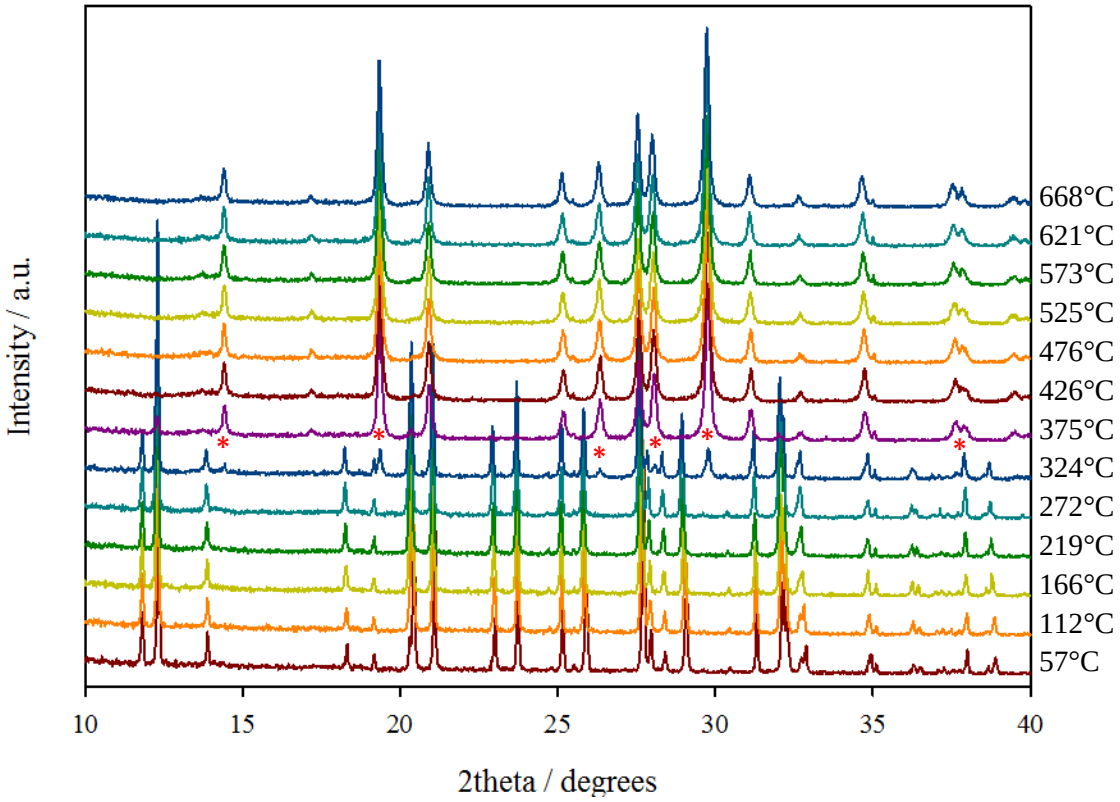

Figure 3.6 – Variable Temperature-XRD stack plot of α-$MgH_2P_2O_7$ with red asterisks indicating emerging $Mg_2P_4O_{12}$ peaks at 324°C

3.3.2 β-$MgH_2P_2O_7$

The synthesis described in 3.2.2 was able to isolate another new polymorph of $MgH_2P_2O_7$ (from here on labelled β-$MgH_2P_2O_7$) whose PXRD pattern could not be matched to any previously reported patterns on the JCPDS database.[17] The PXRD pattern was indexed to find a unit cell using the Crysfire program,[18] which indexes inputted 2 theta values to suggest possible unit cells using various different algorithms. Table 3.3 shows the potential unit cells calculated from Crysfire using 15 inputted peak positions.

Table 3.3 - Unit cells calculated using Crysfire[18] for β-$MgH_2P_2O_7$

I20	Merit	Symmetry	*a* (Å)	*b* (Å)	*c* (Å)	*α* (°)	*β* (°)	*γ* (°)	Volume (Å³)
15	36.4	Monoclinic	6.9041	7.7441	9.2399	90	101.57	90	483.980
15	36.2	Monoclinic	6.9046	7.7442	9.2399	90	101.55	90	484.061
15	8.1	Orthorhombic	6.1202	15.0412	15.1650	90	90	90	1396.020
15	6.5	Orthorhombic	4.2323	5.8731	56.9700	90	90	90	1416.067

The orthorhombic cells were discarded as they possessed low figures of merit. The monoclinic lattice parameters were then input into Chekcell,[19] a cell refinement program which can also be used to predict possible space groups. Chekcell confirmed the product was single phase, and predicted the space groups $C2/c$ and $P2_1/m$.

Thermogravimetric analysis was used to confirm the composition. A sample of β-$MgH_2P_2O_7$ was heated at 10K min^{-1} to 600°C and a plot of resulting data is shown in figure 3.7.

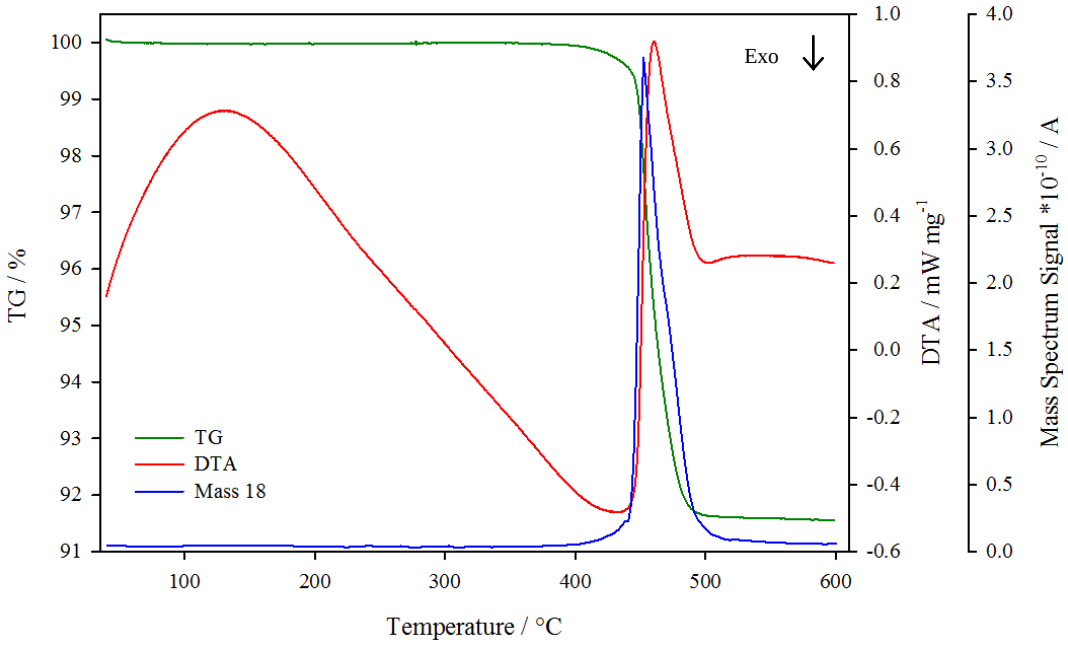

Figure 3.7 - TGA-MS plot of β-$MgH_2P_2O_7$

The mass is steady as the temperature increases, but at approximately 450°C there is a large mass loss of ~8.5% which coincides with a sharp endothermic peak in the DTA and a peak in the mass spectrum signal for mass 18. A diffraction pattern obtained post TG analysis was matched to $Mg_2P_4O_{12}$. Just as with α-$MgH_2P_2O_7$, the mass loss equates to 1 unit of water, which confirms the composition as $MgH_2P_2O_7$, and confirms its purity.

This led to a search for structures with similar symmetry and containing M_2O_7 structural units. Calcium acid pyrophosphate,[20] $CaH_2P_2O_7$, was found as a structural model. $CaH_2P_2O_7$ has monoclinic symmetry, space group $C2/c$, with the following lattice parameters: a = 7.3276(1) Å; b = 8.1282(1) Å; c = 9.7632(1) Å; β = 101.239°.

3.3.2.1 Crystal structure of β-$MgH_2P_2O_7$

The crystal structure of β-$MgH_2P_2O_7$ was determined via Rietveld refinement of neutron powder diffraction data, using $CaH_2P_2O_7$ as a structural model. The refinement converged at a low R_{wp} value of 0.79%. The sample was not deuterated, which gives the refinement a high background. The refinement, shown in figure 3.8, confirms that β-$MgH_2P_2O_7$ adopts the $CaH_2P_2O_7$ type structure, crystallising into the monoclinic space group $C2/c$ with lattice parameters a = 6.9041(1) Å, b = 7.7394(1) Å, c = 9.2352(2) Å and β = 101.582(1)°. Table 3.4 shows the refined structural parameters, with selected bond lengths and angles given in table 3.5.

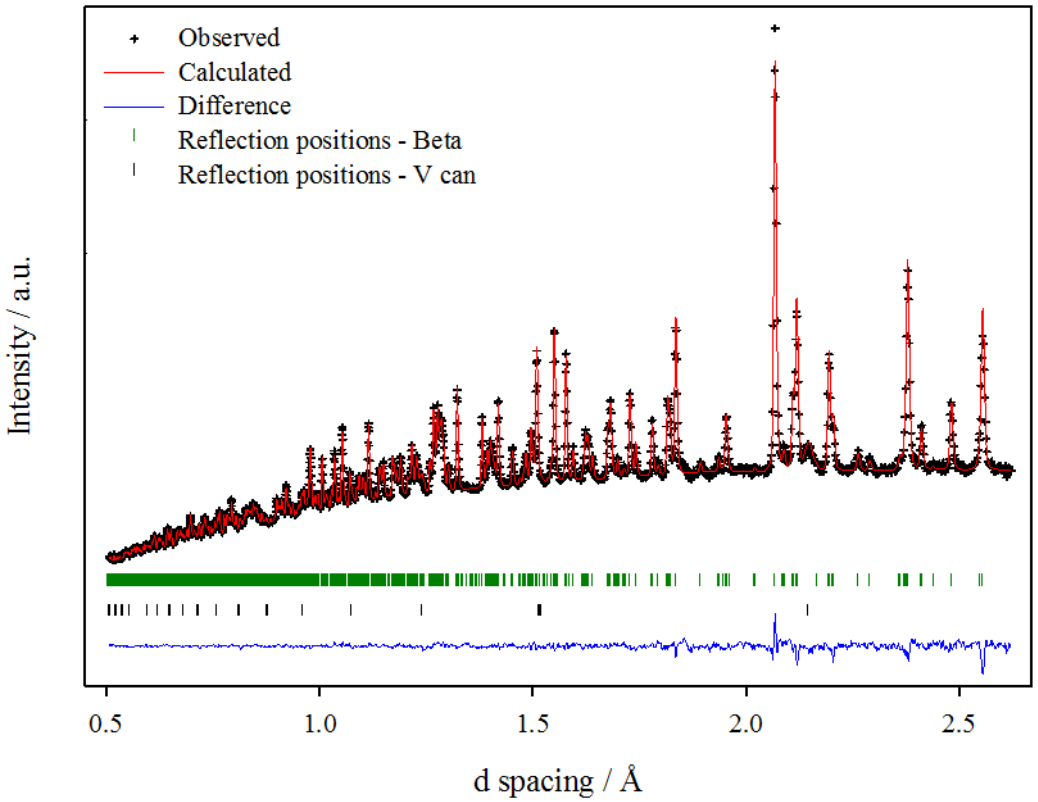

Figure 3.8 - Rietveld refinement plot of β-$MgH_2P_2O_7$

Table 3.4 - Refined structural parameters of β-$MgH_2P_2O_7$ at room temperature

Atom	Site	Occupancy	x	y	z	U_{iso} / Å^2	BVS
Mg	4*a*	1	0	0	0	0.0066(3)	2.11
P	8*f*	1	0.3271(1)	0.1257(1)	0.8129(1)	0.0039(2)	5.01
O(1)	4*e*	1	0.5	0.0325(2)	0.75	0.0062(2)	2.09
O(2)	8*f*	1	0.2406(1)	-0.0099(1)	0.8904(9)	0.0074(2)	1.77
O(3)	8*f*	1	0.1724(1)	0.8271(1)	0.1667(1)	0.0068(2)	2.07
O(4)	8*f*	1	0.0932(1)	0.2232(1)	0.1038(1)	0.0094(2)	1.92
H	8*f*	1	0.3089(3)	0.2062(2)	0.3652(2)	0.0192(4)	0.73

Space group *C*2/*c*; a = 6.9041(1) Å, b = 7.7394(1) Å, c = 9.2352(2) Å and β = 101.582(1)°. Figures of merit: R_{wp} = 0.79%, R_p = 1.02%, χ^2 = 3.190

Table 3.5 - Selected bond lengths (Å) and angles (°) for β-$MgH_2P_2O_7$

Mg-O2	2.0875(9)	**O2-Mg-O3**	86.21(4)
Mg-O3	2.2004(9)	**O2-Mg-O4**	92.10(4)
Mg-O4	1.9833(9)	**O3-Mg-O4**	86.00(4)
P-O1	1.600(1)	**O1-P-O2**	105.77(8)
P-O2	1.487(1)	**O1-P-O3**	102.61(6)
P-O3	1.588(1)	**O1-P-O4**	110.67(8)
P-O4	1.477(1)	**O2-P-O3**	108.95(8)
H-O3	0.997(2)	**O2-P-O4**	118.42(8)
P-O3_H	111.3(1)	**O3-P-O4**	109.23(8)

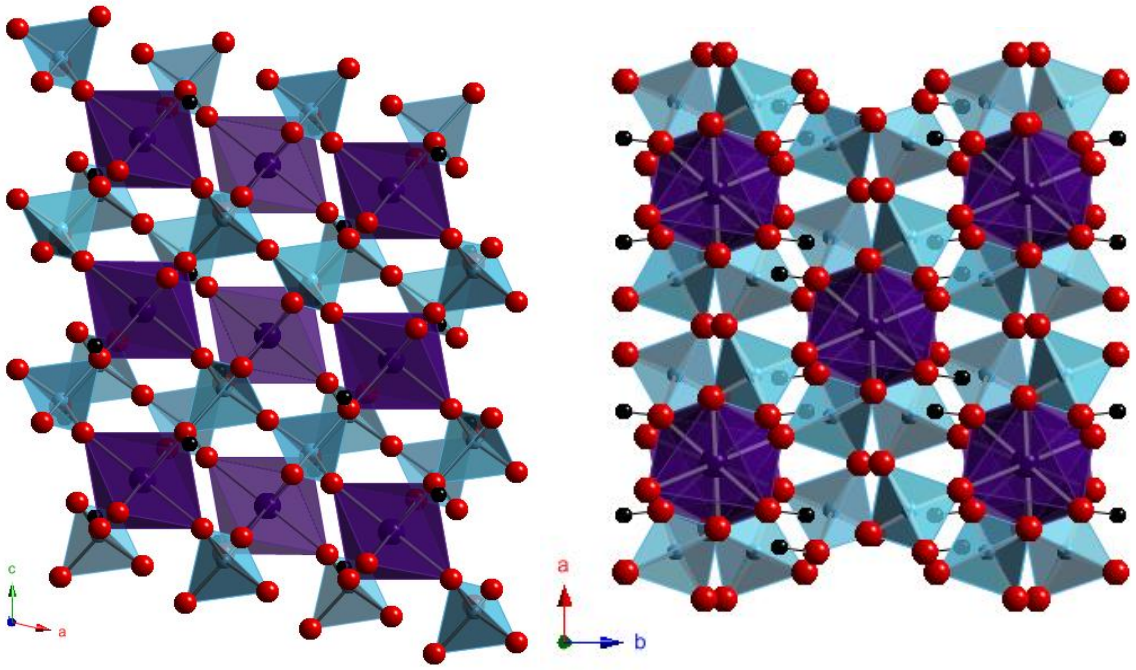

Figure 3.9 - Structure of β-$MgH_2P_2O_7$ in the *ac* and *ab* planes, where the MgO_6 octahedra are purple and the PO_4 tetrahedra are blue, protons are black spheres

The structure consists of layers of isolated MgO_6 octahedra, interconnected by corner-sharing pyrophosphate units. These layers form in the *ab* plane and stack along *c*. This is in contrast to α-$MgH_2P_2O_7$ where the MgO_6 octahedra form edge-sharing chains. Protons are bound to an oxygen which bridges the magnesium octahedra and a phosphate group. This leads to a relatively long Mg–O bond length of 2.2004(9) Å and a somewhat long P–O bond length of 1.588(1) Å (see figure 3.10).

The other Mg–O bonds are of similar lengths, within 5% of each other, and within 10% of the longest Mg–O bond. The longest P–O bond is 1.600(1) Å which is the bond to the bridging oxygen in the pyrophosphate unit, a similar length to the P–O(3)H, the remaining two P–O bonds are within 10% of the longest bond.

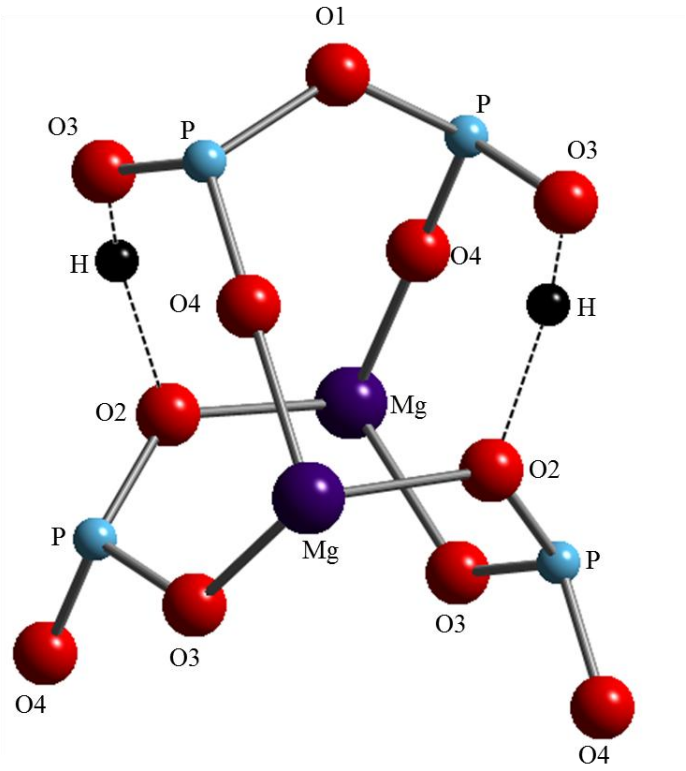

Figure 3.10 - Ball and stick model of β-$MgH_2P_2O_7$ showing the hydrogen bonding network

Bond valence sum calculations indicate that Mg is slightly over bonded, with a calculated valence of +2.11 v.u.. The BVS for P is calculated as +5.01 v.u. which is the expected value. The Global Instability Index value calculated for β-$MgH_2P_2O_7$ is 0.15 v.u. which implies that the structure is strained, compared to the value calculated for α-$MgH_2P_2O_7$ of 0.059 v.u, which is much lower. The ability of Mg^{2+} to form both polymorphic structures of $MH_2P_2O_7$ will be discussed further in section 3.3.3.

3.3.2.2 ^{31}P MAS-NMR

MAS-NMR was used once again to confirm the presence of one distinct P environment. Using the structural model, a simulated ^{31}P spectrum was produced and compared to the experimental data, and this is shown in figure 3.11. The experimental spectrum fits very well with the simulated data, indicating one P environment. Upon closer inspection, the peak appears to be split. This may signify a second environment, which does not fit with the structural model. However, NMR probes the local structure, whereas Rietveld refinement of NPD data looks at the average structure of a material, so whilst the local structure may indicate two slightly different P environments, on an average view, as provided by diffraction, only one P environment is observed.

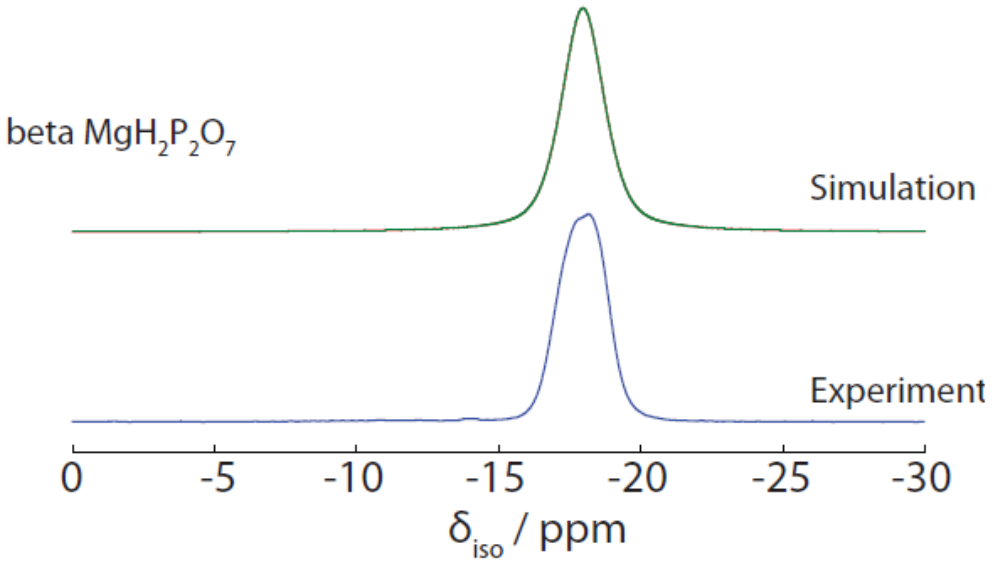

Figure 3.11 – ^{31}P Cross-polarisation spectra of β-$MgH_2P_2O_7$ at 9.4 T (10kHz MAS)

3.3.2.3 Thermal Behaviour of β-$MgH_2P_2O_7$

Variable temperature XRD was used to confirm the decomposition pathway. A sample was heated in an MRI heating stage in an alumina sample holder, and diffraction patterns were taken at approximately 50°C intervals from 50 to 650°C. A stack plot is shown in figure 3.12.

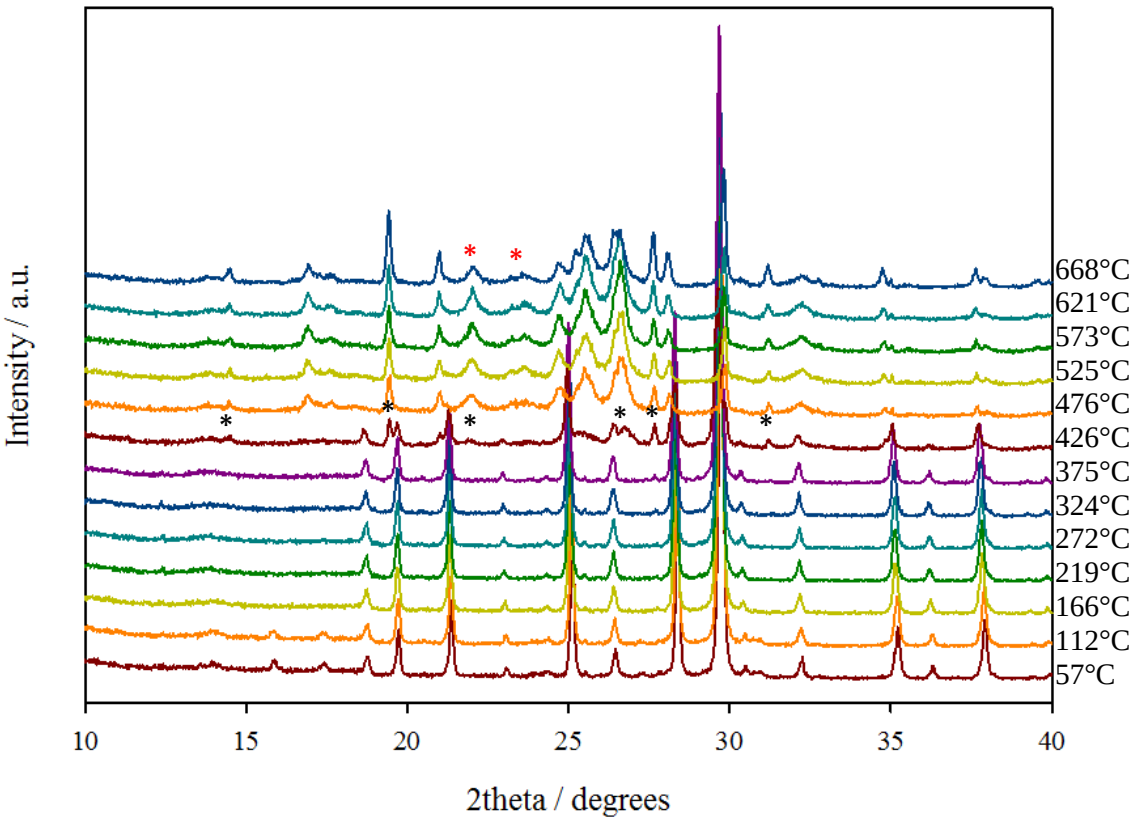

Figure 3. 12 – Variable Temperature-XRD stack plot of β-$MgH_2P_2O_7$. Black asterisks indicate the peaks belonging to $Mg_2P_4O_{12}$ at 426°C and red asterisks indicates the peaks that can be attributed to the Al_2O_3 sample holder

The structure remains stable until approximately 426°C where condensation begins to occur and peaks belonging to $Mg_2P_4O_{12}$ begin to appear. By 476°C, β-$MgH_2P_2O_7$ has fully condensed to $Mg_2P_4O_{12}$. The peaks indicated by the red asterisks do not belong to either phase, but they can be matched to alumina on the JCPDS

database,[17] which originate from the alumina sample holder. The decomposition temperature for the condensation observed in the VT-XRD matches closely with the temperature observed in the TGA-MS plot, which means the condensation reaction is much faster in β-$MgH_2P_2O_7$ compared to α-$MgH_2P_2O_7$.

3.3.3 Polymorphism in $MgH_2P_2O_7$

This study has shown that $M^{II}H_2P_2O_7$ exists as at least two structural polymorphs; the alpha polymorph, also adopted by Fe,[16] Ni,[8] and Co;[8] and the beta polymorph also adopted by Ca.[20] It is interesting to note that magnesium is able to adopt both structures, through the use of different reaction temperatures and the use of seed crystals. The initial synthesis of β-$MgH_2P_2O_7$ used a reaction temperature of 250°C and produced a single phase product. However, subsequent syntheses were unable to produce β-$MgH_2P_2O_7$ as a single phase. Addition of a small amount of $CaH_2P_2O_7$ (~1 mg) to the reaction melt at 180°C resulted in a mixture of both alpha and beta polymorphs. Use of a higher reaction temperature (>200°C) produces single phase β-$MgH_2P_2O_7$.

Magnesium's ability to form both structural polymorphs may be linked to cation size. The metal cations that form the alpha polymorph and their ionic radii are shown in table 3.6.

Table 3.6 – Metal cation ionic radii and polymorph formation

Cation	Ionic Radii (pm) [21]	Polymorph
Ca^{2+}	100	β
Mn^{2+}	83 (hs)	β
Fe^{2+}	78 (hs)[16]	α
Co^{2+}	74.5 (hs)[8]	α
Mg^{2+}	72	α & β
Ni^{2+}	69	α

The cations that form the alpha polymorph are all similar sizes, and smaller than those that form the beta polymorph. The dense arrangement of the MO_6 octahedra in the alpha polymorph may only accommodate small cations. Higher reaction temperatures and the presence of a larger cation make the formation of the beta polymorph more favourable, resulting in a single phase. $MnH_2P_2O_7$ (see chapter 4) also adopts the beta structure. The ionic radius of Mn^{2+} is 83 pm (high spin), so the ideal cation size for the MO_6 arrangement in the alpha polymorph must be below 80 pm. Seeding the reaction with a small amount of $CaH_2P_2O_7$ and increasing the reaction temperature by 20°C produces β-$MgH_2P_2O_7$ exclusively, however this leads to a strained structure as shown by a GII value of 0.15 v.u. compared to α-$MgH_2P_2O_7$. The ability for a smaller cation like Mg^{2+} to be able to form both polymorphs via higher reaction temperatures and with crystal seeding may mean that there is potential for synthesising the beta polymorph of the Ni, Co and Fe acid pyrophosphate, or mixed metal systems, which may have interesting magnetic behaviour.

3.3.4 Li-Doped $MgH_2P_2O_7$

Yang *et al*.[22] also investigated lithium incorporation in $NiH_2P_2O_7$/$CoH_2P_2O_7$ to explore the effect on magnetic properties, forming $LiM_2H_3(P_2O_7)_2$ where M = Ni or Co. Magnetic properties are not applicable to α-$MgH_2P_2O_7$, but its channelled nature could provide potential for Li ion conduction. This was investigated through the attempted replacement of protons for lithium ions in the structure. Initial ion exchange via aqueous lithium chloride solution was unsuccessful due to the dissolution of α-$MgH_2P_2O_7$. Repeated ion exchange using an ethanol based LiCl

solution was also unsuccessful, with the diffraction pattern of the precipitate identical to that of α-$MgH_2P_2O_7$. Ion exchange was also attempted with β-$MgH_2P_2O_7$, but also without success.

Attempts to directly synthesise a mixed Mg-Li pyrophosphate were carried out using various Mg:Li:P ratios and reaction times and temperatures. A ratio of 1:1:4 and a reaction time of 48 hours at 180°C yielded the most crystalline product. Figure 3.13 compares the diffraction pattern of the Li-doped magnesium pyrophosphate to that of α-$MgH_2P_2O_7$. The diffraction patterns are very similar, but with a few significant differences, including changes in intensity, apparent splitting of peaks and the appearance of new peaks. A noticeable difference is the broadness of the peaks at 25.3 and 26.1° was also evident and may indicate overlapping peaks, and perhaps multiple phases.

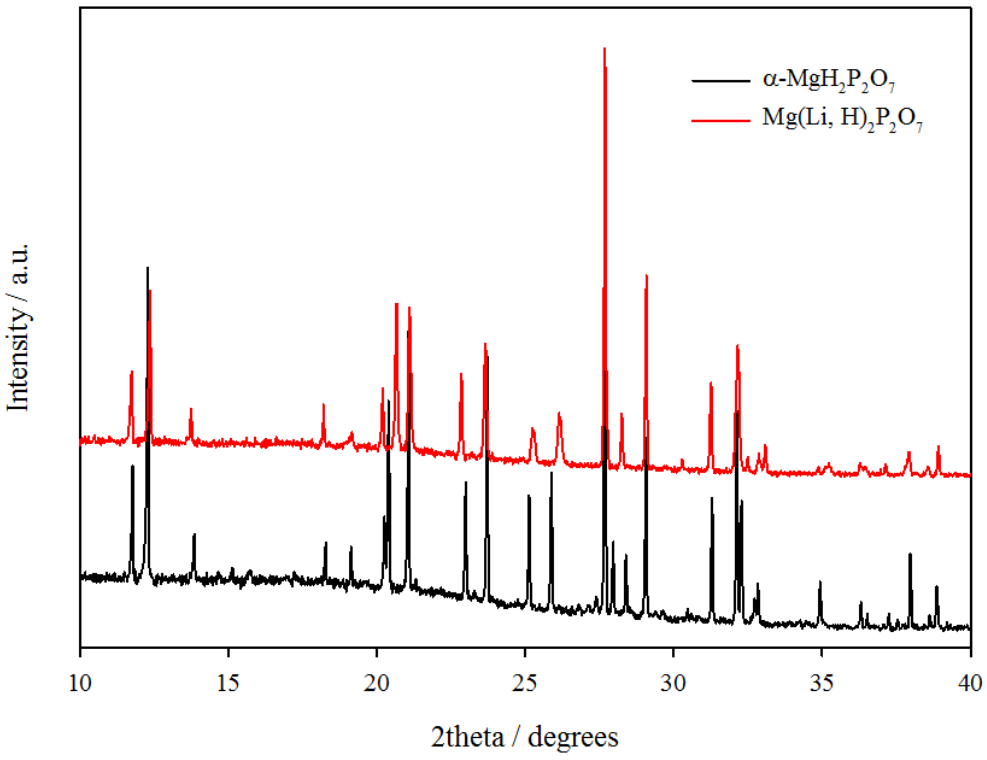

Figure 3.13 - PXRD patterns of α-$MgH_2P_2O_7$ and Li-doped $MgH_2P_2O_7$

Figure 3.13 continued

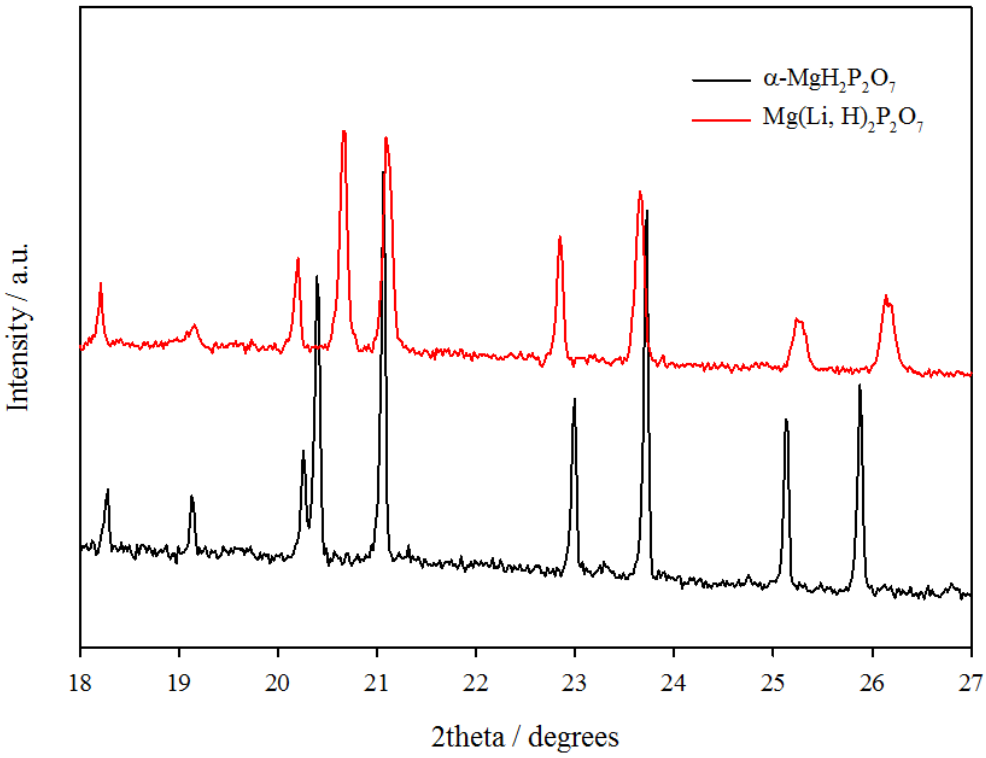

The pattern was then indexed using Crysfire and the suggested unit cells are shown in table 3.7. The cell with the highest figure of merit indexed all 20 inputted 2 theta positions, and is similar in size to the cell of α-$MgH_2P_2O_7$.

Table 3.7 - Unit cells calculated using Crysfire[18] for Li-doped $MgH_2P_2O_7$

I20	Merit	Symmetry	*a* (Å)	*b* (Å)	*c* (Å)	*α* (°)	*β* (°)	*γ* (°)	Volume (Å³)
20	15	Monoclinic	9.651	12.8571	8.9519	90	106.501	90	1065.038
19	7	Monoclinic	19.7113	6.7356	14.6547	90	99.523	90	1918.871
19	6	Monoclinic	10.3256	11.1483	7.291	90	100.589	90	824.995
18	6	Orthorhombic	21.0416	12.8823	9.7645	90	90	90	2646.798
17	8	Monoclinic	19.702	4.6831	14.6636	90	99.386	90	1334.845

The presence of lithium in the sample was confirmed by flame emission photometry (see appendix 2). Assuming a pure sample, the stoichiometry suggested was $MgLi_{0.9}H_{1.1}P_2O_7$.

3.3.4.1 Thermal Behaviour of Li-Doped $MgH_2P_2O_7$

TGA-MS data were collected and compared to the data collected for α-$MgH_2P_2O_7$. If half of the protons had been replaced by Li then we would expect to find a smaller mass loss related to water. Figure 3.14 shows the TGA-MS plot for the Li-doped pyrophosphate. The plot is similar to that of α-$MgH_2P_2O_7$, with a small 1% mass loss consistent with the loss of surface water between 100-150°C. A large mass loss of ~8% at 400°C coinciding with a broad endothermic peak in DTA and a broad peak in the mass spectrum signal for mass 18. The mass spectrum peak appears to have 2 shoulders, which may indicate 3 separate water loss events. The mass loss is comparable to those observed for both α & β-$MgH_2P_2O_7$, which is unusual considering the stoichiometry suggested by flame photometry. This could indicate that there is uncertainty in the stoichiometry calculated.

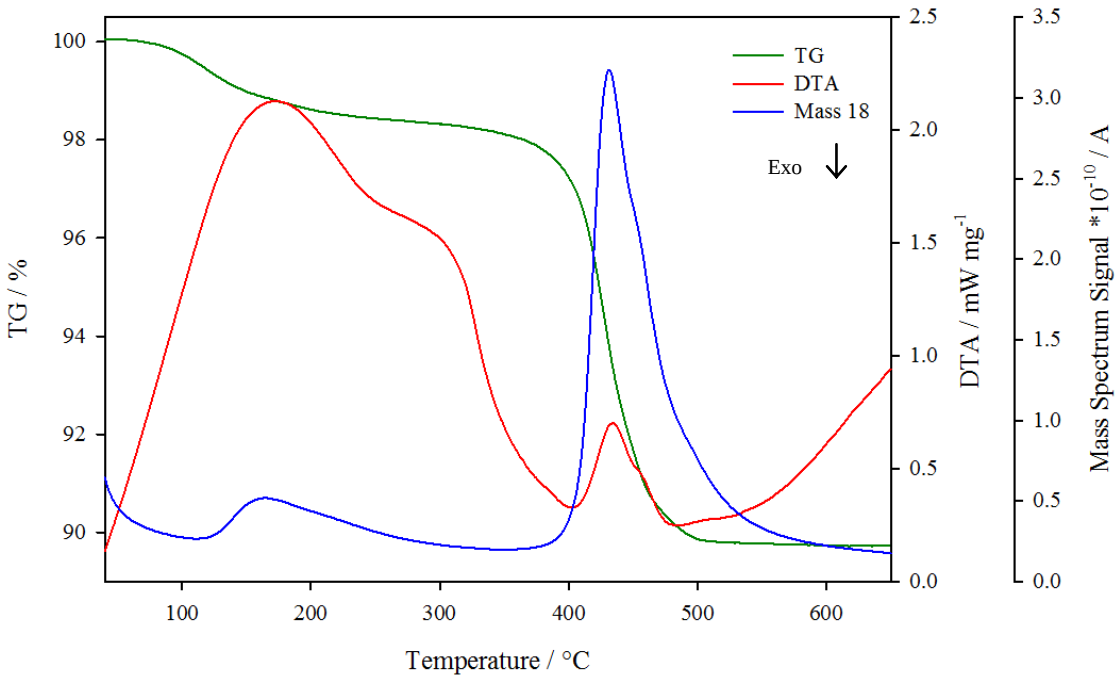

Figure 3.14 - TGA-MS plot for Li-doped $MgH_2P_2O_7$

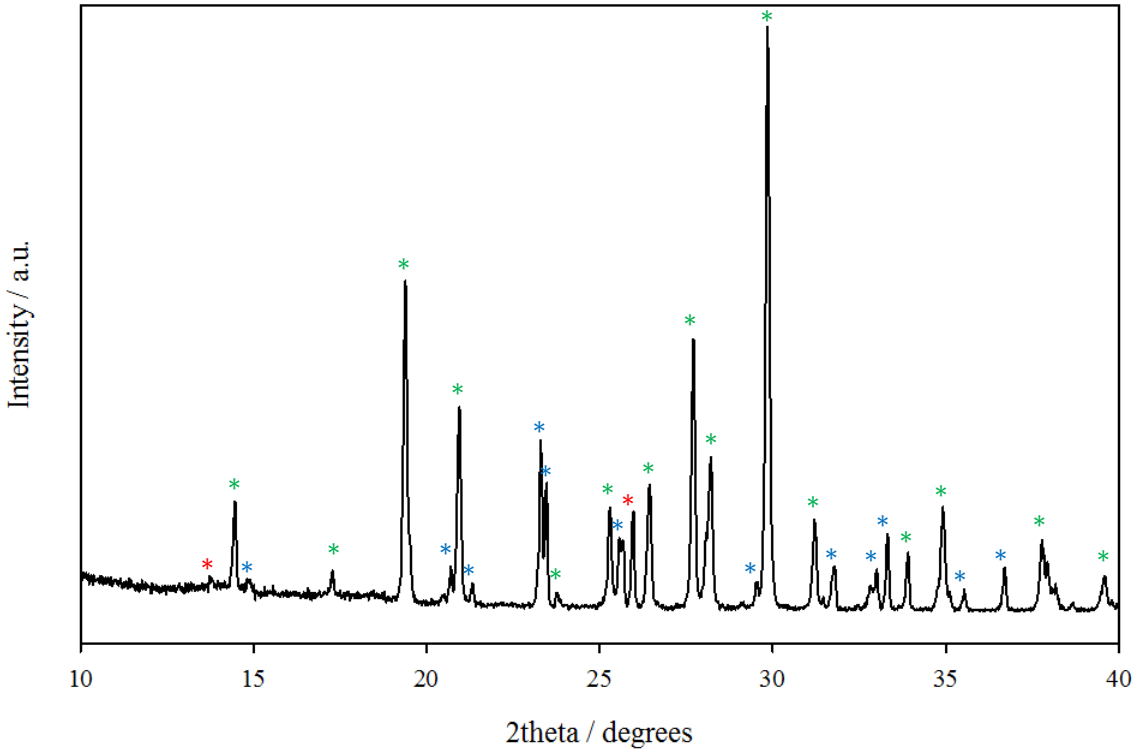

Figure 3.15 - PXRD pattern of heat treated Li-doped $MgH_2P_2O_7$, $Mg_2P_4O_{12}$ peaks are indicated by green asterisk, unknown peaks are indicated by red asterisks, $LiMg(PO_3)_3$ peaks are indicted by blue asterisks

Unlike with the pure $MgH_2P_2O_7$ phases, the PXRD pattern of the sample after heat treatment shows multiple phases (shown in figure 3.15). A search on the JCPDS database matched two phases, $Mg_2P_4O_{12}$ and $LiMg(PO_3)_3$,[23] further confirming the presence of Li; additional peaks were observed but could not be matched to a known phase on the database.

Variable temperature XRD was used to confirm the decomposition pathway. A sample was heated in an MRI heating stage in an alumina sample holder, and diffraction patterns were taken at approximately 50°C intervals from 50 to 650°C. A stack plot is shown in figure 3.16.

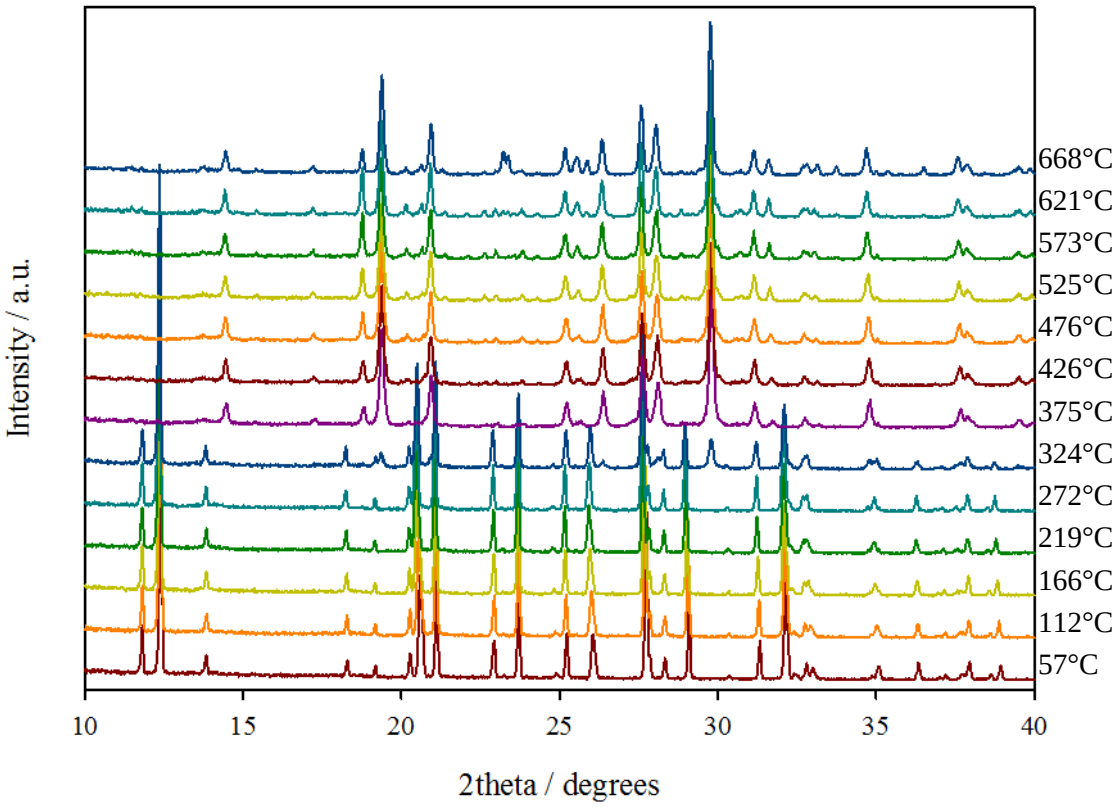

Figure 3.16 – Variable Temperature-XRD stack plot for Li-doped $MgH_2P_2O_7$

The structure remains stable and unchanged up to approximately 272°C; peaks belonging to $Mg_2P_4O_{12}$ begin to appear at 324°C and the structure appears to be fully condensed by 375°C. This data matches quite closely with the TGA-MS data and decomposition temperature of α-$MgH_2P_2O_7$. The peaks belonging to the unknown phase and $LiMg(PO_3)_3$ do not appear until 621°C which may indicate that the Li containing phases crystallises from an amorphous component which may form during the condensation reaction.

3.3.4.2 Crystal Structure of Li-Doped $MgH_2P_2O_7$

The crystal structure of Li-doped $MgH_2P_2O_7$ was determined via Rietveld refinement of neutron powder diffraction data, using α-$MgH_2P_2O_7$ as a structural

model, due to the similarity of their XRD patterns. The sample was not deuterated, and therefore the background was high, but a good fit was obtained, converging at low R_{wp} value of 0.55% and χ^2 value of 5.917. The refinement, shown in figure 3.17, used α-$MgH_2P_2O_7$ as a model, and placing lithiums on proton positions. To stabilise the refinement, a global isotropic thermal parameter was used for each atom type. Occupancies of the proton/lithium sites were refined, giving a stoichiometry of $MgLi_{0.8}H_{1.2}P_2O_7$, in good agreement with the stoichiometry obtained by flame emission photometry (see section 3.3.3).

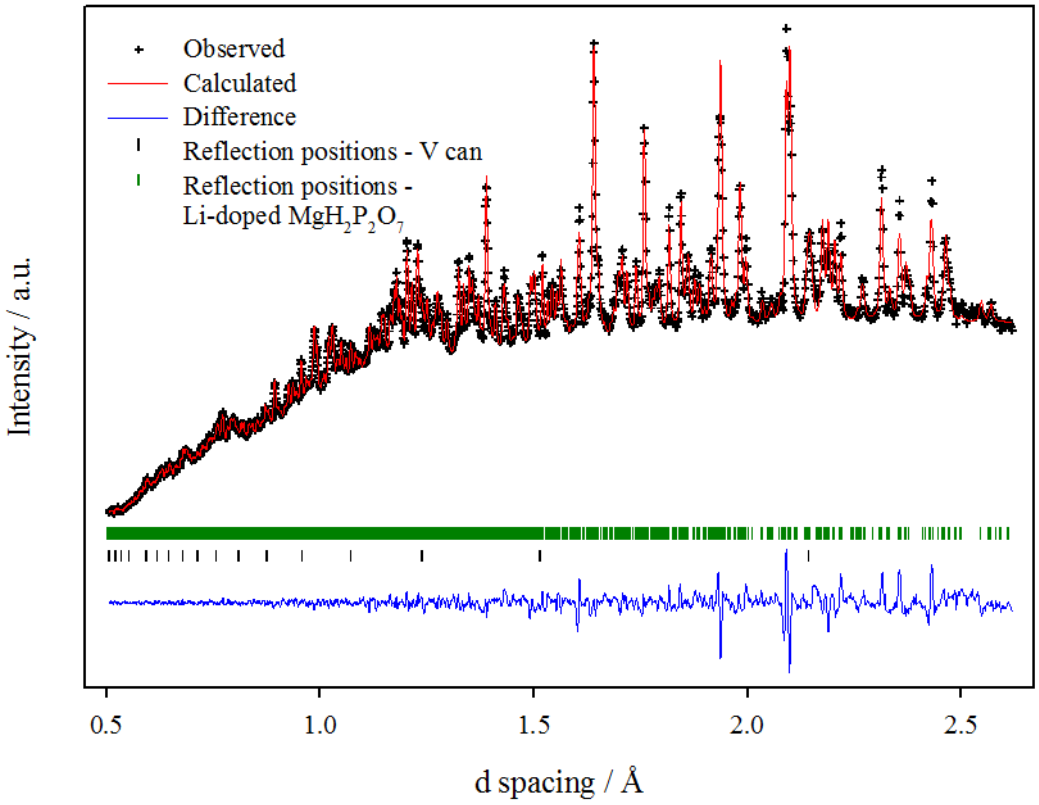

Figure 3.17 - Rietveld refinement plot of Li-doped $MgH_2P_2O_7$

There are some areas where there is a mismatch of intensity, particularly at higher d space. The refinement shows the structure adopts a monoclinic cell, space group $P2_1/c$ with lattice parameters; a = 8.9559(4) Å, b = 12.8281(5) Å, c = 9.6449(4)

and β = 106.626(2)°. An additional peak from the sample holder (vanadium can) was visible at 2.14 Å. Tables 3.8 & 3.9 show the refined structural parameters, and selected bond lengths and angles.

Table 3.8 - Refined structural parameters of $MgLi_{0.8}H_{1.2}P_2O_7$ at room temperature

Atom	Site	Occupancy	x	y	z	U_{iso} (Å^2)	BVS
Mg1	4*e*	1	0.2640(9)	0.2436(6)	0.2538(9)	0.0081(7)	2.19
Mg2	4*e*	1	0.246(1)	0.4034(3)	0.004(1)	0.0081	2.16
P1	4*e*	1	0.4893(8)	0.2895(6)	0.5637(8)	0.0043(4)	5.16
P2	4*e*	1	0.4733(8)	0.0442(6)	0.2843(7)	0.0043	4.64
P3	4*e*	1	-0.0031(8)	0.2126(6)	-0.0758(8)	0.0043	4.86
P4	4*e*	1	0.0365(8)	0.4530(6)	0.2246(7)	0.0043	5.23
O1	4*e*	1	0.1570(9)	0.3893(7)	0.179(1)	0.0129(2)	1.97
O2	4*e*	1	0.3483(9)	0.1090(6)	0.3261(9)	0.0129	2.03
O3	4*e*	1	0.4328(8)	0.3270(6)	0.4150(9)	0.0129	1.84
O4	4*e*	1	0.0500(8)	0.1851(6)	0.0880(8)	0.0129	1.39
O5	4*e*	1	0.3827(9)	0.2786(8)	0.1170(9)	0.0129	2.20
O6	4*e*	1	-0.0481(8)	0.3795(5)	0.3167(7)	0.0129	2.19
O7	4*e*	1	0.3802(8)	-0.0431(5)	0.1741(7)	0.0129	2.03
O8	4*e*	1	0.1015(8)	0.5561(6)	0.2878(6)	0.0129	2.12
O9	4*e*	1	0.1222(9)	0.2204(8)	0.3896(9)	0.0129	1.98
O10	4*e*	1	0.0946(8)	0.5159(5)	-0.1036(8)	0.0129	1.95
O11	4*e*	1	0.5194(7)	0.3907(5)	0.6554(7)	0.0129	2.11
O12	4*e*	1	0.3804(8)	0.5197(6)	0.1020(9)	0.0129	1.91
O13	4*e*	1	0.6603(8)	0.2378(6)	0.6139(8)	0.0129	1.90
O14	4*e*	1	-0.1640(9)	0.2636(6)	-0.0983(9)	0.0129	2.91
H1/Li1	4*e*	1/0	0.045(2)	0.604(1)	0.336(2)	0.033(1)	0.75
H2/Li2	4*e*	1/0	0.557(2)	0.414(1)	0.353(2)	0.033	0.98
H3/Li3	4*e*	0.30(5)/0.70(5)	0.212(2)	0.726(2)	0.056(2)	0.033	1.68
H4/Li4	4*e*	0.13(4)/0.87(4)	0.720(3)	0.255(1)	0.209(2)	0.033	0.88

Space group $P2_1/c$; a = 8.9559(4) Å, b = 12.8281(6) Å, c = 9.6449(5) Å and β = 106.626(2)°. Figure of merit: R_{wp} = 0.55%, R_p = 1.02%, χ^2 = 5.917

Table 3.9 - Selected bond lengths (Å) and angles (°) for $MgLi_{0.8}H_{1.2}P_2O_7$

Mg1-O1	2.13(1)	**Mg2-O1**	2.07(2)
Mg1-O2	1.93(1)	**Mg2-O2**	2.17(1)
Mg1-O3	2.12(1)	**Mg2-O5**	2.12(1)
Mg1-O4	2.25(1)	**Mg2-O9**	2.06(1)
Mg1-O5	1.97(1)	**Mg2-O10**	2.05(1)
Mg1-O9	2.09(1)	**Mg2-O12**	1.98(1)
O1-Mg1-O2	176.0(7)	**O1-Mg2-O2**	171(3)
O1-Mg1-O3	87.9(4)	**O1-Mg2-O5**	79.3(4)
O1-Mg1-O4	80.9(4)	**O1-Mg2-O9**	95.6(5)
O1-Mg1-O5	81.3(5)	**O1-Mg2-O10**	97.0(5)
O1-Mg1-O9	92.5(5)	**O1-Mg2-O12**	90.0(4)
O2-Mg1-O3	93.6(4)	**O2-Mg2-O5**	92.2(4)
O2-Mg1-O4	97.1(4)	**O2-Mg2-O9**	78.8(4)
O2-Mg1-O5	102.5(5)	**O2-Mg2-O10**	91.1(5)
O2-Mg1-O9	83.8(5)	**O2-Mg2-O12**	95.4(5)
O3-Mg1-O4	167.0(4)	**O5-Mg2-O9**	80.6(2)
O3-Mg1-O5	88.2(4)	**O5-Mg2-O10**	174.4(6)
O3-Mg1-O9	92.6(4)	**O5-Mg2-O12**	98.0(5)
O4-Mg1-O5	96.5(4)	**O9-Mg2-O10**	95.6(4)
O4-Mg1-O9	81.4(4)	**O9-Mg2-O12**	173.9(6)
O5-Mg1-O9	173.7(7)	**O10-Mg2-O12**	86.2(3)
P1-O3	1.46(1)	**P2-O2**	1.54(1)
P1-O5	1.49(1)	**P2-O7**	1.60(1)
P1-O11	1.55(1)	**P2-O11**	1.65(1)
P1-O13	1.61(1)	**P2-O12**	1.48(1)
O3-P1-O5	117.1(7)	**O2-P2-O7**	105.8(5)
O3-P1-O11	103.8(6)	**O2-P2-O11**	106.4(5)
O3-P1-O13	117.6(6)	**O2-P2-O12**	118.5(6)
O5-P1-O11	108.5(6)	**O7-P2-O11**	92.8(5)
O5-P1-O13	107.6(6)	**O7-P2-O12**	121.6(6)
O11-P1-O13	100.3(5)	**O11-P2-O12**	107.9(5)
P3-O4	1.56(1)	**P4-O1**	1.52(1)
P3-O6	1.55(1)	**P4-O6**	1.62(1)
P3-O9	1.53(1)	**P4-O8**	1.50(1)
P3-O14	1.54(1)	**P4-O10**	1.45(1)
O4-P3-O6	116.9(6)	**O1-P4-O6**	109.2(6)
O4-P3-O9	108.7(5)	**O1-P4-O8**	111.5(6)
O4-P3-O14	104.0(6)	**O1-P4-O10**	113.1(6)
O6-P3-O9	110.5(6)	**O6-P4-O8**	118.5(6)
O6-P3-O14	100.2(6)	**O6-P4-O10**	101.7(5)
O9-P3-O14	116.6(6)	**O8-P4-O10**	102.4(6)
P1-O11-P2	144.6(5)	**P3-O6-P4**	137.5(6)
H1/Li1-O8	0.99(4)	**H3/Li3-O14**	0.69(2)
H2/Li2-O7	0.89(2)	**H4/Li4-O13**	0.93(2)

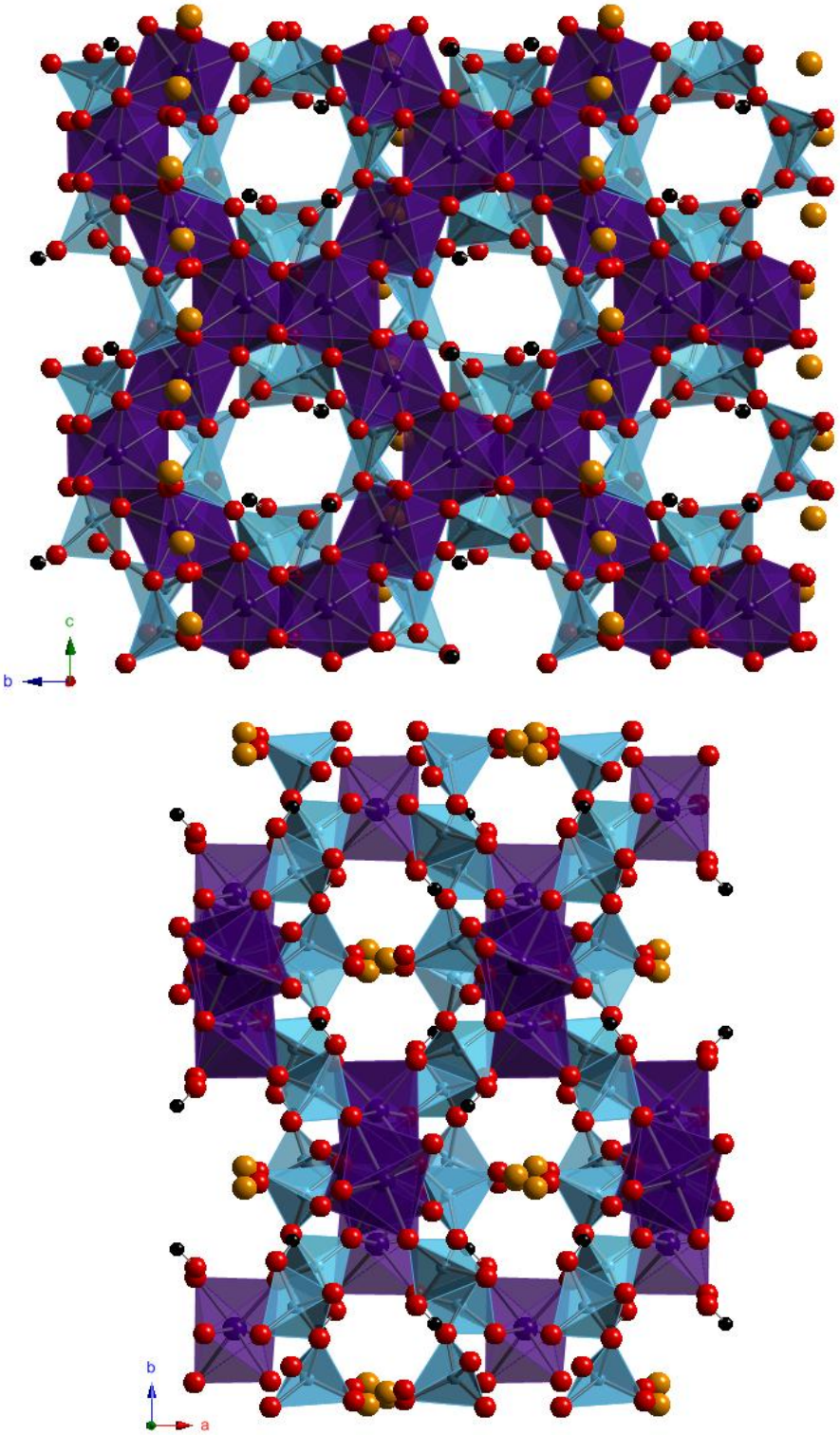

Figure 3.18 - Structure of $MgLi_{0.8}H_{1.2}P_2O_7$ as viewed in the *ab* and *bc* planes. MgO_6 octahedra are purple, PO_4 tetrahedra are blue. For clarity, H/Li sites 1 & 2 are shown as black spheres (protons) and H/Li sites 3 & 4 are shown a orange spheres (lithium)

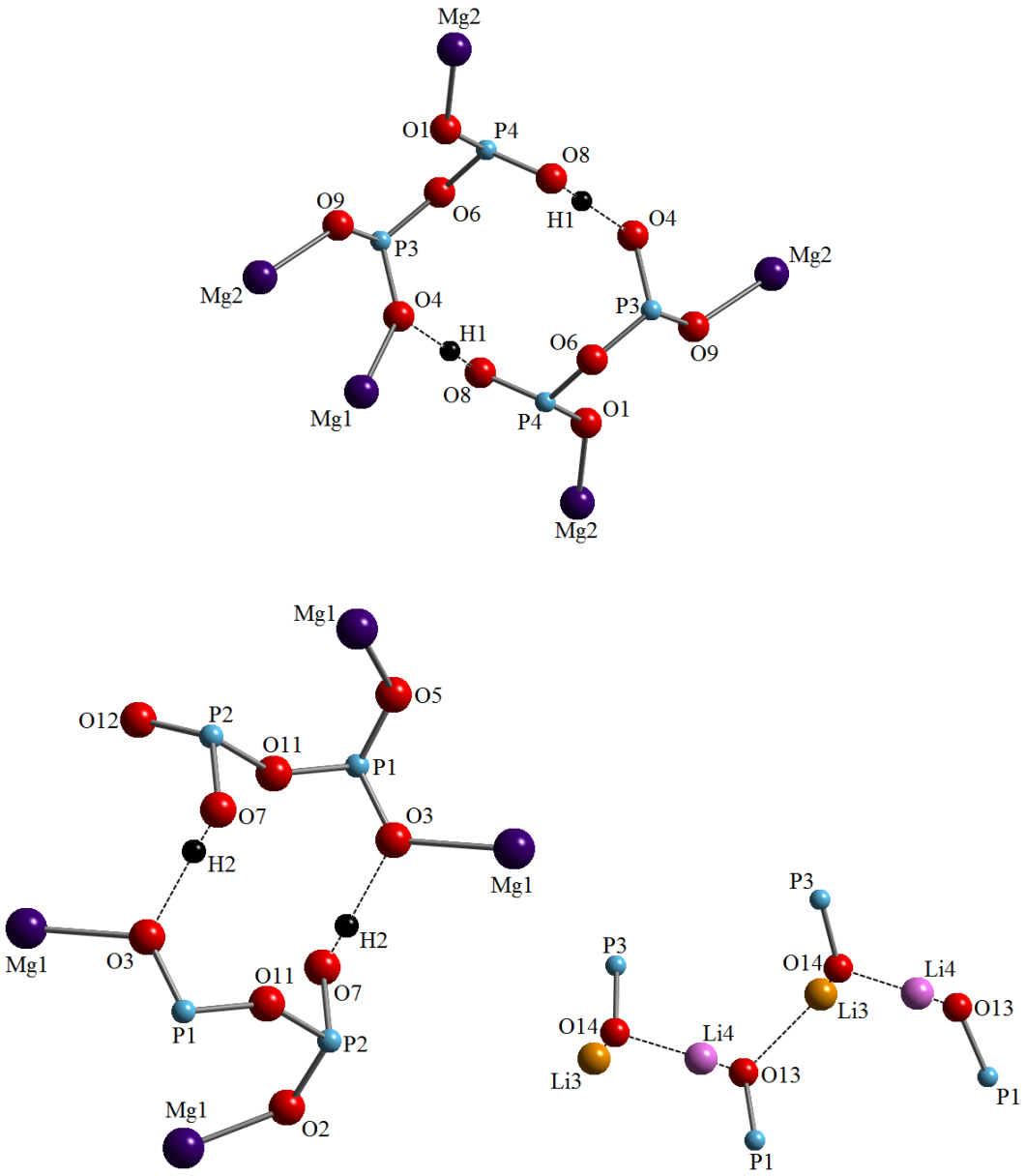

Figure 3.19 - Ball and stick models displaying the hydrogen bonding network within $MgLi_{0.8}H_{1.2}P_2O_7$

The structure is very similar to that of α-$MgH_2P_2O_7$, which is described in section 3.3.1.2. The structure consists of zigzag edge-sharing MgO_6 chains running along the *c* axis, which stack along *a*, with PO_4 tetrahedra interconnecting these chains via corner-sharing oxygens.

As the PXRD pattern for the Li-doped $MgH_2P_2O_7$ closely resembled that of α-$MgH_2P_2O_7$, it was unlikely that Li would be replacing either Mg or P in the structure due to their significant difference in X-ray scattering factors, therefore the mostly like site for Li to occupy would be the proton sites as they both scatter X-rays poorly.

Lithium-proton occupancies were refined for all 4 proton sites. Occupancies for H1/Li1 and H2/Li2 were refined and no lithium was found on either site. This may be due to the extra stabilisation the protons in these sites receive by forming a hydrogen bond with the nearest oxygen neighbour (see figure 3.19). For both, this is an oxygen bridging the Mg octahedra and the phosphate tetrahedra. H1 forms a hydrogen bond with O4 with a length of 1.64(2) Å, and H2 forms a hydrogen bond with O3, with a length of 1.79(2) Å. This leads to slightly longer Mg1–O3/4 bonds.

Lithium occupancies were refined for H3 and H4 sites, giving occupancies of 0.70(5) for H3 and 0.87(4) for H4. These sites lie within the channel along *c*, which is likely to be more accommodating to a larger cation. The bond length for H3/Li3 is 0.69(2) Å, which is shorter than for an O–H bond, and much shorter than expected for a Li–O bond. The bond length for H/Li4 is 0.93(2) Å, which is similar to the O–H bond lengths we see in both the α and β polymorphs of $MgH_2P_2O_7$. Clearly these unusually short bond lengths cast doubt on the reliability of these Li positions in this refinement. This is not unexpected given that Li has a small neutron scattering length

of -1.90,[24] as compared to H scattering length of -3.79,[24] making Li more difficult to locate.

BVS calculations indicate that both Mg 1 & 2 are slightly overbonded, with calculated valences of +2.19 and +2.16, with an average BVS of +2.18; P 1 & 4 appear to be over bonded with calculated valences of +5.16 and +5.23 whereas P 2 & 3 are underbonded, with calculated valences of +4.64 and +4.86 respectively leading to an overall average valence of +4.97 and so is close to the predicted value.

Although the fit using the α-$MgH_2P_2O_7$ model is good, there are some intensity differences especially at higher TOF. This promoted a search for another structural model and $LiNi_2H_2(P_2O_7)_2$[22] was found. A Rietveld refinement based on this model was carried out, which converged at a low R_{wp} of 0.63% and χ^2 of 7.836, shown in figure 3.20. The refinement shows the structure adopts a monoclinic cell, space group $C2/c$ with lattice parameters; a = 11.1253(6) Å, b = 12.8288(7) Å, c = 8.9555(5) and β = 123.840(1)°.

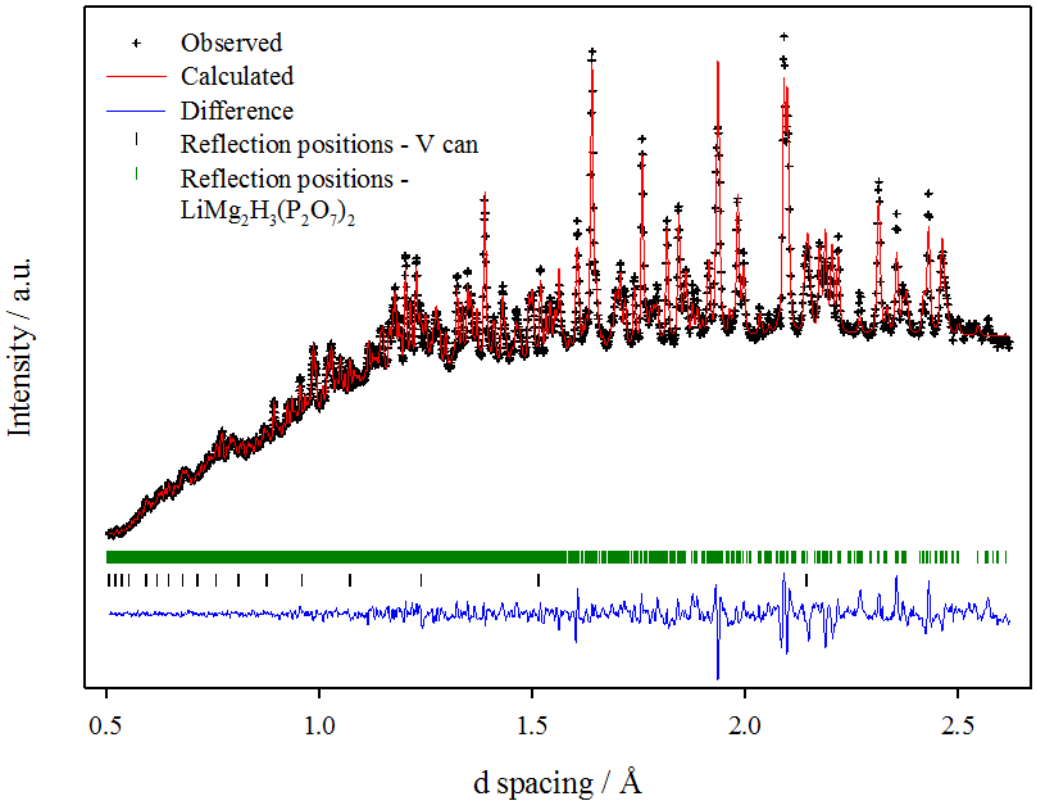

Figure 3.20 - Rietveld refinement of $LiMg_2H_3(P_2O_7)_2$

Visually, the fit is improved with the second structural model. Once again there are still issues with intensity mismatches; however the fit above 2 Å is better compared to the initial refinement based upon α-$MgH_2P_2O_7$. Tables 3.10 & 3.11 show the refined structural parameters, and selected bond lengths and angles.

Table 3.10 - Refined structural parameters of $LiMg_2H_3(P_2O_7)_2$

Atom	Site	Occupancy	x	y	z	U_{iso} (Å^2)	BVS
Mg1	4*e*	1	0	0.4054(3)	0.25	0.0032(7)	2.17
Mg2	4*d*	1	0.25	0.25	0.5	0.0066(9)	2.14
P1	8*f*	1	0.2195(4)	0.4533(3)	0.6875(4)	0.0045(6)	5.08
P2	8*f*	1	0.0705(3)	0.2139(3)	0.0748(4)	0.0063(6)	5.11
O1	8*f*	1	0.1777(3)	0.3894(3)	0.5243(4)	0.0098(6)	2.06
O2	8*f*	1	0.3074(4)	0.5474(3)	0.6944(6)	0.0269(9)	2.06
O3	8*f*	1	0.1136(3)	0.2799(2)	0.2325(4)	0.0070(5)	2.18
O4	8*f*	1	-0.1015(4)	0.5169(3)	0.2914(5)	0.0153(7)	1.92
O5	8*f*	1	0.0848(4)	0.1772(3)	0.5261(5)	0.0158(7)	1.75
O6	8*f*	1	0.1033(4)	0.2604(3)	-0.0570(5)	0.0178(8)	1.64
O7	8*f*	1	0.3290(4)	0.3858(3)	0.8644(5)	0.0185(8)	2.12
Li1	4*e*	1	0	0.361(2)	-0.25	0.080(9)	0.94
H1	8*f*	1	0.3457(8)	0.5963(6)	0.791(1)	0.040(2)	0.92
H2	8*f*	0.5	0.061(3)	0.298(2)	0.092(4)	0.106(9)	0.76

Space group *C*2/*c*; a = 11.1253(6) Å, b = 12.8288(7) Å, c = 8.9555(5) Å and β = 123.840(1) °. Figure of merit: R_{wp} = 0.63%, R_p = 1.17%, χ^2 = 7.836

Table 3.11 - Selected bond lengths (Å) and angles (°) for $LiMg_2H_3(P_2O_7)_2$

Mg1-O1	2.140(3)	**Mg2-O1**	2.022(3)
Mg1-O3	2.105(4)	**Mg2-O3**	2.035(3)
Mg1-O4	1.981(5)	**Mg2-O5**	2.188(3)
O1-Mg1-O1	169.0(3)	**O1-Mg2-O1**	180
O1-Mg1-O3	78.7(2)	**O1-Mg2-O3**	83.1(1)
O1-Mg1-O3	92.9(3)	**O1-Mg2-O3**	96.9(1)
O1-Mg1-O4	96.5(2)	**O1-Mg2-O5**	87.6(1)
O1-Mg1-O4	91.5(5)	**O1-Mg2-O5**	92.4(1)
O3-Mg1-O3	80.3(2)	**O3-Mg2-O3**	180
O3-Mg1-O4	173.8(2)	**O3-Mg2-O5**	95.0(1)
O3-Mg1-O4	96.3(1)	**O3-Mg2-O5**	85.0(1)
O4-Mg1-O4	87.5(2)	**O5-Mg2-O5**	180
P1-O1	1.506(5)	**P2-O3**	1.479(4)
P1-O2	1.533(5)	**P2-O5**	1.511(4)
P1-O4	1.477(5)	**P2-O6**	1.536(5)
P1-O7	1.611(5)	**P2-O7**	1.582(5)
O1-P1-O2	108.2(3)	**O3-P1-O5**	113.9(3)
O1-P1-O4	116.7(3)	**O3-P1-O6**	114.9(3)
O1-P1-O7	108.5(2)	**O3-P1-O7**	110.0(2)
O2-P1-O4	112.6(3)	**O5-P1-O6**	110.1(3)
O2-P1-O7	105.5(3)	**O5-P1-O7**	107.9(3)
O4-P1-O7	104.7(3)	**O6-P1-O7**	98.8(3)
H1-O2	0.96(1)	**Li1-O4**	2.08(2)
H2-O3	1.07(3)	**Li1-O6**	1.94(2)

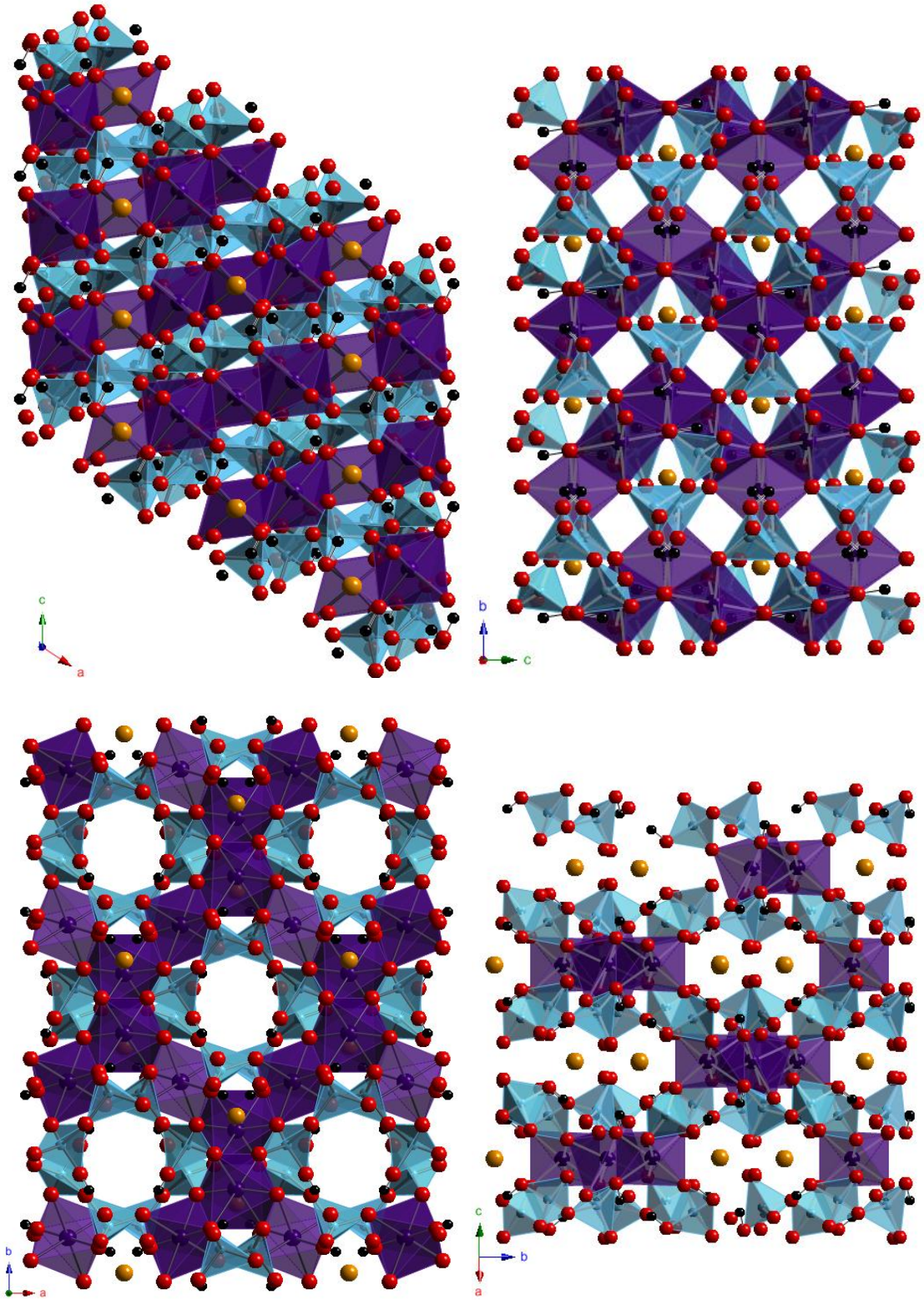

Figure 3.21 - Structure of $LiMg_2H_3(P_2O_7)_2$ as shown in the *ab*, *bc*, *ac* planes. MgO_6 octahedra are purple, PO_4 tetrahedra are blue. Protons are black spheres (protons) and lithiums are orange spheres

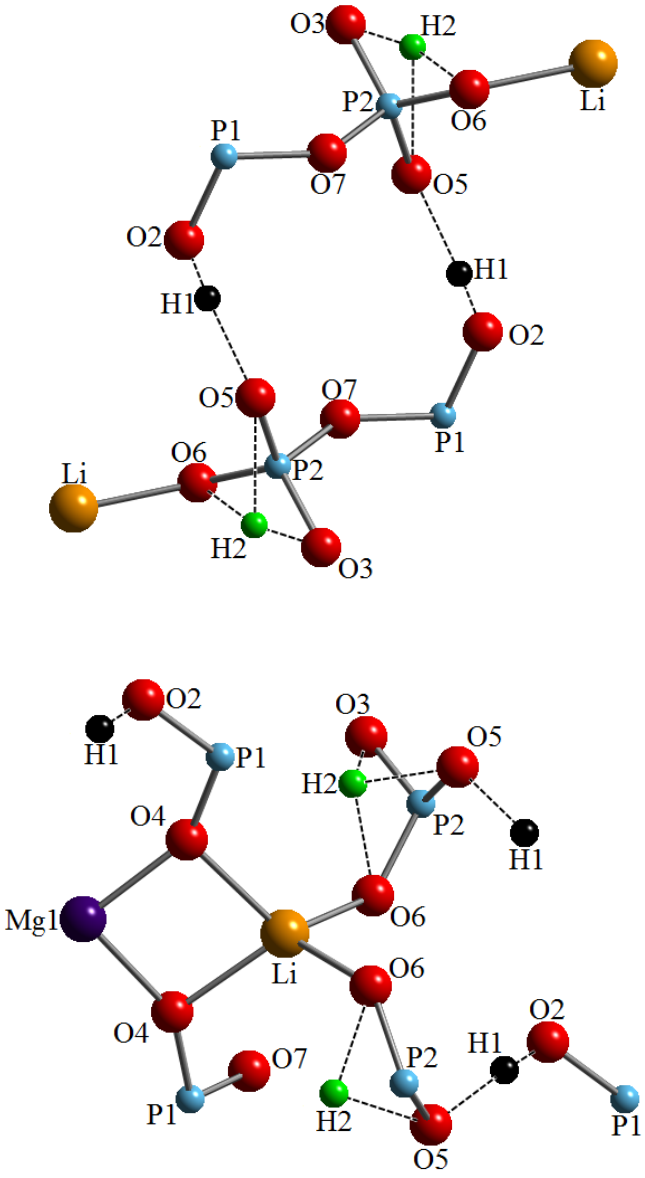

Figure 3.22 - Ball and stick model displaying the hydrogen bonding and Li environment in $LiMg_2H_3(P_2O_7)_2$

The structure (see figure 3.21) consists of zigzag chains of edge-sharing MgO_6 octahedra along the *a*-axis, which stack along the *b*-axis. The PO_4 units interconnect these chains via corner shared oxygens. Lithium is tetrahedrally coordinated, and resides in a two-fold axis. The Li-O bond lengths of 2.08(2) Å and 1.94(2) Å are more realistic compared to those in $MgLi_{0.8}H_{1.2}P_2O_7$. There are two proton sites; H2 is half

occupied, according to charge balance. H1 is located as a hydroxyl unit with O2, on P1. It is able to form a hydrogen bond of 1.714(8) Å with O5, a corner-shared oxygen bound to both Mg and P1 (see figure 3.22). H2 is bound to O3, and forms a hydrogen bond to of 1.69(3) Å to O6, the adjacent oxygen in the PO_4 unit, and a hydrogen bond of 2.02(3) Å to O5. O3 is also bound to Mg1, Mg2 and P2, which leads to a slightly longer O–H bond.

BVS calculations indicate that both Mg1 and Mg2 are marginally overbonded, with calculated valences of +2.17 and 2.14. P1 and P2 are also slightly overbonded with valences of +5.08 and +5.11.

Topologically, the two structures appear nearly identical. The symmetry has increased from $P2_1/c$ for $MgLi_{0.8}H_{1.2}P_2O_7$ to $C2/c$ for $LiMg_2H_3(P_2O_7)_2$. All atoms sit on general sites in the $P2_1/c$ structure, whereas Mg1, Mg2 and Li1 reside on special sites; Mg1 and Li1 reside on two fold axis and Mg2 resides on an inversion centre. The increase in symmetry also leads to few P and O sites, going from 4 unique P sites to 2, and from 14 individual O sites to 7. Viewing $MgLi_{0.8}H_{1.2}P_2O_7$ down the *a* axis, the structure looks very similar to that of $LiMg_2H_3(P_2O_7)_2$ as viewed down the *c* axis. Figure 3.23 shows the simulated PXRD patterns for each structural model. The patterns for each structural model are very similar in terms of peak position and peak intensity, although this does differ slightly between the models.

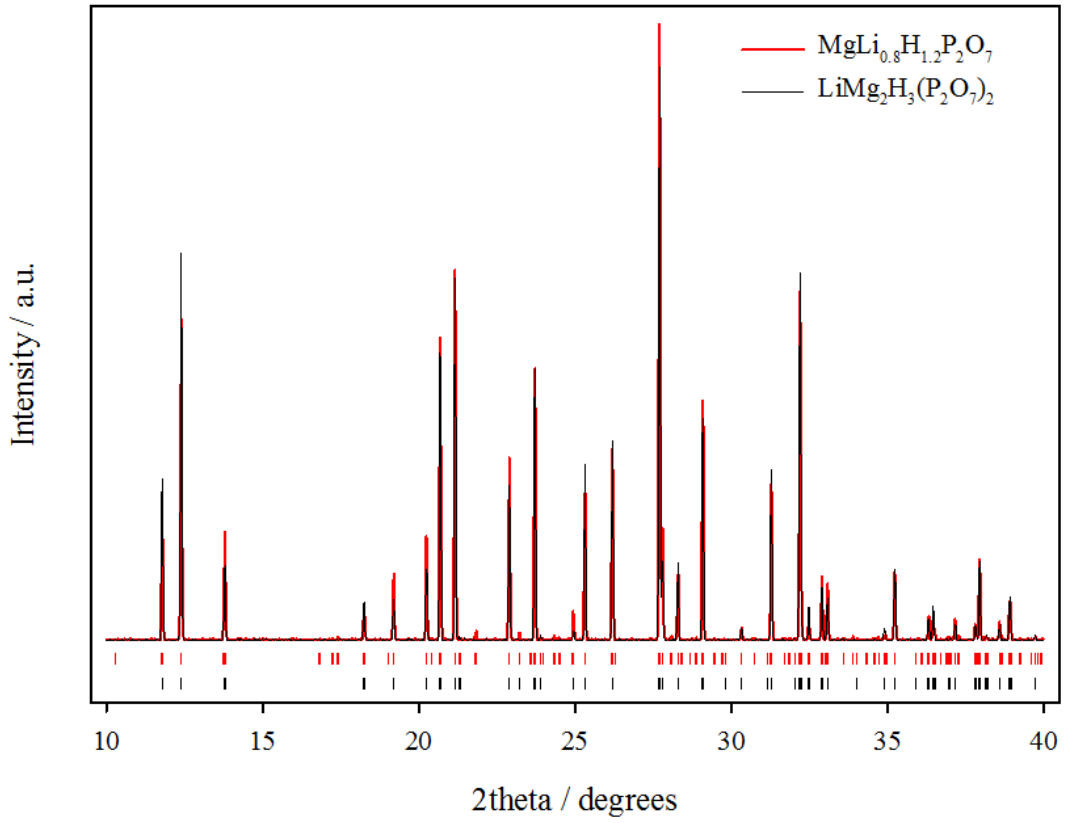

Figure 3.23 - Simulated PXRD patterns for $MgLi_{0.8}H_{1.2}P_2O_7$ (red) and $LiMg_2H_3(P_2O_7)_2$ (black)

Both models give similar, reasonable fits to the NPD data, but they both have intensity mismatches for different peaks in the NPD pattern at 1.93 Å, and between 2.089 and 2.46 Å. On balance, with the data available and given the second model (based on $LiNi_2H_3(P_2O_7)_2$) has higher symmetry and fewer variables, it likely that this is currently the better model. Importantly, it also provides Li-O bond lengths and Li coordination environments that are much more chemically sensible compared with the initial model. Clearly, further high quality diffraction data would provide a more definitive conclusion.

Additionally, solid state NMR could help provide a further insight into the structure by looking at the individual environments. ^{1}H, ^{31}P and ^{7}Li NMR would be

extremely helpful in determining the structure adopted due to the differing number of H, P and Li sites between these two models.

3.3.5 Crystal Morphology

SEM was used to investigate the crystal morphology of Li-doped $MgH_2P_2O_7$ compared to that of α-$MgH_2P_2O_7$ and β-$MgH_2P_2O_7$. Figure 3.24 show SEM images of α-$MgH_2P_2O_7$, β-$MgH_2P_2O_7$ and Li doped $MgH_2P_2O_7$.

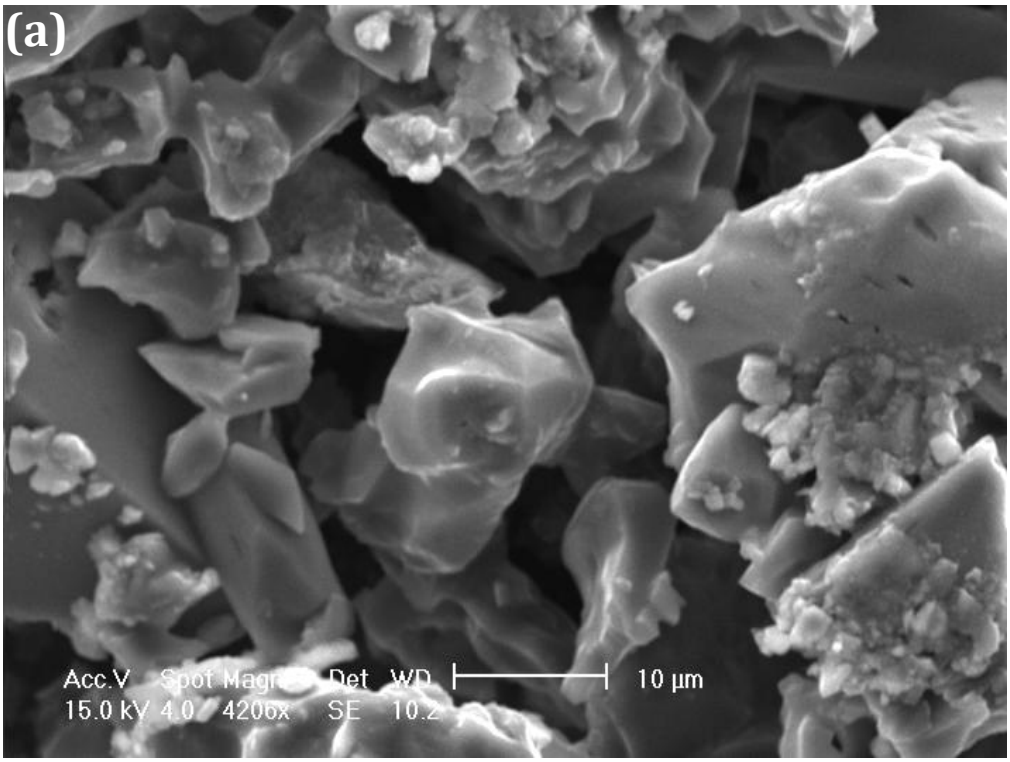

Figure 3.24 - SEM images of (a) α-$MgH_2P_2O_7$, (b) β-$MgH_2P_2O_7$ and (c) Li-doped $MgH_2P_2O_7$

Figure 3.24 continued

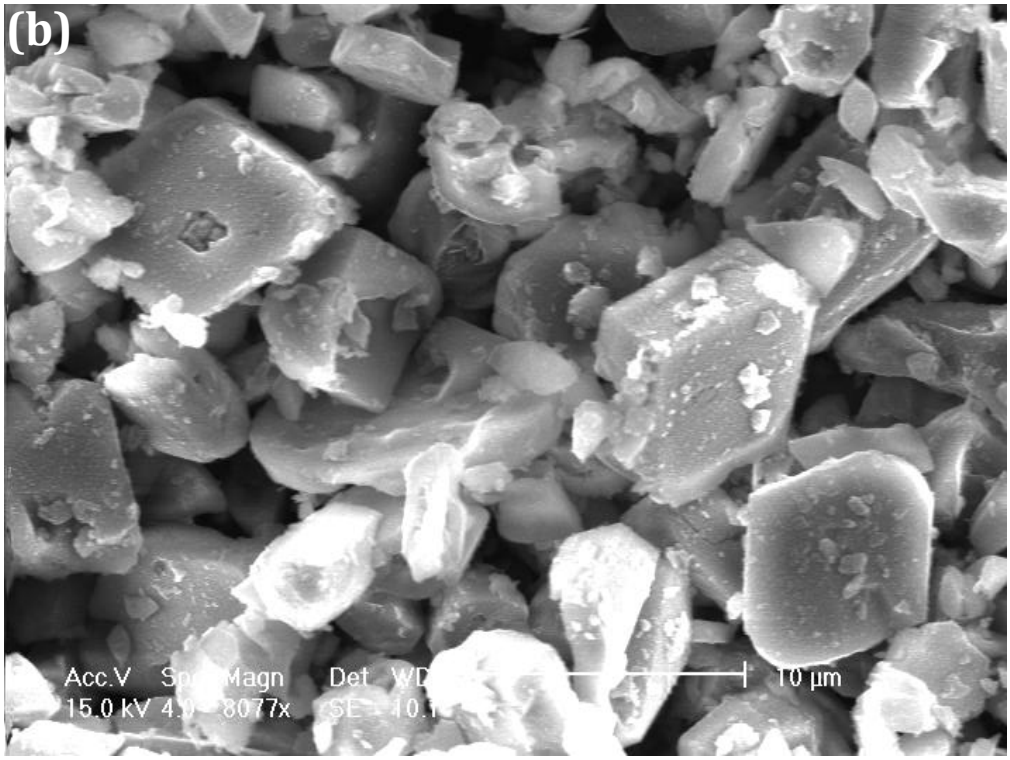

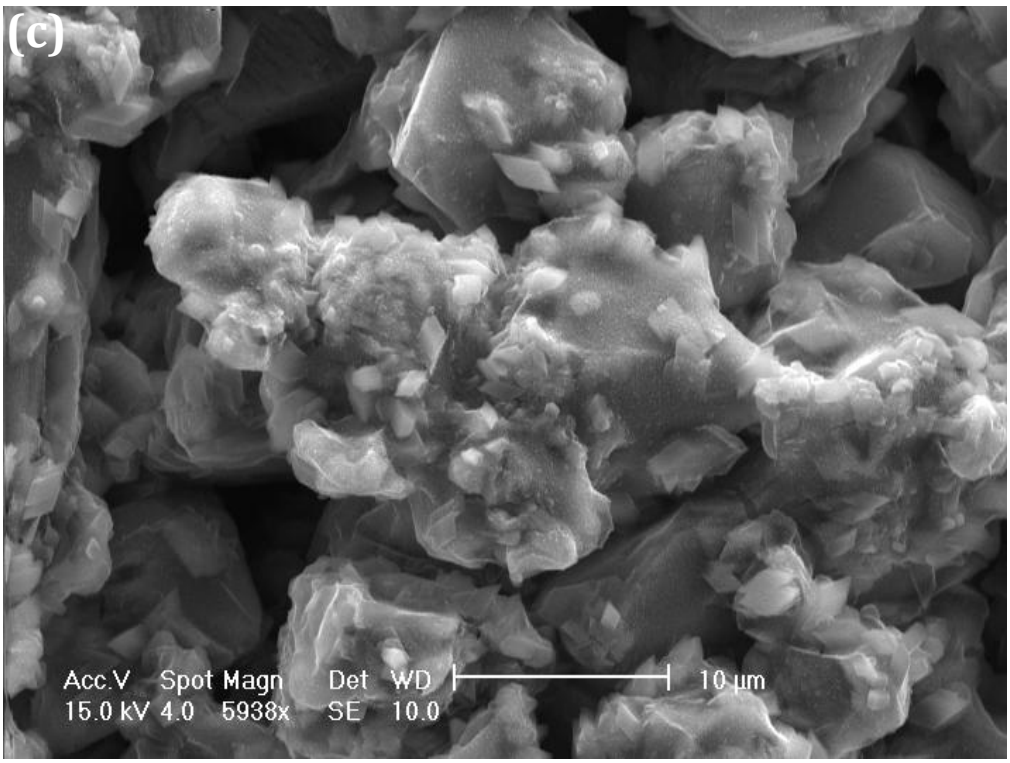

The SEM image of α-$MgH_2P_2O_7$ shows agglomerated particles with no real distinct crystal morphology. The crystal morphology of β-$MgH_2P_2O_7$, in contrast, is much more defined, forming diamond shaped crystals. Li-doped $MgH_2P_2O_7$ appears to form a mixture of the two types; there are areas of agglomerated particles like in α-$MgH_2P_2O_7$, but there are also areas of small distinct diamond shaped crystals, which may indicate the presence of more than one phase.

3.4 Conclusion

Two polymorphs of $MgH_2P_2O_7$ were successfully synthesised in a novel synthetic route for magnesium phosphates. α-$MgH_2P_2O_7$ was synthesised using an acid melt, crystallising into the monoclinic space group $P2_1/c$. Composition was confirmed via TGA-MS and a Rietveld refinement was carried out using $NiH_2P_2O_7$ as a structural model, which gave an excellent fit.

β-$MgH_2P_2O_7$ was successfully synthesised as a single phase initially using a higher reaction temperature, and later using $CaH_2P_2O_7$. TGA-MS confirmed the composition, and a Rietveld refinement carried out using $CaH_2P_2O_7$ as a structural model gave an excellent fit, confirming the structure type. GII calculations were used to indicate structural strain; a value of 0.059 v.u. indicates α-$MgH_2P_2O_7$ is not a strained structure, whereas a value of 0.15 v.u. suggests that β-$MgH_2P_2O_7$ is strained.

Lithium-proton ion exchange of both α & β-$MgH_2P_2O_7$ via solution was unsuccessful, so lithium was introduced directly into the melt, resulting in a new phase, which when indexed gave similar lattice parameters to that of α-$MgH_2P_2O_7$. Flame emission photometry and VT-XRD confirm the presence of Li in the sample. A

Rietveld refinement was carried out initially using α-$MgH_2P_2O_7$ which gave a good fit but some intensity differences. Refining Li/H occupancies gave a stoichiometry of $MgLi_{0.8}H_{1.2}P_2O_7$, but also provided some problems with the viability of the Li locations suggested. A second structural model of higher symmetry was found in the form of $LiNi_2H_3(P_2O_7)_2$, and a second Rietveld refinement was carried out which also gave a similarly good fit to the previous model, but now contained more sensible Li environments and therefore is a more suitable model. However, inadequacies in the models still exist and broad peaks in the PXRD pattern and different particle morphologies present in the SEM image could indicate the presence of more than one phase. Further work will need to be carried out to fully confirm the structure, and investigate the likelihood of multiple phases being present.

References

1. M. R. Cave, D. Farrar and A. J. Wright, *Journal of Physics and Chemistry of Solids*, 2007, **68**, 431-437.
2. A. Bigi and G. Cojazzie, *Journal of Inorganic Biochemistry*, 1997, **68**, 45-51.
3. R. Murugan, A. Ramakrishna and P. R. K., *Materials Letters*, 2006, **60**, 2844-2847.
4. L. M. Grover, U. Gbureck, A. J. Wright, M. Tremayne and J. E. Barralet, *Biomaterials*, 2006, **27**, 2178-2185.
5. N. Eidelman, W. E. Brown and J. L. Meyer, *Journal of Crystal Growth*, 1991, **113**, 643-652.
6. V. Aravindan, J. Gnanaraj, Y. S. Lee and S. Madhavi, *Journal of Materials Chemistry A*, 2013, **1**, 3518-3539.
7. T. R. Hinsch, W. Guse and H. Saalfeld, *Journal of Crystal Growth*, 1986, **79**, 205-209.
8. T. Yang, J. Ju, G. Li, S. Yang, J. Sun, F. Liao, J. Lin, J. Saski and N. Toyota, *Inorganic Chemistry*, 2007, **46**, 2343-2344.
9. *Inorganic Crystal Structure Database*, http://icsd.cds.rsc.org/.
10. H. M. Rietveld, *Journal of Applied Crystallography*, 1969, **2**, 65-71.

11. A. C. Larson and R. B. Von Dreele, Los Alamos National Laboratory, Los Alamos NM, Editon edn., 1994.
12. B. H. Toby, *Journal of Applied Crystallography,* 2001, **34**, 210-213.
13. I. D. Brown and D. Altermatt, *Acta Crystallographica* 1985, **B41**, 244-247.
14. A. Salinas-Sanchez, J. L. Garcia-Muńoz, J. Rodriguez-Carvajal, R. Saez-Puche and J. L. Martinez, *Journal of Solid State Chemistry*, 1992, **100**, 201-211.
15. A. G. Nord and K. B. Lindberg, *Acta Chemica Scandinavica A*, 1975, **29**, 1-6.
16. V. Pralong, R. Baies, V. Caignaert and B. Raveau, *Inorganic Chemistry*, 2009, **48**, 6835-6844.
17. P.L., in *JCPDS International Centre for Diffraction Data, Swarthmore, Pennsylvania, PA 19081, USA*, Editon edn., 1990.
18. R. Shirley, The Lattice Press, 41 Guildford Park Avenue, Guildford, Surrey GU2 7NL, England, Editon edn., 2002.
19. J. Laugier and B. Bochu, Laboratoire des Materiaux et du Génie Physique de l'Ecole Supérieure de Physique de Grenoble http://www.inpg.fr/LMGP/, Editon edn.
20. J. Trommer, M. Schneider, H. Worzala and A. N. Fitch, *Materials Science Forum*, 2000, **321**, 374-379.
21. R. D. Shannon and C. T. Prewitt, *Acta Crystallographica Section B*, 1969, **25**, 925-946.
22. T. Yang, S. Yang, F. Liao and J. Lin, *Journal of Solid State Chemistry*, 2008, **181**, 1347-1353.
23. M. T. Averbuch-Pouchot and E. Rakotomahanina-Ralaisoa, *Bulletin de la Société Française de Minéralogie et de Cristallographie*, 1970, **93**, 394-396.
24. V. F. Sears, *Neutron News*, 1992, **3**, 29-37.

Chapter 4

Synthesis and Characterisation of $MnH_2P_2O_7$ and Li-Doped $MnH_2P_2O_7$

4.1 Introduction

In recent years manganese phosphates have received a large amount of interest due to their wide range of applications including ionic conductors,[1] catalysts[2] and inorganic pigments.[3] Manganese's variable oxidation states, non-toxicity and optical properties make it suitable for use in Li-ion battery materials and pigment materials. Manganese violet, $NH_4MnP_2O_7$,[4] has been used as a pigment material in cosmetics and plastics due to its intense purple colouration, which arises from the distorted Mn^{3+} environment, which has also been observed in other similar systems.[3] $LiMnPO_4$ is an attractive cathode material due to its high operating voltage.[1] Its strong P-O bond makes it a safe and stable material, unlikely to decompose during operation. Related materials like $Li_2MnP_2O_7$[5] and $Li_2Mn_{1-x}Fe_xP_2O_7$[6] have also lately been of interest due to their good electrochemical performance and stable structural frameworks. This chapter details investigation into isolating novel Mn phosphates, particularly pyrophosphates, and the potential for lithium doping. The study focuses on the structural characterisation of a new $MnH_2P_2O_7$, and its thermal and magnetic properties.

4.2 Experimental

4.2.1 Synthesis of $MnH_2P_2O_7$

$MnH_2P_2O_7$ was prepared via an acid melt, using a solution of MnO and H_3PO_4, with a Mn:P ratio of 1:6. This was stirred on a hotplate at 150°C for 3 hours in a porcelain crucible and the crucible was then placed in an oven at 200°C for 72 hours and allowed to cool to room temperature. The resulting paste was then washed with deionised water and suction filtered, leaving a pale pink powder.

4.2.2 Synthesis of Li-Doped $MnH_2P_2O_7$

Li-doped $MnH_2P_2O_7$ was prepared in a similar fashion to the parent phase. Li_2CO_3 and MnO were ground together and then added to H_3PO_4 in a porcelain crucible, with a Mn:Li:P ratio of 1:1:6. The solution was stirred on a hotplate at 150°C for 3 hours until a melt was formed. The crucible was then heated in an oven at 200°C for 72 hours. The resulting paste was then washed with deionised water and suction filtered, leaving a pale pink powder.

4.2.3 Collection of Diffraction Data

Powder diffraction data were collected on the Bruker AXS: D8 Advance diffractometer in transmission mode using a 2θ range of 5-90°. Neutron powder diffraction data of the un-doped $MnH_2P_2O_7$ and the Li-doped $MnH_2P_2O_7$ were recorded on the TOF powder diffractometer Polaris instrument at ISIS, Rutherford Appleton Laboratory. Variable temperature data were collected on the Bruker AXS: D8 Advance diffractometer, fitted with the Anton Paar HTK1200 heating stage.

4.3 Results & Discussion

4.3.1 $MnH_2P_2O_7$

Synthesis of a single phase product, now identified as $MnH_2P_2O_7$, was achieved. Its PXRD pattern could not be matched on the JCPDS database[7] to any previously reported patterns. The X-ray diffraction pattern was then indexed using the Crysfire program[8] to find potential unit cells. Table 4.1 shows the potential unit cells calculated using Crysfire using 20 inputted peak positions.

Table 4.1 - Unit cells calculated by Crysfire[8] for $MnH_2P_2O_7$

I20	Merit	Symmetry	a (Å)	b (Å)	c (Å)	α (°)	β (°)	γ (°)	Volume (Å^3)
20	37	Monoclinic	7.0686	7.9041	9.4006	90	101.52	90	514.641
17	9	Orthorhombic	10.142	11.0616	15.8154	90	90	90	1774.352
17	9	Orthorhombic	10.142	11.0616	15.8154	90	90	90	1774.352

The orthorhombic cells were rejected as they had a low figure of merit compared to the monoclinic cell. The monoclinic lattice parameters were inputted into Chekcell[9] which suggested possible space groups of $C2/c$ or $P2_1/m$.

To confirm the composition of $MnH_2P_2O_7$ the sample underwent thermogravimetric analysis. A sample of $MnH_2P_2O_7$ was heated in a nitrogen atmosphere at 10K min^{-1} to 800°C. The TGA-MS plot is shown in figure 4.1.

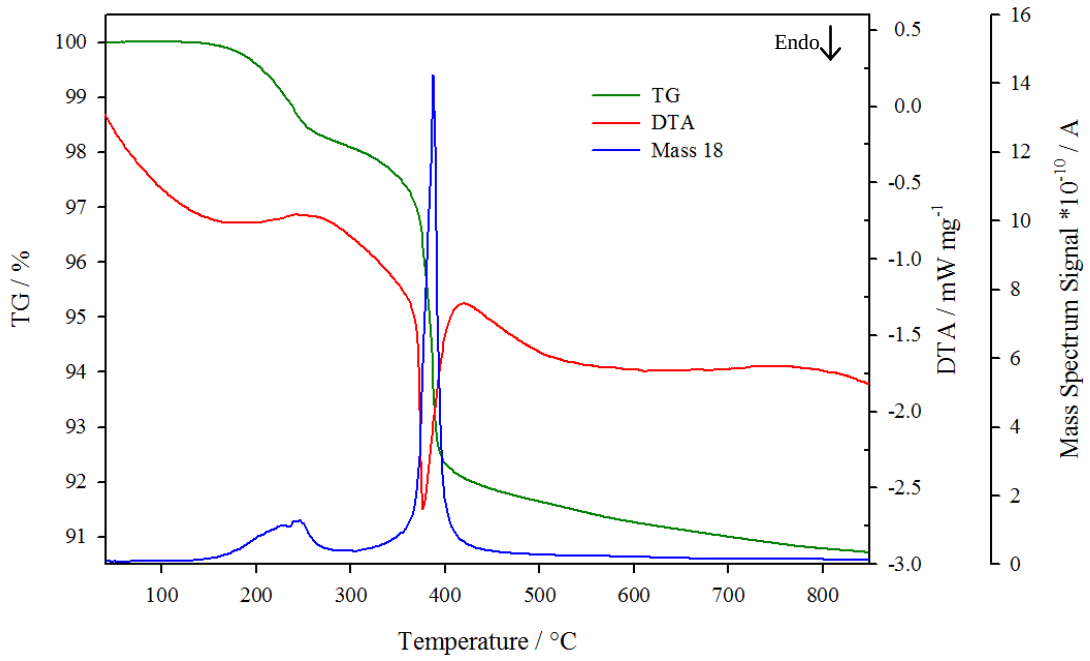

Figure 4.1 - TGA-MS plot of $MnH_2P_2O_7$

The mass obtained is unchanged as the temperature increases up until 200°C where upon there is a mass loss of ~1.7 %, which coincides with a small broad peak in the mass spectrum signal for mass 18. A further, much larger mass loss of ~7.5 % occurs at approximately 375°C, coinciding with a large sharp peak in the MS signal for mass 18 and a sharp endothermic peak in the DTA. The diffraction pattern of the sample after such a heat treatment is consistent with that of $Mn_2P_4O_{12}$,[10] a cyclic tetraphosphate. Therefore the large mass loss is consistent with a loss of water via a condensation reaction, confirming the presence of protons in the structure, and the smaller initial mass loss may be due to a loss of surface water. Based upon the final product of $Mn_2P_4O_{12}$, the large mass loss is equivalent to 2 moles of water evolving as two HP_2O_7 combine to form $Mn_2P_4O_{12}$, giving the stoichiometry $MnH_2P_2O_7$, shown in equation 4.1, and demonstrates the purity of this sample. The small mass loss is equivalent to 0.2 moles of associated/surface water.

$$2MnH_2P_2O_7 \rightarrow Mn_2P_4O_{12} + 2H_2O \quad (4.1)$$

With the stoichiometry calculated and purity confirmed, a search for a model with P_2O_7 structural units displaying monoclinic symmetry was undertaken. $CaH_2P_2O_7$[11] was found as possible model, and has monoclinic symmetry, $C2/c$ with the following lattice parameters: a = 7.3276(1) Å; b = 8.1282(1) Å; c = 9.7632(1) Å; β = 101.239°.

4.3.1.1 Crystal structure of $MnH_2P_2O_7$

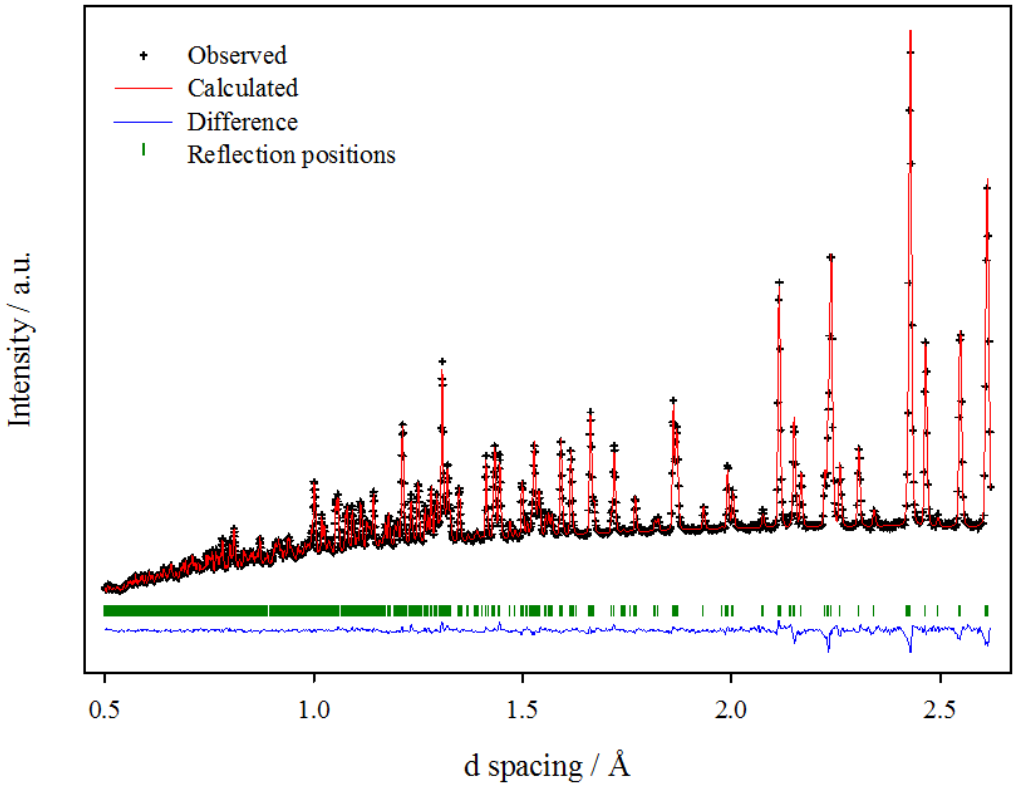

Figure 4.2 - Rietveld refinement plot of $MnH_2P_2O_7$

The crystal structure of $MnH_2P_2O_7$ was therefore determined via Rietveld refinement[12] using the GSAS suite[13] of programs and EXPGUI[14] of neutron powder diffraction data with $CaH_2P_2O_7$[11] as the starting model. The refinement converged at

a low R_{wp} value of 0.85%. The refinement (shown in figure 4.2) confirms that $MnH_2P_2O_7$ adopts the β-type acid pyrophosphate structure (as described in chapter 3) with space group $C2/c$ and lattice parameters a = 7.0828(8) Å, b = 7.9050(8) Å, c = 9.3936(1) Å and β = 101.190(1)°. Table 4.2 shows the refined structural parameters, and selected bond lengths and angles are given in table 4.3.

Table 4.2 - Refined structural parameters at room temperature of $MnH_2P_2O_7$

Atom	Site	Occupancy	x	y	z	U_{iso} / Å^2	BVS
Mn	4*a*	1	0	0	0	0.0049(3)	2.14
P	8*f*	1	0.3316(1)	0.1236(1)	0.8129(1)	0.0054(2)	4.90
O(1)	4*e*	1	0.5	0.0305(2)	0.75	0.0056(2)	2.05
O(2)	8*f*	1	0.2447(1)	0.9859(1)	0.8904(9)	0.0073(2)	2.04
O(3)	8*f*	1	0.1805(1)	0.8253(1)	0.1719(9)	0.0062(2)	2.06
O(4)	8*f*	1	0.0932(1)	0.2232(1)	0.1038(1)	0.0110(2)	1.91
H	8*f*	1	0.3021(2)	0.2059(2)	0.3575(2)	0.0186(4)	0.75

Space group $C2/c$; a = 7.0828(8) Å, b = 7.9050(8) Å, c = 9.3936(1) Å and β = 101.190(1)°. Figures of merit: R_{wp} = 0.85%, R_p = 1.16%, χ^2 = 4.625

Table 4.3 - Selected bond distances (Å) and angles (°) for $MnH_2P_2O_7$

Mn-O2	2.1840(8)	**O2-Mn-O4**	93.23(4)
Mn-O3	2.3129(8)	**O2-Mn-O4**	86.77(4)
Mn-O4	2.0612(8)		
P-O1	1.608(1)	**O1-P-O2**	104.37(7)
P-O2	1.506(1)	**O1-P-O3**	103.80(6)
P-O3	1.585(1)	**O1-P-O4**	110.57(8)
P-O4	1.484(1)	**O2-P-O3**	108.38(7)
O3-H	0.998(2)	**O2-P-O4**	118.28(8)
P-O3-H	111.9(1)	**O3-P-O4**	110.35(7)

The structure, shown in figure 4.3, consists of layers of isolated MnO_6 octahedra, which are interconnected by pyrophosphate units. These layers run along the *ab* plane, and stack along the *c* axis. Protons are located on the oxygen bridging MnO_6 and PO_4 units as OH units, as shown in figure 4.4. Bonding of this proton leads

to a longer Mn–O bond length of 2.3129(8) Å, and a relatively long P–O bond of 1.585(1) Å.

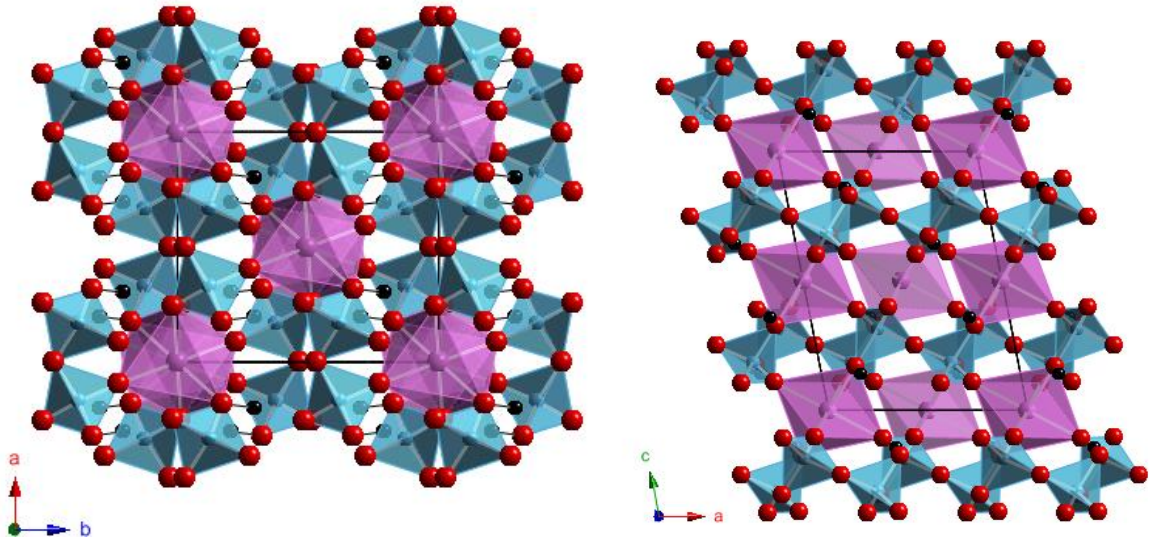

Figure 4.3 - Structure of $MnH_2P_2O_7$ viewed down the c- and b-axes, where the MnO_6 octahedra are purple, the PO_4 tetrahedra are blue, protons are black spheres. The unit cell is represented by a thin black line

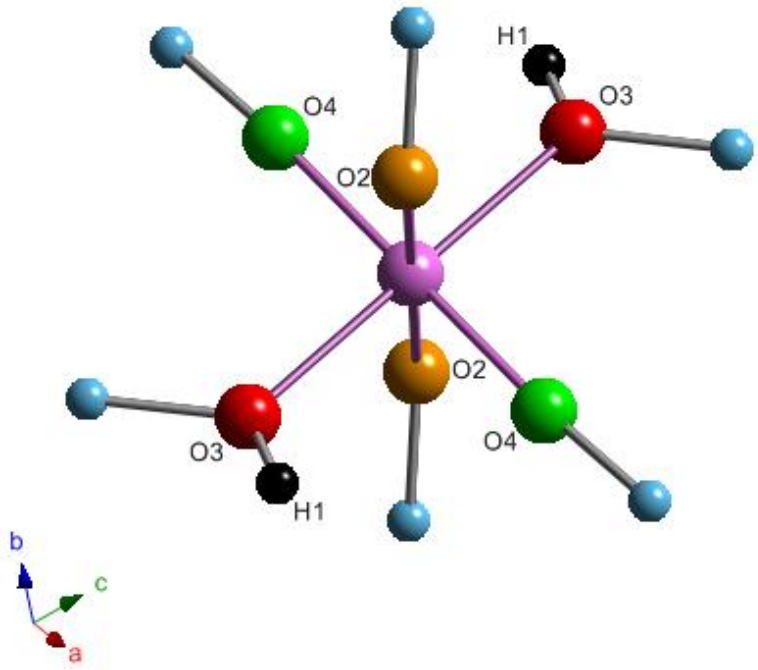

Figure 4.4 – Ball and stick model of Manganese (purple) metal centre displaying the metal-P-OH bonding where the P atoms are blue

Table 4.3 shows the bonding of Mn, which consists of 2 long bonds, 2 short bonds and 2 medium length bonds, which suggests a strained structure. The P–O bond lengths are all of a similar length, with a slightly longer P–O bond length for the bridging oxygen in the P_2O_7 unit. The proton is bound to O3, giving a bond length of 0.998(2) Å, and is able to hydrogen bond with O2, with a hydrogen bond length of 1.614(2) Å. The overall BVS[15] of Mn is +2.14, which indicates it is slightly over bonded, compared with P, which appears to be slightly under bonded with its BVS of +4.90. The Global Instability Index[16] which can be used as a measure of the strain within a structure, a value of 0.15 v.u. was calculated, suggesting the structure is strained.

4.3.1.2 Thermal Behaviour of $MnH_2P_2O_7$

Variable temperature XRD was used to confirm the decomposition pathway. A sample was heated in an Anton Paar HTK1200 heating stage and a diffraction pattern was taken at approximately 50°C intervals from 50°C to 650°C. A stack plot of the diffraction patterns is shown in figure 4.4. The structure remains intact from 45°C up until at least 304°C. At 345°C $MnH_2P_2O_7$ has fully converted to the cyclic triphosphate, which is a lower temperature than that suggested by the TGA-MS data. This is mostly likely due to reaction kinetics like α-$MgH_2P_2O_7$; the condensation of $MnH_2P_2O_7$ is a slow reaction and so occurs at a lower temperature in the VT-XRD heating stage compared to the TGA. In the VT-XRD heating stage the sample is heated in 50°C steps and then held there for a length of time, which allows the condensation to complete. In the TGA the sample is heated linearly at 10°C min^{-1} to 850°C and so

the condensation reaction occurs whilst the TGA is still heating, leading to condensation at a higher temperature.

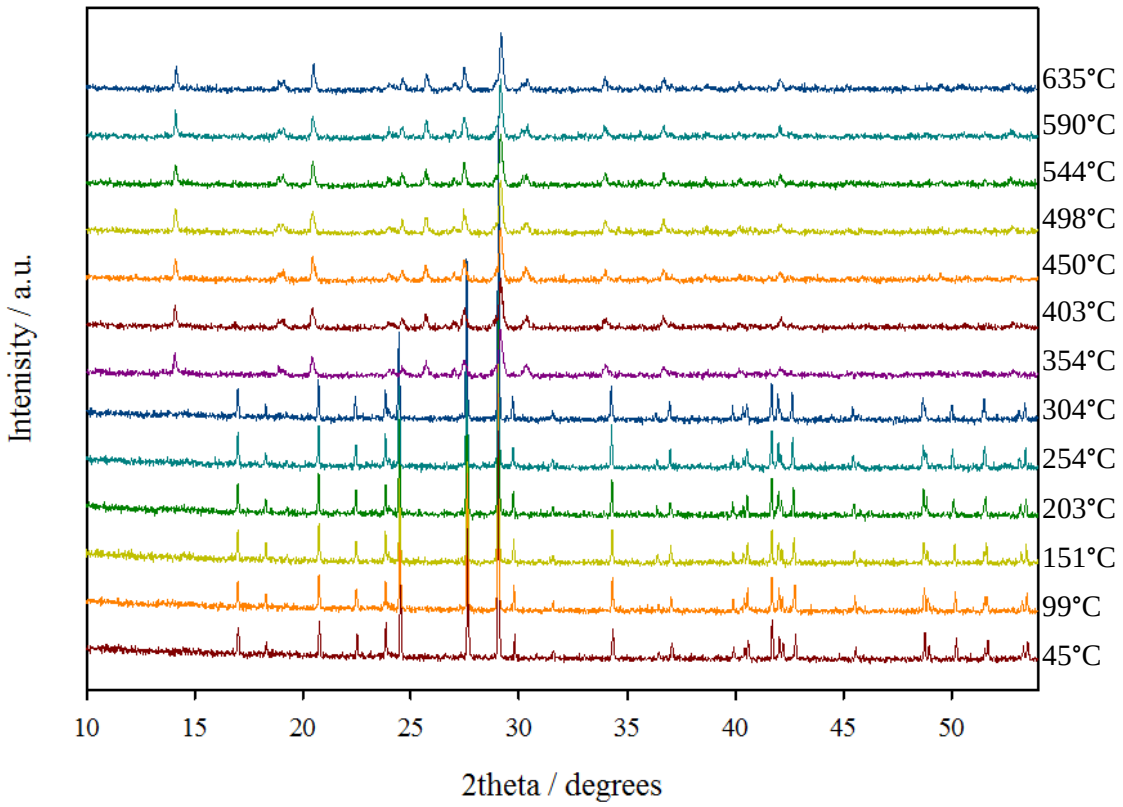

Figure 4.5 - VT-XRD stack plot of $MnH_2P_2O_7$, showing the presence of $MnH_2P_2O_7$ until 304°C, whereupon a conversion to $Mn_2P_4O_{12}$ is evident

4.3.1.3 Magnetic Analysis of $MnH_2P_2O_7$

MPMS data were collected to investigate the magnetic properties of $MnH_2P_2O_7$. The magnetic susceptibility data and Curie-Weiss plot is shown in Figure 4.6. $MnH_2P_2O_7$ displays paramagnetic behaviour, with a Weiss constant (θ) of −6.01 K, indicating a small antiferromagnetic component. The effective magnetic moment of 5.78 μ_B is consistent with the spin only moment for high spin Mn^{2+} of 5.92 μ_B (calculated from the gradient of $1/\chi$ versus temperature plot – see figure 4.6 inset).

Slight curvature to the Curie-Weiss fit indicates some deviation from the ideal Curie-Weiss law.

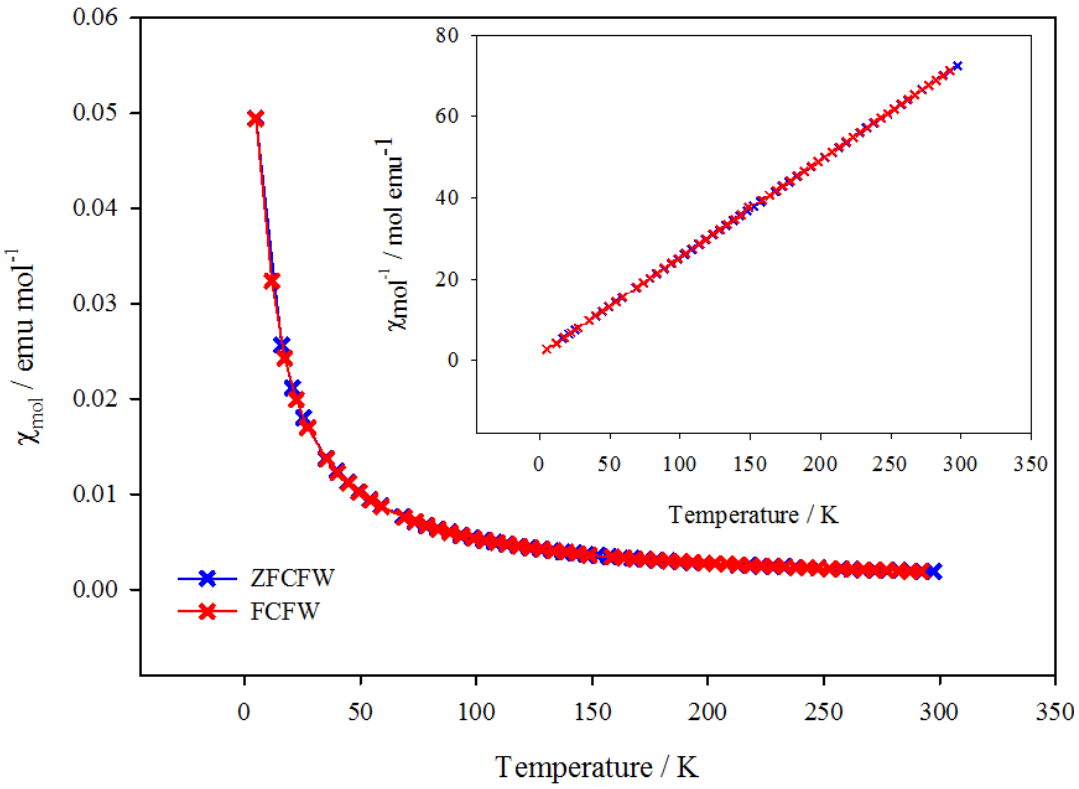

Figure 4.6 - Plot of molar susceptibility against temperature for $MnH_2P_2O_7$, inset shows Curie-Weiss fit

4.3.1.4 Polymorphism

$MH_2P_2O_7$ has been shown to exist in one of two known polymorphs, the 'alpha' polymorph where M^{2+} = Fe,[17] Ni,[18] Co[18] & Mg, and the 'beta' polymorph where M = Ca[11] and Mg (as discussed in chapter 3). The alpha polymorph appears to preferentially form when M^{2+} has an ionic radius below 80 pm, whereas the beta polymorph form with much larger cations, such as Ca^{2+}. In this study, Mn^{2+} adopts the high spin electronic configuration (as confirmed in 4.3.1.3) and so has a larger ionic radius of 83 pm,[19] meaning it would be expected to adopt the beta structure, which is confirmed by Rietveld refinement. In chapter 3 we observe that magnesium is able

to form both polymorphs despite having an ionic radius of 72 pm.[19] The ability for a smaller cation like Mg^{2+} to be able to form both polymorphs via higher reaction temperatures and with crystal seeding may mean that the synthesis of α-$MnH_2P_2O_7$ or mixed Mn-$MH_2P_2O_7$ system may be possible. Although not possible in this work, future studies could explore these magnetically interesting one-dimensional magnetic interactions in the MO_6 chains observed in the Ni, Co and Fe systems.

4.3.2 Li-Doped $MnH_2P_2O_7$

Incorporation of lithium into $MnH_2P_2O_7$ was attempted for potential battery applications and to investigate the influence on magnetic properties. This was achieved via addition of Li_2CO_3 to the initial melt. Initial characterisation via PXRD, pattern shown in figure 4.7, shows very little difference compared to the PXRD pattern for $MnH_2P_2O_7$, but there is some evidence of intensity differences and shifting of peaks to lower 2 theta. There is no evidence of any impurity peaks in the PXRD pattern.

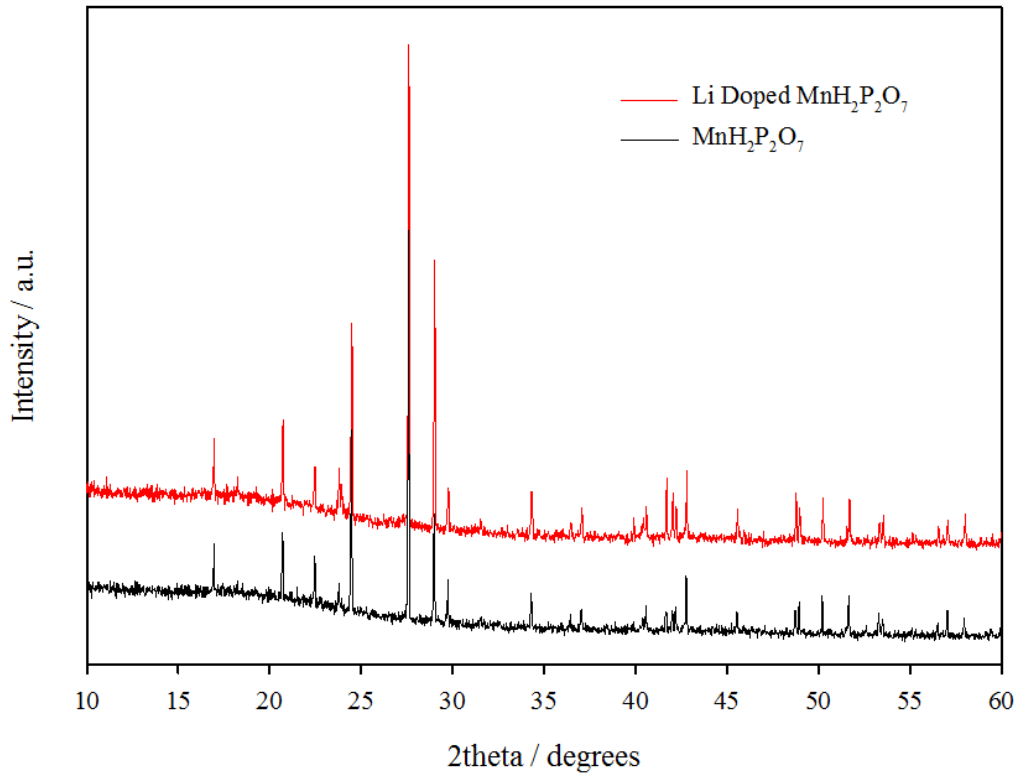

Figure 4.7 - PXRD pattern of $MnH_2P_2O_7$ and Li-doped $MnH_2P_2O_7$

4.3.2.1 Thermal behaviour of Li-Doped $MnH_2P_2O_7$

To check the composition of the Li-doped $MnH_2P_2O_7$, a sample underwent thermogravimetric analysis; the TGA-MS plot is shown in figure 4.8. The sample underwent a large mass loss of ~6.5 % starting at 325°C, which coincides with a sharp endothermic peak in the DTA and a large peak in the mass spectrum signal for mass 18, consistent with loss of water from the structure. This mass loss is smaller than that of the parent compound, and equates to approximately 0.89 moles of water lost, which may indicate some protons have been exchanged for lithium. A diffraction pattern of the heat treated sample was obtained and is shown in figure 4.9. Two known phases were identified; $Mn_2P_4O_{12}$[10] and $LiMn(PO_3)_3$.[20] Some unknown impurity peaks were also observed.

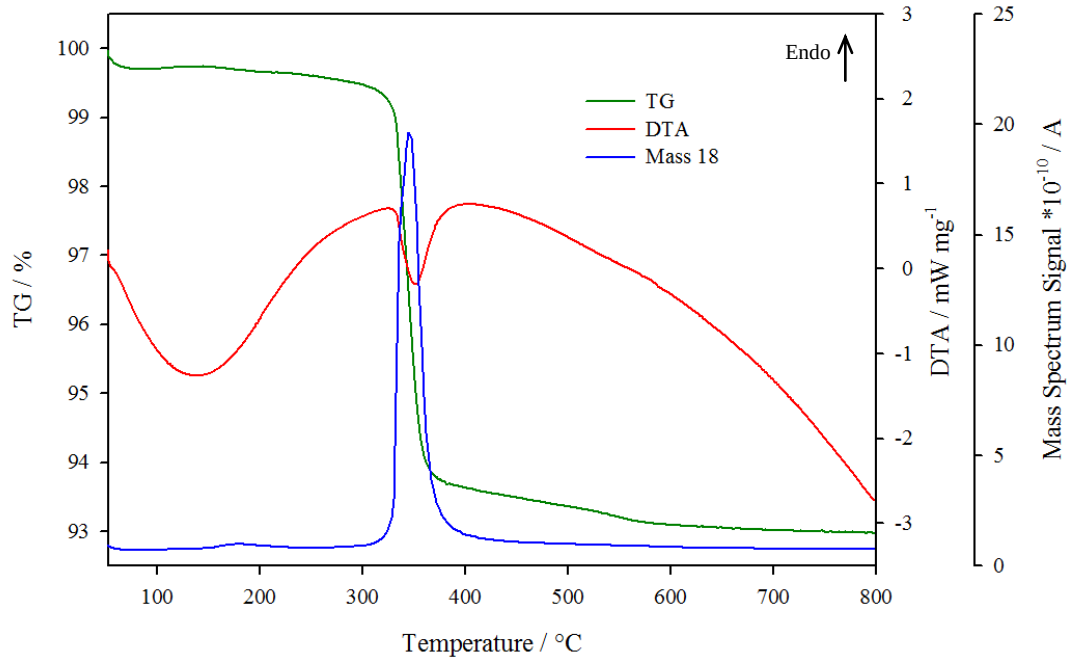

Figure 4.8 - TGA-MS plot of Li-doped $MnH_2P_2O_7$

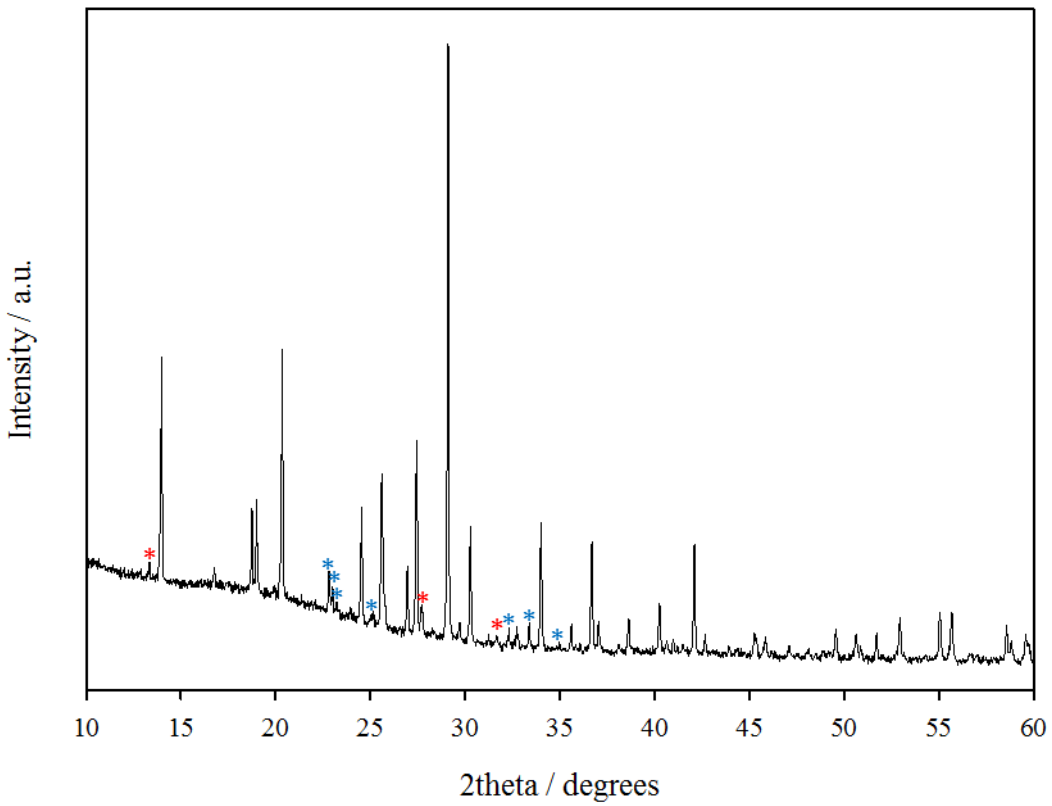

Figure 4.9 - PXRD pattern of heat treated Li-doped sample. Unknown impurity peaks are shown by red asterisks and $LiMn(PO_3)_3$ peaks are shown by blue asterisks

Variable temperature XRD was used once again to confirm the decomposition pathway, which is shown in figure 4.10. The structure remains intact from 45°C up until 304°C where it is converted to $Mn_2P_4O_{12}$. This is approximately 50°C lower than the parent phase, which might be due to the lithium occupying some of the proton sites, destabilising the structure.

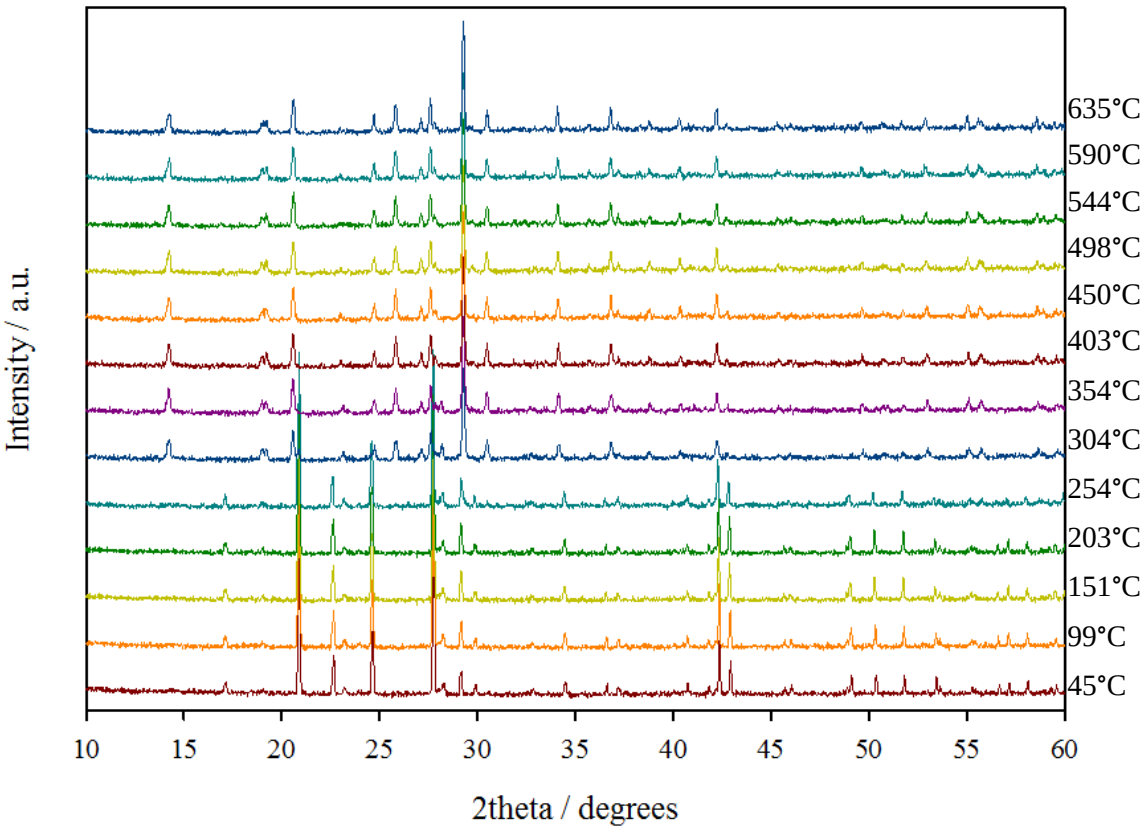

Figure 4.10 - VT-XRD plot of Li-doped $MnH_2P_2O_7$

4.3.2.2 Crystal Structure of Li-Doped $MnH_2P_2O_7$

Using $MnH_2P_2O_7$ as a structural model, a Rietveld refinement[12] was carried out with no Li addition to the model, which gave an adequate fit, shown in figure 4.11. The difference line shows some small additional peaks in the back scattered bank, which may indicate an impurity. Additional peaks are also evident in the 90°, 50°

and the 25° banks, shown in figure 4.12. The additional peaks could not be indexed to a single phase, nor could they be matched to a known lithium or manganese phase. As this impurity cannot be seen in the X-ray data it may be a lithium rich impurity or a magnetic impurity. Two phase refinements were carried out with addition of potential impurities, including various metal oxides (Mn, Li, Mn-Li), phosphates (Mn, Li, Mn-Li) and lithium carbonate but no match was established.

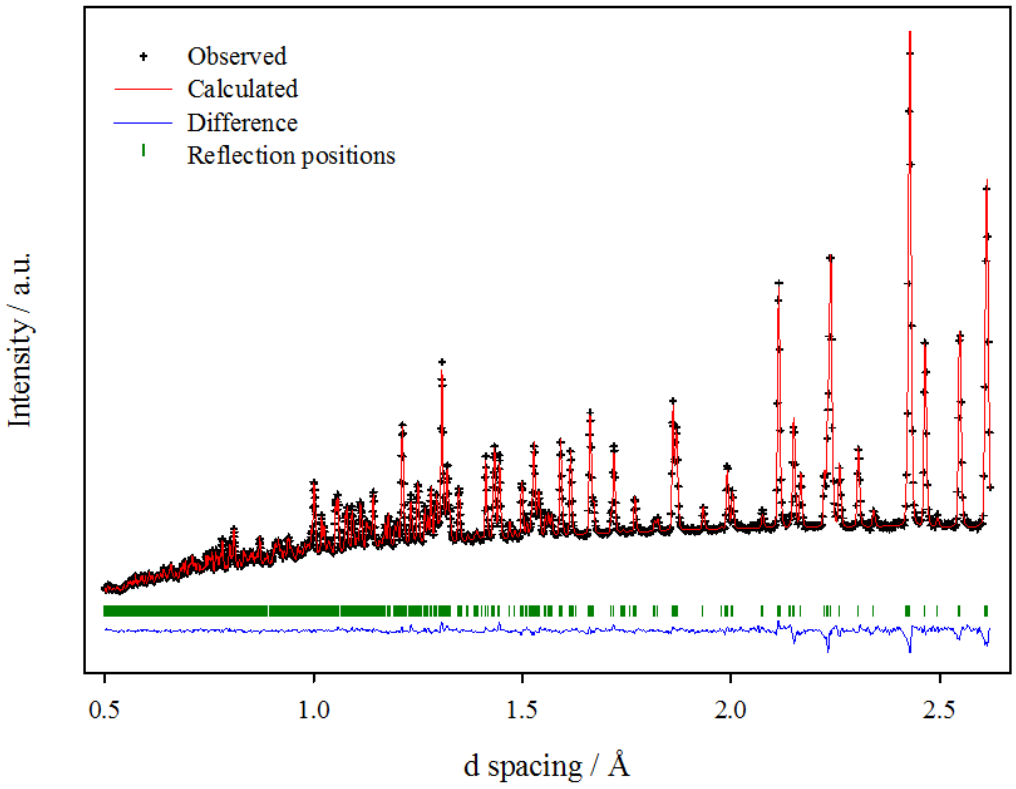

Figure 4.11 - Rietveld plot of NPD of Li-doped $MnH_2P_2O_7$

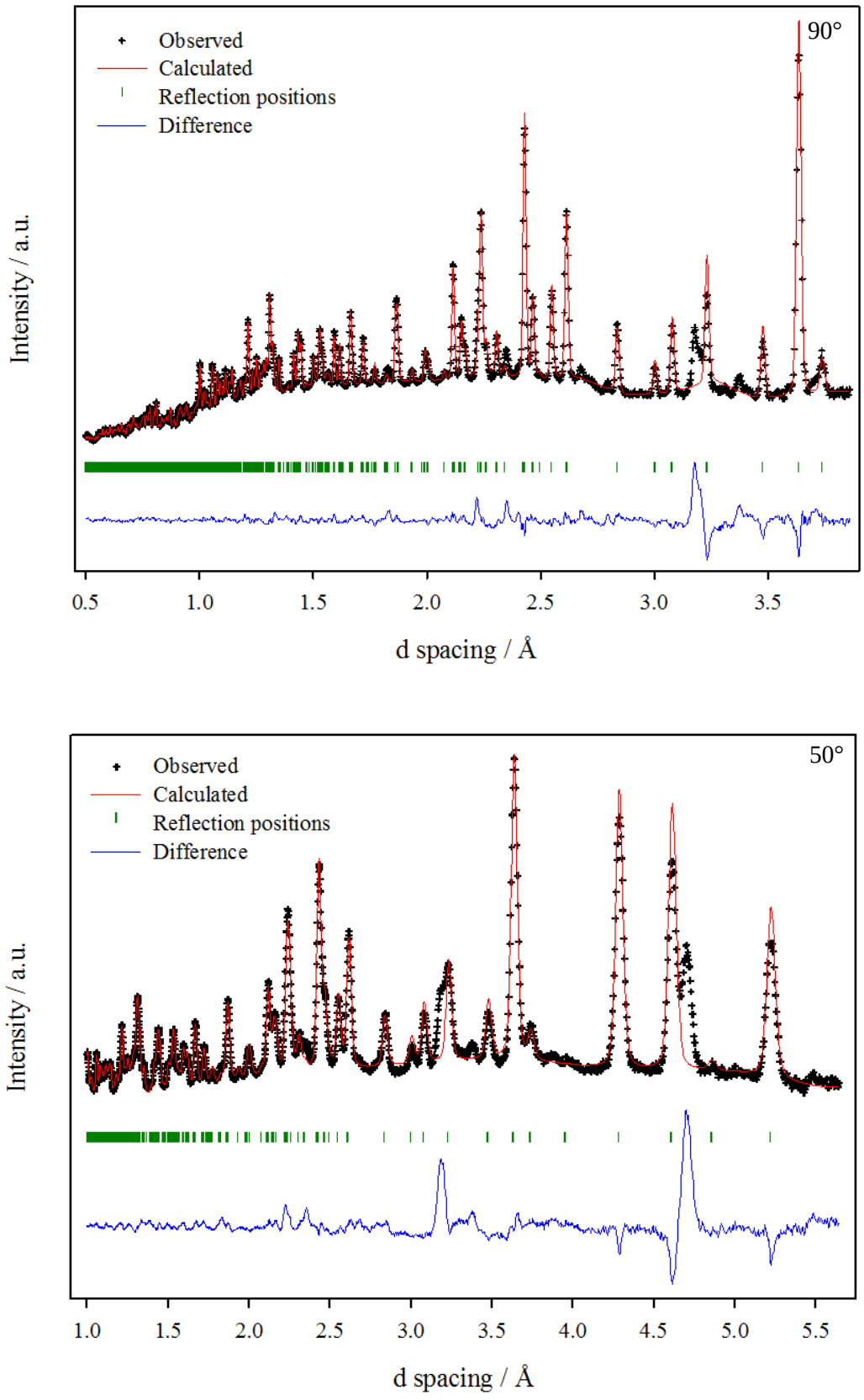

Figure 4.12 – Rietveld refinements of the 90, 50 & 25° banks

Figure 4.12 continued

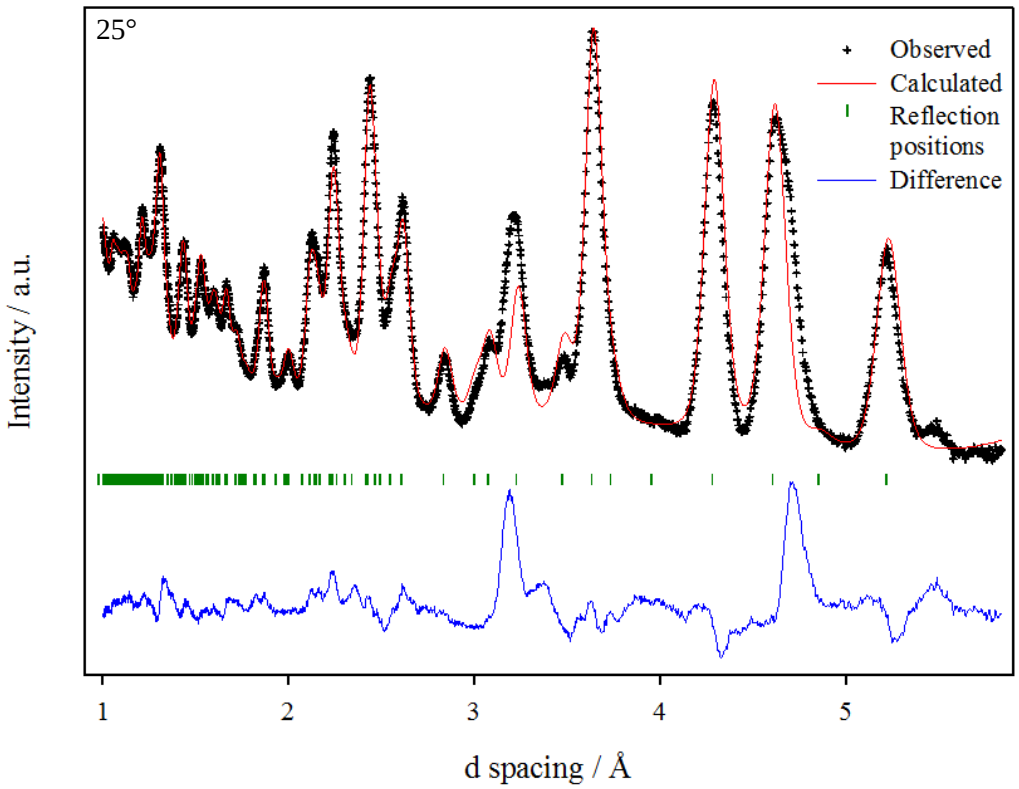

The refined structural parameters are shown in tables 4.4 and 4.5. The refined lattice parameters show a slight increase in cell volume which may be due to lithium replacement of protons. Site occupancy of the proton site with lithium added was refined to give an occupancy of 0.25(2), which would give a stoichiometry of $MnLi_{0.5}H_{1.5}P_2O_7$, but due to the poor fit of the Rietveld refinement and the additional phase, the stoichiometry is prone to significant uncertainty.

Table 4.4 - Refined structural parameters at room temperature of Li-doped $MnH_2P_2O_7$

Atom	Site	Occupancy	x	y	z	U_{iso} / Å²
Mn	4*a*	1	0	0	0	0.0049(3)
P	8*f*	1	0.3321(4)	0.1242(3)	0.8123(3)	0.0054(2)
O(1)	4*e*	1	0.5	0.0295(4)	0.75	0.0056(2)
O(2)	8*f*	1	0.2412(3)	-0.0168(3)	-0.1119(3)	0.0073(2)
O(3)	8*f*	1	0.1804(3)	0.8250(3)	0.1716(2)	0.0062(2)
O(4)	8*f*	1	0.0933(4)	0.2231(3)	0.1045(3)	0.0110(2)
H/Li	8*f*	0.75(2)/0.25(2)	0.3000(6)	0.2075(6)	0.3598(5)	0.0186(4)

Space group *C*2/*c*; *a* = 7.0835(4) Å, *b* = 7.9047(4) Å, *c* = 9.3955(4) Å and *β* = 101.198(2)°. Figures of merit: R_{wp} = 1.99%, R_p = 2.27%, χ^2 = 24.76

Table 4.5 - Selected bond lengths (Å) and bond angles (°)

Mn-O2	2.172(2)	**O2-Mn-O4**	94.2(1)
Mn-O3	2.306(2)	**O2-Mn-O4**	85.8(1)
Mn-O4	2.061(3)		
P-O1	1.611(2)	**O1-P-O2**	103.5(2)
P-O2	1.540(3)	**O1-P-O3**	103.7(2)
P-O3	1.594(3)	**O1-P-O4**	111.9(2)
P-O4	1.470(4)	**O2-P-O3**	106.1(2)
O3-H	1.003(5)	**O2-P-O4**	119.3(2)
P-O3-H	116.7(1)	**O3-P-O4**	110.2(2)

4.3.2.3 Magnetic Analysis of Li-Doped $MnH_2P_2O_7$

MPMS data were collected to investigate the magnetic properties of Li-doped $MnH_2P_2O_7$ and to compare with data from the parent phase. The magnetic susceptibility data and Curie-Weiss plot are shown in Figure 4.13. Li-doped $MnH_2P_2O_7$ displays paramagnetic behaviour, with a Weiss constant of −7.7 K, indicating a small antiferromagnetic component, which is very similar to that of $MnH_2P_2O_7$. The effective magnetic moment was calculated to be 5.67 μ_B which again is very similar to that for $MnH_2P_2O_7$ (5.78 μ_B) and is still consistent with the spin only

moment for high spin Mn^{2+} of 5.92 μ_B. Slight curvature to the Curie-Weiss fit once again, indicates some deviation to the ideal Curie-Weiss law. Overall there is no evidence for any difference in magnetic properties on incorporation of Li. This is not unexpected if all that happened is the replacement of some H^+ by Li^+.

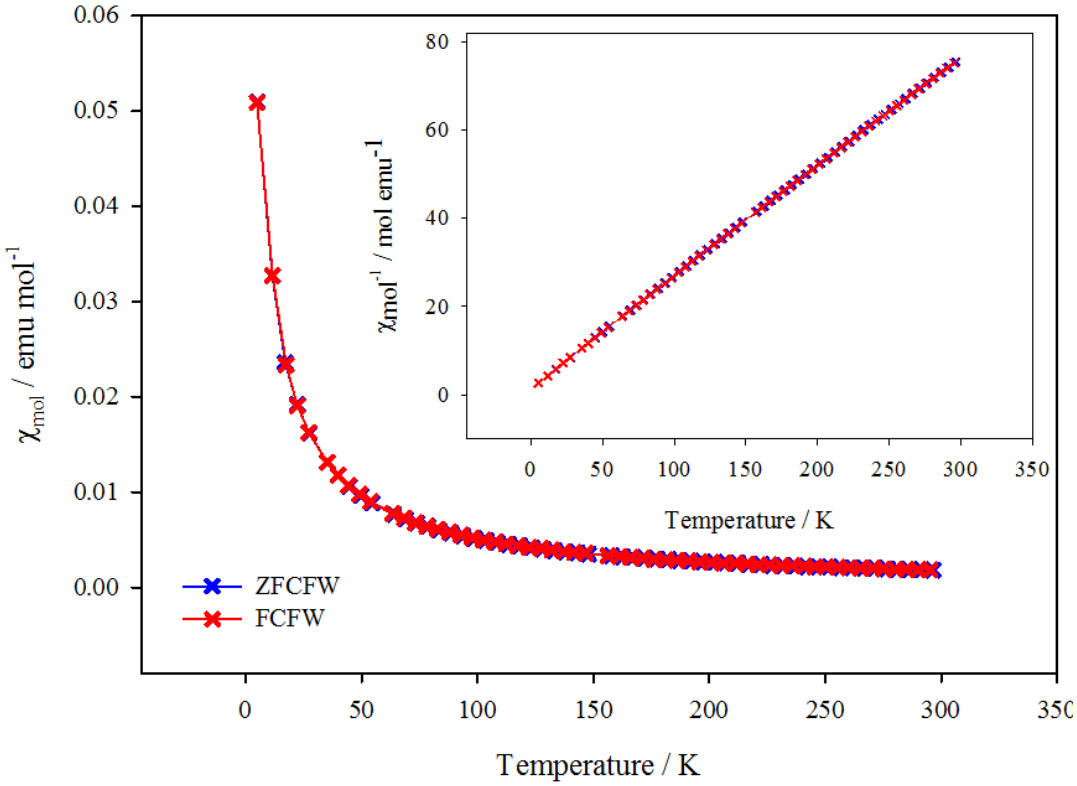

Figure 4.13 - Plot of molar susceptibility against temperature for Li-doped $MnH_2P_2O_7$, inset shows Curie-Weiss fit

4.4 Conclusion

$MnH_2P_2O_7$ was successfully synthesised using an acid melt, crystallising into the monoclinic space group *C*2/*c*. The composition was confirmed by TGA-MS and a Rietveld refinement was carried out using $CaH_2P_2O_7$ as a structural model, which gave an excellent fit. GII calculations suggest that the structure is strained. Magnetic measurements indicate that $MnH_2P_2O_7$ is paramagnetic with $\theta = -6.01$ K indicating a

small antiferromagnetic component and the effective magnetic moment is consistent with Mn^{2+} being high spin.

Rietveld refinement of the Li-doped $MnH_2P_2O_7$ suggests a similar structure to that of $MnH_2P_2O_7$ with partial replacement of protons to give the stoichiometry of $MnLi_{0.5}H_{1.5}P_2O_7$, however due to the presence of an unknown impurity this stoichiometry may be prone to uncertainty. Magnetic measurements show that Li-doped $MnH_2P_2O_7$ behaves similarly to its parent, displays paramagnetism with an antiferromagnetic component (θ = −7.7 K), and a moment suggestive of high spin Mn^{2+}. Thermally the Li-doped $MnH_2P_2O_7$ is less stable than the parent phase, undergoing condensation ~50°C lower than $MnH_2P_2O_7$, forming $Mn_2P_4O_{12}$ and $LiMn(PO_3)_3$, which also confirms the presence of Li in the sample. Further work will need to be undertaken to confirm the presence of Li in the structure, as well as identifying the unknown impurity phase.

References

1. V. Aravindan, J. Gnanaraj, Y. S. Lee and S. Madhavi, *Journal of Materials Chemistry A*, 2013, **1**, 3518-3539.
2. B. Y. Jibril, *Industrial and Engineering Chemistry Research*, 2005, **44**, 702-706.
3. Y. Begum and A. J. Wright, *Journal of Materials Chemistry*, 2012, **22**, 21110-21116.
4. J. D. Lee and L. S. Browne, *Journal of the Chemical Society A*, 1968, 559-561.
5. L. Adam, A. Guesdon and B. Raveau, *Journal of Solid State Chemistry*, 2008, **181**, 3110-3115.
6. H. Zhou, S. Upreti, N. A. Chernova, G. Hautier, G. Ceder and M. S. Whittingham, *Chemistry of Materials*, 2011, **23**, 293-300.

7. JCPDS, *International Centre for Diffraction Data*, 1999, P.1., Swathmore, Pennsylvania, PA 19081, USA 11990
8. R. Shirley, The Lattice Press, 41 Guildford Park Avenue, Guildford, Surrey GU2 7NL, England, Editon edn., 2002.
9. J. Laugier and B. Bochu, Laboratoire des Materiaux et du Génie Physique de l'Ecole Supérieure de Physique de Grenoble http://www.inpg.fr/LMGP/, Editon edn.
10. R. Glaum, H. Thauern, A. Schmidt and M. Gerk, *Zeitschrift fur Anorganische und Allgemeine Chemie*, 2002, **628**, 2800-2808.
11. J. Trommer, M. Schneider, H. Worzala and A. N. Fitch, *Materials Science Forum*, 2000, **321**, 374-379.
12. H. M. Rietveld, *Journal of Applied Crystallography*, 1969, **2**, 65-71.
13. A. C. Larson and R. B. Von Dreele, Los Alamos National Laboratory, Los Alamos NM, Editon edn., 1994.
14. B. H. Toby, *Journal of Applied Crystallography,* 2001, **34**, 210-213.
15. I. D. Brown and D. Altermatt, *Acta Crystallographica* 1985, **B41**, 244-247.
16. A. Salinas-Sanchez, J. L. Garcia-Muńoz, J. Rodriguez-Carvajal, R. Saez-Puche and J. L. Martinez, *Journal of Solid State Chemistry*, 1992, **100**, 201-211.
17. V. Pralong, R. Baies, V. Caignaert and B. Raveau, *Inorganic Chemistry*, 2009, **48**, 6835-6844.
18. T. Yang, J. Ju, G. Li, S. Yang, J. Sun, F. Liao, J. Lin, J. Saski and N. Toyota, *Inorganic Chemistry*, 2007, **46**, 2343-2344.
19. R. D. Shannon and C. T. Prewitt, *Acta Crystallographica Section B*, 1969, **25**, 925-946.
20. E. V. Murashova and N. N. Chudinova, *Crystallography Reports*, 2001, **46**, 942-947.

Chapter 5

Low Temperature Synthesis of TiP_2O_7 and V-Doped TiP_2O_7

5.1 Introduction

Titanium pyrophosphate is a member of the $A^{IV}X_2O_7$ series (where A^{IV} = Ce,[1] Ti,[2] Zr,[3] Si,[4] U,[5] Hf,[6] Ge,[7] Sn,[8] and X^{V} = P,[9] V,[9] or As[10]) that has garnered recent attention due to its ability to host a wide range of A^{4+} cations, and exhibit complex structures,[1] some of which show negative thermal expansion at high temperatures.[3, 5] The structures of this series have been well debated; many were initially thought to be cubic, with $a \approx 8$ Å, but many have since been shown to adopt cubic[2] or orthorhombic superstructures.[6] The most well-studied member of this series is ZrP_2O_7 and the vanadium-doped system, $ZrV_xP_{2-x}O_7$, which displays NTE above 100°C.[3] These $A^{IV}X_2O_7$ materials are of interest for a variety of applications including catalysis,[11] proton conductivity in fuel cells,[8] intercalation of Li^+/Na^+ in battery applications[12] and negative thermal expansion applications.[3] This chapter details the investigation of low temperature synthesis of TiP_2O_7 and V-doped TiP_2O_7. This study focuses on the structural characterisation, as well as thermal properties and particle morphology.

5.2 Experimental

5.2.1 Low Temperature Synthesis of TiP_2O_7

TiP_2O_7 was prepared via an acid melt. A mixture of TiO_2 and H_3PO_4, with a Ti:P ratio of 1:6, was stirred on a hotplate at 150°C for 3 hours in a porcelain crucible. The crucible was then placed in an oven at 200°C for 72 hours and allowed to cool to room temperature. The resulting paste was then washed with deionised water and suction filtered, leaving a white powder.

5.2.2 Synthesis of V-Doped TiP_2O_7

V-doped TiP_2O_7 was prepared in a similar fashion to the parent phase. TiO_2 and a vanadium source were ground together and then added to orthophosphoric acid in a porcelain crucible, with a Ti:V ratio ranging from 9:1 to 1:9, whilst maintaining a M:P ratio of 1:6. The solution was stirred on a hotplate at 150°C for 3 hours until a melt was formed. The crucible was then heated in an oven at 200°C for 72 hours. The resulting paste was then washed with deionised water and suction filtered, leaving a coloured powder, depending on the initial vanadium source. Vanadium metal gives a yellow-orange powder, vanadium (V) oxide a yellow powder and vanadium (IV) oxide a dark green powder.

5.2.3 Collection of Diffraction Data

X-ray powder diffraction data were collected on a Bruker AXS: D8 Advance diffractometer in transmission mode using a 2θ range of 5-90°. Neutron powder diffraction data of V-doped TiP_2O_7 were recorded on the TOF powder diffractometer

Polaris instrument at ISIS, Rutherford Appleton Laboratory. Variable temperature X-ray powder diffraction data were collected on a Bruker AXS: D8 Advance diffractometer, fitted with the Anton Paar HTK1200 heating stage, and the Siemens D5000, fitted with an Oxford cryostream. Selected area electron diffraction data were collected by Dr Zoe Schnepp at the Centre of Electron Microscopy, University of Birmingham. The SAED films were developed by staff at the Centre of Electron Microscopy.

5.3 Results & Discussion

5.3.1 TiP_2O_7

A literature search for the synthesis of MP_2O_7 found synthetic temperatures ranging from 600 to 1350°C[1, 5, 6, 8, 11, 13, 14] mainly via ceramic routes, with synthetic temperatures for TiP_2O_7 mainly quoted as between 600-700°C.[11, 13, 15, 16] The acid melt synthetic procedure had previously been seen to be successful in the synthesis of similar pyrophosphate materials, and so a low temperature synthesis of TiP_2O_7 was attempted. Synthesis resulted in what appeared to be a majority single phase product which was indexed to the cubic sub-cell[14] of the TiP_2O_7 superstructure, with space group $Pa\bar{3}$ where a = 7.8884(1) Å. A Rietveld refinement[17] was carried out using the GSAS suite[18] of programs and EXPGUI,[19] using the cubic sub-cell as a structural model; this lead to the discovery of two TiP_2O_7 phases with different lattice parameters. With such a small difference in lattice parameter no modelling of differences was undertaken and therefore the model was constrained to be the same except for lattice parameters. The refined structural parameters are shown in table

5.1, and selected bond distances and angles are shown in tables 5.2 and 5.3. The Rietveld refinement plot of PXRD data is shown in figure 5.1. A small impurity peak is observed at 24°, the identity of this impurity is unknown as no satisfactory match was found on the JCPDS database.[20] Repeated syntheses were unable to remove this impurity but found the relative intensity of this additional peak changed when compared to the main phase, and so was consistent with an impurity phase, rather than superstructure.

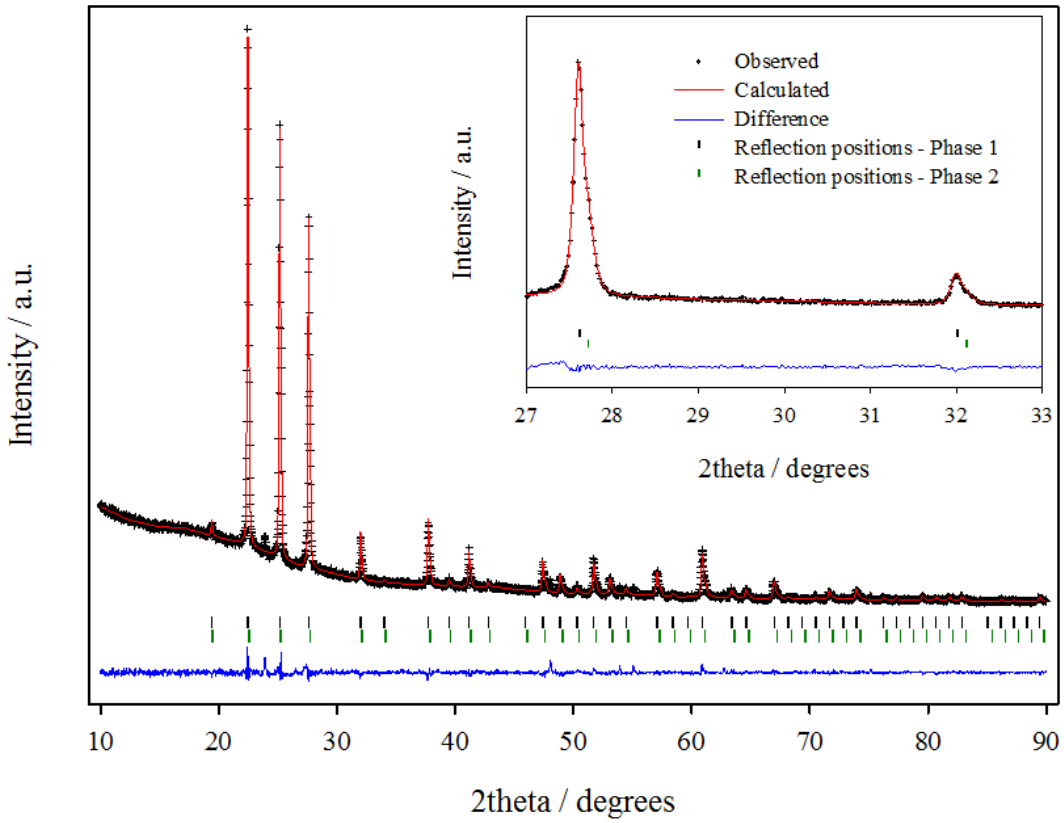

Figure 5.1 - Rietveld refinement plot of low temperature synthesised TiP_2O_7, inset shows the absence of super-cell peaks

Table 5.1 - Refined structural parameters of low-temperature synthesised TiP_2O_7 (both phases)

Atom	Site	Occupancy	x	y	z	U_{iso} (Å^2)
Ti	4*a*	1	0	0	0	0.0257(8)
P	8*c*	1	0.3908(2)	0.3908(2)	0.3908(2)	0.0095(9)
O1	24*d*	1	0.4400(3)	0.2223(5)	0.4229(5)	0.070(2)
O2	4*b*	1	0.5	0.5	0.5	0.116(4)

Space group: $Pa\bar{3}$; Phase 1: a = 7.8889(2) Å; Phase 2: a = 7.8526(3) Å. Figures of merit: R_{wp} = 4.88%, R_p = 3.43%, χ^2 = 2.405. Refined weight percent: phase 1 = 79.7(1)%, phase 2 = 20.3(2)%

Table 5.2 - Selected bond lengths (Å) and angles (°) of LTS TiP_2O_7 – Phase 1

Ti_O1	1.915(3)	**P_O1**	1.408(3)
O1_Ti_O1	89.2(1)	**P_O2**	1.492(3)
O1_Ti_O1	90.8(1)	**O1_P_O1**	112.4(2)
P_O2_P	180	**O1_P_O2**	106.4(2)

Table 5.3 - Selected bond lengths (Å) and angles (°) of LTS TiP_2O_7 – Phase 2

Ti_O1	1.906(3)	**P_O1**	1.402(3)
O1_Ti_O1	89.2(1)	**P_O2**	1.486(3)
O1_Ti_O1	90.8(1)	**O1_P_O1**	112.4(2)
P_O2_P	180	**O1_P_O2**	106.4(2)

The refinement gives a good fit to the sub-cell model, converging at an R_{wp} of 4.88%. The presence of two separate TiP_2O_7 phases is particularly noticeable in the peak shape, especially at higher angles. There is no evidence of any super-cell reflections in the pattern; however, this does not mean that both phases adopt the sub-cell structure. Due to the low weight percentage of the secondary TiP_2O_7 phase, if this phase did adopt the superstructure, the low intensity super-cell peaks would not be observed over the background intensity. The thermal parameters are quite high, especially O2 which is extremely high. This may indicate that the oxygen, which sits on an inversion axis, is in an incorrect position. This may also mean that the symmetry of the structural model is incorrect. Oxygen positions are difficult to

determine using XRD as they are relatively weak X-ray scatterers compared to the other heavier elements in the structure, and so are less reliable in XRD refinements. This means other techniques need to be employed to determine the positions of the oxygen atoms within the structure accurately. Bond valence sum calculations (see appendix 1) indicate that both Ti^{4+} and P^{5+} are over bonded, with calculated values of +4.58 and +6.68 respectively. Due to the symmetry restrictions of the space group, the Ti-O and P-O bond lengths are both relatively short, which leads to the high calculated valences. This could be a further indication that there are inadequacies with the structural model.

A recent study by Palacín *et al.*[12] also investigated the low temperature synthesis of TiP_2O_7 (LT-TiP_2O_7) which resulted in a single phase product that adopts the simple cubic sub-cell. This was achieved via the dissolution of Ti metal into orthophosphoric acid at 170°C, a similar synthetic procedure to the synthesis used in this study, albeit at a lower temperature and with a different titanium source.

The reason for the presence of two seemingly identical phases with differing lattice parameters is unknown; there may be differences in composition or differences in structure. Neither lattice parameter match previously reported values for TiP_2O_7.

5.3.1.1 Thermal Stability of LTS – TiP_2O_7

Given the relatively low temperature synthesis, the thermal stability of LTS-TiP_2O_7 was investigated using TG analysis. A sample was heated at 10K min^{-1} to 1000°C under an O_2/N_2 atmosphere. The TGA-MS plot is shown in figure 5.2.

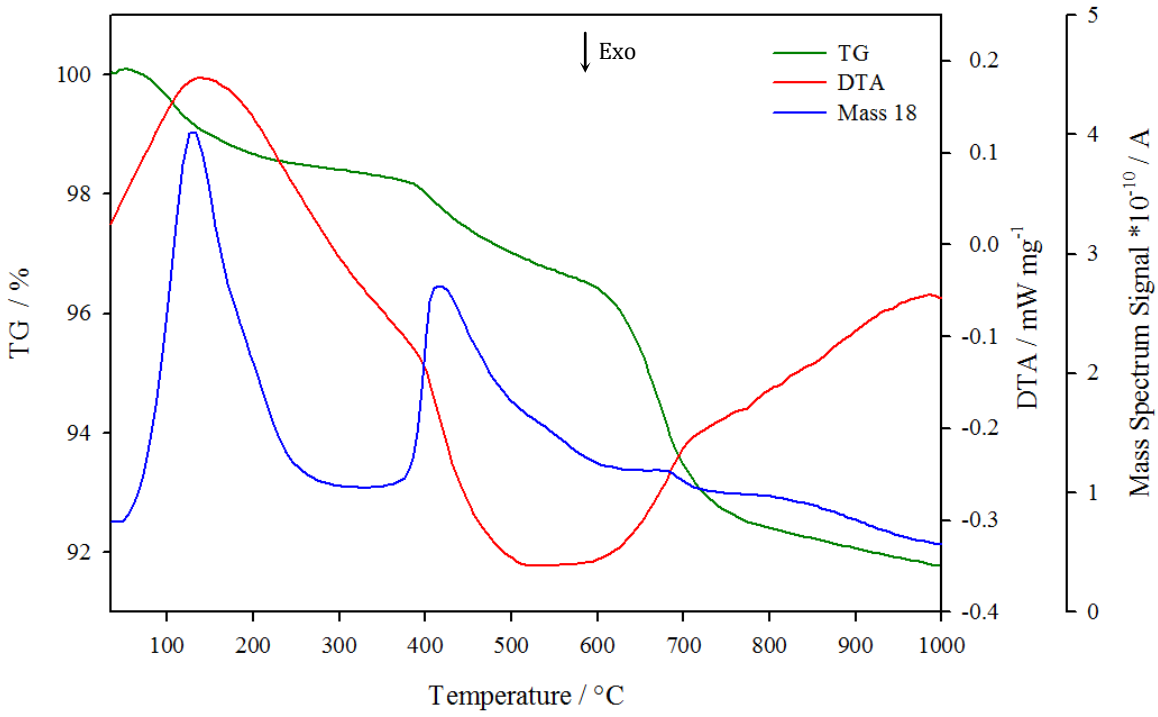

Figure 5.2 - TGA-MS plot of LTS TiP_2O_7

Initially there was a mass loss of ~1.5% at 120°C, which coincided with a broad peak in the MS signal for mass 18, which appears consistent with the loss of surface water. A second mass loss of ~1.75% occurs over a very broad temperature range, 400-600°C. The MS signal for mass 18 shows a broad peak in this temperature range; the peak has an apparent shoulder to it, which may indicate there are multiple origins of the water evolved in this region and is therefore consistent with the presence of two similar TiP_2O_7-type phases. A further mass loss of ~5% occurs at

650°C and given that there is a small peak in the mass 18 MS signal it is unlikely that is final mass loss is due to loss of water. To provide some scale to this, if the sample is considered to contain purely $TiP_2O_7.nH_2O$ and the overall mass loss was purely due to water, the loss would equate to n = 1.25 moles of water. If only the first two mass losses are included, it would equate to n = 0.34 moles of water. This large mass loss in the 650°C region has also been observed by Palacín *et al.* for LT-TiP_2O_7,[12] with no MS signal above m/z = 225; however the mass loss observed was much larger, ~12%, occurring above 550°C. The author suggests this mass loss is due to decomposition of amorphous phosphates/pyrophosphates, to form water and P_xO_y which then sublimes (P_4O_{10} is reported to sublime over 450°C).[21] There is no evidence of any signal in the mass spectrum up to m/z = 225 around 550°C to support this, however if the transfer line from TGA to the mass spectrometer is significantly cooler than the furnace it may lead to solidification of the sublimed phosphorus oxide, leading to no signal in the MS. EDS analysis[12] of LT-TiP_2O_7 post heat treatment is in agreement with the loss of phosphorus oxide from the sample.

The PXRD pattern post heat treatment showed additional peaks, which could be indexed onto the cubic super-structure, space group $Pa\bar{3}$, reported by Norberg *et. al*.[2] The Rietveld refinement plot is shown in figure 5.3, oxygen positions were not refined and a global isotropic thermal parameter was used for each atom type. The refinement gave a good fit, converging at a low R_{wp} of 4.41%, with a lattice parameter a = 23.5692(5) Å (see appendix 3 for more details). There is no evidence of any additional unmatched peaks indicating that the cubic structure is indeed adopted, and the sample is phase pure.

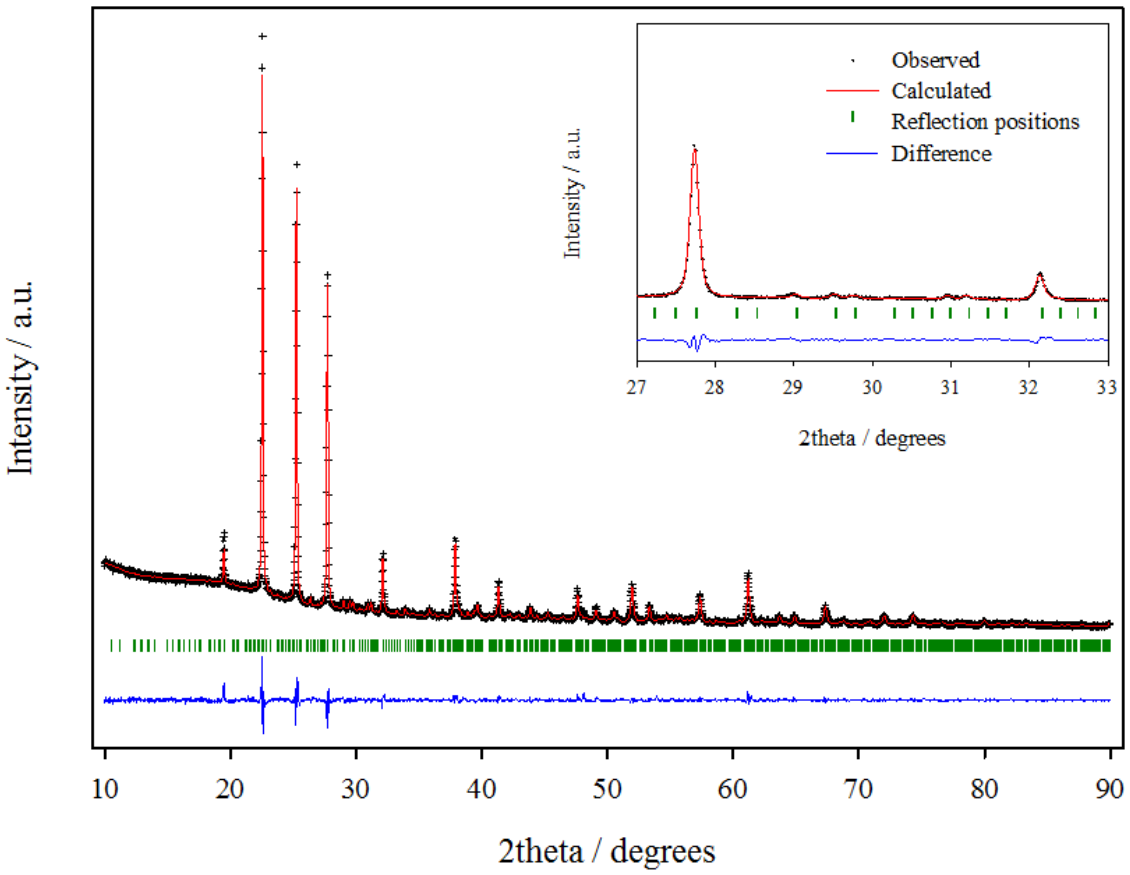

Figure 5.3 - Rietveld refinement plot of heat treated TiP_2O_7 with the cubic superstructure model, superstructure peaks shown in inset

To quantify the amorphous component of LTS-TiP_2O_7, a crystalline reference material TiO_2 was ground with LTS-TiP_2O_7 in a 1:4 weight % ratio respectively, and XRD data were collected on the mixed sample and a multiple phase refinement was carried out. The phase fractions were allowed to vary, which gave phase fractions of 61.8(2)% and 13.4(2)% for phases 1 and 2 of LTS-TiP_2O_7 and 24.8(2)% for TiO_2. This confirms the presence of amorphous material. The weight fraction of a crystalline phase, w_i, in the Rietveld method is calculated by the following equation:

$$w_i = \frac{S_i M_i V_i}{\sum_j S_j M_j V_j} \times 100\% \qquad (5.1)$$

where S is a phase fraction scale factor, M is the mass of the unit cell and V is the volume of the unit cell, summed over all the crystalline phases present, j, based on the condition that $\Sigma(w_i) = 100\%$. The Rietveld method will only model crystalline phases, so the weight fractions are always summed to 100%. The actual weight % of added TiO_2 is known (20 wt%), but in the refinement the weight percent for TiO_2 is 24% higher. This would give phase fractions of 49.8% for phase 1, 10.6% for phase 2 and an amorphous content of 19%. If we consider the original LTS-TiP_2O_7 sample (i.e. without added TiO_2), then the estimate of the amorphous component equates to 24%. This was repeated with samples that had been heat treated at 500°C and at 1000°C, and they displayed reduced amorphous contents of 16% and 5% respectively as the temperature was increased. A sample that had been heat treated to 1200°C was found to have negligible amorphous content and consisted purely of TiP_2O_7. Bamberger *et al.*[22] reported that TiP_2O_7 begins to decompose at 1200°C to form TiO_2 and P_2O_5 after a prolonged period of heating. The loss of amorphous material appears to correlate with the mass losses in the TGA-MS measurements. It is possible that the amorphous material could consist of hydrated phases, such as $TiP_2O_7.H_2O$ or $Ti(HPO_4)_2{\cdot}H_2O$. Sanz *et al.*[16] reported that during synthesis of TiP_2O_7, α-$Ti(HPO_4)_2{\cdot}H_2O$ and H_3PO_4 were the main constituents. The first water loss is consistent with surface/associated water; the second with a condensation reaction. $Ti(HPO_4)_2{\cdot}H_2O$ could account for the first two mass losses in the TG signal. Solid state NMR might give a further insight into the composition of the amorphous content.

Variable temperature XRD was used to follow the thermal decomposition pathway. A sample was heated in an Anton Paar HTK1200 heating stage, with diffraction patterns taken at 25-50°C intervals from 50 to 1000°C and upon cooling.

Figure 5.4 shows a stack plot of the diffraction patterns. It is apparent that the structure is maintained upon heating, but upon closer inspection it appears there is an area of negative thermal expansion. This is shown more clearly in figure 5.5, where the presence of a secondary TiP_2O_7 phase is apparent as a sizeable shoulder in the peak at 22.4°, especially at low temperatures. The sample becomes more crystalline as it is heated; this is apparent in the increased intensity of (*111*) peak at 19.5°.

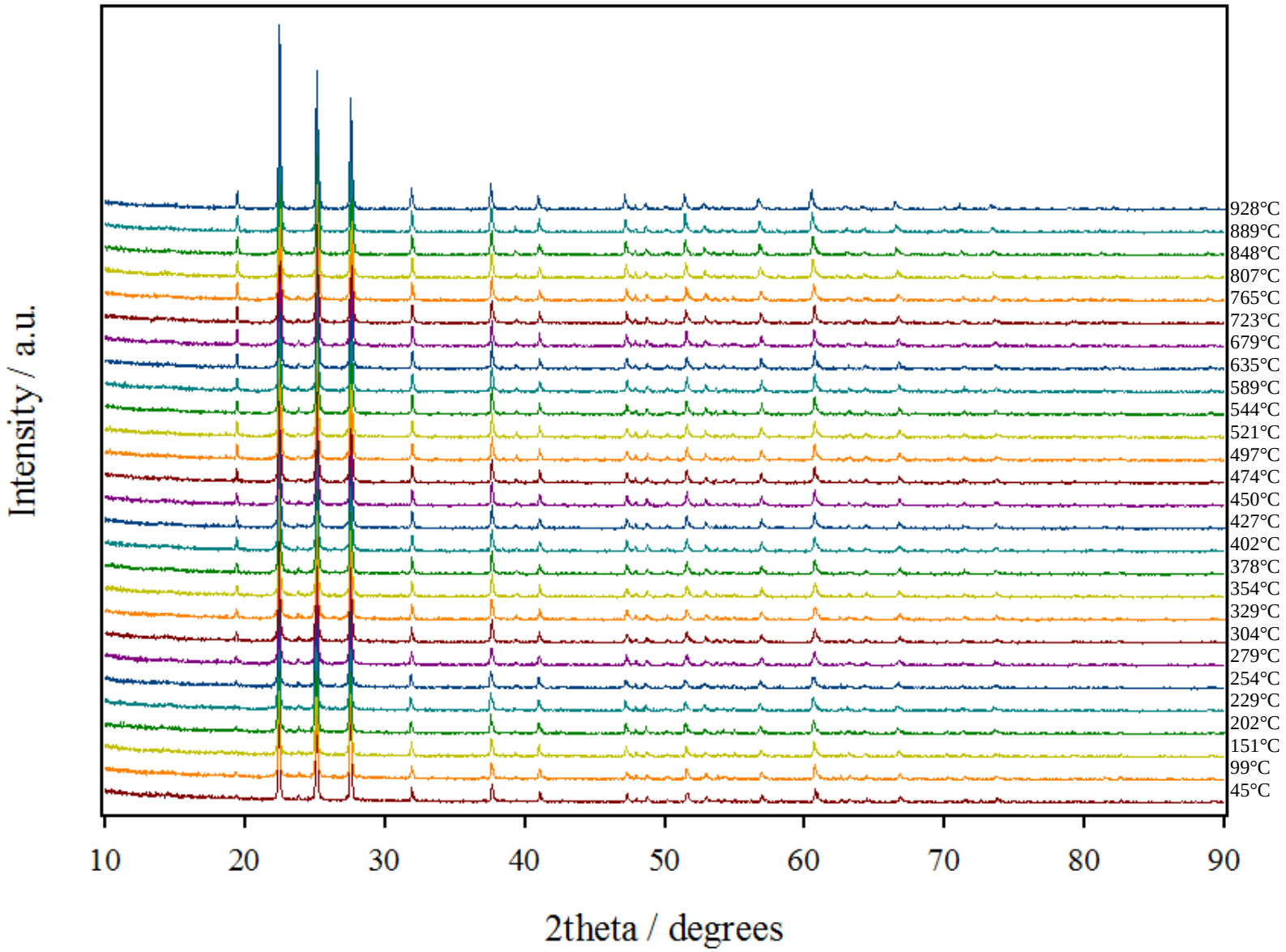

Figure 5.4 - Stack plot of Variable Temperature-XRD data of LTS-TiP_2O_7 upon heating

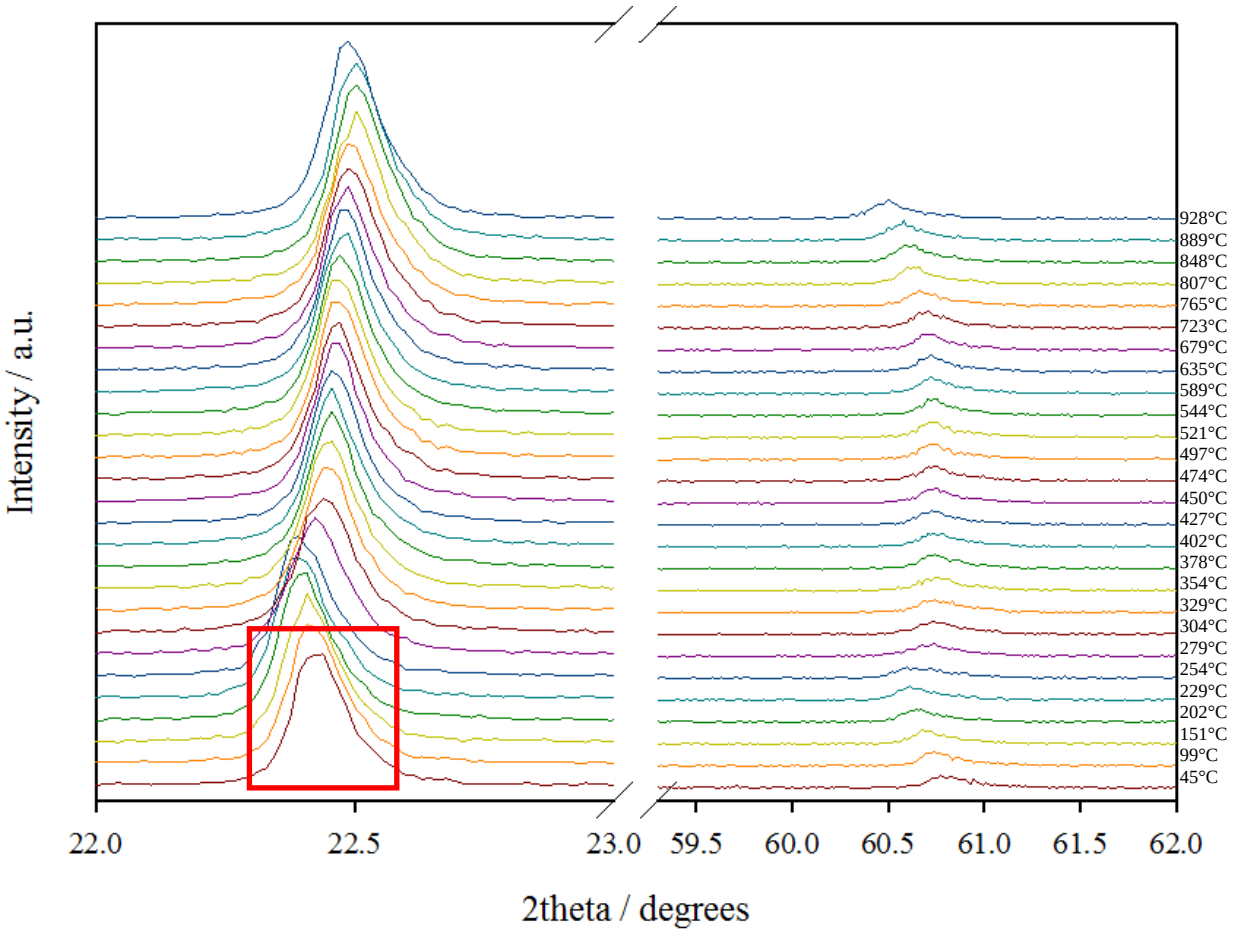

Figure 5.5 - Stack plot of VT-XRD data of LTS-TiP_2O_7 upon heating, the red box highlights the presence of a secondary TiP_2O_7 phase as a shoulder on the peak at 22.4°

Positive thermal expansion is observed from 45-254°C through a shifting of the peaks to lower 2theta, leading to a larger d-spacing and therefore a larger lattice parameter, *a*. The peaks then begin to shift to higher 2theta at 279°C, leading to a smaller d-spacing indicating negative thermal expansion until 329°C. From this point the positive thermal expansion is observed again until 928°C with shifting of the peaks to lower 2theta.

Diffraction patterns were taken every 50°C upon cooling, which are shown in figure 5.6. There is no evidence of any expansion which would be evident if the cell

underwent true negative thermal expansion upon heating. Upon cooling the peaks shift to higher 2theta signifying cell contraction. Above 723°C the cubic sub-cell is adopted, however below this temperature, the appearance of additional faint peaks between 27 and 32° indicate that the super-structure is adopted.

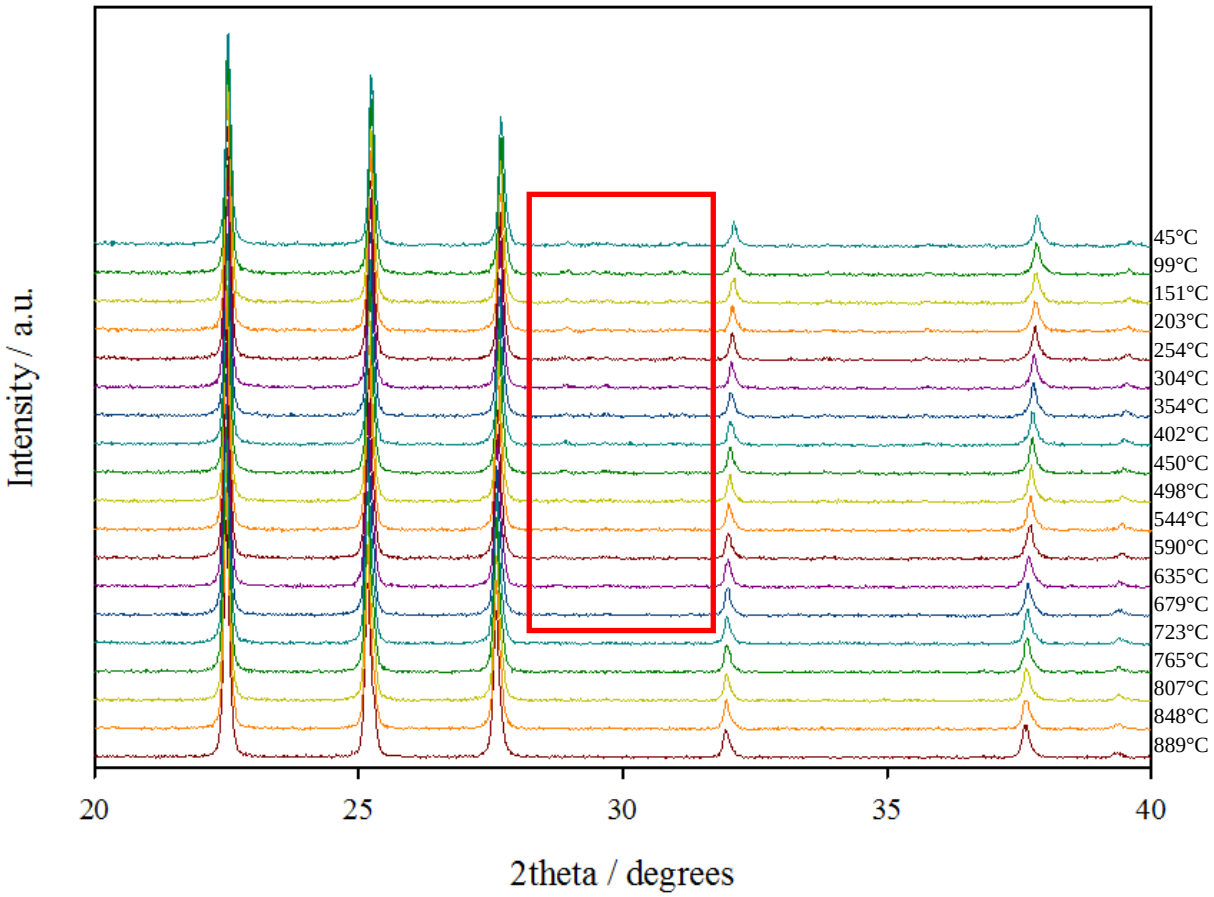

Figure 5.6 - Stack plot of VT-XRD data of LTS – TiP_2O_7 upon cooling, with super-cell region highlighted by red box

GSAS was used to obtain lattice parameters for the two phases. A plot of the lattice parameters upon heating is shown in figure 5.7 and cooling in figure 5.8.

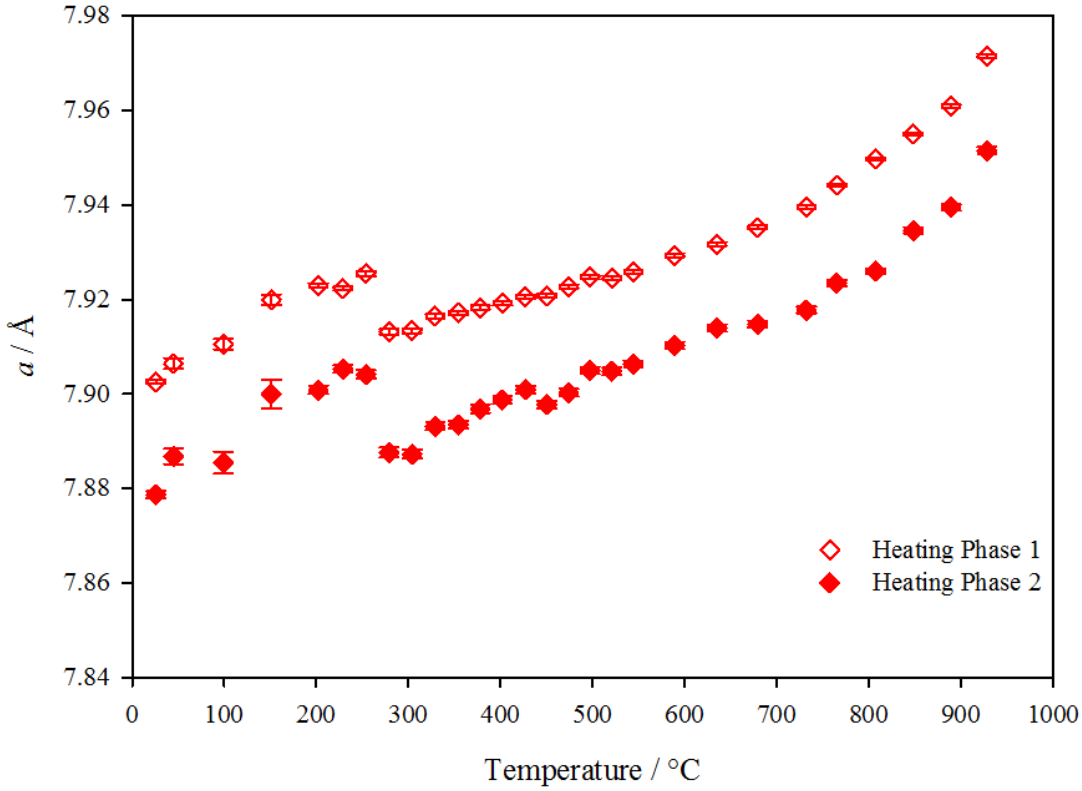

Figure 5.7 - Lattice parameter plot of two phase LTS – TiP_2O_7 indexed using the cubic sub-cell, space group $Pa\bar{3}$ versus temperature upon heating

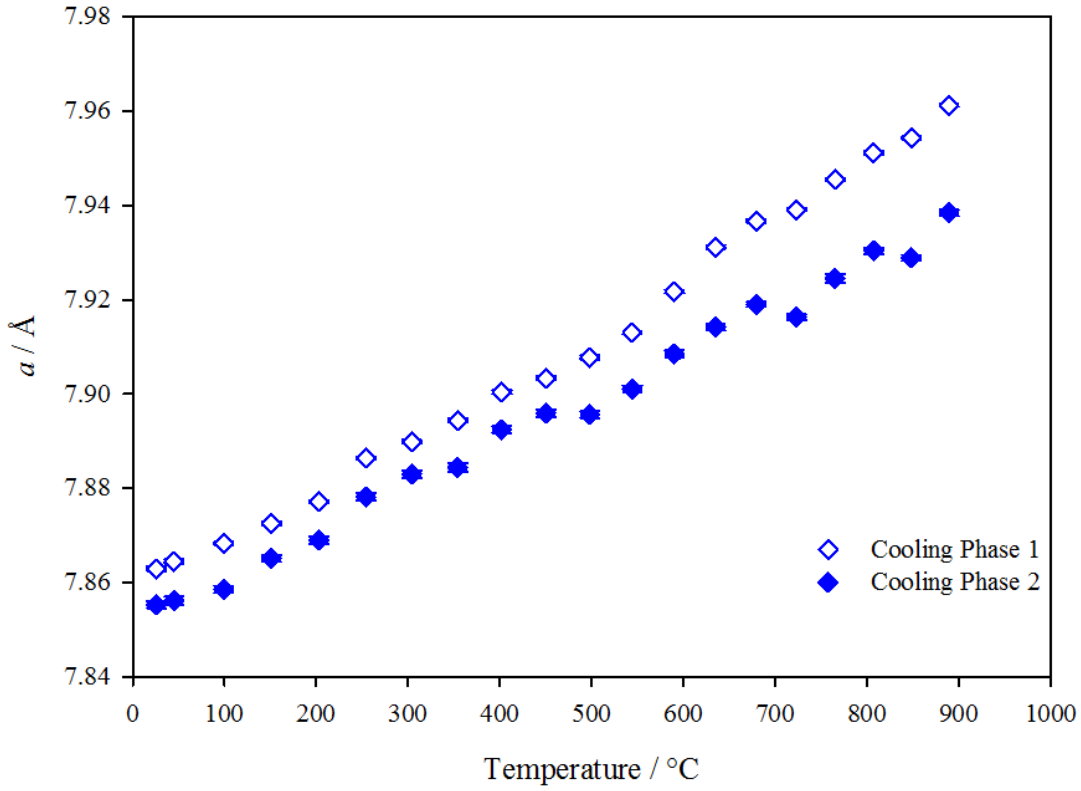

Figure 5.8 - Lattice parameter plot of two phase LTS – TiP_2O_7 upon cooling

It is evident as the sample was heated, positive thermal expansion occurs through an increase in *a* from room temperature to 279°C for both phases. From this point there is very small decrease of 0.1%. There is a very small expansion from 378 to 544°C, with a larger increase above 800°C. The lattice parameter for phase 2, the minority phase, is noticeably smaller than phase 1 during heating.

Upon cooling there is a contraction of the unit cell, leading to a smaller unit cell overall after heat treatment than the initial starting model. The lattice parameters for both phases are much closer in size upon cooling; two phases can be refined however the reliability of the results is questionable. The refined weight percent of phase 2 decreases upon heating which questions the validity of assigning two phases in these heat-treated samples. Higher resolution data is needed to clarify the presence of the secondary phase.

Due to the low weight percentage of the second phase and its reduction on heating, the refinement was carried out as a single phase refinement, replacing the two phases. The lattice parameter plot is shown in figure 5.9. The lattice parameter matches closely that of phase 1 upon heating and cooling, which is not unexpected as phase 1 is the majority phase.

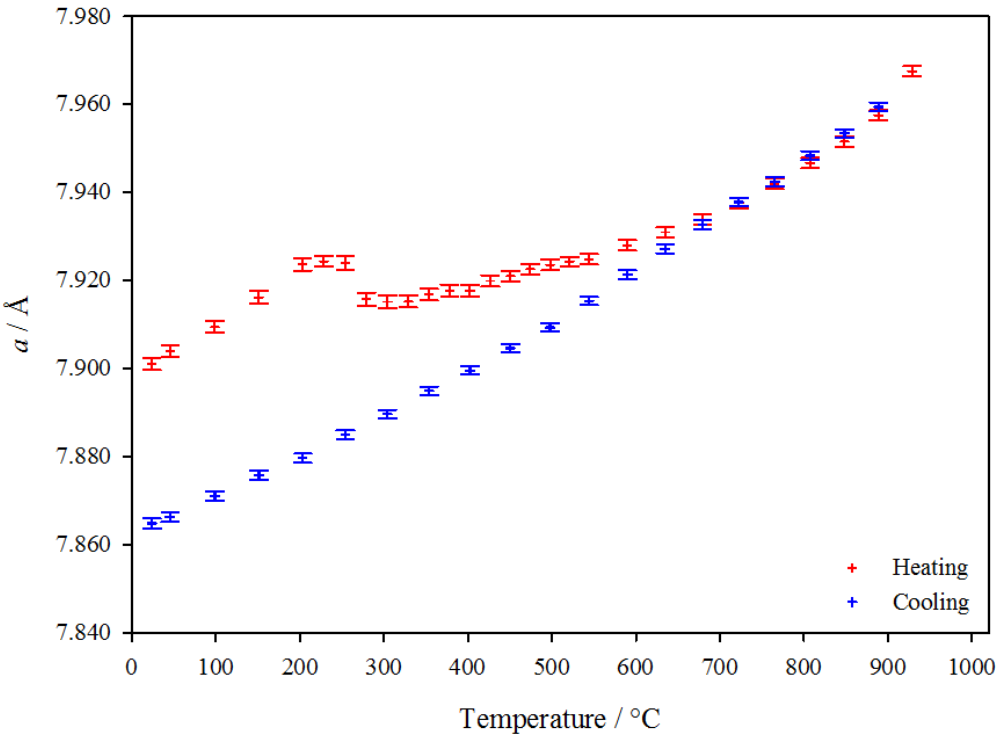

Figure 5.9 - Lattice parameter plot of single phase LTS – TiP_2O_7 indexed using the cubic sub-cell, space group $Pa\bar{3}$ versus temperature

There is no evidence of any expansion upon cooling in either cooling plot. This indicates that the NTE is not reversible, and therefore is not true NTE. It is more likely that a phase transition is occurring that traverses through a more compact transition state.

The sample then underwent a second heat treatment in the VT-XRD, with the single phase lattice parameter plot shown in figure 5.10. The plot shows that upon heating positive thermal expansion occurs leading to a larger cell. Upon cooling the cell contracts as it does during the first cooling cycle. There is no evidence of any NTE during the second VT-XRD cycle, which may indicate that LTS–TiP_2O_7 is a meta-stable polymorph of TiP_2O_7. The super-cell peaks are present in the second heat cycle until between 723°C and 765°C, where the structure adopts the cubic sub-cell. The super-cell peaks appear at the same temperature range during cooling.

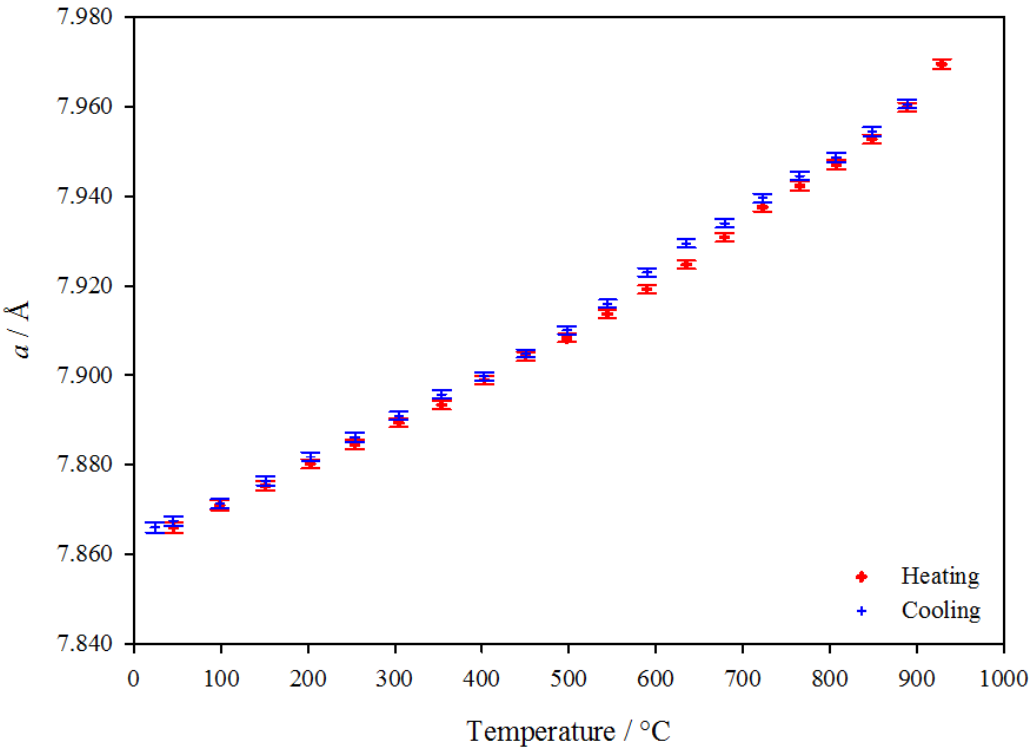

Figure 5.10 - Lattice parameter plot of LTS – TiP_2O_7 indexed using the cubic sub-cell upon second VT-XRD

5.3.2 Vanadium-Doped TiP_2O_7

Vanadium-doped ZrP_2O_7 is known to exhibit NTE,[3] and so vanadium doping of TiP_2O_7 via low temperature synthesis was attempted to investigate whether this behaviour was present in the analogous titanium-based system. Vanadium metal was introduced into the melt in various Ti:V ratios, which resulted in an yellow-orange powder. Washings of the precipitate gave a green solution, suggesting the solution contains V^{3+} and therefore that not all of the vanadium in the melt had been incorporated into the structure. Figure 5.11 shows the indexed lattice parameters for the V-doped samples. Increasing the initial V content in the starting melt leads to a very small increase in *a*. Above the nominal 50% doping the samples appear less

crystalline and at higher levels a vanadium based impurity, $VH_2P_3O_{10}$,[23] is apparent in the diffraction patterns of samples.

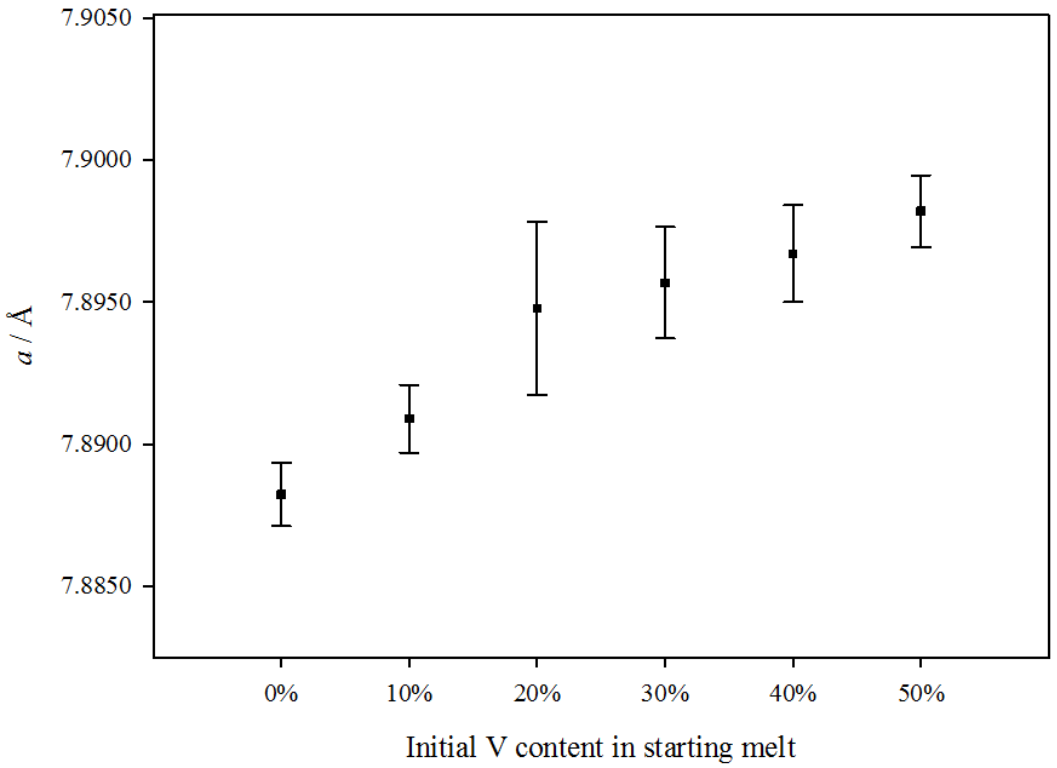

Figure 5.11 - Lattice parameter plot of V-doped TiP_2O_7 with increasing V content in initial reaction

Due to the small cell expansion and the colour of the washing solution it is unlikely that a large amount of vanadium is incorporated into the structure. XRF was used initially to quantify the vanadium content in the synthesised samples, and the data is shown in table 5.4. XRF measures the vanadium content in the whole sample, not just in the TiP_2O_7 structure. The results show that as the vanadium content in the initial melt increases, the vanadium content in the sample also increases. The results are from loose powder which does not give the most accurate weight percentage due to matrix effects, including particle size/surface effects. Fused beads are commonly used to minimise these effects and give a more accurate elemental composition. The results from the fused bead of the nominal 50% doped sample gives a Ti:V:P molar

ratio of 0.37:0.08:1, which would give a composition of $Ti_{0.74}V_{0.16}P_2O_7$, which shows an excess of phosphorus/deficiency of Ti/V. There is some uncertainty in the weight percentages of Ti and V due to overlap of the Ti $K\beta_1$ and V $K\alpha_1$ and $K\alpha_2$ emission lines at 4.9 and 5.0 keV. Further work is needed confirm the actual composition, but based on the XRF measurements we can estimate the V content is between 10-20 mol% which is assumed to be all in the main phase. This level of V content is consistent with the lattice parameter changes in figure 5.11, in that above ~20% there is a discernible plateau.

Table 5.4 – XRF calculated compositions from loose powder measurements

Initial V content	Weight %			Molar Ratio		
(molar %)	Ti	P	V	Ti	P	V
0	13.59	23.3	0	0.755	2	0
10	17.43	22.2	1.50	1.015	2	0.081
20	15.59	22.2	2.10	0.909	2	0.117
30	14.69	22.4	2.87	0.849	2	0.155
40	14.71	22.3	3.11	0.853	2	0.169
50	12.83	18.3	3.30	0.907	2	0.220
50*	15.54	27.14	3.61	0.742	2	0.162

*Fused bead measurement

Within the structure there are two possible sites for the vanadium to occupy: the Ti site or the P site. Table 5.5 compares the ionic radii of vanadium oxidation states to the potential sites the vanadium could occupy.

Table 5.5 - List of ionic radii and coordination

Ion & Coordination	Ionic Radii (pm)[24]
Ti^{4+} (octahedral)	74.5
P^{5+} (tetrahedral)	31
V^{3+} (octahedral)	78
V^{4+} (octahedral)	72
V^{5+} (tetrahedral)	49.5
Zr^{4+} (octahedral)	86

In $ZrV_xP_{2-x}O_7$, vanadium occupies the phosphorus site[3] as V^{5+}, which is most likely due to cation size. Based on size, the most likely site the vanadium could occupy would be the Ti^{4+} site, as V^{4+} is much closer in size to Ti^{4+} than V^{5+} is to P^{5+}. To confirm the presence of vanadium in the sample, XRF and EDS were used, with ESR confirming the presence of V^{4+},[25, 26] shown in figure 5.12; the spectrum matched the reported spectra in Wiench *et al.*[26] Unfortunately the presence of solely V^{4+} could not be confirmed as V^{5+} is d^0 and so no signal would be observed in the ESR spectrum, nor does it quantify the amount of V^{4+} is in the sample. There is also the possibility that some vanadium is not included in the structure, but forms an amorphous component in the sample.

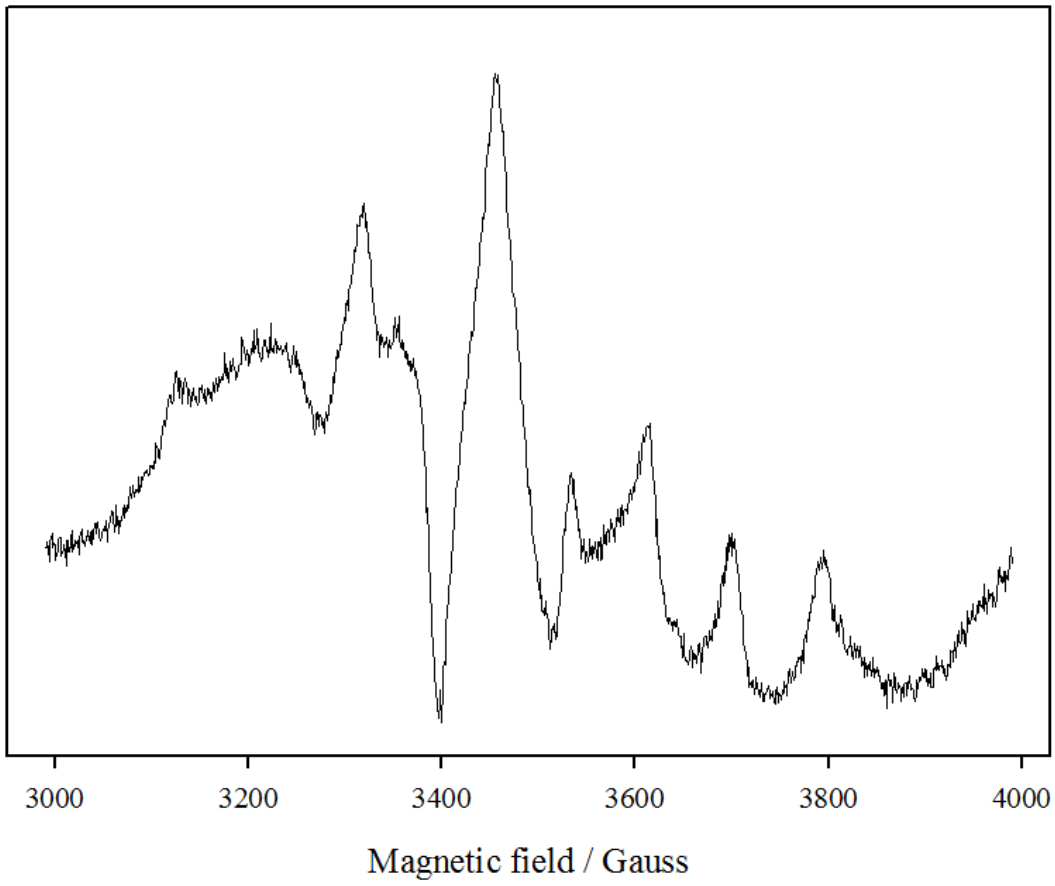

Figure 5.12 - ESR spectrum of V-doped TiP_2O_7, the signal is indicative of V^{4+}[26]

The most crystalline sample was the nominal 50% doped sample. A Rietveld refinement was carried out using on the 50% doped sample using the cubic sub-cell as the structural model and this gave an excellent fit, converging at an R_{wp} of 3.76%. Due to the similarity in X-ray atomic scattering factors for Ti and V, such a refinement is unable to differentiate between them to calculate site occupancies and therefore V was not modelled in the refinement. The Rietveld refinement plot is shown in figure 5.13, with the refined structural parameters and selected bond lengths and angles shown in tables 5.6 and 5.7. There is no evidence of any super-cell peaks or of the multiple phases that were seen in LTS-TiP_2O_7.

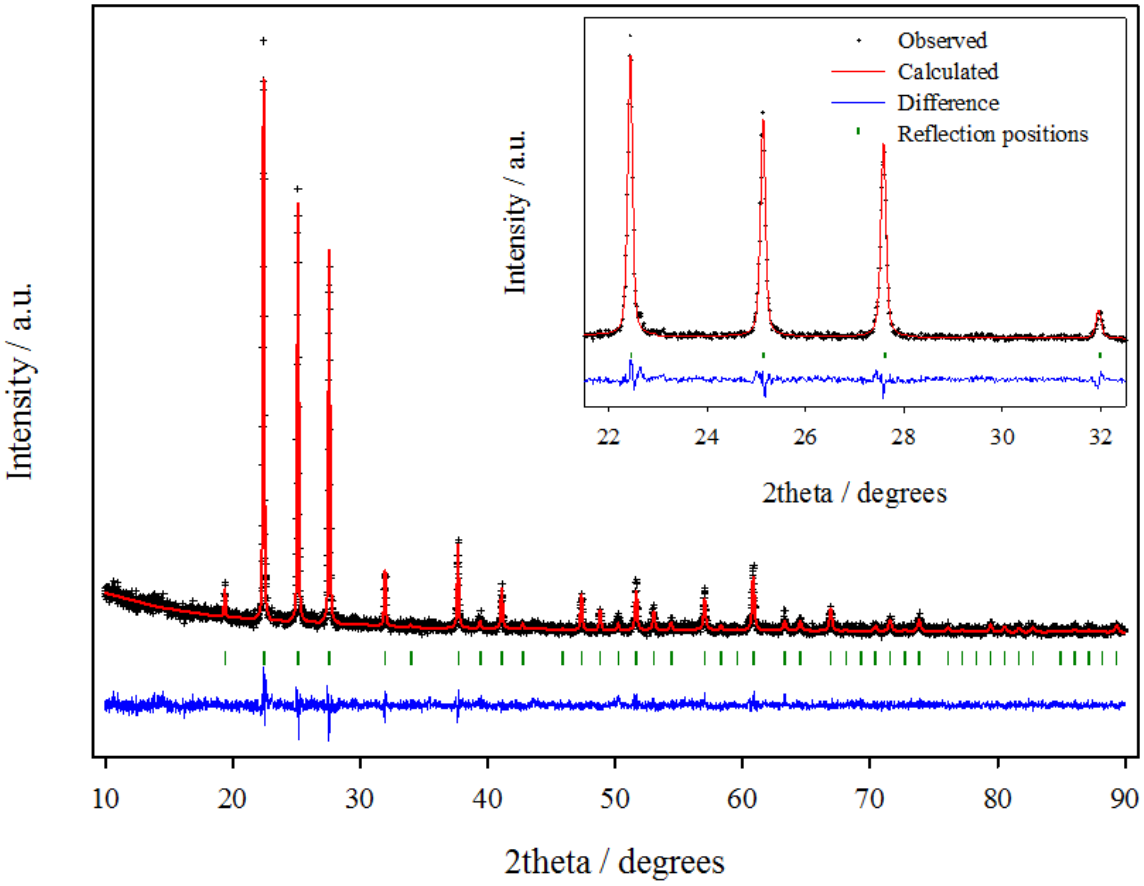

Figure 5.13 - Rietveld refinement plot of V-doped TiP_2O_7

Table 5.6 – Refined structural parameters of V-doped TiP_2O_7

Atom	Site	Occupancy	x	y	z	U_{iso} (Å²)
Ti	4*a*	1	0	0	0	0.009(1)
P	8*c*	1	0.3912 (4)	0.3912(4)	0.3912(4)	0.007(2)
O1	24*d*	1	0.4431(5)	0.2197(8)	0.4268(8)	0.064(3)
O2	4*b*	1	0.5	0.5	0.5	0.131(7)

Space group $Pa\bar{3}$; a = 7.8975(3) Å. Figures of merit: R_{wp} = 3.76%, R_p = 2.83%, χ^2 = 1.408

Table 5.7 - Selected bond lengths (Å) and angles (°) of V-doped TiP_2O_7

Ti_O1	1.878(5)	**P_O1**	1.449(4)
O1_Ti_O1	90.3(2)	**P_O2**	1.488(5)
O1_Ti_O1	89.7(2)	**O1_P_O1**	113.1(3)
P_O2_P	180	**O1_P_O2**	105.5(4)

The refined structure fits well to the cubic sub-cell, giving a slightly larger lattice parameter compared to both phases of LTS-TiP_2O_7. The refined thermal parameters are lower than that of LTS-TiP_2O_7, apart from O2 which is similarly higher. Again this may indicate a problem with O2 position, and so the structural model may not be providing a complete description of the subtlety of the framework.

5.3.2.1 Thermal Stability of V-Doped TiP_2O_7

TGA-MS was used to investigate and compare the thermal stability of V-doped TiP_2O_7 to that of LTS-TiP_2O_7. A sample was heated at 10K min^{-1} to 1000°C under an O_2/N_2 atmosphere. The TGA-MS plot is shown in figure 5.14.

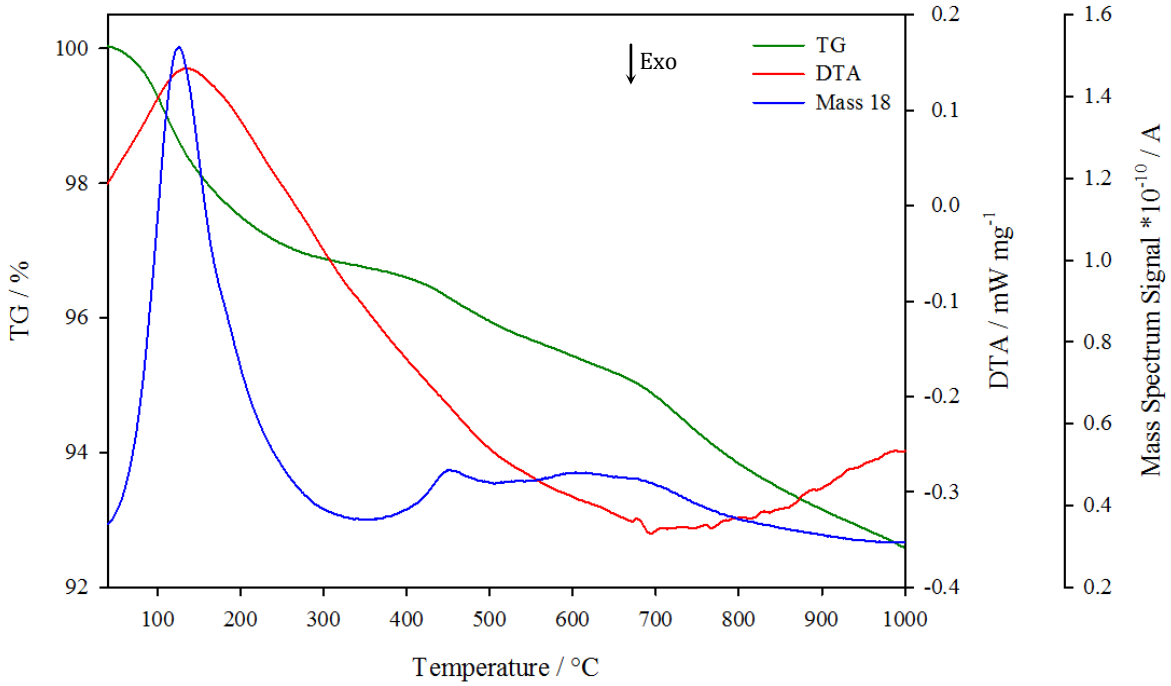

Figure 5.14 - TGA-MS plot of V-doped TiP_2O_7

Initially there was a mass loss of ~3.3% occurring over a 250°C range, coinciding with a broad peak in the mass spectrum signal for mass 18 and a broad endothermic peak in the DTA signal. A second smaller mass loss of ~1.7% occurred between 400-700°C, with a weak broad signal for mass 18. A final mass loss of ~2.5% occurred from 700-1000°C, with no signal in the mass spectrum for water. The three mass losses occur at similar temperature ranges for both LTS-TiP_2O_7 and V-doped TiP_2O_7; the final mass loss, which may be due to amorphous phosphates, is half the size in V-doped TiP_2O_7 compared to LTS-TiP_2O_7. The PXRD pattern of V-doped TiP_2O_7 post heat treatment also showed additional peaks indicating it too adopts the cubic super-structure, which is shown in figure 5.15. As with the previous heat treated sample, oxygen positions were not refined and a global isotropic thermal parameter was used for each atom type. The refinement gave an excellent fit, converging at a low R_{wp} of 2.66% with a larger lattice parameter of a = 23.6010(3) Å,

compared to that of HT TiP_2O_7 where a = 23.5688(5) Å. Refinement details can be found in appendix 3.

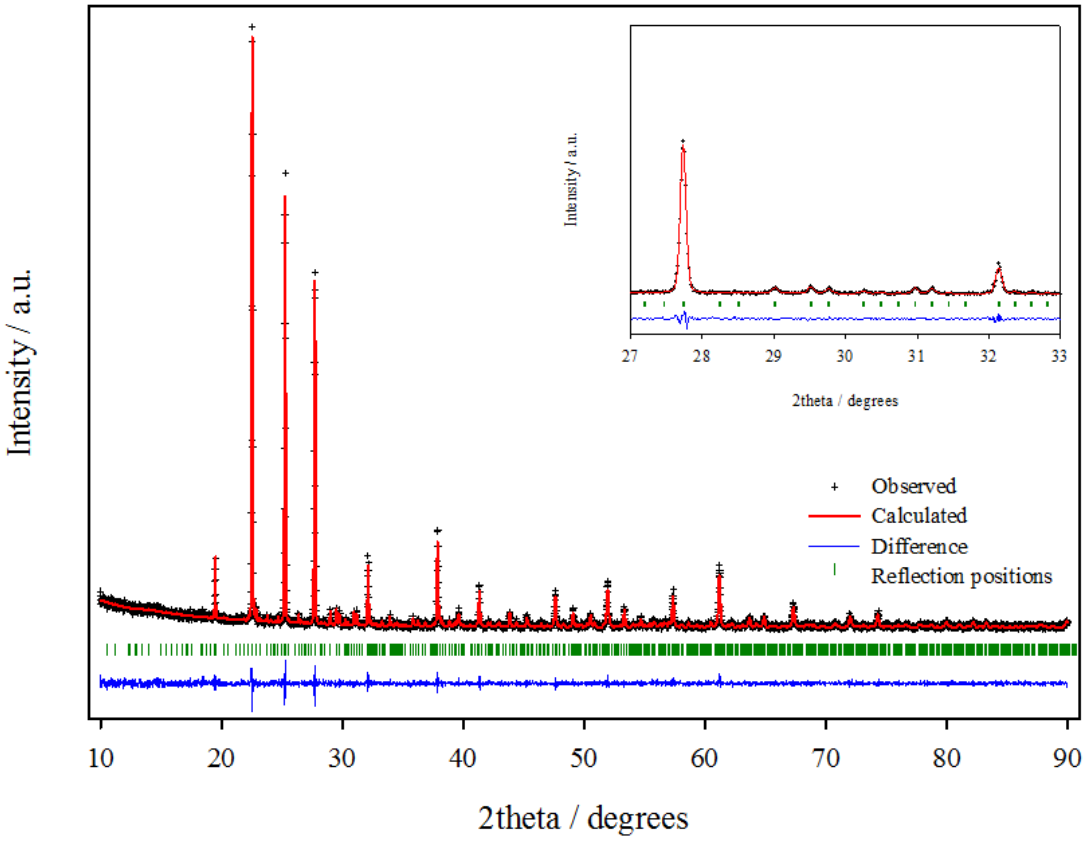

Figure 5.15 - Rietveld refinement plot of heat treated V-doped TiP_2O_7 with the cubic super-structure model, inset shows super-structure peaks

Analysis using XRF and EDS (see appendix 4) confirms the presence of vanadium in the sample after heat treatment. There was no evidence of any additional peaks, showing the sample is single phase, with no detectable vanadium-based impurities. If the vanadium was part of an amorphous component and so would not be visible in the PXRD pattern after heat treatment, then there would be a significant amorphous component remaining post heat treatment.

To investigate this, two phase refinements were carried out on as synthesised V-doped TiP_2O_7 and heat treated V-doped TiP_2O_7 as was described in 5.3.1.2. The

amorphous content calculated for as synthesised V-doped TiP_2O_7 was 19%, and 3% for the heat treated sample. If we assume a level of V-doping between 10-20 mol% as suggested from XRF ($Ti_{0.74}V_{0.16}P_2O_7$), then the low level of overall amorphous content cannot account for all the vanadium content and indicates that at least part of the vanadium content is contained within the crystalline component of the sample and so is incorporated into the structure. It is also interesting to note that the addition of V leads to a more crystalline product overall, almost as though the vanadium is acting like a sintering aid. Full width at half maximum measurements confirm this; FWHM of the (200) peak were measured for each sample, pre and post heat treatment (1000°C). The FWHM for 2 phase LTS-TiP_2O_7 decreased from 0.136° to 0.125°, and the FWHM for single phase V-doped TiP_2O_7 decreased from 0.098° to 0.063°.

Variable temperature XRD was used again to follow the thermal decomposition pathway and to ascertain if the V-doped TiP_2O_7 underwent the same phase transition as LTS-TiP_2O_7. A sample was treated in the same manner as LTS-TiP_2O_7; stack plots are shown in figure 5.16 and 5.17.

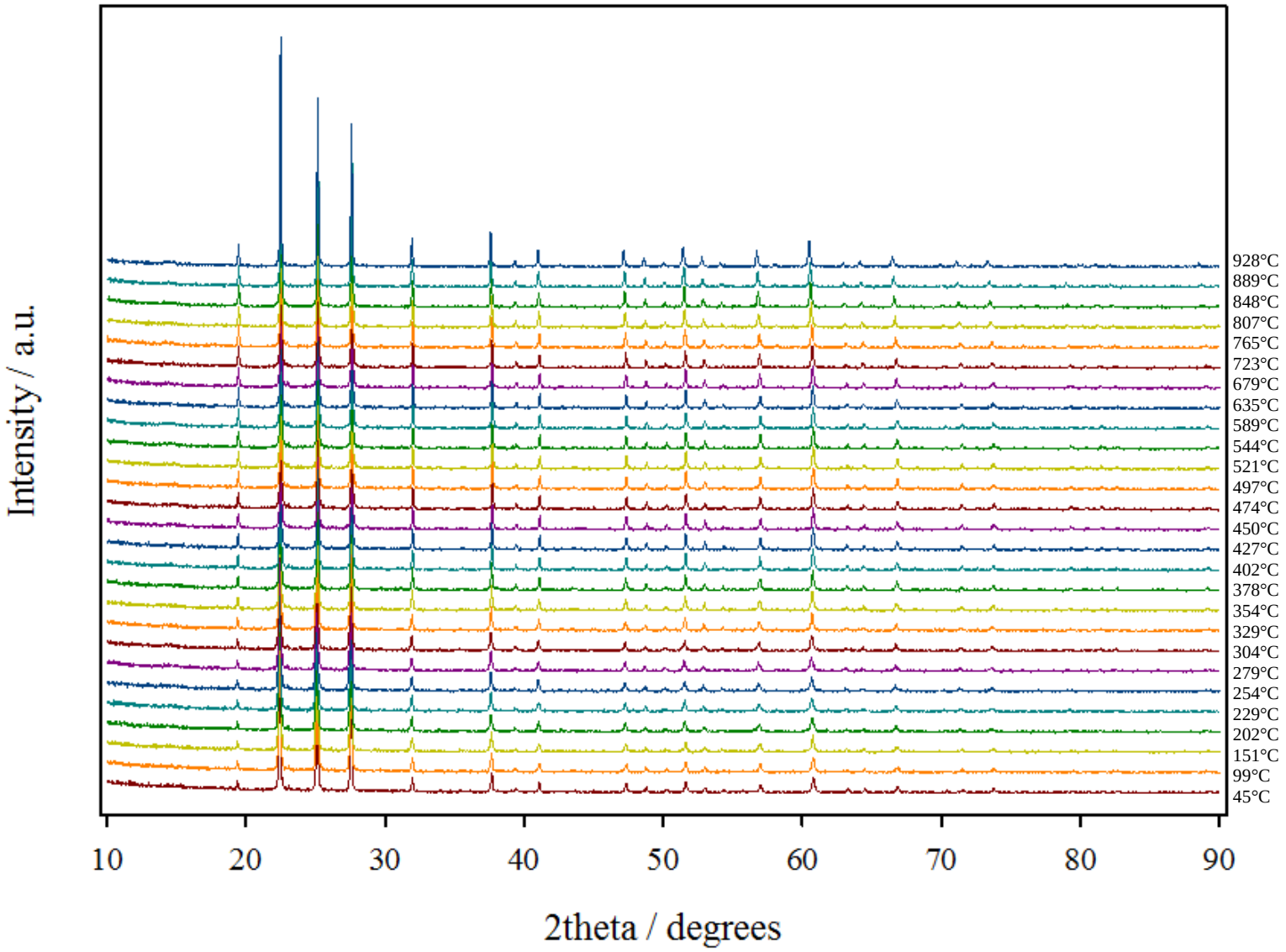

Figure 5.16 - Stack plot of VT-XRD data of V doped TiP_2O_7 upon heating

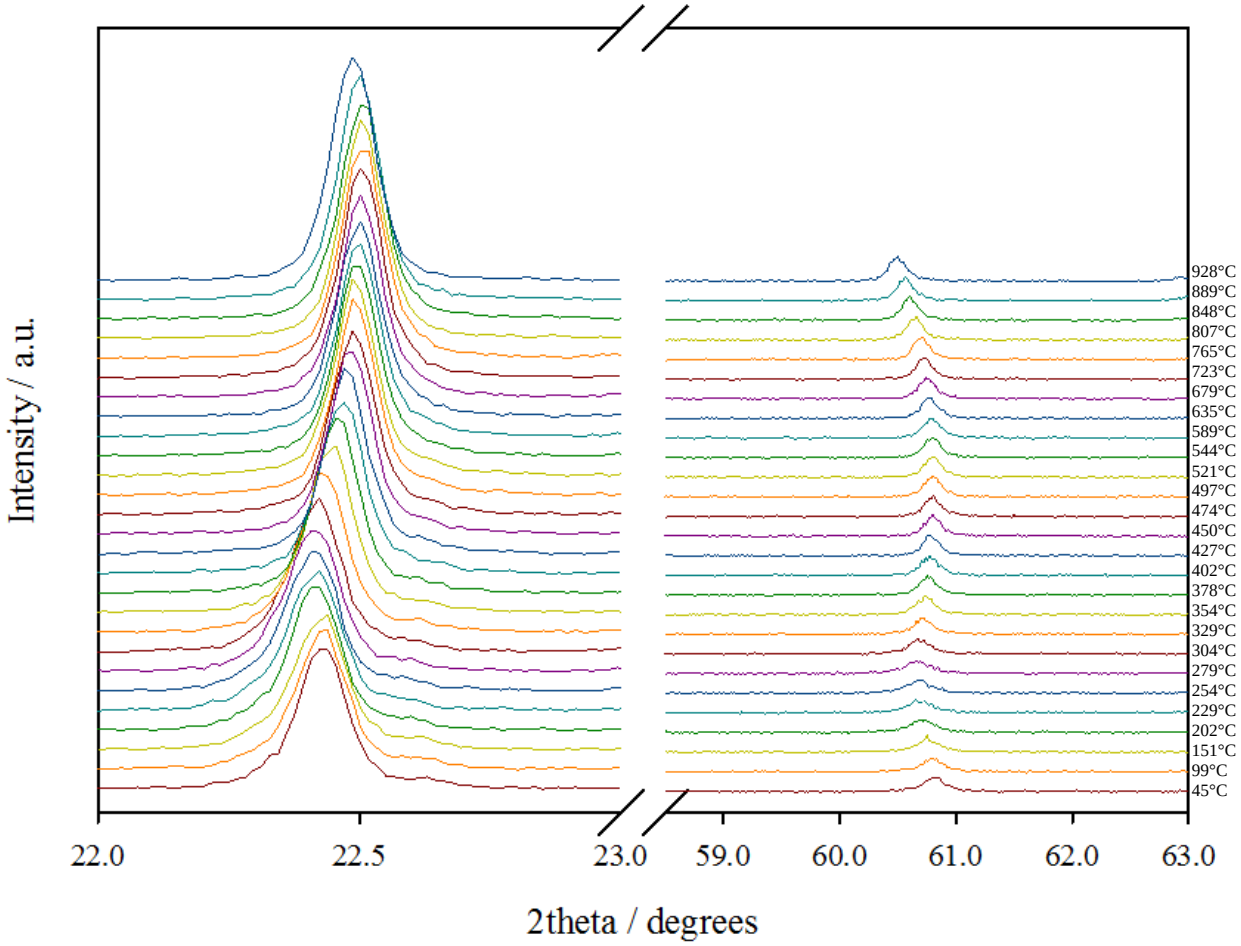

Figure 5.17 - Stack plot of VT-XRD data of V-doped TiP_2O_7 upon heating

Positive thermal expansion is evident in the diffraction pattern from 45 to 279°C from a shifting of peak to lower 2theta. From 304 to 450°C there is an area of apparent negative thermal expansion, beyond which positive thermal expansion is observed again. Upon cooling a contraction of the cell occurs, and super-cell peaks appear at 590°C, which is shown in figure 5.18.

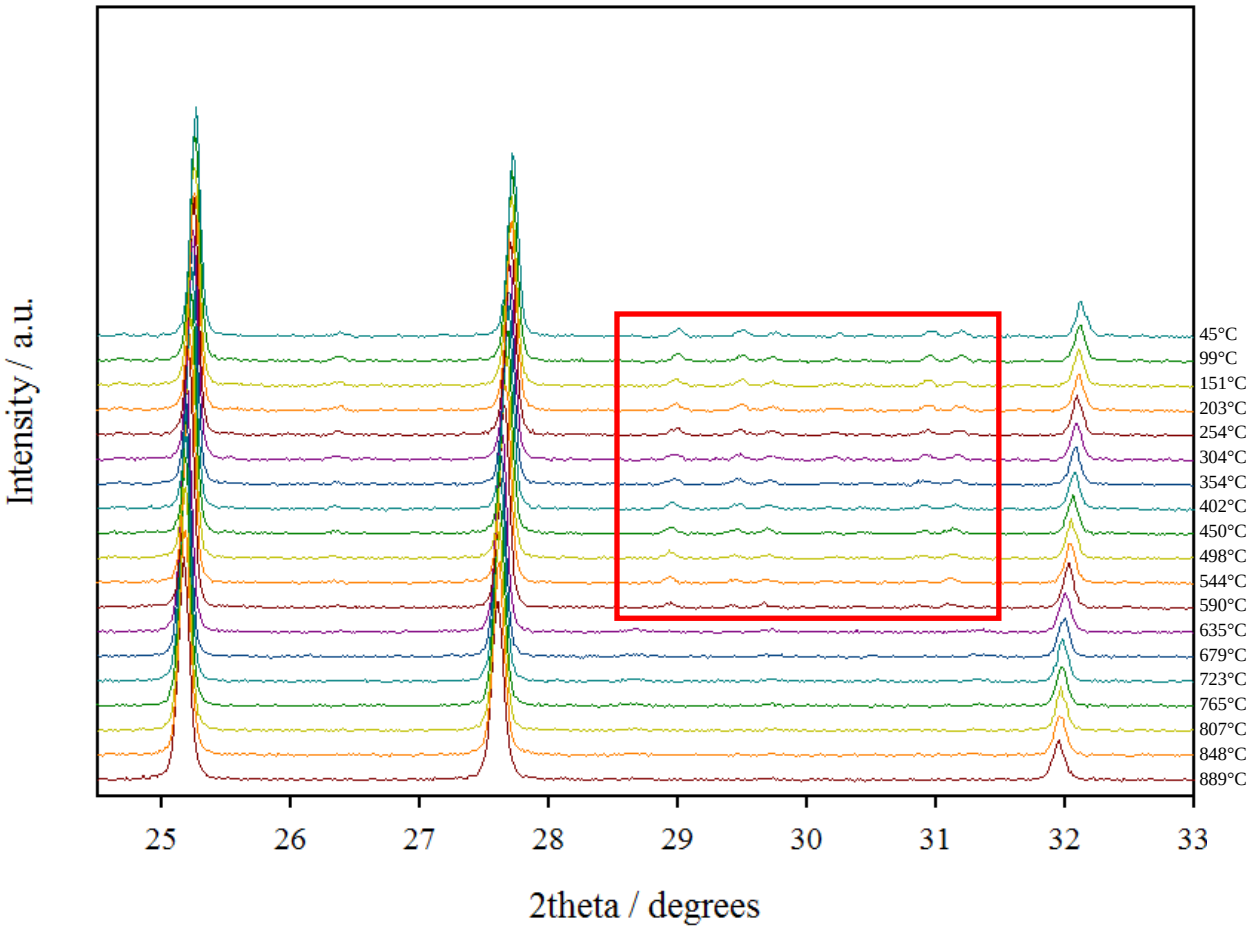

Figure 5.18 - Stack plot of VT-XRD data of V-doped TiP_2O_7 upon cooling with super-cell region highlighted by red box

The patterns were analysed using GSAS and the lattice parameters were plotted against temperature, which is shown in figure 5.19. The plot is very similar to that of LTS-TiP_2O_7 (see section 5.3.1.2). Upon cooling, the cell contracts with no evidence of any expansion, very similar to LTS-TiP_2O_7, showing that the contraction upon heating is not true negative thermal expansion, but likely due to a phase change. Super-cell peaks appear at 590°C, where the heating and cooling plots diverge.

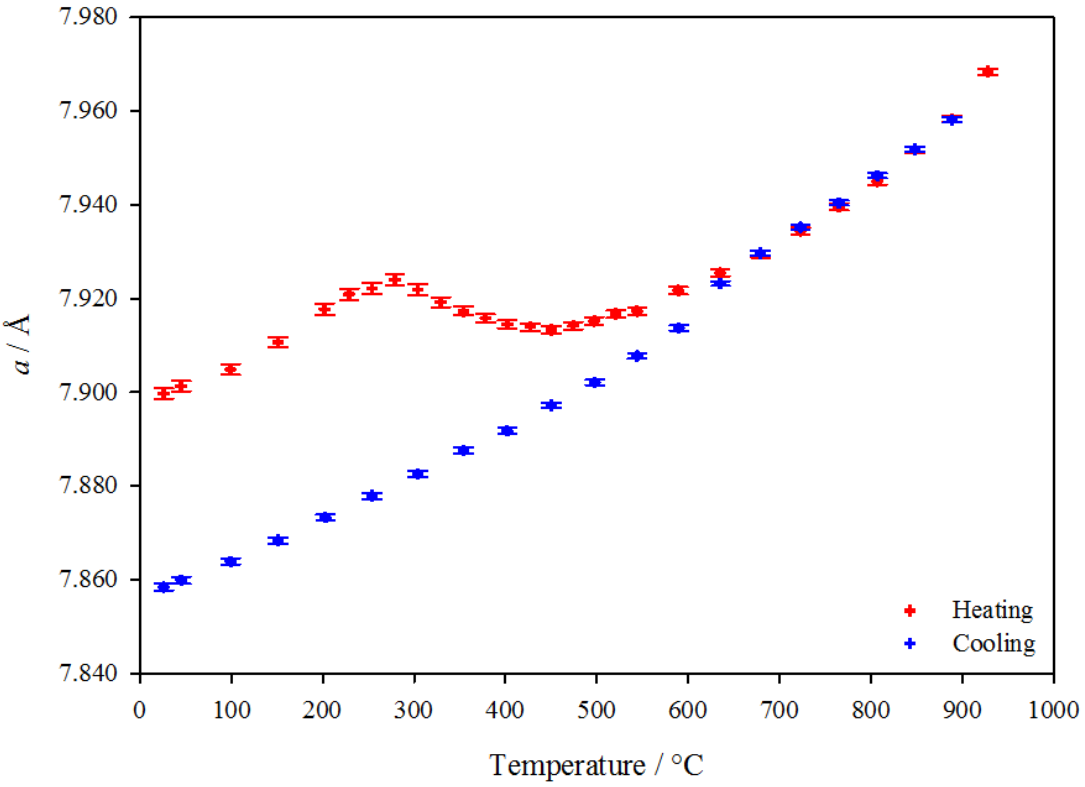

Figure 5.19 – Lattice parameter plot of V-doped TiP_2O_7 – first heat treatment

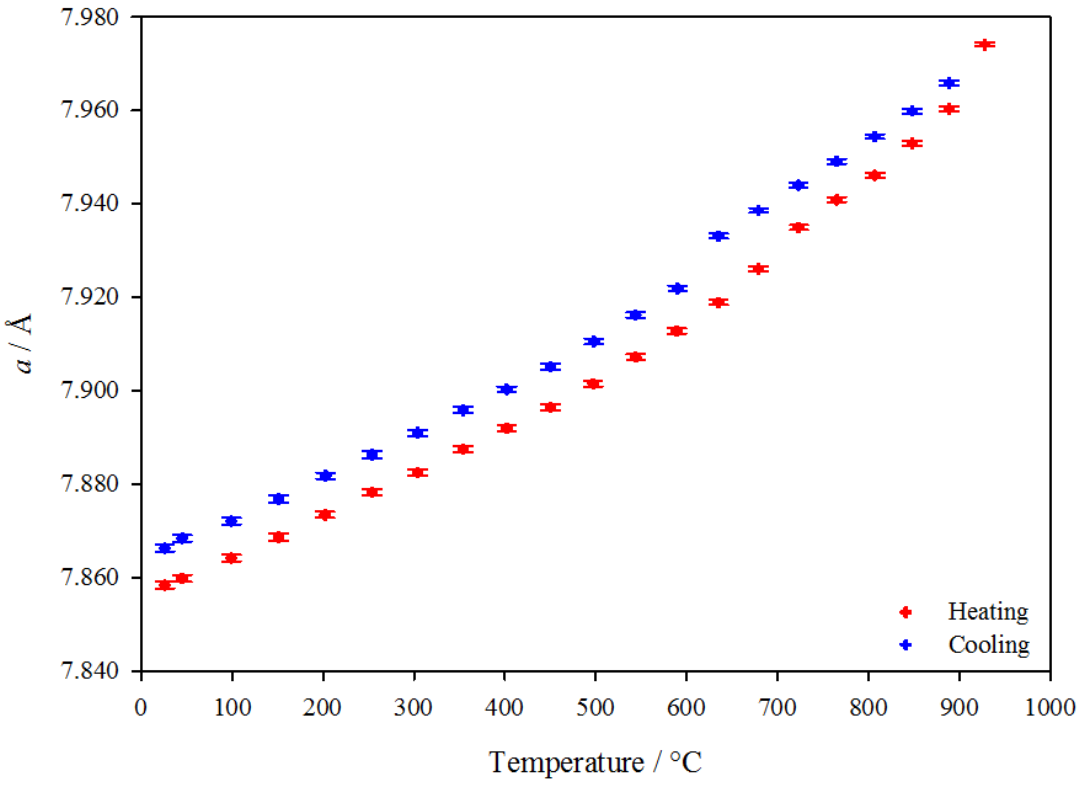

Figure 5.20 – Lattice parameter plot of V-doped TiP_2O_7 – second heat treatment

Figure 5.20 is a lattice parameter plot of V-doped TiP_2O_7 after a second VT-XRD heat treatment. Lattice parameter *a* increases with temperature, showing positive thermal expansion. Super-cell peaks are present up until 723°C where the sub-cell is adopted. Super-cell peaks appear at 590°C, leading to a deviation in the lattice parameter plot. SnP_2O_7[8] also adopts a pseudo-cubic $3 \times 3 \times 3$ super-structure at room temperature, which shows a triclinic sub-cell distortion when heated above 287°C, and a rhombohedral distortion above 557°C. ZrP_2O_7 has been found to adopt an orthorhombic super-structure at room temperature.[27] Above 290°C a phase transition occurs where the structure reverts to a cubic sub-cell. These temperature transitions are much lower than those found in LTS-TiP_2O_7 and V-doped TiP_2O_7. LT-TiP_2O_7[12] also shows a temperature transition above 300°C from the cubic sub-cell to the cubic super-structure, which is still apparent at 800°C, higher than the temperature at which LTS-TiP_2O_7 and V-doped TiP_2O_7 both revert to the cubic sub-cell.

The temperature range over which NTE occurs in the V-doped TiP_2O_7 is different to that of LTS-TiP_2O_7. The NTE occurs at a slightly higher temperature in V-doped TiP_2O_7 and over a larger temperature range compared to LTS-TiP_2O_7. The reason for this is unclear. However, it prompted a further investigation into the structure, details of which are presented in the following section.

5.3.2.2 Crystal Structure of V-Doped TiP_2O_7

Neutron powder diffraction data were collected on the V-doped TiP_2O_7. Vanadium itself is effectively invisible in neutron diffraction as it has a very small coherent scattering cross section. This means that any vanadium in the structure would not be directly visible in the pattern, so the presence of vanadium was investigated by looking for vacancies on the Ti site and P site. Initially the cubic sub-cell was used as a structural model and figure 5.21 shows the Rietveld fit of V-doped TiP_2O_7, which converged at a low R_{wp} of 2.32%, with refined structural parameters and bond lengths and angles shown in tables 5.8 and 5.9.

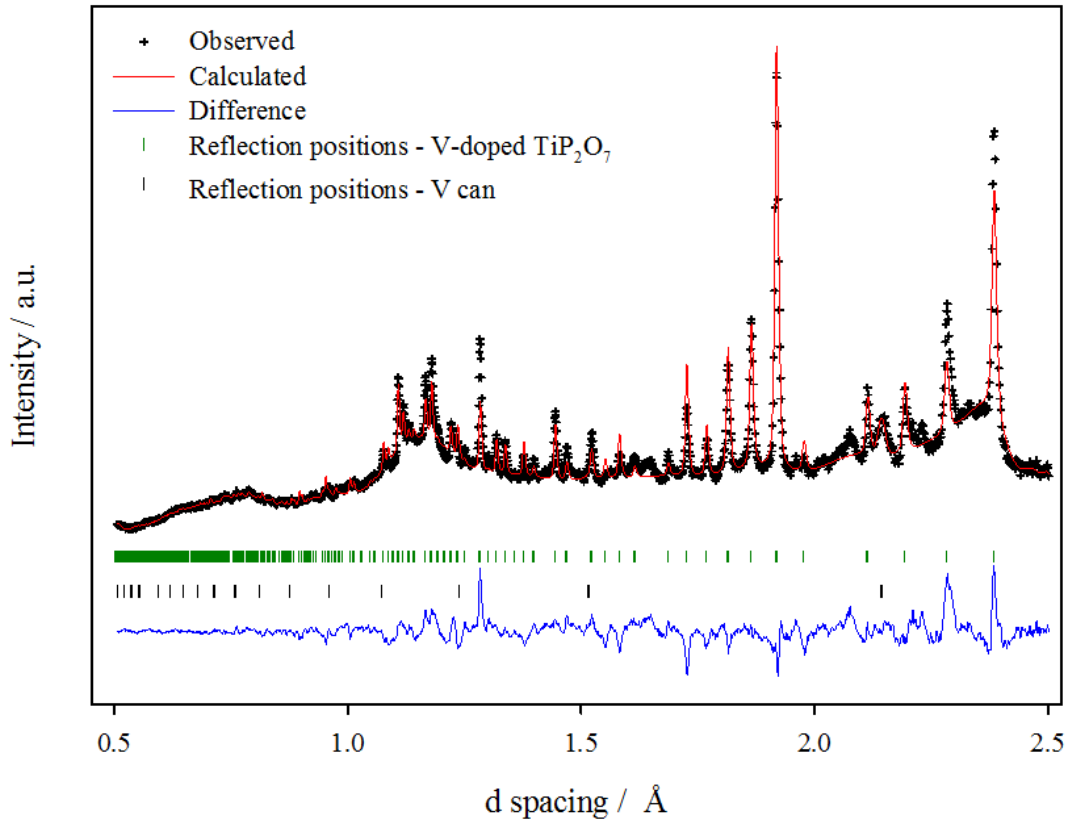

Figure 5.21 - Rietveld refinement plot of V-doped TiP_2O_7

Table 5.8 - Refined structural parameters of V-doped TiP_2O_7 using cubic sub-cell model

Atom	Site	Occupancy	x	y	z	U_{iso} (Å^2)
Ti/V	4*a*	0.86(4)/0.14(4)	0	0	0	0.052(6)
P	8*c*	1	0.3903(5)	0.3903(5)	0.3903(5)	0.0163(7)
O1	24*d*	1	0.4455(6)	0.2105(9)	0.4128(6)	0.067(2)
O2	4*b*	1	0.5	0.5	0.5	0.149(9)

Space group $Pa\bar{3}$; a = 7.907(1) Å. Figures of merit: R_{wp} = 2.32%, R_p = 2.93%, χ^2 = 14.01

Table 5.9 - Bond lengths (Å) and angles (°) of V-doped TiP_2O_7

Ti_O1	1.854(7)	**P_O1**	1.496(7)
O1_Ti_O1	92.2(2)	**P_O2**	1.504(6)
O1_Ti_O1	87.8(2)	**O1_P_O1**	110.8(3)
P_O2_P	180	**O1_P_O2**	108.1(3)

The background of the pattern is relatively high, due to the incoherent scattering of the protons (from the associated water seen in the TGA-MS, section 5.3.1.1) and the presence of amorphous content. A peak due to the vanadium sample holder can be observed at 2.14 Å and is modelled in the refinement. Overall the fit is generally good; however there are areas where there are underestimations of intensity, particularly the (*611*), (*311*) and (*222*) at 1.28, 2.28 and 2.38 Å respectively. These lattice planes all relate to the position of O2, which sits on an inversion axis in the unit cell. The position of this oxygen leads to a strained P-O2-P bond angle of 180°, giving O2 a high thermal parameter of 0.149(9); a high thermal parameter for O2 is also observed in other members of the series including SiP_2O_7[4] and ThP_2O_7.[14] Moving O2 off-site to reduce the strain was attempted but proved unsuccessful as it led to an unstable refinement. Additional weak peaks which cannot be indexed onto the cubic cell can be observed at 2.236, 2.468 and 2.692 Å. This may indicate an impurity phase or a reduction in symmetry.

The refinement indicates no evidence of any vanadium on the phosphorus site. Occupancy of vanadium on the titanium site was refined, giving a value of 0.86(4)/0.14(4) for Ti/V, similar to the values determined by XRF. Thermal parameters are higher than that of the X-ray refinement shown in section 5.3.2 for Ti/V, P and O2. Neutron powder diffraction can be more accurate at determining atomic position compared to PXRD, especially for weak X-ray scatterers such as oxygen. Higher thermal parameters may indicate uncertainty in their atomic positions within the unit cell, which could imply a problem with the symmetry of the structural model. P-O bond lengths are comparable to those reported for the TiP_2O_7 super-structure[2] and LT-TiP_2O_7,[12] whereas the Ti-O1 bond lengths are slightly shorter. BVS calculations for Ti^{4+}/V^{4+} and P^{5+} give values of +5.40 and +5.52 respectively, indicating both are over-bonded, Ti/V in particular, which could be another indication the structural model is not optimised.

Selected area electron diffraction (SAED) was used to investigate the symmetry of V-doped TiP_2O_7. A simulated electron diffraction pattern using SingleCrystal™, based upon the refined model is shown in figure 5.22, as viewed along the *a* axis.

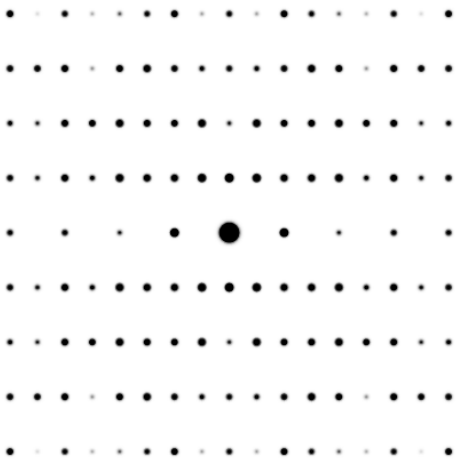

Figure 5.22 - Simulated electron diffraction pattern of V-doped TiP_2O_7 using the cubic sub-cell, space group $Pa\bar{3}$, viewed along the *a* axis

The electron diffraction film obtained of V-doped TiP_2O_7 is shown in figure 5.23; the orientation of the crystal is unknown. The pattern was indexed and d-spacings were calculated from the wavelength of the incident radiation (electron beam), camera length of the TEM and the distance between the central spot and the diffracted spots measured on the original film. The diffracted spots are labelled in figure 5.23 and the d-spacings shown in table 5.10. The diffraction pattern obtained is not consistent with the simulated pattern, specifically the spot labelled a, the d spacing of which could not be indexed onto the cubic sub-cell. This indicates that the structure is unlikely to be cubic. Faint spots are visible close to more intense spots; this may indicate a twinned crystal.

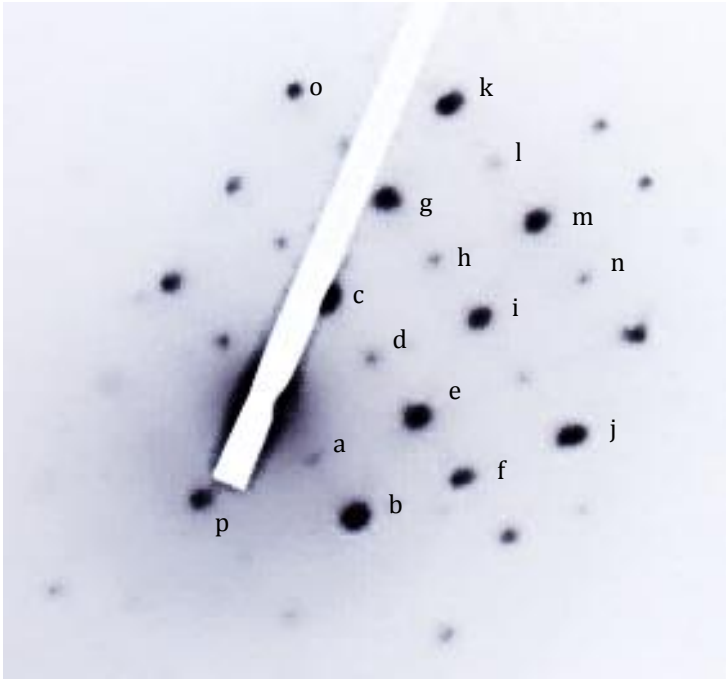

Figure 5.23 - Labelled SAED pattern of V-doped TiP_2O_7 (200% original size)

Table 5.10 – Calculated d-spacings of the SAED pattern of V-doped TiP_2O_7

Spot	Distance from central spot (m)	d spacings (Å)	Spot	Distance from central spot (m)	d space (Å)
a	3.05×10^{-3}	7.197	i	1.123×10^{-2}	1.955
b	7.16×10^{-3}	3.066	j	1.495×10^{-2}	1.468
c	5.38×10^{-3}	4.080	k	1.649×10^{-2}	1.331
d	4.80×10^{-3}	4.573	l	1.569×10^{-2}	1.399
e	7.36×10^{-3}	2.983	m	1.581×10^{-2}	1.388
f	1.45×10^{-2}	1.514	n	1.67×10^{-2}	1.314
g	1.126×10^{-2}	1.950	o	1.546×10^{-2}	1.420
h	1.056×10^{-2}	2.079	p	5.31×10^{-3}	4.134

The calculated d-spacings (see appendix 6) could not be indexed onto the cubic sub-cell, and so a search for a suitable model was carried out. As the PXRD pattern fits very well to the cubic sub-cell, the topology of the heavier scatterers, Ti and P, must be very similar to that of the cubic model. UP_2O_7 adopts a triclinic structure,[5] where the topology is very similar to the cubic structure. The two

structures are shown in figure 5.24, and the simulated electron diffraction pattern is shown in figure 5.25.

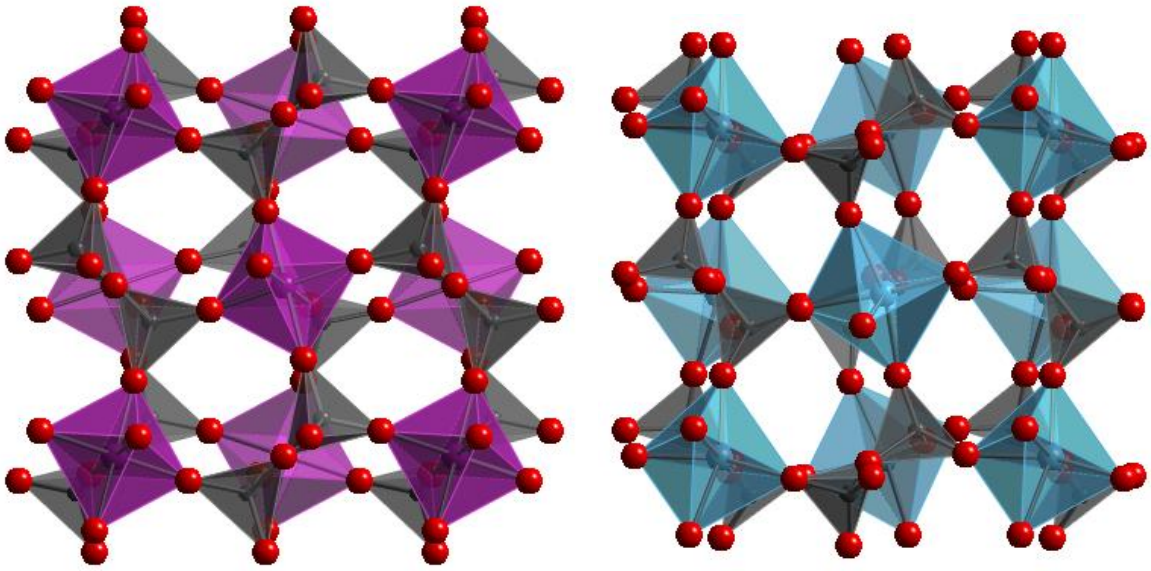

Figure 5.24 - Structural comparison of the $Pa\bar{3}$ model[14] (left, with purple MO_6 octahedra) and $P1$[5] (right, with blue MO_6 octahedra) as viewed down the *c* axis

Figure 5.25 - Simulated electron diffraction pattern of MP_2O_7 using the $P1$ symmetry, viewed along the *a* axis (left) and along the (*111*) direction (right)

The structures look very similar in topology; upon closer inspection the lack of symmetry is apparent in the *P*1 model compared to cubic model. The simulated diffraction pattern is very similar to that of the cubic sub-cell; however more reflections are observed due to the lack of symmetry in the *P*1 space group. The

pattern viewed down the (111) direction looks similar to the experimental however they do not appear to match.

To determine the triclinic structure, Wallez *et al.*[5] recorded synchrotron powder diffraction data at −173°C, which allowed the triclinic distortion to be observed by the splitting of the peaks.

Low temperature XRD was carried out at −173°C on V-doped TiP_2O_7 to investigate any observable structural distortions. Overall, cell contraction was observed, giving a cubic lattice parameter a = 7.8869(2) Å. The diffraction pattern is shown in figure 5.26, with the inset focusing on the (*511*) peak. From room temperature to −173°C, the FWHM of the (*511*) increases from 0.248° to 0.255°, which may indicate a distortion. The profile of the peak suggests the presence of multiple peaks; however the resolution is not high enough in order to see the peak separation. Further higher quality data, such as low temperature synchrotron powder diffraction data used by Wallez *et al.*[5], is required.

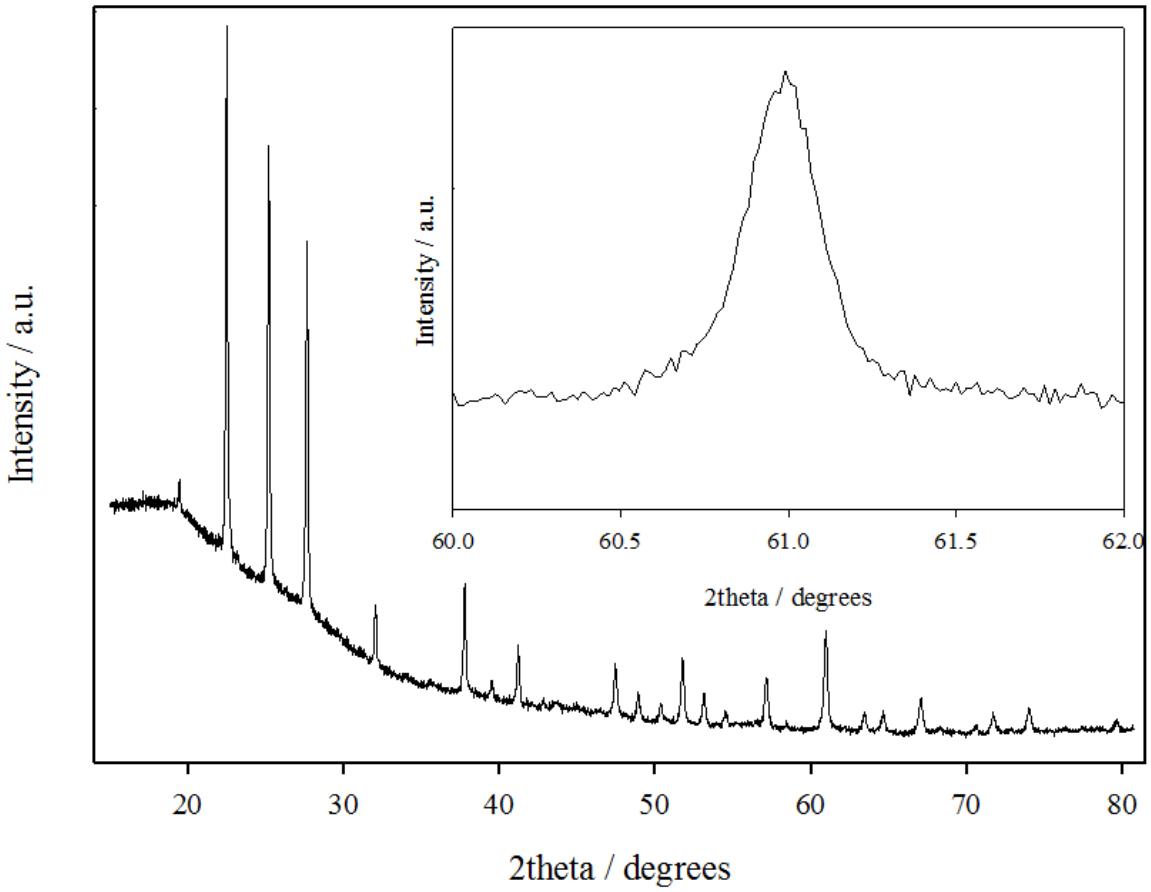

Figure 5.26 - PXRD pattern of V-doped TiP_2O_7 at −173°C, inset shows the (*511*) peak

Using the evidence of a lower symmetry cell given by the SAED pattern, Rietveld refinement was carried out using lower symmetry structural models. Initially the *P*1 model was used, however, due to the lack of symmetry and the large increase in the number of parameters to refine, the refinement was very unstable and could not converge. It would appear that higher resolution data will be needed in order to find a suitable structural model for this system.

A SAED pattern was also obtained of the heat treated V-Doped TiP_2O_7. The diffraction pattern is shown in figure 5.27.

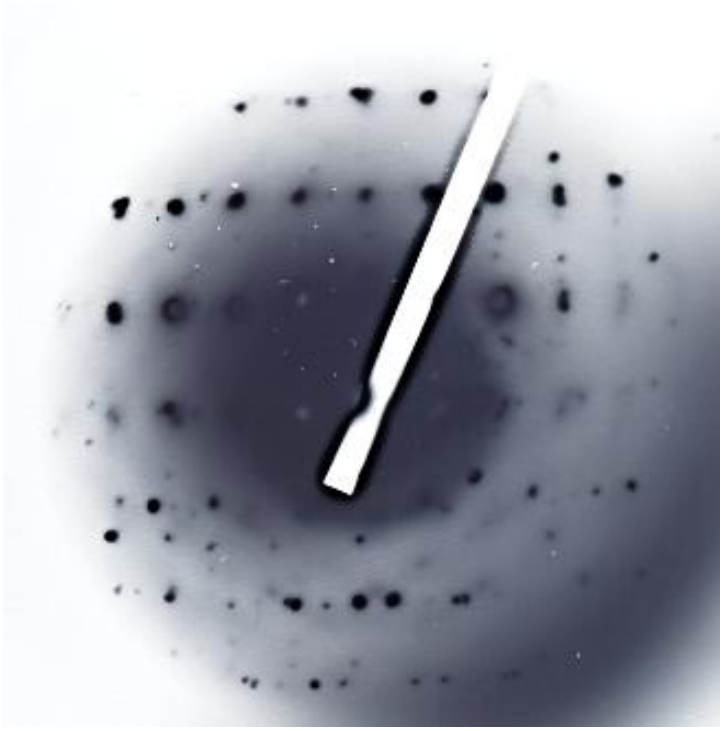

Figure 5.27 - SAED pattern of heat treated V-doped TiP_2O_7; orientation of the crystal is unknown

The diffraction pattern shows additional spots and smearing; this may indicate a polycrystalline sample. Simulated electron diffraction patterns for the two reported superstructures are shown in figure 5.28. The pattern is not particularly clear, and so a super-structure cannot be definitively assigned. Higher resolution synchrotron powder diffraction data or neutron powder diffraction would give a more conclusive evidence for the symmetry of the super-structure.

Figure 5.28 - Simulated ED patterns of TiP_2O_7 using the cubic super-structure (left) and orthorhombic super-structure (right) as viewed down the *a* axis

5.3.3 Crystal Morphology

Crystal morphology was investigated via scanning electron microscopy, to see if any insight into the crystal structure could be obtained via the morphology. Particle size, morphology and surface areas are also all important factors in the areas of catalysis, battery and fuel cell applications, where the AX_2O_7 materials may have potential applications.

5.3.3.1 LTS-TiP_2O_7 Crystal Morphology

The morphology of as-synthesised LTS-TiP_2O_7 is shown in figures 5.29 and 5.30. The particle morphology is unremarkable; there is neither a distinct shape nor size to the crystals, giving no indication to the symmetry. The potential amorphous content is not obvious in the image.

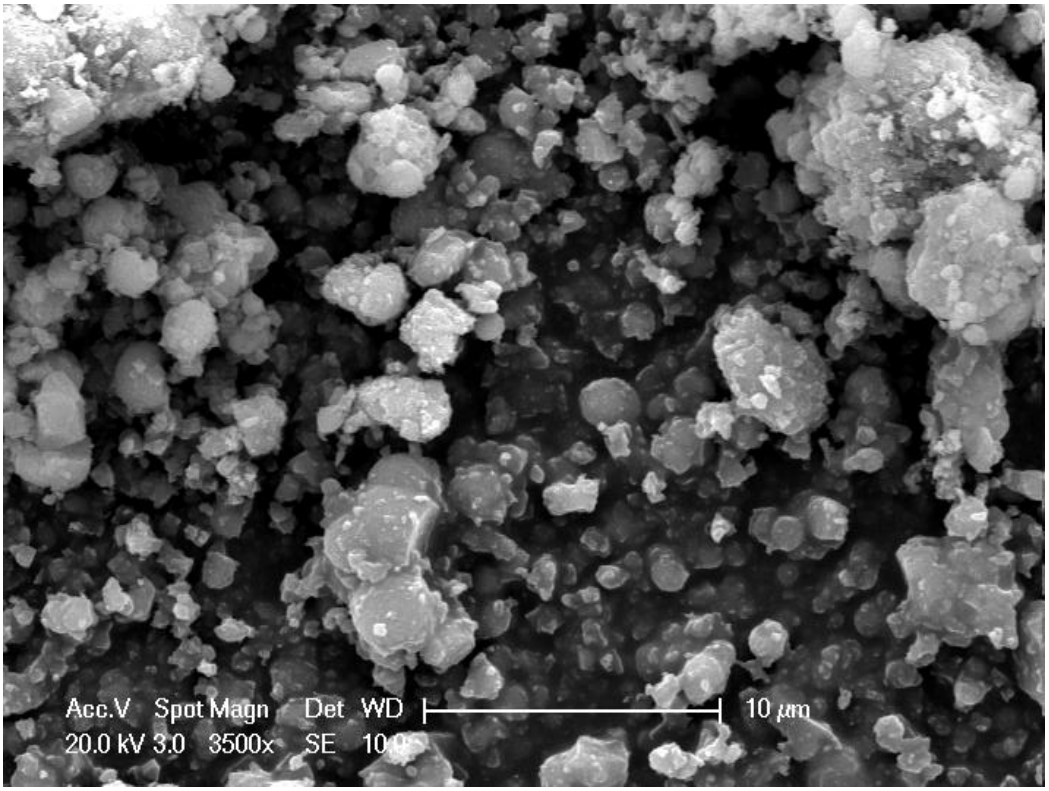

Figure 5.29 - SEM image of LTS-TiP_2O_7 (3500× magnification)

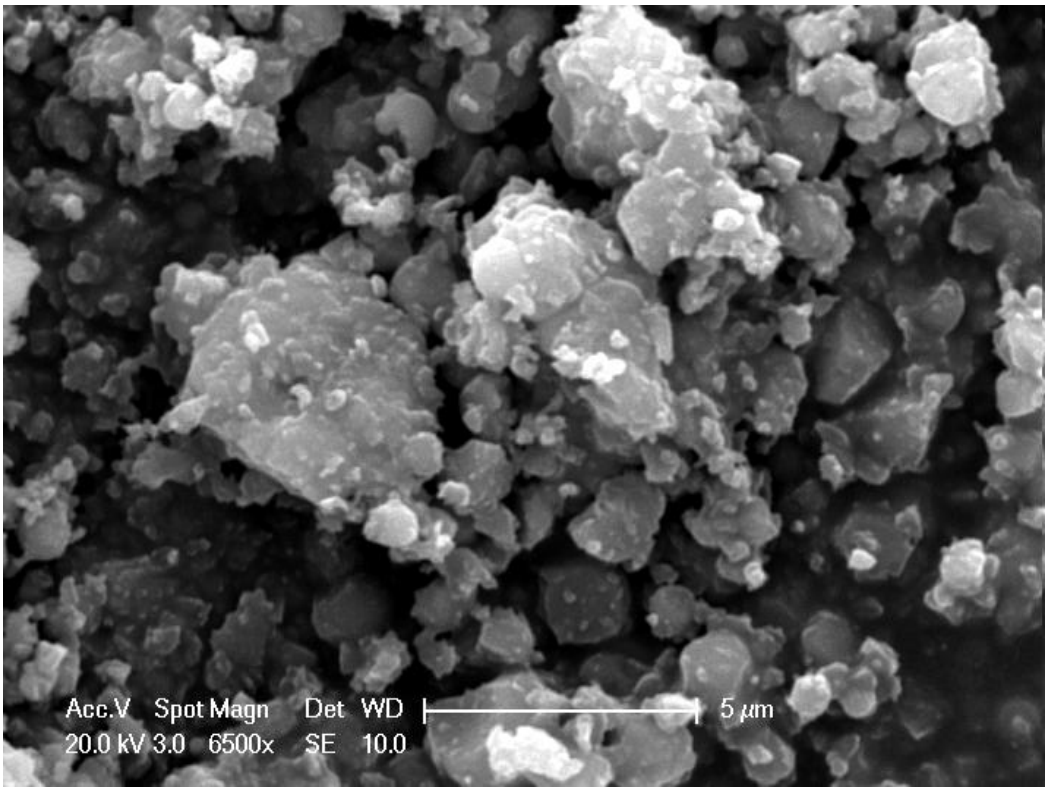

Figure 5.30 - SEM image of LTS-TiP_2O_7 (6500× magnification)

The morphology of LTS-TiP_2O_7 post heat treatment (at 1000°C) is shown in figure 5.31. The morphology remains unchanged after heat treatment, with some particle aggregation. After heat treatment at 1000°C the amorphous content was found to be very low, therefore as the morphology remains unchanged the amorphous content of the as synthesised LTS-TiP_2O_7 cannot be assigned.

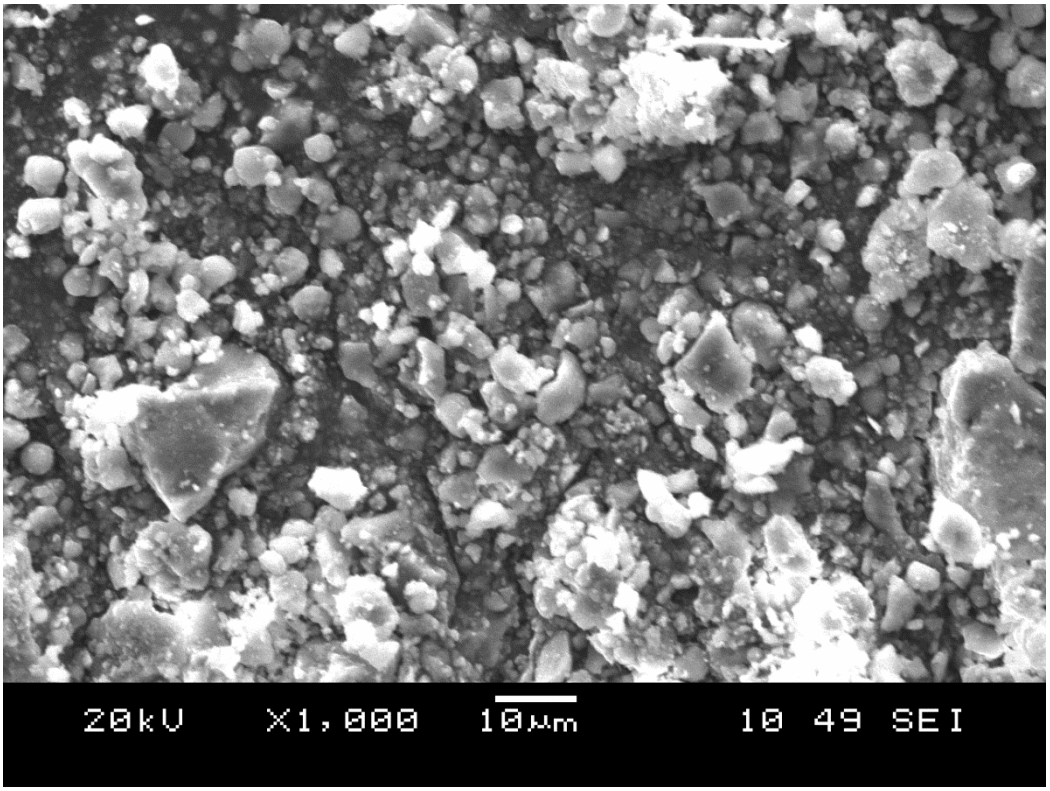

Figure 5.31 - SEM image of heat treated LTS-TiP_2O_7 (1000× magnification)

5.3.3.1 V-Doped TiP_2O_7 Crystal Morphology

The morphology of V-doped TiP_2O_7 (50%) is shown in figures 5.32 and 5.33. Unlike the parent phase, the V-doped TiP_2O_7 adopts an unusual mono-dispersed spherical morphology, with particles approximately 3µm in diameter.

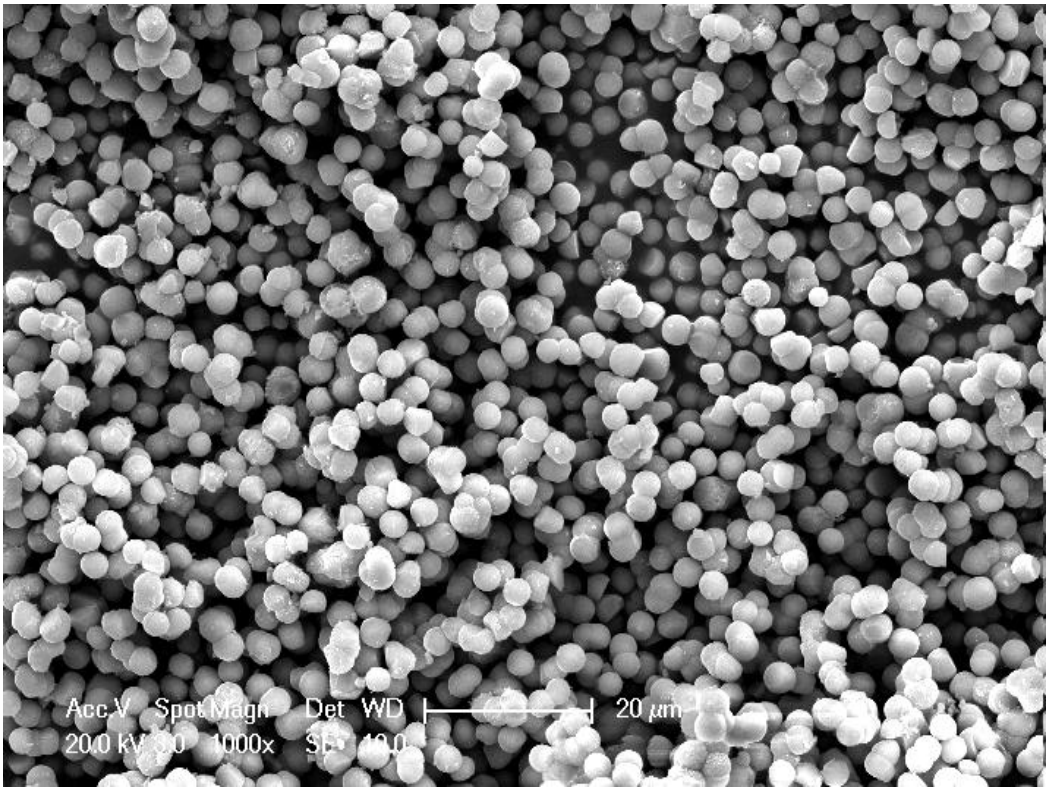

Figure 5.32 - SEM image of V doped TiP_2O_7 (50%) (1000× magnification)

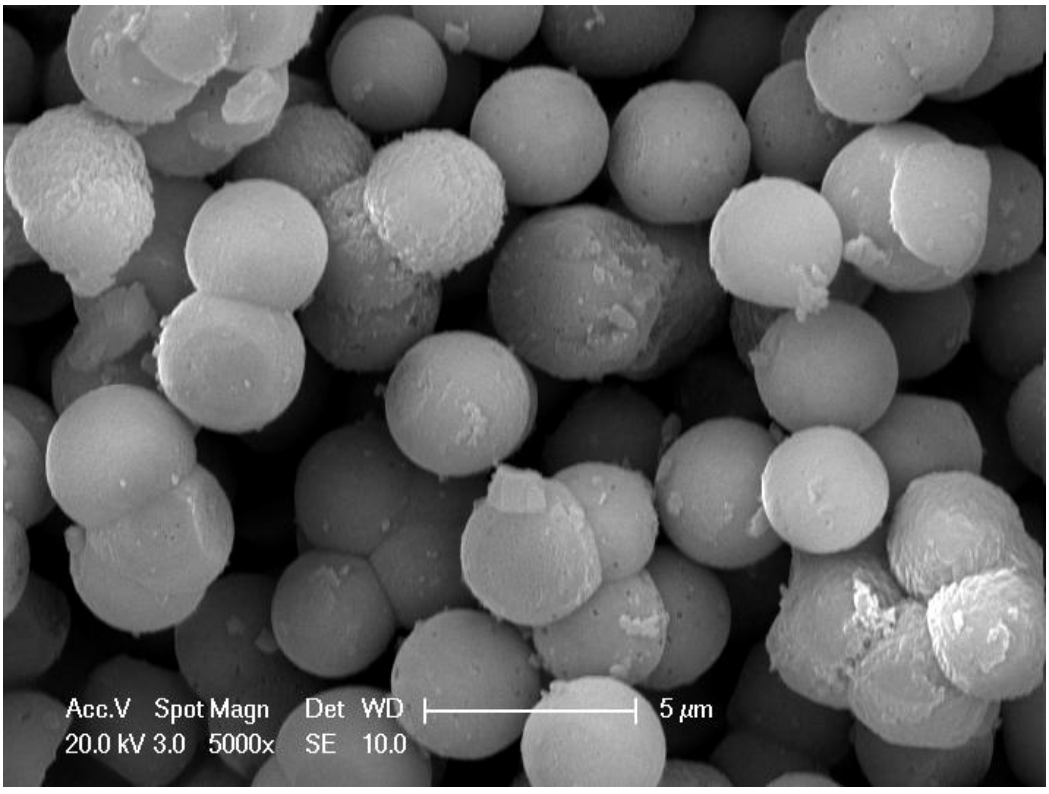

Figure 5.33 - SEM image of V doped TiP_2O_7 (50%) (5000× magnification)

At 5000 times magnification (figure 5.33) the crystal morphology is unmistakable. The surface of the spheres appears to be mainly smooth, and there is evidence of how the spheres grow in the form of conjoined crystals.

TEM was carried out on the V-doped TiP_2O_7 spheres, and the images shown in figure 5.34. The image appears to show a conjoined sphere.

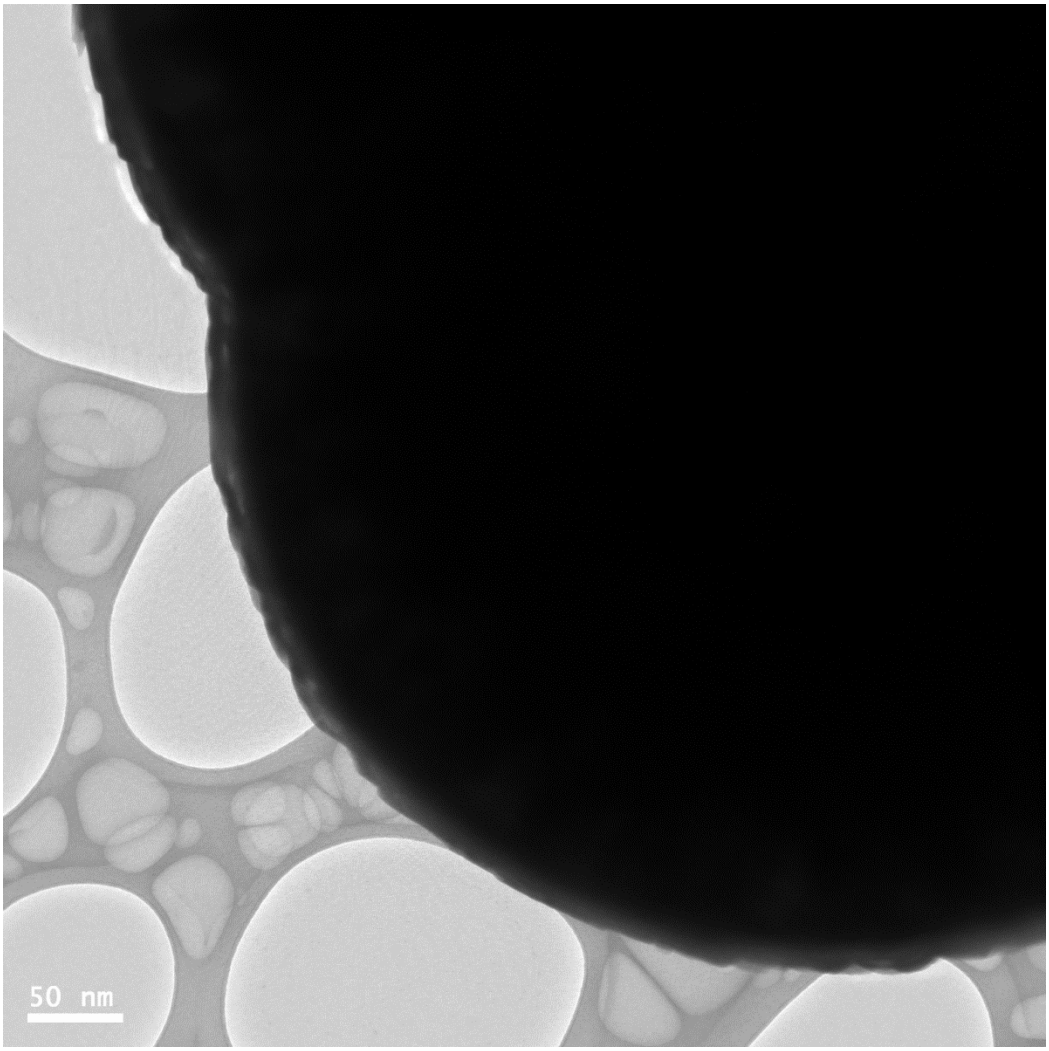

Figure 5.34 - TEM image of V-doped TiP_2O_7

The edge of one of the spheres was examined more closely, which is shown in figure 5.35.

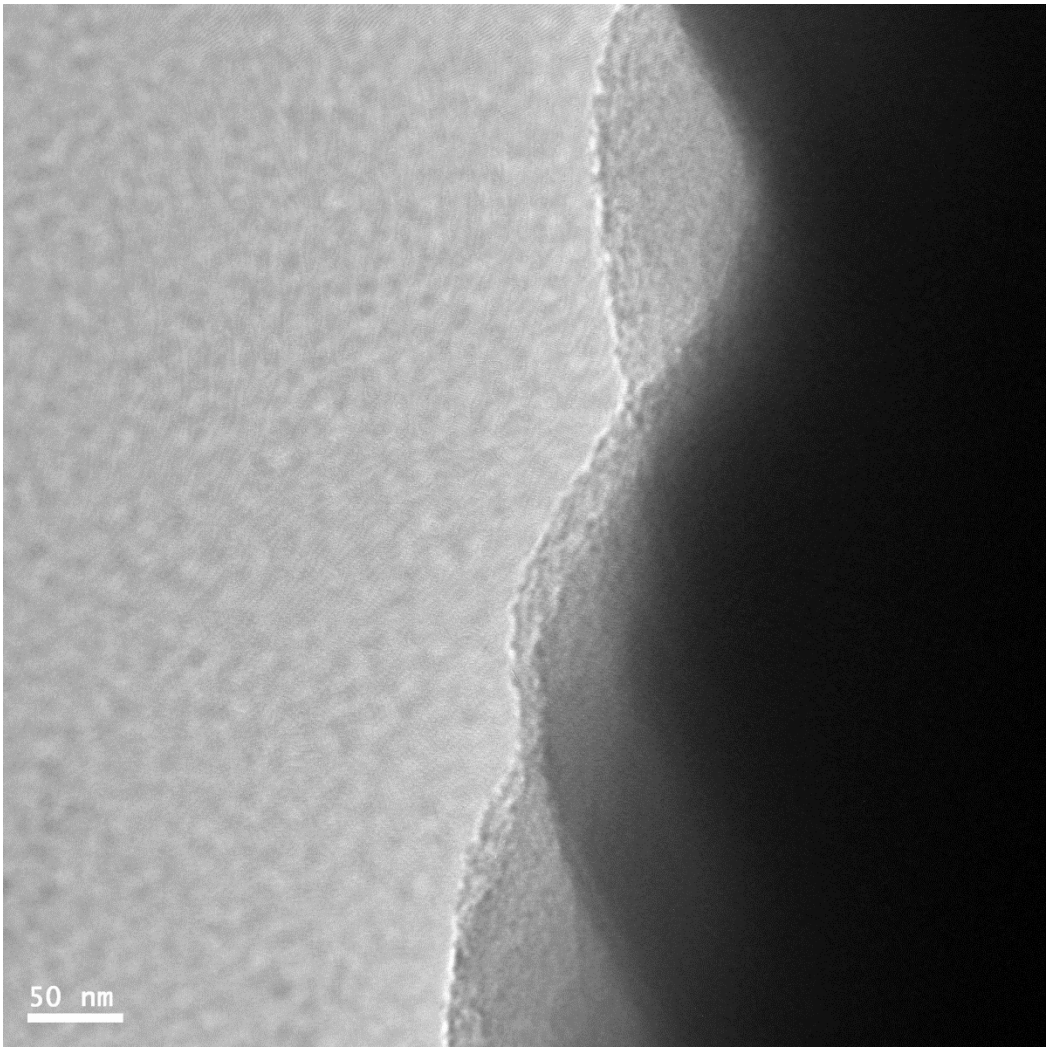

Figure 5.35 - TEM image of V-doped TiP_2O_7

SAED patterns were taken along the edge of the sphere and were found to be identical. This indicates the spheres are either aligned crystals or single crystals. Due to the shape of the particles and the lack of straight edges it looks unlikely that they are single crystals. The spheres could be polycrystalline, formed of crystals growing in the same direction with the same orientation, which would explain why the ED pattern is identical

The crystal growth was monitored after 12 hours; SEM images of each are shown in figures 5.36 and 5.37. After 12 hours the spheres have formed, although

size is not uniform. This could indicate a ripening mechanism, such as Ostwald ripening[28], a thermodynamically driven process which involves the deposition of smaller crystals/particles onto larger species.

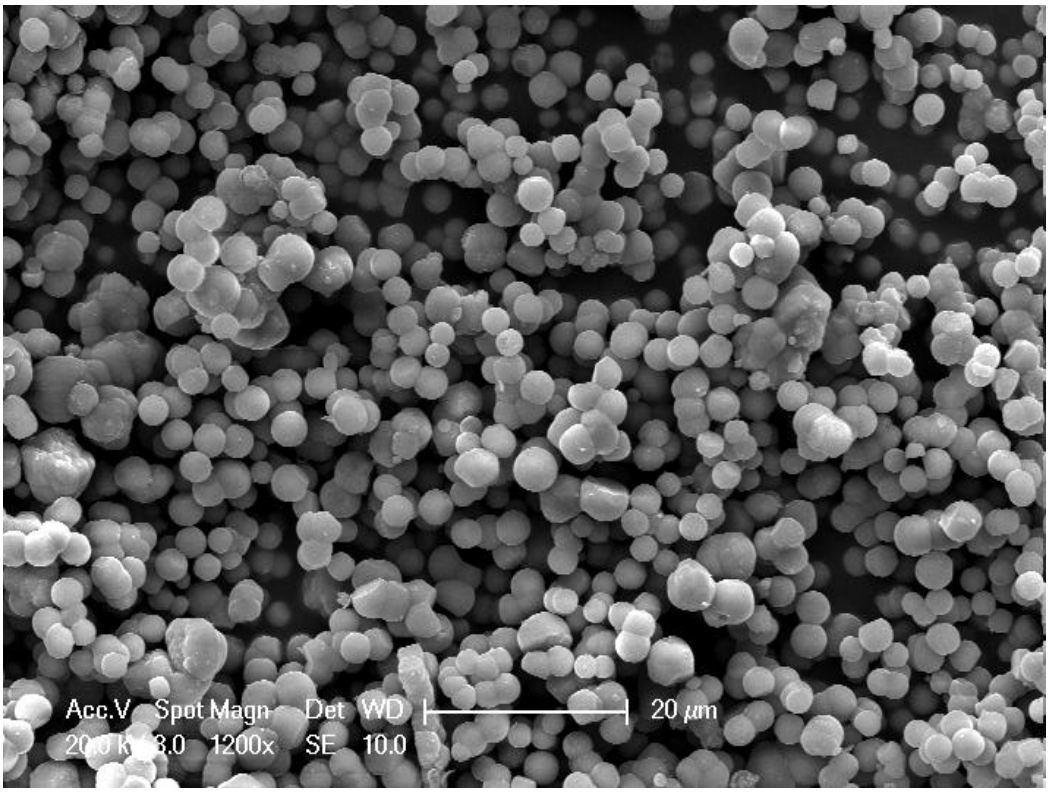

Figure 5.36 - SEM image of V-doped TiP_2O_7 (50%) after 12 hour synthesis (1200× magnification)

There are areas of agglomeration of the spheres, which can be seen closer in figure 5.36.

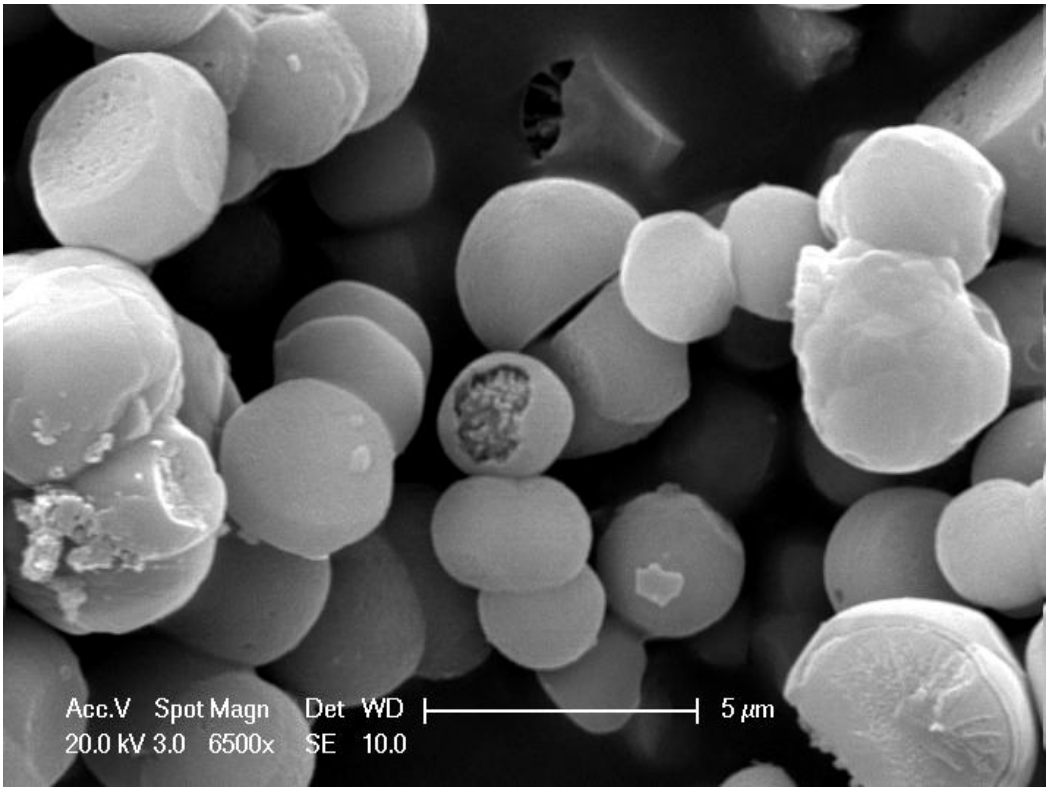

Figure 5.37 - SEM image of V-doped TiP_2O_7 (50%) after 12 hours synthesis (6500× magnification)

The stability of the spherical particle morphology was investigated by SEM, after heat treatment to 1200°C the morphology is retained, which is shown in figure 5.38. On the right there appears to be some particle agglomeration, but the bulk shows that the spherical particular shape is preserved.

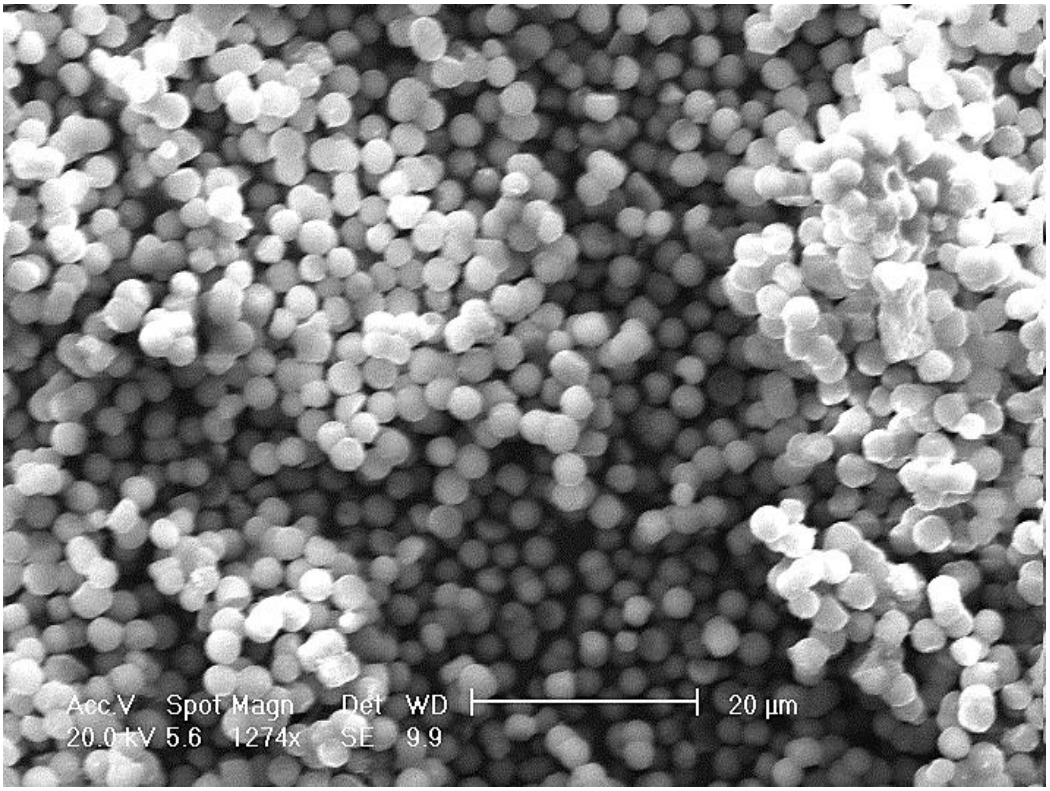

Figure 5.38 - SEM image of heat treated V-doped TiP_2O_7 (1200°C) (1274× magnification)

After repeated heat treatments the spherical particle morphology begin to break down. The particles agglomerate and become more angular, which is more in keeping with the presence of a crystalline phase. Much smaller particles also appear to be present on the surface of the larger particles. Figures 5.39 and 5.40 show SEM images of V-doped TiP_2O_7 after 3 heat treatments to 1000°C.

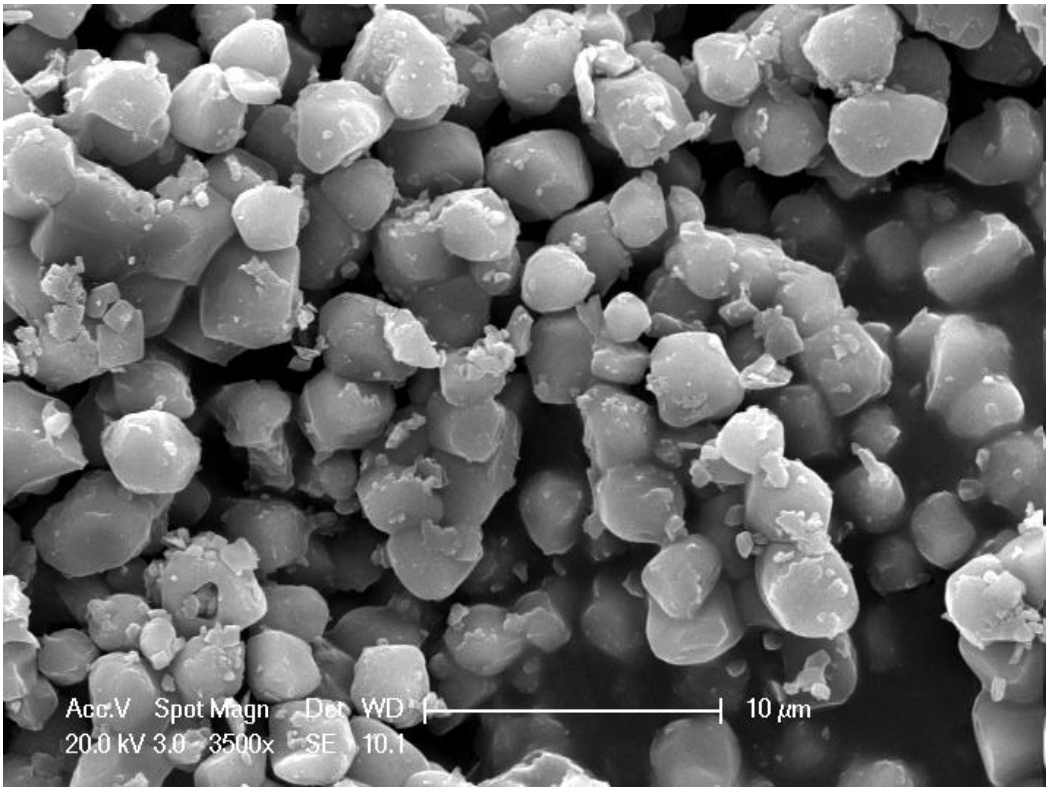

Figure 5.39 - SEM image of heat treated (× 3) V-doped TiP_2O_7 (3500× magnification)

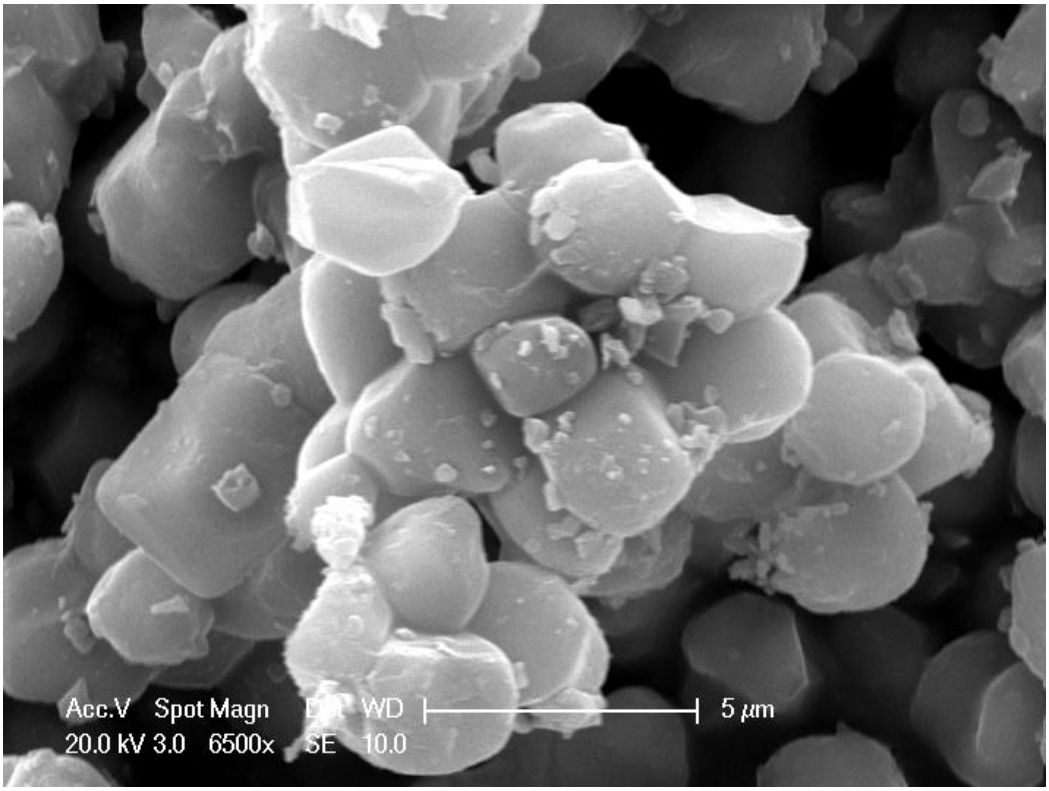

Figure 5.40 - SEM image of heat treated (× 3) V-doped TiP_2O_7 (6500× magnification)

TEM was used to investigate the smaller particles, TEM images are shown in figures 5.41 and 5.42.

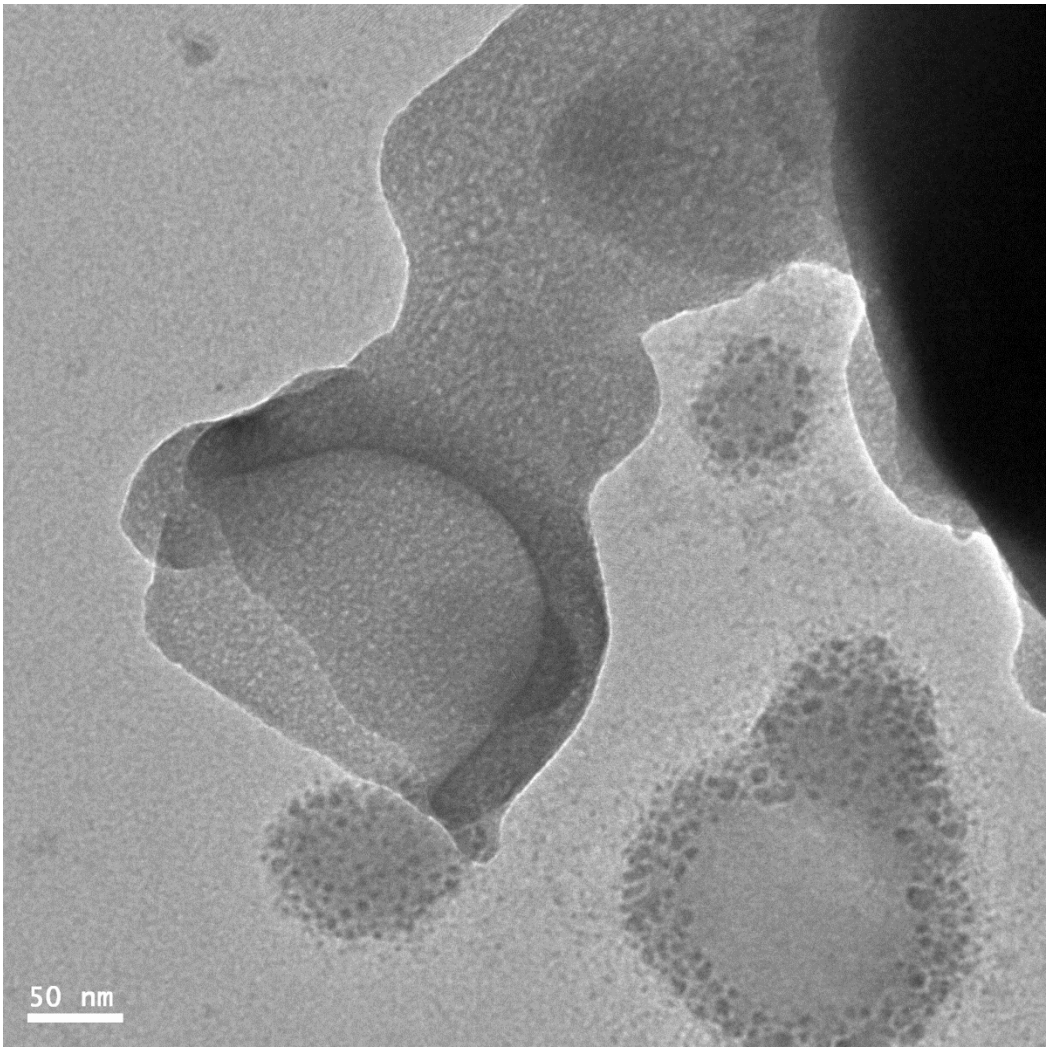

Figure 5.41 - TEM image of heat treated (×3) V-doped TiP_2O_7

The smaller particles are polycrystalline, shown by SAED. They appear to form hollow bubble like particles on the surface of the deformed spheres, shown burst in figure 5.41 and whole in figure 5.42.

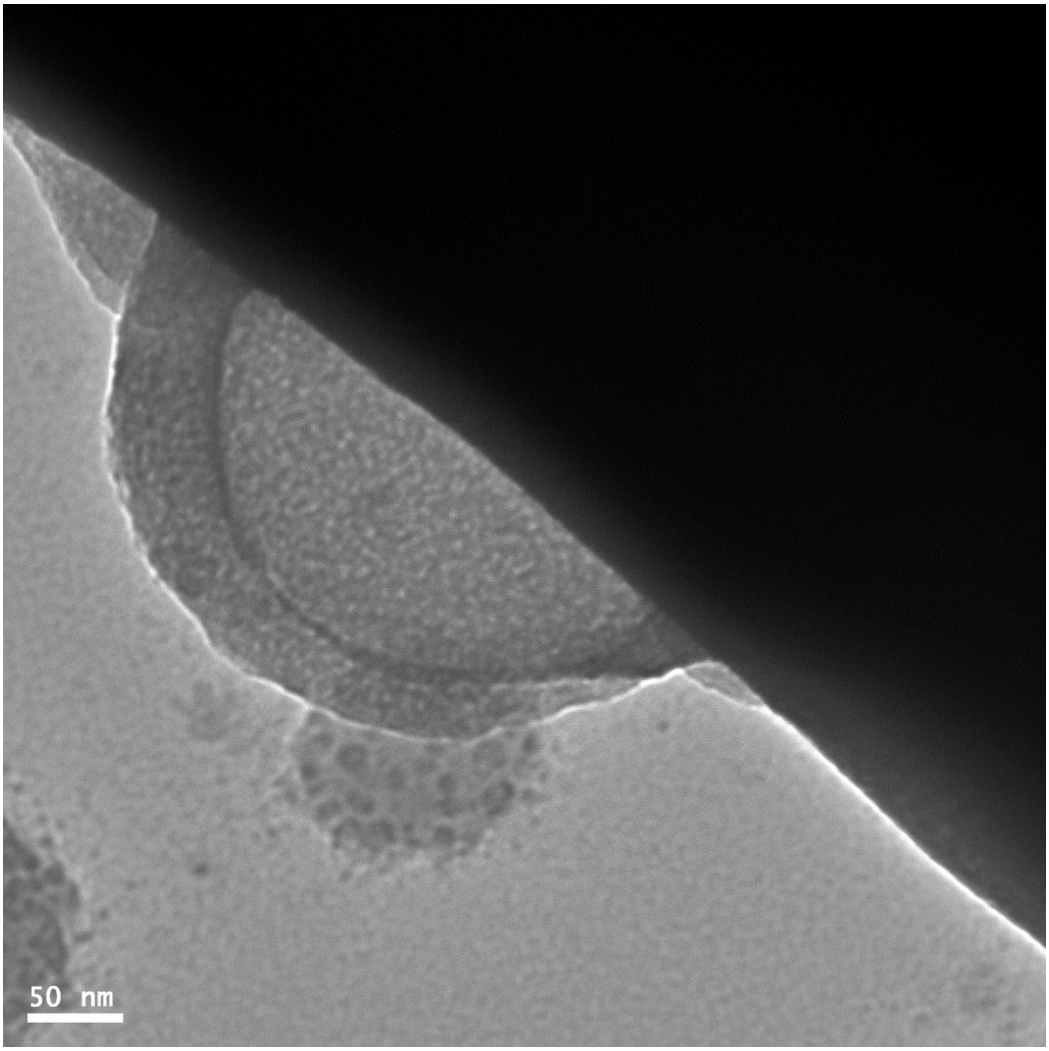

Figure 5.42 - TEM image of heat treated (×3) V-doped TiP_2O_7

5.3.3.2 Vanadium's Effect on Crystal Morphology

The presence of vanadium in the melt appears to have a profound effect on the morphology of the crystals. The samples investigated thus far only include the vanadium metal doped TiP_2O_7 (50% initial melt molar ratio). Is this level of vanadium in the starting melt required for the spherical particle formation? Figure 5.43 shows a SEM image of 10% vanadium metal doped (initial melt molar ratio) TiP_2O_7.

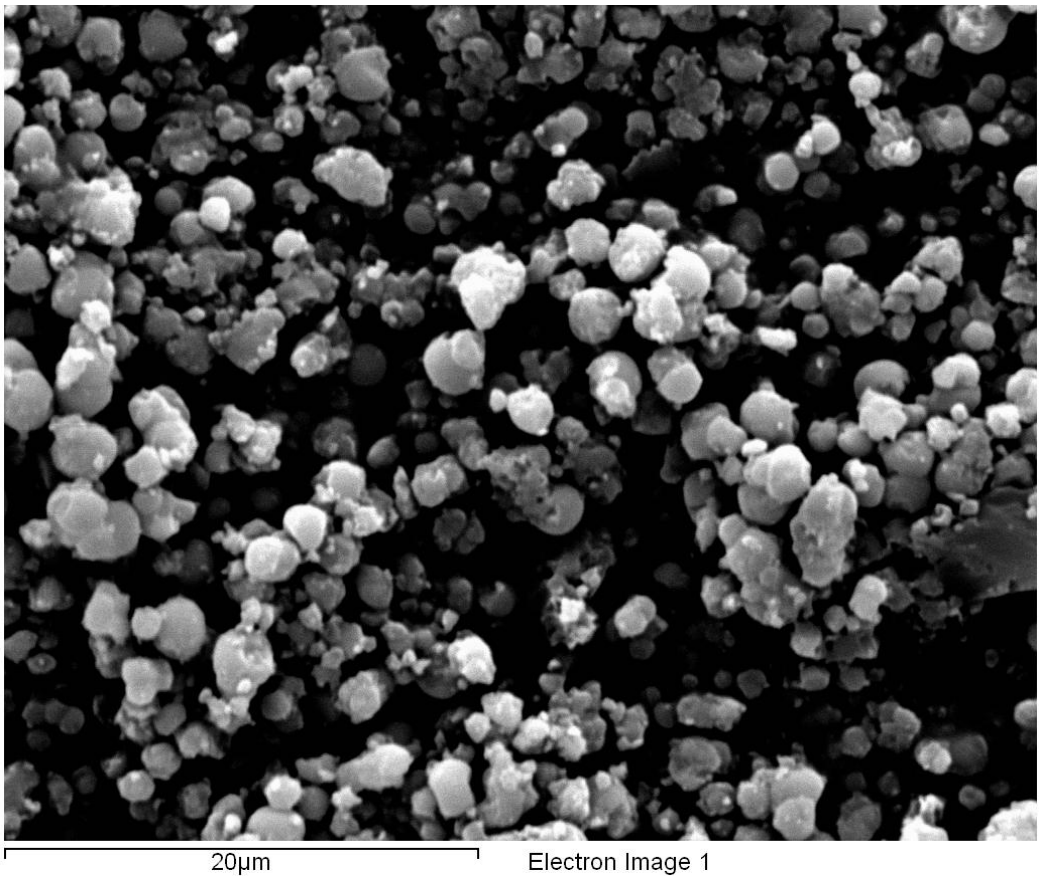

Figure 5.43 - SEM image of 10% V doped TiP_2O_7 (2700x magnification)

The morphology of the 10% doped TiP_2O_7 is quite different to that of the parent phase; the particles appear to be a more uniform size and more spherical. At the other end of the range, figure 5.44 shows a SEM image of 80% vanadium metal doped (initial melt molar ratio) TiP_2O_7. This image shows a much more defined spherical morphology with both larger and smaller particles. A vanadium based impurity, $VH_2P_3O_{10}$, is evident in the form of large monoclinic crystals.

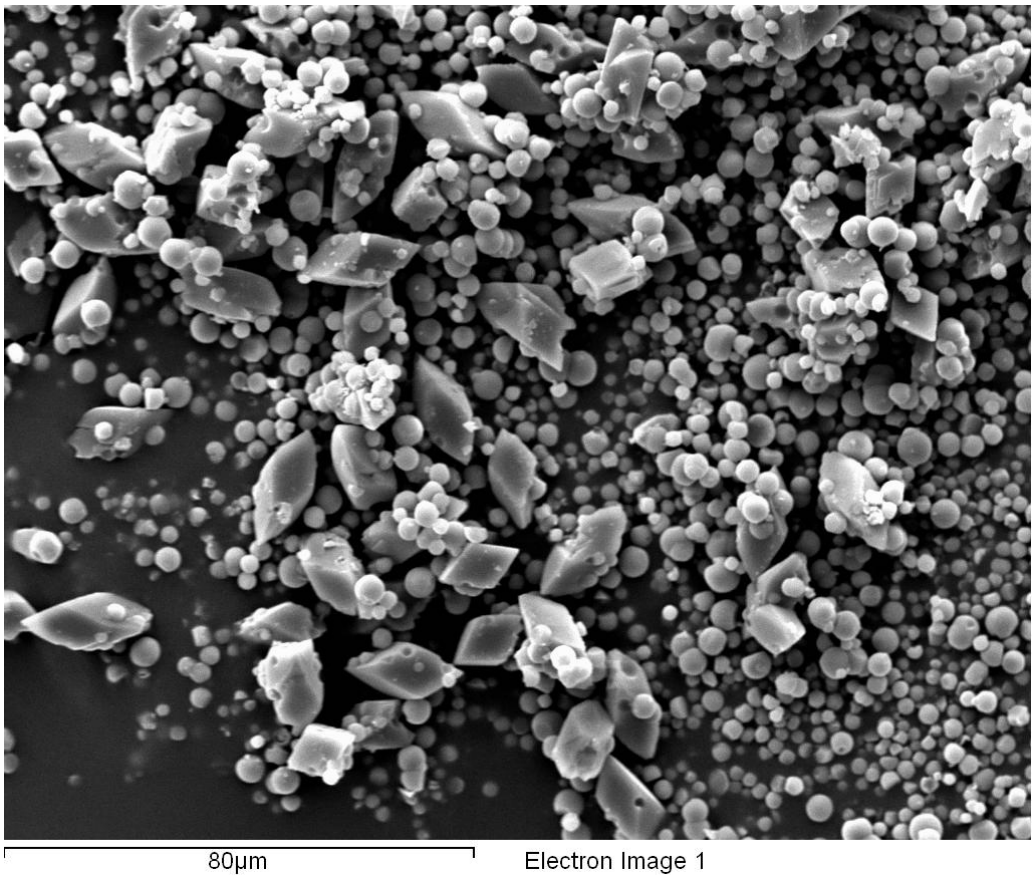

Figure 5.44 - SEM image of 80% V-doped TiP_2O_7 (673x magnification)

Vanadium clearly has an effect on the morphology of the crystals, but is it only vanadium metal that has this effect. The use of other vanadium sources, in this case vanadium oxides, in synthesis was investigated. Using the same molar ratio (50%) as original sample, V-doped TiP_2O_7 was synthesised using both VO_2 and V_2O_5, which resulted products with very similar diffraction patterns to the original vanadium doped TiP_2O_7. Samples of V-doped TiP_2O_7 using VO_2 and V_2O_5 were synthesised and supplied by Katie Fernyhough (Masters student). Figures 5.45 and 5.46 show SEM images of the samples to display their morphology.

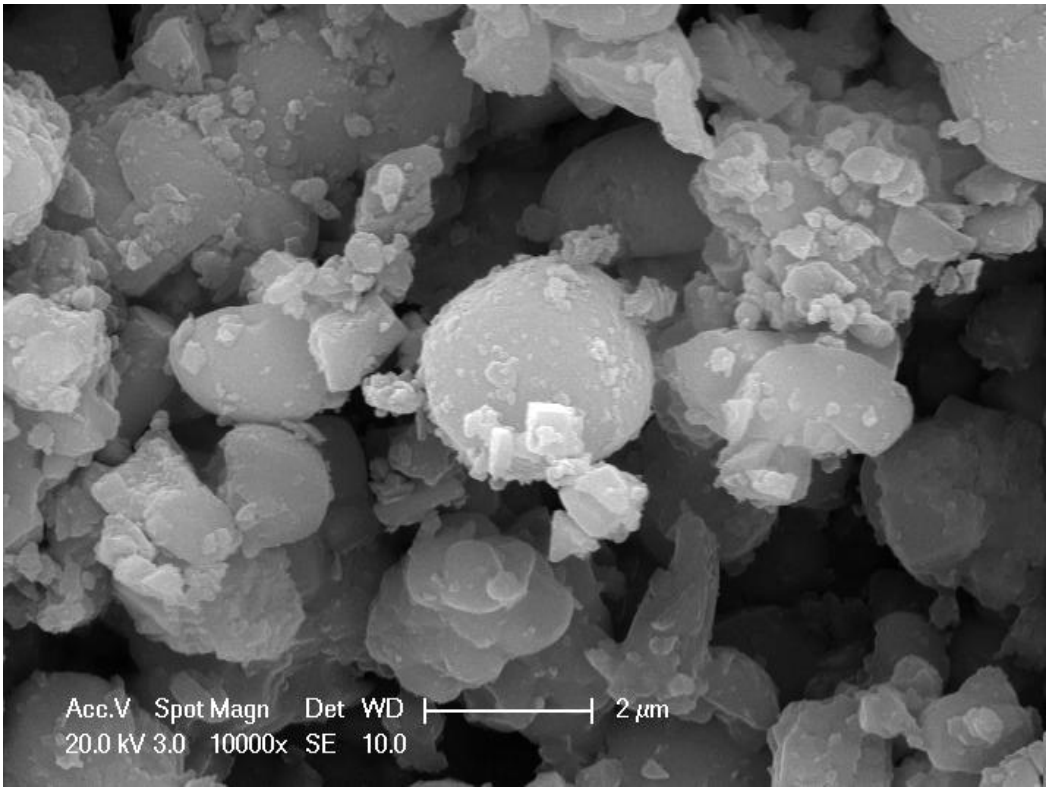

Figure 5.45 - SEM image of V-doped TiP_2O_7 using VO_2 as vanadium source (10000x magnification)

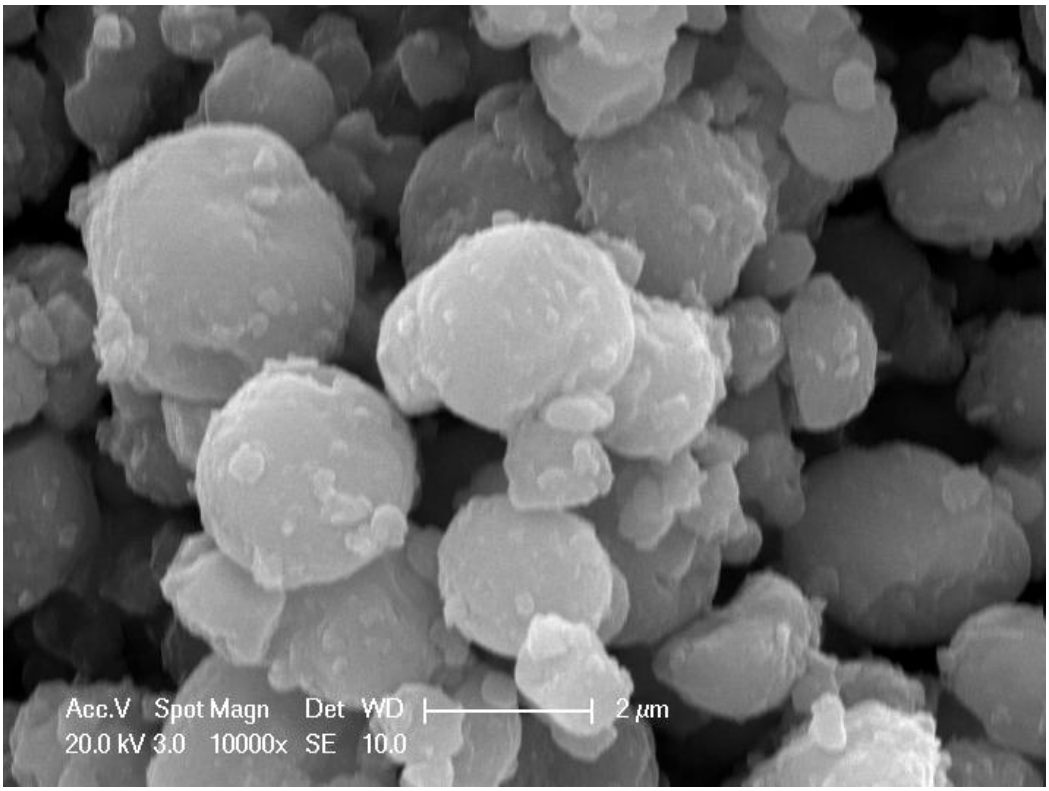

Figure 5.46 - SEM image of V-doped TiP_2O_7 using V_2O_5 as vanadium source (10000x magnification)

Both doped samples show a spherical morphology with particles approximately 3 μm in diameter, however the morphology is not as monodispersed as it is in the original doped sample. The VO_2 sample in particular has more of a variety of particle sizes and morphologies compared to the V_2O_5 sample which appears to be more similar in appearance to the original V metal doped sample. Both show particle agglomeration.

The presence of vanadium clearly has an impact on the morphology. How this occurs is unclear. The availability of vanadium in solution, solubility of the vanadium salt in the phosphoric acid or the starting material particle size may all be factors in the final crystal morphology.

5.4 Conclusion

A meta-stable polymorph of TiP_2O_7 was successfully synthesised via a low temperature acid melt synthesis and appears to adopt the cubic sub-cell structure of the AX_2O_7 series, space group $Pa\bar{3}$. There is evidence in the Rietveld refinement of a second TiP_2O_7 phase, approximately 20 wt. %. There is doubt as to the true structure due to high thermal parameters and high calculated bond valences, which may indicate issues with the structural model. Upon heating a phase transition occurs between 279 – 378°C leading to the adoption of the true cubic structure, which when cooled below 679°C cubic superstructure peaks appear in the diffraction pattern.

Vanadium was successfully doped into TiP_2O_7 via incorporation of vanadium metal into the acid melt synthesis, leading to an expansion of the cubic sub-cell lattice parameter. XRF confirms the presence of vanadium, and ESR confirms the presence

of V^{4+}, suggesting a potential stoichiometry of $Ti_{0.74}V_{0.16}P_2O_7$, however there is uncertainty in the weight percentages. V-doped TiP_2O_7 also undergoes a phase transition at a slightly higher temperature range (304-450°C) to form the true cubic sub-cell, which converts to the cubic superstructure when cooled below 590°C. SAED and neutron powder diffraction have shown that the synthesised V-doped TiP_2O_7 does not adopt the true cubic structure; NPD shows that it is close to the simple cubic structure; however attempts to find a structural model have failed. Vanadium also appears to affect the crystal morphology. Addition of vanadium leads to the formation of spherical particles approximately 3 μm in diameter. Different vanadium sources also lead to spherical particles although these are less uniform in size and shape. Further work will need to be undertaken in order to identify the structure of the meta-stable polymorph of TiP_2O_7, the location of the V within the structure and how the vanadium affects the formation of the crystal morphology.

References

1. K. M. White, P. L. Lee, P. J. Chupas, K. W. Chapman, E. A. Payzant, A. C. Jupe, W. A. Bassett, C.-S. Zha and A. P. Wilkinson, *Chemistry of Materials*, 2008, **20**, 3728-3734.
2. S. T. Norberg, G. Svensson and J. Albertsson, *Acta Crystallographica Section C*, 2001, **C57**, 225-227.
3. V. Korthius, N. Khosrovani, A. W. Sleight, N. Roberts, R. Dupree and J. W. W. Warren, *Chemistry of Materials*, 1995, **7**, 412-417.
4. E. Tillmanns, W. Gebert and W. H. Baur, *Journal of Solid State Chemistry*, 1973, **7**, 69-84.

5. G. Wallez, P. E. Raison, N. Dacheux, N. Clavier, D. Bykov, L. Delevoye, K. Popa, D. Bregiroux, A. N. Fitch and R. J. M. Konings, *Inorganic Chemistry*, 2012, **51**, 4314-4322.
6. G. W. Stinton, M. R. Hampson and J. S. O. Evans, *Inorganic Chemistry*, 2006, **45**, 4352-4358.
7. E. R. Losilla, A. Cabeza, S. Bruque, M. A. G. Aranda, J. Sanz, J. L. Iglesias and J. A. Alonso, *Journal of Solid State Chemistry*, 2001, **156**, 213-219.
8. R. K. B. Gover, N. D. Withers, S. Allen, R. L. Withers and J. S. O. Evans, *Journal of Solid State Chemistry*, 2002, **166**, 42-48.
9. A. W. Sleight, *Annual Review of Materials Science*, 1998, **28**, 29-43.
10. W. T. A. Harrison, T. E. Gier and G. D. Stucky, *European Journal of Solid State Inorganic Chemistry*, 1993, **30**, 761-771.
11. I. C. Marcu, I. Sandulescu and J. M. M. Millet, *Applied Catalysis A-General*, 2002, **227**, 309-320.
12. P. Senguttuvan, G. Rousse, J. Oro-Sole, J. M. Tarascon and M. R. Palacin, *Journal of Materials Chemistry A*, 2013, **1**, 15284-15291.
13. S. Carlson and A. M. K. Anderson, *Journal of Applied Crystallography*, 2001, **34**, 7-12.
14. N. Clavier, G. Wallez, N. Dacheux, D. Bregiroux, M. Quarton and P. Beaunier, *Journal of Solid State Chemistry*, 2008, **181**, 3352-3356.
15. S. Loridant, I. C. Marcu, G. Bergeret and J. M. M. Millet, *Physical Chemistry Chemical Physics*, 2003, **5**, 4384-4389.
16. J. Sanz, J. E. Iglesias, J. Soria, E. R. Losilla, M. A. G. Aranda and S. Bruque, *Chemistry of Materials*, 1997, **9**, 996-1003.
17. H. M. Rietveld, *Journal of Applied Crystallography*, 1969, **2**, 65-71.
18. A. C. Larson and R. B. Von Dreele, Los Alamos National Laboratory, Los Alamos NM, Editon edn., 1994.
19. B. H. Toby, *Journal of Applied Crystallography,* 2001, **34**, 210-213.
20. JCPDS, *International Centre for Diffraction Data*, 1999, P.1., Swathmore, Pennsylvania, PA 19081, USA 11990
21. A. D. F. Toy, ed., *Comprehensive Inorganic Chemistry*, Pergamon, Oxford, 1973.

22. C. E. Bamberger and G. M. Begun, *Journal of the Less Common Metals*, 1987, **134**, 201-206.
23. A. S. Lyakhov, K. K. Palkina and V. A. Lyutsko, *Izvestiya Akademii Nauk SSSR Neorganicheskie Materialy*, 1990, **26**, 1064-1068.
24. R. D. Shannon and C. T. Prewitt, *Acta Crystallographica Section B*, 1969, **25**, 925-946.
25. J. F. Woodworth, University of Iowa, 2006.
26. J. W. Wiench, C. J. Fontenot, J. F. Woodworth, G. L. Schrader, M. Pruski and S. C. Larsen, *The Journal of Physical Chemistry B*, 2005, **109**, 1756-1762.
27. H. Birkedal, A. M. K. Andersen, A. Arakcheeva, G. Chapuis, P. Norby and P. Pattison, *Inorganic Chemistry*, 2006, **45**, 4346-4351.
28. W. Ostwald, *Lehrbuch der Allgemeinen Chemie*, Leipzig, 1896.

Chapter 6

Conclusions and Further Work

6.1 Research Summary

A novel synthetic route for magnesium phosphates was successfully used to synthesise two polymorphs of $MgH_2P_2O_7$, hereby assigned as α- & β-$MgH_2P_2O_7$. A synthetic route to α-$MgH_2P_2O_7$ had been previous reported, but without reporting structural details, whereas β-$MgH_2P_2O_7$ was previously unknown. Both polymorphs crystallised into monoclinic space groups, with α-$MgH_2P_2O_7$ isostructural with $NiH_2P_2O_7$ and β-$MgH_2P_2O_7$ isostructural with $CaH_2P_2O_7$. Rietveld refinements using neutron powder diffraction data were carried using the Ni and Ca models, both giving excellent fits. Global instability index calculations were used to indicate structural strain. The value calculated for α-$MgH_2P_2O_7$ suggests the structure is not strained, whereas the value calculated for β-$MgH_2P_2O_7$ indicates a strained structure.

The introduction of lithium carbonate into the acid melt during synthesis resulted in a new phase with a similar PXRD pattern and lattice parameters to that of α-$MgH_2P_2O_7$. The presence of lithium was confirmed by flame photometry and VT-XRD. A Rietveld refinement of NPD was carried out using α-$MgH_2P_2O_7$ as a structural model, which gave a good fit and a stoichiometry of $MgLi_{0.8}H_{1.2}P_2O_7$. A second Rietveld refinement was carried out using $LiNi_2H_3(P_2O_7)_2$ which also gave a good fit.

Broad peaks in the PXRD and different particle morphologies in the SEM image suggest there may be multiple phases in the sample.

The acid melt synthetic route was also used to synthesise $MnH_2P_2O_7$. It was found to be isostructural with $CaH_2P_2O_7$. A Rietveld refinement of NPD carried out using the Ca structural model gave an excellent fit. GII calculations indicate that it is also strained, like β-$MgH_2P_2O_7$. There are two known polymorphs of $MH_2P_2O_7$: α - Mg, Fe, Ni, Co and β – Ca, Mg and Mn. The size of the M^{2+} cation appears to have a strong influence over the final structure; however chapter 3 shows that polymorph formation can be influenced by reaction temperature and crystal seeding. Magnetic analysis suggests that $MnH_2P_2O_7$ is paramagnetic with a small underlying antiferromagnetic component, and an effective moment consistent with a high spin Mn^{2+} ion.

Incorporation of lithium was also achieved via addition of lithium carbonate into the acid melt, with VT-XRD confirming the presence of Li in the sample. Rietveld refinement of NPD suggests a similar structure to $MnH_2P_2O_7$ and a composition of $MnLi_{0.5}H_{1.5}P_2O_7$, however there is doubt about this stoichiometry due to the presence of an unknown impurity. Magnetic analysis suggests that Li-doped $MnH_2P_2O_7$ is also paramagnetic, with a small antiferromagnetic component. The effective moment is also consistent with a high spin Mn^{2+} ion and therefore shows no evidence of a change to the Mn oxidation state upon the inclusion of lithium.

A meta-stable polymorph of TiP_2O_7 was successfully synthesised and appears to adopt the ideal cubic structure of the AX_2O_7 series. Rietveld refinement of XRD data reveals the presence of a second TiP_2O_7 phase, approximately 20 wt. %. High

thermal parameters and calculated valences throw doubt on the refined structure, suggesting that it is not truly cubic.

Vanadium was successfully incorporated into TiP_2O_7 through the addition of vanadium metal into the acid melt, leading to an expansion of the unit cell. The presence of V in the sample is confirmed by XRF and ESR with a potential stoichiometry of $Ti_{0.74}V_{0.16}P_2O_7$, however there is uncertainty in the weight percentages.

Both LTS-TiP_2O_7 and V-doped TiP_2O_7 undergo a phase transition when heated above 304°C (279°C for LTS-TiP_2O_7) to the ideal cubic structure, and upon cooling form the cubic superstructure. SAED and NPD show the V-doped TiP_2O_7 is not cubic.

The addition of vanadium leads to the formation of remarkably uniform spherical particles of approximately 3 μm in diameter. At present the reasons for the formation of such monodisperse spherical particles with vanadium is unclear, however, although different vanadium sources also lead to spherical particles, these appear less uniform in size and shape. Initial TEM and SAED results show that the spheres are either single crystals or crystals that are aligned, with aligned crystals more likely due to the shape of the particles and the lack of straight edges. TEM results of the spheres after multiple heat treatments show the formation of polycrystalline hollow bubble-like particles on the surface of the spheres.

6.2 Further Work

To characterise fully $MgH_2P_2O_7$, further MAS-NMR could be carried out, such as ^{1}H and ^{25}Mg NMR, which would confirm the number of Mg and H environments in each polymorph. MAS-NMR could also be used to elucidate the structure of Li-doped

$MgH_2P_2O_7$, which would indicate how many Li, P, and H environments are present. Higher resolution powder diffraction data, such as synchrotron data, would also help confirm the presence of multiple phases. The presence of protons and lithium ions in the structure could show potential for ionic conductivity. Conductivity measurements could be carried out to explore their potential.

MAS-NMR could be used to investigate the number of lithium environments in Li-doped $MnH_2P_2O_7$ – if more than 1 site is observed then it may indicate a lithium based impurity – and to confirm the structure of $MnH_2P_2O_7$. Low temperature neutron diffraction below 5 K could be used to investigate if $MnH_2P_2O_7$ and Li-doped $MnH_2P_2O_7$ magnetically order below the lower temperature limit used in SQUID measurements, and to investigate the unknown impurity phase.

To confirm the symmetry of both LTS-TiP_2O_7 and V-doped TiP_2O_7 and the structural transition, higher resolution powder diffraction data such as synchrotron data could be used in a similar way to the studies of CeP_2O_7 and UP_2O_7. MAS-NMR would also help confirm the symmetry; ^{31}P NMR will show the number of P environments, and ^{51}V NMR will confirm the location of the vanadium within the structure. Potential protonic conductivity and catalytic activity could also be investigated as potential applications for these materials.

To understand the morphology of V-doped TiP_2O_7, detailed TEM studies could be undertaken to try to establish the formation of the spherical morphology and investigate the local structure and composition. The formation of the spherical morphology occurs with the addition of V metal to the melt. This may not be unique to V itself, and may occur through the addition of other metals, and so further

synthetic/SEM studies could be conducted to investigate this. Initial syntheses using Fe metal have shown that spherical particles are formed upon the addition of Fe metal to the acid melt synthesis.

Appendix 1

The Bond Valence Sum (BVS) Model and the Global Instability Index (GII)

The Bond Valence Sum model[1] states that the atomic valence (V_i) of an ion, *i*, is equal to the sum of the bond valences (S_{ij}) surrounding the ion in question:

$$V_i = \sum_j S_{ij} \tag{A1.1}$$

The relationship between bond length and bond valence is shown in equation A1.2:

$$S_{ij} = exp\left(\frac{R_O - R_{ij}}{B}\right) \tag{A1.2}$$

where R_O is the characteristic bond length, R_{ij} is the bond length between atoms *i* and *j* which has been determined experimentally, and B is an empirical constant, which for most compounds was found to be 0.37 Å.

If the calculated valence is close to the expected valence of the atom in question, then this is a good indication that the correct coordination environment and oxidation state has been assumed. BVS calculations can also be used to indicate if there is strain within a lattice, which can be evident from the presence of both low and high calculated valence sums around some atoms in the lattice. The GII,[2, 3] which has been derived from the BVS model, can be used as a measure of the strain in the lattice.

$$GII = \sqrt{\frac{\left(\sum_j S_{ij} - V_i\right)^2}{N}} \tag{A1.3}$$

where V_i is the formal valence and N is the number of atoms in the asymmetric unit. GII values below 0.05 valence units (vu) suggest that there is little to no strain present; whereas values above 0.20 vu indicate that the lattice is so strained that is unstable, which can be an indication that the structure has been incorrectly determined.

References

1. I. D. Brown and D. Altermatt, *Acta Crystallographica* 1985, **B41**, 244-247.
2. A. Salinas-Sanchez, J. L. Garcia-Muńoz, J. Rodriguez-Carvajal, R. Saez-Puche and J. L. Martinez, *Journal of Solid State Chemistry*, 1992, **100**, 201-211.
3. I. D. Brown, *The Chemical Bond in Inorganic Chemistry*, Oxford University Press, Oxford, 2002.

Appendix 2

Lithium Flame Photometry Data

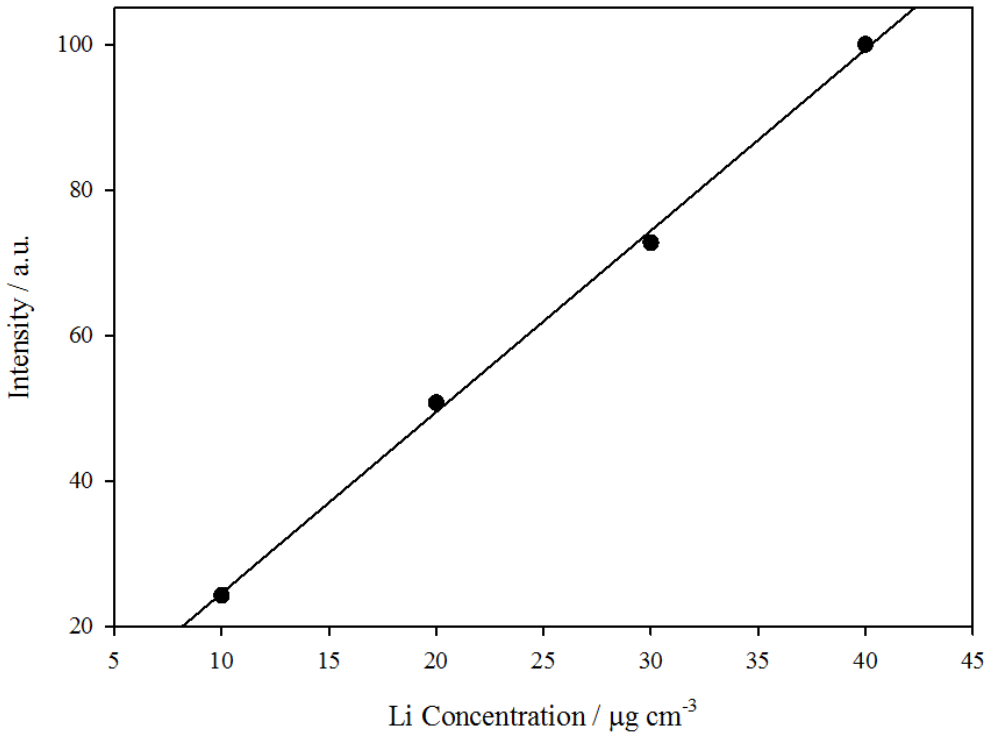

Figure A2.1 - Calibration plot

Table A2.1 - Raw data

Li concentration/ µg cm^{-3}	**Reading**				**Average reading**
	1	**2**	**3**	4	
10	24	24	24.5	24.5	24.25
20	50.5	51	51	50.5	50.75
33	73.5	72.5	72.5	72.5	72.75
40	100	100	100	100	100
Sample	22.5	23	22.5	22.5	22.63

Appendix 3

Rietveld Refinement Details of Heat Treated TiP_2O_7 and V-Doped TiP_2O_7

All thermal parameters were constrained to universal for each atom type.

Table A3.1 - Refined structural parameters of heat treated TiP_2O_7

Atom	Site	Occupancy	x	y	z	U_{iso} (Å^2)
Ti1	24*d*	1	0.6576(9)	0.164(1)	0.1753(9)	0.004(1)
Ti2	24*d*	1	0.8392(7)	-0.000(1)	0.1765(8)	0.004(1)
Ti3	24*d*	1	0.1578(8)	-0.0060(8)	0.1765(8)	0.004(1)
Ti4	24*d*	1	0.500(1)	-0.0060(8)	0.1663(8)	0.004(1)
Ti5	8*c*	1	0.8339(9)	0.3339(9)	0.1661(9)	0.004(1)
Ti6	4*a*	1	0	0	0	0.004(1)
P1	24*d*	1	0.791(1)	0.126(1)	0.133(2)	0.013(2)
P2	24*d*	1	0.869(2)	0.201(1)	0.198(1)	0.013(2)
P3	24*d*	1	0.628(1)	0.032(1)	0.203(1)	0.013(2)
P4	24*d*	1	0.712(1)	-0.048(1)	0.134(1)	0.013(2)
P5	24*d*	1	0.799(1)	0.027(1)	-0.039(1)	0.013(2)
P6	24*d*	1	0.866(1)	-0.024(1)	0.037(1)	0.013(2)
P7	24*d*	1	0.286(1)	0.030(1)	0.201(1)	0.013(2)
P8	24*d*	1	0.369(1)	-0.034(1)	0.113(1)	0.013(2)
P9	8*c*	1	0.127(2)	0.127(2)	0.127(2)	0.013(2)
P10	8*c*	1	0.700(1)	0.200(1)	0.300(1)	0.013(2)
P11	8*c*	1	0.543(1)	-0.043(1)	0.043(1)	0.013(2)
O1	24*d*	1	0.8119	0.1768	0.1717	0.029(1)
O2	24*d*	1	0.6867	0.0019	0.1779	0.029(1)
O3	24*d*	1	0.8173	0.0110	0.0212	0.029(1)
O4	24*d*	1	0.3129	-0.0080	0.1459	0.029(1)
O5	8*c*	1	0.6609	0.1609	0.3391	0.029(1)
O6	4*b*	1	0.5	0	0	0.029(1)
O7	24*d*	1	0.7251	0.1281	0.1424	0.029(1)
O8	24*d*	1	0.8712	-0.0774	0.1915	0.029(1)
O9	24*d*	1	0.8099	0.0709	0.1654	0.029(1)
O10	24*d*	1	0.8582	0.2643	0.2011	0.029(1)
O11	24*d*	1	0.6811	0.2332	0.1421	0.029(1)
O12	24*d*	1	0.1813	-0.0823	0.1788	0.029(1)
O13	24*d*	1	0.6341	0.0888	0.2025	0.029(1)
O14	24*d*	1	0.5807	0.0059	0.1638	0.029(1)
O15	24*d*	1	0.1235	-0.0001	0.2400	0.029(1)
O16	24*d*	1	0.7758	-0.0392	0.1440	0.029(1)
O17	24*d*	1	0.8679	0.3132	0.0947	0.029(1)

Atom	Site	Occupancy	x	y	z	U_{iso} (Å²)
O18	24*d*	1	0.5074	-0.0745	0.2037	0.029(1)
O19	24*d*	1	0.4929	0.0367	0.2314	0.029(1)
O20	24*d*	1	0.9044	0.0327	0.2117	0.029(1)
O21	24*d*	1	0.1758	-0.0103	0.0854	0.029(1)
O22	24*d*	1	0.8782	-0.0002	0.1049	0.029(1)
O23	24*d*	1	0.9196	-0.0069	0.0068	0.029(1)
O24	24*d*	1	0.0836	-0.0444	0.1428	0.029(1)
O25	24*d*	1	0.2234	0.0247	0.1860	0.029(1)
O26	24*d*	1	0.5861	0.1949	0.1920	0.029(1)
O27	24*d*	1	0.8025	-0.0047	0.2500	0.029(1)
O28	24*d*	1	0.4176	-0.0188	0.1629	0.029(1)
O29	24*d*	1	0.4879	0.0647	0.1213	0.029(1)
O30	24*d*	1	0.6221	0.1406	0.0987	0.029(1)
O31	24*d*	1	0.1211	0.0655	0.1499	0.029(1)
O32	24*d*	1	0.6912	0.1788	0.2416	0.029(1)
O33	24*d*	1	0.5074	-0.0443	0.0932	0.029(1)

Space group *Pa*-3; a = 23.5692(5) Å. Figures of merit: R_{wp} = 4.41%, R_p = 3.15%, χ^2 = 2.489

Table A3.2 - Refined structural parameters of heat treated V-doped TiP_2O_7

Atom	Site	Occupancy	x	y	z	U_{iso} (Å²)
Ti1	24*d*	1	0.655(1)	0.159(1)	0.171(9)	0.003(1)
Ti2	24*d*	1	0.840(1)	-0.002(1)	0.178(1)	0.003(1)
Ti3	24*d*	1	0.154(1)	-0.007(1)	0.1653(9)	0.003(1)
Ti4	24*d*	1	0.495(1)	-0.005(1)	0.162(2)	0.003(1)
Ti5	8*c*	1	0.833(1)	0.333(1)	0.167(1)	0.003(1)
Ti6	4*a*	1	0	0	0	0.003(1)
P1	24*d*	1	0.794(2)	0.121(2)	0.134(2)	0.008(2)
P2	24*d*	1	0.859(2)	0.204(2)	0.206(2)	0.008(2)
P3	24*d*	1	0.628(2)	0.025(2)	0.207(2)	0.008(2)
P4	24*d*	1	0.711(2)	-0.036(2)	0.130(2)	0.008(2)
P5	24*d*	1	0.794(2)	0.028(2)	-0.036(2)	0.008(2)
P6	24*d*	1	0.868(2)	-0.019(1)	0.041(2)	0.008(2)
P7	24*d*	1	0.285(2)	0.030(2)	0.194(2)	0.008(2)
P8	24*d*	1	0.381(2)	-0.037(2)	0.122(2)	0.008(2)
P9	8*c*	1	0.127(2)	0.127(2)	0.127(2)	0.008(2)
P10	8*c*	1	0.699(2)	0.199(2)	0.301(2)	0.008(2)
P11	8*c*	1	0.542(2)	-0.042(2)	0.042(2)	0.008(2)
O1	24*d*	1	0.8119	0.1768	0.1717	0.023(2)
O2	24*d*	1	0.6867	0.0019	0.1779	0.023(2)
O3	24*d*	1	0.8173	0.0110	0.0212	0.023(2)

Atom	Site	Occupancy	x	y	z	U_{iso} (Å^2)
O4	24*d*	1	0.3129	-0.0080	0.1459	0.023(2)
O5	8*c*	1	0.6609	0.1609	0.3391	0.023(2)
O6	4*b*	1	0.5	0	0	0.023(2)
O7	24*d*	1	0.7251	0.1281	0.1424	0.023(2)
O8	24*d*	1	0.8712	-0.0774	0.1915	0.023(2)
O9	24*d*	1	0.8099	0.0709	0.1654	0.023(2)
O10	24*d*	1	0.8582	0.2643	0.2011	0.023(2)
O11	24*d*	1	0.6811	0.2332	0.1421	0.023(2)
O12	24*d*	1	0.1813	-0.0823	0.1788	0.023(2)
O13	24*d*	1	0.6341	0.0888	0.2025	0.023(2)
O14	24*d*	1	0.5807	0.0059	0.1638	0.023(2)
O15	24*d*	1	0.1235	-0.0001	0.2400	0.023(2)
O16	24*d*	1	0.7758	-0.0392	0.1440	0.023(2)
O17	24*d*	1	0.8679	0.3132	0.0947	0.023(2)
O18	24*d*	1	0.5074	-0.0745	0.2037	0.023(2)
O19	24*d*	1	0.4929	0.0367	0.2314	0.023(2)
O20	24*d*	1	0.9044	0.0327	0.2117	0.023(2)
O21	24*d*	1	0.1758	-0.0103	0.0854	0.023(2)
O22	24*d*	1	0.8782	-0.0002	0.1049	0.023(2)
O23	24*d*	1	0.9196	-0.0069	0.0068	0.023(2)
O24	24*d*	1	0.0836	-0.0444	0.1428	0.023(2)
O25	24*d*	1	0.2234	0.0247	0.1860	0.023(2)
O26	24*d*	1	0.5861	0.1949	0.1920	0.023(2)
O27	24*d*	1	0.8025	-0.0047	0.2500	0.023(2)
O28	24*d*	1	0.4176	-0.0188	0.1629	0.023(2)
O29	24*d*	1	0.4879	0.0647	0.1213	0.023(2)
O30	24*d*	1	0.6221	0.1406	0.0987	0.023(2)
O31	24*d*	1	0.1211	0.0655	0.1499	0.023(2)
O32	24*d*	1	0.6912	0.1788	0.2416	0.023(2)
O33	24*d*	1	0.5074	-0.0443	0.0932	0.023(2)

Space group *Pa*-3; a = 23.6010(3) Å. Figures of merit: R_{wp} = 2.66%, R_p = 1.92%, χ^2 = 1.253

Appendix 4

EDS Spectra of V-Doped TiP_2O_7 and Heat Treated V-Doped TiP_2O_7

V-Doped TiP_2O_7

Spectrum processing :
No peaks omitted

Processing option : All elements analyzed (Normalised)
Number of iterations = 6

Standard :
O SiO2 1-Jun-1999 12:00 AM
P GaP 1-Jun-1999 12:00 AM
Ti Ti 1-Jun-1999 12:00 AM
V V 1-Jun-1999 12:00 AM

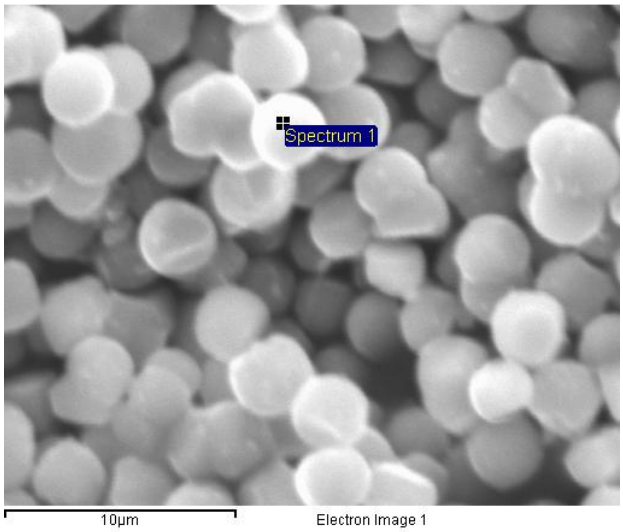

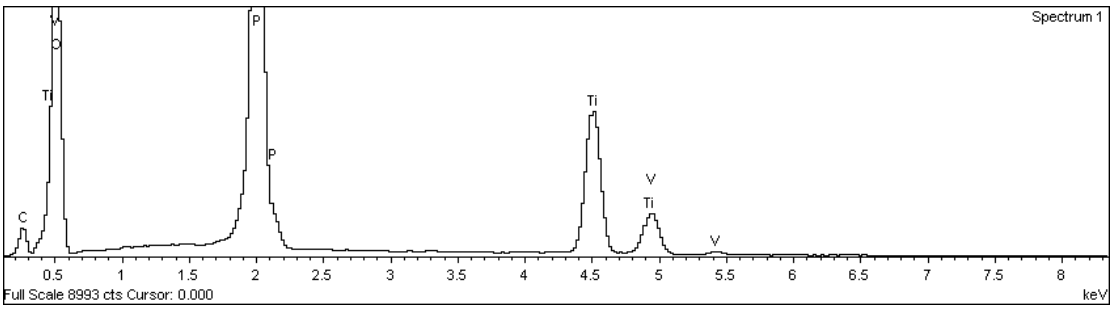

Element	Weight%	Atomic%
O K	59.27	76.61
P K	24.90	16.62
Ti K	13.23	5.71
V K	2.61	1.06
Totals	100.00	

Heat Treated V-Doped TiP_2O_7

Spectrum processing :
No peaks omitted

Processing option : All elements analyzed (Normalised)
Number of iterations = 6

Standard :
O SiO2 1-Jun-1999 12:00 AM
Si SiO2 1-Jun-1999 12:00 AM
P GaP 1-Jun-1999 12:00 AM
Ti Ti 1-Jun-1999 12:00 AM
V V 1-Jun-1999 12:00 AM

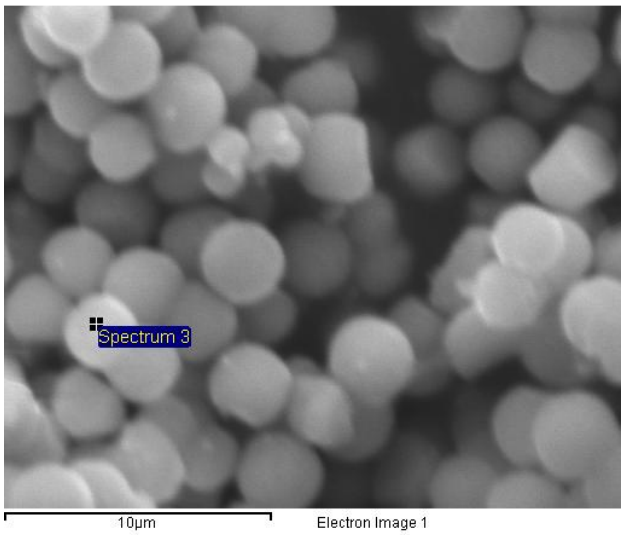

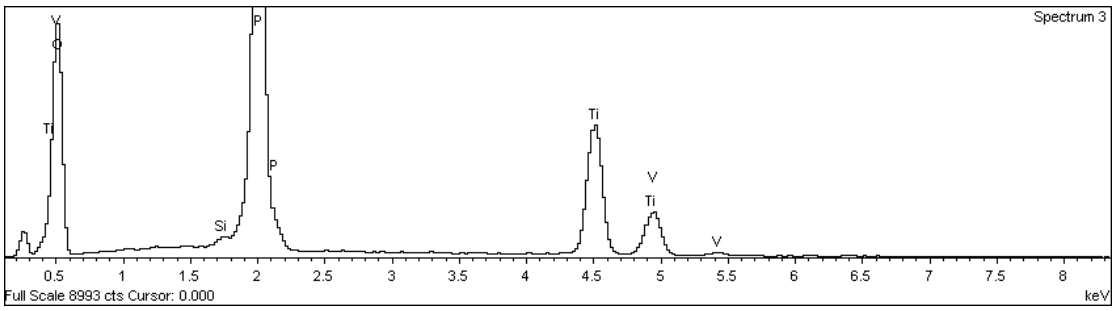

Element	Weight%	Atomic%
O K	55.16	73.55
Si K	0.25	0.19
P K	26.69	18.38
Ti K	14.28	6.36
V K	3.62	1.51
Totals	100.00	

Appendix 5

Refined VT-XRD Lattice Parameters of LTS-TiP_2O_7 and V-Doped TiP_2O_7

Table A5.1 - Refined lattice parameters for LTS-TiP_2O_7 upon heating – 1st cycle

Temperature / °C	*a* / Å	Error	Zero Error	Error
32	7.901063	0.00048	-2.24421	0.175099
45	7.903942	0.000453	-1.82932	0.167599
99	7.909416	0.000453	-1.09349	0.167148
151	7.916127	0.000475	0.0321318	0.173234
202	7.923604	0.000468	1.16117	0.17055
229	7.924287	0.000384	9.0791	0.14388
254	7.923979	0.000527	0.942436	0.186604
279	7.915763	0.000495	1.15315	0.177702
304	7.915134	0.000475	2.92885	0.172379
329	7.915194	0.000445	3.62347	0.162757
354	7.91676	0.000443	4.60267	0.163331
378	7.9177	0.000448	5.24302	0.164288
402	7.917673	0.00044	5.48548	0.161365
450	7.919859	0.000424	6.28749	0.156255
474	7.921002	0.000402	6.96988	0.149974
497	7.922555	0.000401	7.78067	0.149246
521	7.923499	0.000402	8.47854	0.14911
544	7.92426	0.000385	9.07494	0.144082
589	7.924867	0.000393	9.537	0.146158
635	7.927929	0.000393	10.8816	0.146611
679	7.930941	0.000378	12.2304	0.142766
723	7.933837	0.000395	13.5484	0.147321
765	7.937557	0.000404	15.0451	0.150088
807	7.941941	0.000397	16.4641	0.148316
848	7.946721	0.000385	18.0047	0.143346
889	7.951524	0.000373	19.6208	0.137884
928	7.957515	0.000376	21.1572	0.138313

Table A5.2 - Refined lattice parameters for LTS-TiP_2O_7 upon cooling – 1st cycle

Temperature / °C	*a* / Å	Error	Zero Error	Error
889	7.959406	0.000329	20.7964	0.122171
848	7.953372	0.000334	19.2558	0.123392
807	7.94838	0.000326	17.7038	0.122576
765	7.942406	0.000341	15.7336	0.126617
723	7.937819	0.00034	14.3668	0.126488
679	7.93266	0.000347	12.8843	0.128778
635	7.927173	0.00035	11.3922	0.13
590	7.921284	0.000336	9.9462	0.124308
544	7.915334	0.000313	8.50508	0.118001
498	7.909327	0.000307	7.11841	0.11578
450	7.904642	0.000297	6.16323	0.113121
402	7.899512	0.000315	4.92757	0.118502
354	7.894928	0.00032	3.95027	0.120128
304	7.889626	0.000337	2.57222	0.125399
254	7.884946	0.000329	1.46489	0.123784
203	7.879606	0.000351	0.162098	0.130741
151	7.875678	0.000344	-0.621895	0.129598
99	7.870925	0.000359	-1.71139	0.133957
45	7.866259	0.00037	-2.81083	0.137995
32	7.864781	0.000377	-3.21819	0.140625

Table A5.3 - Refined lattice parameters for LTS-TiP_2O_7 upon heating – 2nd cycle

Temperature / °C	*a* / Å	Error	Zero Error	Error
45	7.865938	0.000368	-3.12049	0.137815
99	7.870975	0.000364	-1.69257	0.13698
151	7.875354	0.000355	-0.808179	0.133094
202	7.880199	0.000349	0.399766	0.12995
229	7.884585	0.000337	1.35844	0.12627
254	7.889386	0.00033	2.47274	0.123792
279	7.893372	0.000329	3.38391	0.123354
304	7.898912	0.000317	4.75683	0.119586
329	7.90423	0.000327	6.12904	0.122182
354	7.908339	0.000313	6.95852	0.117988
378	7.9137	0.000312	8.4593	0.117317
402	7.919228	0.000309	9.75885	0.116191
450	7.924721	0.000309	11.072	0.116685
474	7.930862	0.000323	12.5952	0.120857
497	7.937609	0.00034	14.3564	0.126905
521	7.942272	0.000338	15.7139	0.126252
544	7.946992	0.000349	17.1352	0.129369
589	7.952773	0.000338	18.9999	0.124904
635	7.959899	0.000333	20.8184	0.124018
679	7.969556	0.000361	22.5758	0.132229
723	7.865938	0.000368	-3.12049	0.137815
765	7.870975	0.000364	-1.69257	0.13698
807	7.875354	0.000355	-0.808179	0.133094
848	7.880199	0.000349	0.399766	0.12995
889	7.884585	0.000337	1.35844	0.12627
928	7.889386	0.00033	2.47274	0.123792

Table A5.4 - Refined lattice parameters for LTS-TiP_2O_7 upon cooling – 2nd cycle

Temperature / °C	*a* / Å	Error	Zero Error	Error
889	7.960618	0.000323	20.597	0.119232
848	7.954416	0.000325	18.8968	0.119185
807	7.948676	0.000335	17.3801	0.12428
765	7.944535	0.00032	16.0011	0.119341
723	7.939592	0.000325	14.5025	0.121944
679	7.933992	0.000324	12.8245	0.121202
635	7.929484	0.000323	11.5637	0.121615
590	7.923051	0.000308	10.0562	0.116337
544	7.915978	0.000297	8.438	0.112851
498	7.91007	0.000297	7.0793	0.112152
450	7.904874	0.000291	5.85653	0.111022
402	7.899779	0.000318	4.54113	0.118473
354	7.895732	0.000315	3.70902	0.118297
304	7.890922	0.000324	2.65032	0.121609
254	7.886124	0.000339	1.54988	0.125811
203	7.881798	0.000324	0.626704	0.122731
151	7.876406	0.000343	-0.723437	0.127969
99	7.871296	0.000358	-2.02753	0.133556
45	7.867474	0.000361	-2.81438	0.134752
32	7.866007	0.000376	-3.12146	0.139352

Table A5.5 - Refined lattice parameters for V-doped TiP_2O_7 upon heating – 1st cycle

Temperature / °C	*a* / Å	Error	Zero Error	Error
32	7.899654	0.000366	-5.84762	0.135092
45	7.901289	0.000356	-6.13645	0.130156
99	7.90488	0.000381	-5.22149	0.137739
151	7.910699	0.000375	-3.88235	0.135884
202	7.91766	0.000413	-2.85812	0.147473
229	7.920929	0.000403	-2.22925	0.144341
254	7.922153	0.000403	-2.15886	0.144328
279	7.923983	0.000399	-1.41424	0.142686
304	7.921878	0.000384	-1.4941	0.13807
329	7.919236	0.000356	-0.81546	0.128668
354	7.91733	0.000311	0.121452	0.114218
378	7.915811	0.000287	0.939339	0.105969
402	7.914519	0.000281	1.62108	0.103841
450	7.913865	0.000275	2.31259	0.101899
474	7.913321	0.000275	2.83131	0.102008
497	7.914237	0.000279	3.71487	0.103445
521	7.915178	0.00028	4.38185	0.103079
544	7.916676	0.000274	5.23171	0.1012
589	7.917309	0.00027	5.62478	0.099786
635	7.921681	0.000265	7.05239	0.097886
679	7.925459	0.000256	8.33738	0.094756
723	7.929451	0.000257	9.66276	0.094531
765	7.934444	0.000245	11.3408	0.090147
807	7.939552	0.000243	12.9137	0.089768
848	7.945021	0.000239	14.3419	0.08836
889	7.951848	0.00023	16.1858	0.084948
928	7.958265	0.000231	17.4882	0.085404

Table A5.6 - Refined lattice parameters for V-doped TiP_2O_7 upon cooling – 1st cycle

Temperature / °C	*a* / Å	Error	Zero Error	Error
889	7.958066	0.000193	17.4707	0.071906
848	7.951757	0.000179	16.0167	0.067399
807	7.946175	0.000188	14.3989	0.07107
765	7.940438	0.000181	12.6736	0.06821
723	7.935192	0.00018	11.1752	0.067847
679	7.929723	0.000175	9.58875	0.06585
635	7.92322	0.000173	8.04074	0.065436
590	7.913698	0.00019	6.81729	0.071208
544	7.907715	0.00019	5.60082	0.071888
498	7.902106	0.000192	4.33146	0.072665
450	7.897176	0.000196	3.27896	0.073981
402	7.891768	0.000203	2.02031	0.07657
354	7.887457	0.000205	1.13586	0.077526
304	7.882616	0.000213	-4.06E-03	0.080145
254	7.877864	0.000216	-1.07492	0.08165
203	7.873261	0.00022	-2.05877	0.08317
151	7.868425	0.000223	-3.18976	0.084131
99	7.863945	0.000232	-4.1398	0.087382
45	7.85991	0.000237	-5.02901	0.089499
32	7.85843	0.00024	-5.36142	0.090478

Table A5.7 - Refined lattice parameters for V-doped TiP_2O_7 upon heating – 2nd cycle

Temperature / °C	*a* / Å	Error	Zero Error	Error
45	7.85981	0.000243	-5.07008	0.090904
99	7.864202	0.000231	-4.10001	0.087032
151	7.868612	0.000232	-3.118	0.087339
202	7.873433	0.000223	-2.01767	0.084148
229	7.875864	0.000222	-1.5073	0.083462
254	7.878152	0.000219	-1.05405	0.082103
279	7.880307	0.000216	-0.56684	0.08119
304	7.882499	0.000209	-0.11909	0.079101
329	7.885043	0.000214	0.45305	0.08002
354	7.88745	0.000212	1.03886	0.079967
378	7.889868	0.000205	1.59261	0.076713
402	7.891973	0.000199	2.07876	0.074952
450	7.894663	0.000202	2.71076	0.075952
474	7.896505	0.000201	3.08859	0.075356
497	7.899189	0.000201	3.61519	0.07549
521	7.901469	0.000195	4.1629	0.073272
544	7.904585	0.000195	5.04056	0.073112
589	7.907222	0.000196	5.55014	0.073211
635	7.912815	0.000191	6.86175	0.071731
679	7.918876	0.000185	8.18259	0.069632
723	7.926066	0.000179	9.80115	0.067668
765	7.926062	0.000179	9.79726	0.067722
807	7.940925	0.000171	12.9455	0.064074
848	7.946134	0.000171	14.3515	0.064155
889	7.953046	0.000171	16.1495	0.063913
928	7.960272	0.00017	17.8404	0.0637

Table A5.8 - Refined lattice parameters for V-doped TiP_2O_7 upon cooling – 2nd cycle

Temperature / °C	*a* / Å	Error	Zero Error	Error
889	7.965893	0.000167	20.3149	0.066781
848	7.959867	0.000168	18.8493	0.068051
807	7.954387	0.000168	17.3308	0.068802
765	7.949103	0.00017	15.9331	0.069587
723	7.943979	0.000173	14.4677	0.070986
679	7.938629	0.000172	12.8677	0.070821
635	7.933054	0.000176	11.5008	0.072448
590	7.921899	0.000191	10.113	0.078295
544	7.916198	0.000192	8.93864	0.078273
498	7.910454	0.000197	7.65366	0.081227
450	7.905142	0.000198	6.43823	0.08105
402	7.900312	0.000204	5.27968	0.083307
354	7.895772	0.000214	4.28676	0.087538
304	7.890998	0.000217	3.10513	0.088412
254	7.88627	0.000225	2.05679	0.091891
203	7.881809	0.000222	1.03849	0.090937
151	7.876775	0.000235	-0.16451	0.095545
99	7.872143	0.000235	-1.28818	0.096499
45	7.868443	0.000243	-2.0132	0.099091
32	7.86634	0.000243	-2.5615	0.09929

Appendix 6

Selected Area Electron Diffraction Patterns and d-spacing Calculations

Selected area electron diffraction is crystallographic technique which is carried out inside a TEM. A very high energy electron beam is used in TEM and will pass through a thin sample. If the electrons are treated as waves as opposed to particles, the atoms in a crystalline solid can act as a diffraction grating. As a result, a diffraction pattern will be observed on the TEM screen. Each spot will correspond to a particular crystallographic plane in the crystal structure which satisfies Bragg's law. Figure A6.1 is a diagram to show the spot pattern generation in a TEM.

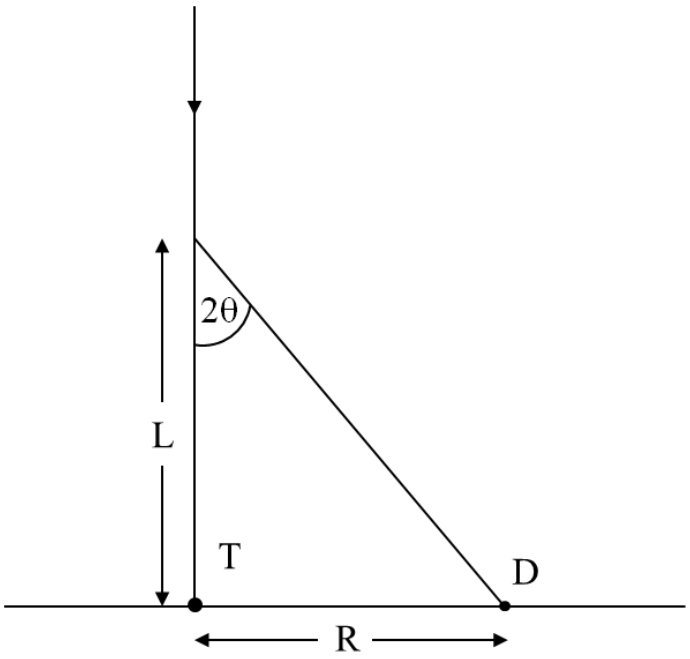

Figure A6.1 - Diagram to show the generation of a spot pattern through electron diffraction by a crystalline sample, where L is the camera length, T is the transmitted beam, D is the diffracted beam and R is the distance between the central spot and the outer spot

Simple geometry shows that from the previous diagram:

$$\tan 2\theta = \frac{R}{L} \tag{A6.1}$$

When θ is small, tan 2θ ≈ sin 2θ, which would give:

$$2 \sin \theta = \frac{R}{L} \tag{A6.2}$$

If we use the Bragg equation:

$$2 \sin \theta = \frac{\lambda}{d} \tag{A6.3}$$

We can derive:

$$Rd = \lambda L \tag{A6.4}$$

where R is the distance between the central spot and the outer spot, d is the d-spacing of the diffracting plane, L is the camera length and λ is the wavelength of the incident electron beam.

The wavelength of the incident electron beam can be calculated from the accelerating voltage of the TEM:

$$\lambda = \frac{12.26}{\sqrt{E}} \tag{A6.5}$$

where E is the accelerating voltage (eV) and λ is the wavelength (Å).

If the TEM has an accelerating voltage over 100 keV, like the microscope used in this work, then relativistic effects need to be considered:

$$\lambda = \frac{12.26}{\sqrt{[E(1 + 0.970 \times 10^{-6} E)]}} \tag{A6.6}$$